

AD _____

Award Number: DAMD17-98-1-8497

TITLE: An On-Line Tomographic Guidance System for Dose
Escalation in Radiotherapy for Adenocarcinoma of the Prostate

PRINCIPAL INVESTIGATOR: David A. Jaffray, Ph.D.

CONTRACTING ORGANIZATION: William Beaumont Hospital
Royal Oak, Michigan 48073-6769

REPORT DATE: August 2001

TYPE OF REPORT: Final, Phase I

PREPARED FOR: U.S. Army Medical Research and Materiel Command
Fort Detrick, Maryland 21702-5012

DISTRIBUTION STATEMENT: Approved for Public Release;
Distribution Unlimited

The views, opinions and/or findings contained in this report are those of the author(s) and should not be construed as an official Department of the Army position, policy or decision unless so designated by other documentation.

20020610 015

REPORT DOCUMENTATION PAGE			Form Approved OMB No. 074-0188	
Public reporting burden for this collection of information is estimated to average 1 hour per response, including the time for reviewing instructions, searching existing data sources, gathering and maintaining the data needed, and completing and reviewing this collection of information. Send comments regarding this burden estimate or any other aspect of this collection of information, including suggestions for reducing this burden to Washington Headquarters Services, Directorate for Information Operations and Reports, 1215 Jefferson Davis Highway, Suite 1204, Arlington, VA 22202-4302, and to the Office of Management and Budget, Paperwork Reduction Project (0704-0188), Washington, DC 20503				
1. AGENCY USE ONLY (Leave blank)	2. REPORT DATE August 2001	3. REPORT TYPE AND DATES COVERED Final, Phase I (1 Oct 98 - 2 Jul 01)		
4. TITLE AND SUBTITLE An On-Line Tomographic Guidance System for Dose Escalation in Radiotherapy for Adenocarcinoma of the Prostate		5. FUNDING NUMBERS DAMD17-98-1-8497		
6. AUTHOR(S) David A. Jaffray, Ph.D.				
7. PERFORMING ORGANIZATION NAME(S) AND ADDRESS(ES) William Beaumont Hospital Royal Oak, Michigan 48073-6769 E-Mail: djaffray@beaumont.edu		8. PERFORMING ORGANIZATION REPORT NUMBER		
9. SPONSORING / MONITORING AGENCY NAME(S) AND ADDRESS(ES) U.S. Army Medical Research and Materiel Command Fort Detrick, Maryland 21702-5012		10. SPONSORING / MONITORING AGENCY REPORT NUMBER		
11. SUPPLEMENTARY NOTES				
12a. DISTRIBUTION / AVAILABILITY STATEMENT Approved for Public Release; Distribution Unlimited			12b. DISTRIBUTION CODE	
13. ABSTRACT (Maximum 200 Words) <p>There is strong evidence to support the hypothesis that increasing radiation dose to the prostate will increase the probability of cure. A major difficulty in pursuing dose escalation is the toxicity induced in the surrounding normal tissues. These normal tissues are irradiated as a consequence of planning margins used to guarantee the delivery of the prescribed dose to the entire clinical target volume (prostate and seminal vesicles). The margins are constructed from clinical knowledge of uncertainties in daily patient positioning and organ motion. In these investigations, a new imaging technology, cone-beam computed tomography (CT) was developed to localize the prostate and surrounding tissues on a daily basis, allowing the radiation field to be applied with great precision. By increasing precision, more conformal treatment fields can be applied, reducing the dose to surrounding normal tissues and allowing the safe pursuit of dose escalation. This new imaging modality, flat-panel based cone-beam CT, has been developed to permit soft-tissue imaging in the radiation therapy setting. Images acquired with this system are of sufficient quality to permit direction of the daily treatment, permitting dramatic (15%) increases in dose escalation. The next major challenge is in the development of a clinical process to employ this valuable new information.</p>				
14. SUBJECT TERMS Prostate			15. NUMBER OF PAGES 197	
			16. PRICE CODE	
17. SECURITY CLASSIFICATION OF REPORT Unclassified	18. SECURITY CLASSIFICATION OF THIS PAGE Unclassified	19. SECURITY CLASSIFICATION OF ABSTRACT Unclassified	20. LIMITATION OF ABSTRACT Unlimited	

Table of Contents

Cover.....	1
SF 298.....	2
Table of Contents.....	3
Introduction.....	4
Body.....	4
Key Research Accomplishments.....	8
Reportable Outcomes.....	9
Conclusions.....	10
Appendices (A-K)	11

Original (Phase I) Proposal Title: An On-Line Tomographic Guidance System for Dose Escalation in Radiotherapy for Adenocarcinoma of the Prostate (DAMD17-98-1-8497)

Original (Phase I) Award Category: New Investigator Award

Principal Investigator (PI): David A. Jaffray, Ph.D.
 Phone: (248) 551-7024
 FAX: (248) 551-0089
 e-mail: djaffray@beaumont.edu
 Organization: William Beaumont Hospital
 Royal Oak, Michigan 48073
 USA

Introduction There is strong evidence to support the hypothesis that increasing radiation dose to the prostate will increase the probability of cure. A major difficulty in pursuing dose escalation is the toxicity induced in the surrounding normal tissues. These normal tissues are irradiated as a consequence of planning margins used to guarantee the delivery of the prescribed dose to the entire clinical target volume (prostate and seminal vesicles). The margins are constructed from clinical knowledge of uncertainties in daily patient positioning and organ motion. In these investigations, it was proposed that a new imaging technology, cone-beam computed tomography (CT), can be used to localize the prostate and surrounding tissues on a daily basis, allowing the radiation field to be applied with great precision. By increasing precision, more conformal treatment fields can be applied, reducing the dose to surrounding normal tissues and allowing the safe pursuit of dose escalation. Preliminary investigations have demonstrated the potential of cone-beam CT in guiding therapy. To bring this exciting technology to the clinic, cone-beam CT must be evaluated specifically for radiotherapy of the prostate, and the dosimetric benefits of the image-guidance method need to be quantified. This has been achieved in these investigations through three tasks: 1) evaluation of a new detector technology (flat-panel imager (FPI)) for cone-beam CT, 2) prediction of the clinical advantages of high-precision image-guidance, and, 3) demonstration of cone-beam CT imaging performance on a small group (15) of patients receiving radiotherapy of the prostate. Tasks #1 and #2 have been completed in their entirety and Task #3 has not been completed due to significant and frustrating delays in the delivery of a hardware assembly necessary for imaging tests on human subjects. Despite these delays, significant progress has been made in the testing, integration, and evaluation of a prototype hardware assembly that was constructed in-house. In the following report, the results of the extensive investigations will be presented with references to the over 11 peer-reviewed publications that have resulted from these investigations, as well as the four grants (3 peer-reviewed extramural, 1 industrial) for which this work has provided preliminary results. The presentation of results will adhere to structure defined by the three tasks set out in the original proposal, identifying areas of great success as well as those fraught with challenges.

Body

Task 1. Determine relationship between delivery precision and allowable target dose for intensity modulated radiation therapy of the prostate, Months 1-8

The evaluation of the potential therapeutic gain required the collection of a large database of clinical CT images for patient's currently undergoing radiotherapy of the prostate. Fortunately, the accelerated recruitment of patients in the study protocol, allowed these images to be collected before the onset of these investigations. However, there has been a significant

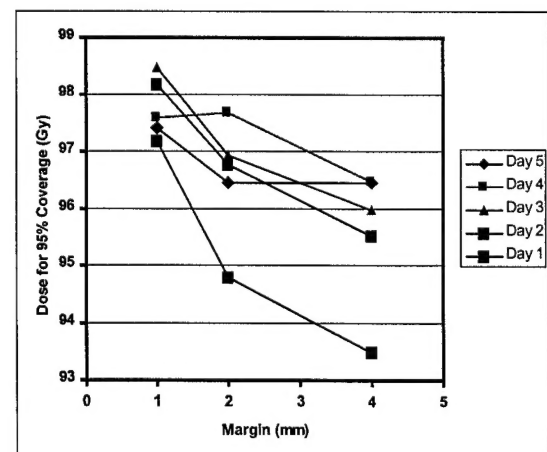


Figure 1: Minimum dose to the planning target volume vs margin for a single patient. Each curve corresponds to a different anatomical configuration of the same patient (i.e. different days).

effort in re-formatting and contouring these clinical CT scans for use in the dose escalation simulations. An initial study based on a small subset of the clinical database demonstrated the potential advantages assuming a fixed relationship between the prostate gland and rectum was accepted for publication (Appendix A). The relationship between minimum delivered dose in the prostate and margin was studied. This study demonstrated that the increase in precision that would be expected with our image-guided approach would allow the minimum prostate dose to exceed 90 Gy, a substantial increase over conventional approaches (70-75 Gy). Figure 1 demonstrates the dramatic effect of reducing margin on dose escalation. It also illustrates the day-to-day variation in the allowable dose that can be delivered for a fixed dose to the rectal wall. The use of larger margins results in more variability in the allowable daily dose. This is a reasonable result considering the fact that the spacing between the rectal wall and prostate is on the order of the margins proposed here (1-8 mm). In some cases, margins less than 4 mm may result in no overlap between the planning target volume and the rectal wall, avoiding the constraints on the escalation imposed by the rectal wall. The study has been completed for 5 patients with 5 scans each from different days. These are evaluated for 3 different margins (1,2,4mm). These results are consistent with that found in our original study, allowing dose escalation by 15% for equivalent dose-volume relationship in the rectal wall. The results of these more detailed investigations are being prepared for publication.

Task 2. Characterize the image quality and targeting precision of the on-line cone-beam CT guidance system, Months 9-24

A major focus of our investigations has been on the demonstration of this technology for visualization of soft-tissue structures in the radiation therapy setting. These developments proceeded with the construction of a precision test bed to allow computer-controlled acquisition of CBCT data at a geometry that exactly replicates the geometry to be employed on the accelerator (Appendix B, Fig. 1). Several aspects of the prototype imaging system were investigated. The results of our investigations into detector lag demonstrate the magnitude of signal lag for a variety of exposure conditions and operating modes of the flat panel detector (Appendix B). The impact of detector lag on cone-beam CT performance was studied using both the bench-top prototype and a simulation model (Appendix C). The results of these investigations have been accepted for publication in the journal

of

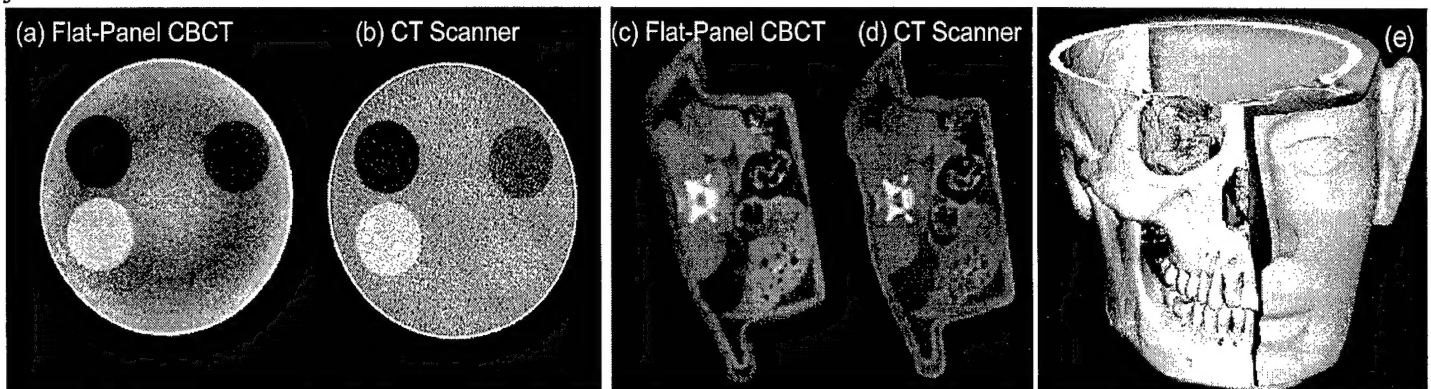


Figure 2. Images acquired with the FPI-CBCT prototype in comparison to a conventional CT scanner at equivalent kVp and exposure. (a and b) Images of a low-contrast phantom containing six inserts (clockwise from top): CT solid water, BR-SR1 breast, BRN-SR2 brain, CB-3 resin, LV1 liver, and polyethylene. (c and d) Axial images of a euthanized rat (e) Image of head phantom demonstrating isotropic resolution of cone-beam approach.

Medical Physics. The magnitude of the lag artifacts depend on the magnitude and lifetime of the lag signal. Our initial measurements of lag suggest that this should not be a significant problem for the detector studied here. Cone-beam images acquired on the prototype demonstrated that the lag is not playing a dramatic role (Fig. 2). The magnitude and effects of x-ray scatter are of significant concern in the cone-beam geometry. While scatter cannot be easily eliminated, our studies suggest that image quality can be restored with an increase in slice thickness (to 0.5 mm) and a 2-3 times increase in dose (Appendix F). Both of these requirements are well

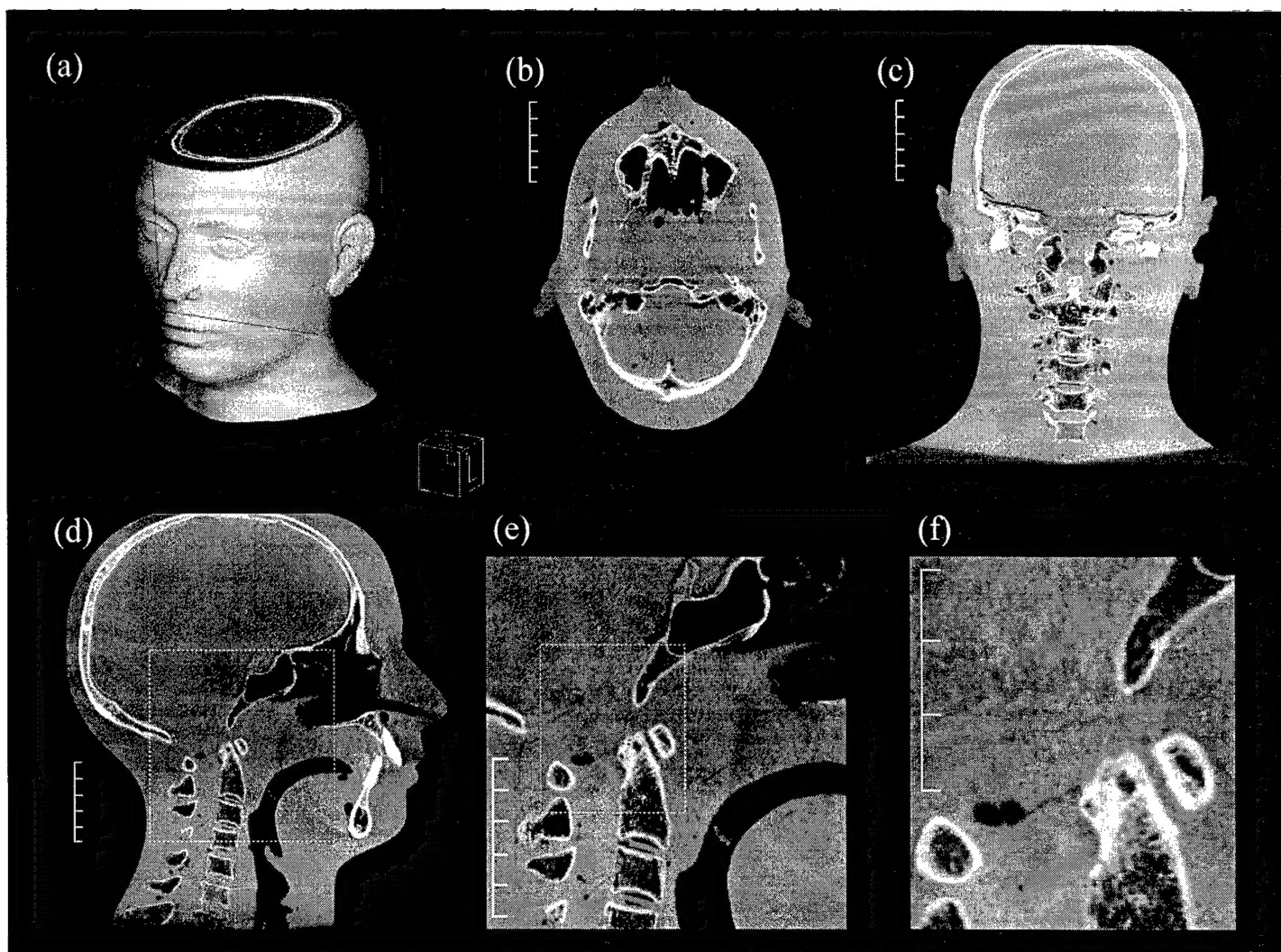


Figure 3. Images acquired with the FPI-CBCT prototype mounted on the medical linear accelerator. These images were acquired in 180s and demonstrate the high spatial resolution that can be achieved with this exciting new technology. The system permits a large (25.6 cm)³ FOV while maintaining 0.5 mm resolution. This is illustrated in (f) All data shown comes from a single rotation of the gantry (see Figure 4).

within the constraints for image-guided radiotherapy. The overall configuration of the cone-beam CT geometry was also analyzed using a unique model to include the effects of x-ray scatter on the detective quantum efficiency of the system (Appendix E). This method demonstrated that the configuration employed in the accelerator mimicking geometry is near the optimal for the focal spot, scatter, and noise performance of the detector employed in our investigations. It also indicates that the use of a high magnification (1.6) is an effective approach to reduce the deleterious effects of scattered x-rays.

The overall performance of the prototype cone-beam CT system was studied using a variety of methods. The results of these investigations have been published in the journal of Medical Physics (paper received Sylvia Sorkin Greenfield award for best paper in Medical Physics, 2000). A major component of these investigations was to measure the noise performance of the cone-beam CT prototype and compare it's performance to that of a conventional diagnostic scanner. These investigations were performed using a simple cylindrical water bath. Images of the water bath were acquired at a range of clinical exposure levels (0.13 – 6.53 R) on both systems and their voxel noise was compared for equivalent exposure, reconstruction filter, and slice thickness. Both systems demonstrate comparable signal-to-noise performance and the expected inverse-root-exposure dependence. Other measures of performance including noise-power studies, modulation transfer measurements, and contrast resolution support the hypothesis that these flat panel detectors can be used to generate high-quality CT images sufficient for use in guiding radiation therapy of the prostate. The images presented in Figs. 2&3 demonstrate the current performance of this system. Given the success of these investigations, it is clear that

the original hypotheses are still valid. In addition to evaluating the performance of the imaging system that has been constructed, a method for predicting the performance of cone-beam CT systems has also been developed (Appendix G). In this approach, the performance can be set to match the imaging task at hand. This concept has been explored further and a proposal to evaluate cone-beam CT for image-guidance in radiation therapy (external beam and brachytherapy) was submitted to the National Institute of Health for funding. This has been funded as an R01 for a 4 year period (D.Jaffray, Principal Investigator). Additional applications for cone-beam CT based upon FPI technology are appearing on a daily basis. The understanding of the cone-beam CT method and our ability to predict the performance has allowed consideration of these applications (Appendix J). Industrial funding for the application of cone-beam CT on a C-arm platform has been secured from Siemens Medical Systems over the next two years. This new funding is a direct by-product of the work performed under this Phase I award.

Additional investigations were also performed to evaluate the relative performance of megavoltage (MV) and kilovoltage (kV) cone-beam CT for patient positioning in radiation therapy (Appendix H). The ability to predict imaging performance at both the kV and MV x-ray range was demonstrated in these investigations. The clear advantage of the kV energy range over MV is demonstrated in Appendix H, Fig. 9. The dose penalty for use of the MV beam is significant for equivalent image quality.

Task 3. Demonstrate the clinical feasibility of performing on-line treatment guidance on a group of men (15) receiving radiation therapy for cancer of the prostate, Months 25-30

The imaging performance of the FPI-based cone-beam CT system for detection of the prostate was investigated using a prostate phantom that was constructed based upon our in-house library of prostate CT scans. The phantom was imaged at a 0.38 cGy dose level and is shown in Appendix J-Fig. 6c. The prostate bounding fat capsule is clearly visible even for a very thin reconstructed slice thickness (1mm). Similar investigations were performed with brachytherapy sources (Pd-103) implanted in the phantom. The application in image-guided brachytherapy is very promising. Given these results, a prototype system based upon the large area detector was constructed (see Figure 4). This system suffers from flex induced by gravity during rotation and requires corrections to maintain image quality. Figure 4 shows a graph of such corrections. Fortunately, these corrections can be applied during the back-projection process without significant delay. The importance of these corrections is illustrated in the publication located in Appendix I (see Fig. 6). Overall, an integrated system for cone-beam CT on the accelerator has been constructed. However, the prototype is too burdensome to employ in the clinical setting, preventing its use in the proposed clinical investigations for Task 3. For this reason, our industrial collaborator (Elekta Oncology Systems) was contacted to construct such an arm. Unfortunately, the proposed time line has slipped by nearly 12 months, preventing collection of the images of patients as originally proposed. In recent discussion with Elekta Oncology Systems, the support arm is now scheduled for delivery at the end of September 2001. It is in the interest of this program of research to complete these investigations by whatever means possible. All other components are in place (software, reconstruction, calibration, etc.). The completion of Task #3 is critical to the pursuit of high-precision radiation therapy of the prostate and will be completed by the end of 2001.

An investigation of the clinical process for image-guided RT of the prostate was examined. The study tested the overall feasibility of cone-beam CT guided radiotherapy on the linear accelerator using a prostate phantom that simulates the CT characteristics of the human prostate. The phantom was formed of polystyrene and contained a machined cavity in the shape of a human prostate. The cavity was filled with a contrasting agent with contrast comparable to the prostate-fat boundary in a human (~50 HU elevation). Using this phantom the complete process of cone-beam imaging (based on the earlier CCD detector system), target localization and contouring, treatment planning, and radiation delivery was tested in a single setting. The blinded delivery of the radiation dose was measured using radiographic film contained within the prostate phantom. The delivered dose distribution was located to within 1.5 mm of the desired location using cone-beam CT guidance. No external fiducials were used in placing the phantom and the location of the prostate within the phantom was not

known prior to setup. This study demonstrated that the tools and technology necessary for on-line tomographic guidance are available. It was also a conclusion of this investigation that additional effort must be made in accelerating reconstruction times and developing a system for rapid planning and image interpretation.. From these investigations it was concluded that it is feasible to pursue the construction of an on-line tomographic imaging system for image-guided radiotherapy of the prostate. The construction of such a system requires substantial funding. A proposal was submitted to the NIH in the form of a combined R21/R33 grant entitled "High-precision radiotherapy of the prostate" and funding was approved. This grant focuses on the development of the clinical tools necessary for the rapid imaging, planning and delivery process required for high-precision radiation therapy of the prostate. The investigations begin with the characterization of high-speed motion of the prostate in the intra-fraction time interval.

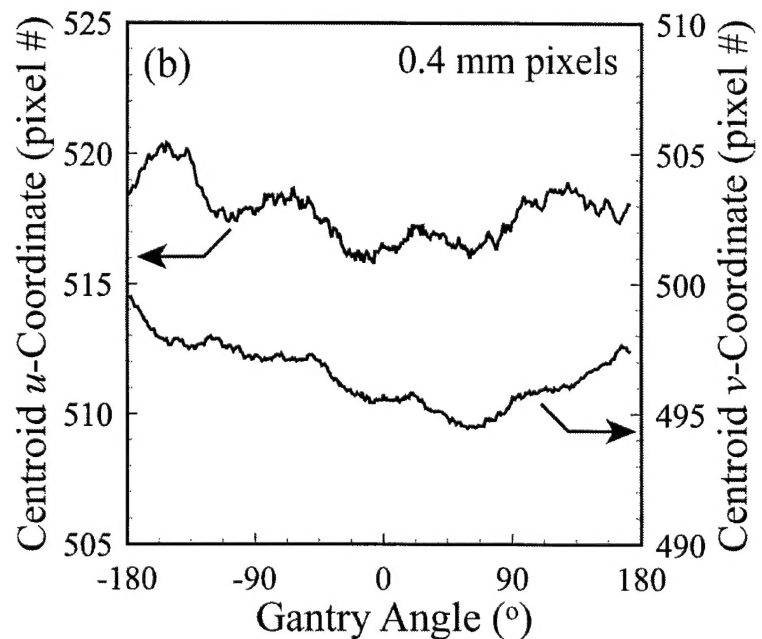
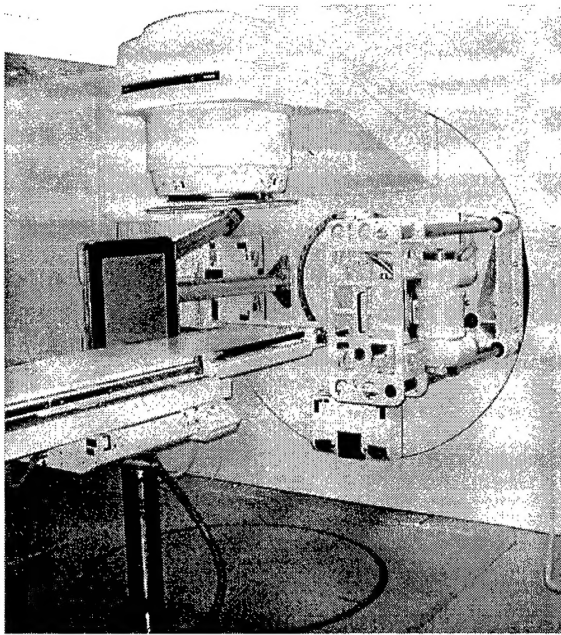


Figure 4. Current configuration of the accelerator-based FPI cone-beam CT system (left). In this configuration, the full-size 41x41 cm² detector is employed to produce a 25.6 cm FOV. Large FOV is to be achieved with a detector offset. By employing this detector in an offset geometry, the cone-beam CT system will achieve a 50 cm aperture. The graph on the right contains a plot of the corrections that must be applied to the back-projection geometry to accommodate the presence of flex in the assembly. The influence of these corrections on image quality is demonstrated in Appendix I.

Key Research Accomplishments:

1. Benchmark evaluation of flat panel technology for cone-beam CT.
2. Demonstration of the importance of x-ray scatter in cone-beam CT.
3. Construction of a model for high-precision radiation therapy of the prostate.
4. Development of a model for the prediction of noise performance in cone-beam CT.
5. Determination of the potential gains in dose escalation given high-precision RT of the prostate.

3. Reportable Outcomes:

Manuscripts:

1. D. A. Jaffray, D. G. Drake, M. Moreau, A. A. Martinez, and J. W. Wong, "A radiographic and tomographic imaging system integrated into a medical linear accelerator for localization of bone and soft-tissue targets," *Int. J. Rad. Onc. Biol. Phys.* 44(5) (1999).
2. Jaffray DA, Siewerdsen JH, and Drake DG, "Performance of a volumetric CT scanner based upon a flat-panel imager," *SPIE Physics of Medical Imaging Vol. 3659204* - 214 (1999).
3. Siewerdsen JH and Jaffray DA, "A ghost story: spatio-temporal response characteristics of an amorphous silicon flat-panel imager," *Med Phys* 26(8) 1624-1641 (1999).
4. Siewerdsen JH and Jaffray DA, "Cone-beam computed tomography with a flat-panel imager: effects of image lag," *Med Phys* 26(12) 2635-2647 (1999).
5. Jaffray DA and Siewerdsen JH, "Cone-beam computed tomography with a flat-panel imager: initial performance characterization," *Med. Phys.* 27(6) 1311-23. (2000)
6. Siewerdsen JH and Jaffray DA, "Optimization of x-ray imaging geometry (with specific application to flat-panel cone-beam computed tomography)," *Med. Phys.* 27(8) (2000)
7. Siewerdsen JH and Jaffray DA, "Cone-beam CT with a flat-panel imager: effects of x-ray scatter," *Med Phys.* 2001 Feb;28(2):220-31
8. D. A. Jaffray, D. G. Drake, D. Yan, L. Pisani, and J. W. Wong, "Conebeam tomographic guidance of radiation field placement for radiotherapy of the prostate," *Int. J. Radiat. Oncol. Biol. Phys.* (Accepted, 1999)
9. Groh B, Siewerdsen JH, Drake DG, Wong JW, and Jaffray DA, "Performance characterization of MV and kV cone-beam CT," *Med. Phys.* (accepted, 2000)
10. D.A. Jaffray, J.H. Siewerdsen, J.W. Wong, A.A. Martinez, "Flat-Panel Cone-Beam Computed Tomography for Image-Guided Radiation Therapy," *Int. J. Radiat. Oncol. Biol. Phys.* (accepted, 2001)
11. J. H. Siewerdsen and D. A. Jaffray, "Cone-beam CT with a flat-panel imager: noise considerations for fully 3-D computed tomography," to appear in *SPIE Physics of Medical Imaging 2000* (February 2000).
12. D. A. Jaffray, J. H. Siewerdsen, and D. G. Drake, "Performance of a volumetric CT scanner based upon a flat-panel imager," in *Medical Imaging 1999: Physics of Medical Imaging*, J. M. Boone and J. T. Dobbins III Eds., *Proceedings of SPIE Vol. 3659*, 204-214 (1999).
13. J.H. Siewerdsen, D.A. Jaffray, G.K. Edmundson, W.P. Sanders, J. Wong, A.A. Martinez, "Flat-Panel Cone-Beam CT: A Novel Imaging Technology for Image-Guided Procedures," *Proceedings of SPIE Medical Imaging: Image Display Visualization and Image-Guided Procedures*, (2001).
14. D.A. Jaffray, J.H. Siewerdsen, "A Volumetric Cone-Beam Computed Tomography System Based on a 41x41 cm² Flat-Panel Imager," *Proceedings of SPIE Medical Imaging: Physics of Medical Imaging Vol. 4320* pg. 800 (2001)

Patents (Pending)

- 1) Flat-panel Cone-beam CT for Image-guided External Beam Radiotherapy, Inventors: D.A. Jaffray, J.H. Siewerdsen, J. Wong, Applicant: William Beaumont Hospital, Representation: Harness, Dickey and Pierce, Troy, MI

Grants (applied for and funded)

- 1) **Principal Investigator**, National Cancer Institute (NCI), NIH, "Flat-Panel Cone-Beam CT for Image-Guided Radiotherapy," 2001, R01-CA89081, (\$1,079,708 – 4 years) –

- 2) **Principal Investigator**, Siemens Medical Systems – SP Group, “Flat-Panel Cone-Beam CT on a Mobile C-arm,” 2001, (\$310,000 – 2 years)
- 3) Co-investigator, William Beaumont Hospital, Internal Grant, “A new 3D optical gelsdosimetry system for clinical verification of highly conformal radiation-therapy techniques,” (Oldham) 2001 (\$78,071 - 1 year)
- 4) **Principal Investigator**, National Cancer Institute/National Institute of Aging, NIH, “High-Precision Image-Guided Radiotherapy of the Prostate,” 2001, R21/R33-AG19381 (\$2,021,038 – 4 years)
- 5) **Principal Investigator**, DOD Prostate Cancer Research Program, Phase 2 - New Investigator Award, “On-line Tomographic Guidance for Radiotherapy of the Prostate,” 2000, - (\$392,000 – 2 years)

Bibliography of All Publications

(see Manuscripts, above)

Personnel paid from this support

- 1). Dr. David A. Jaffray, Ph.D. – Principal Investigator
- 2). Dr. Jeffrey Siewerdsen, Ph.S. – Research Scientist
- 3) Ayush Batra, Summer Student
- 4) B. Groh, Visiting Graduate Student

Conclusions: The results of these investigations have strengthened our initial hypothesis that a significant increase in dose could be pursued with the use of image-guided radiotherapy. Furthermore, the investigations of imager performance have demonstrated that the new flat panel detector technology offers the performance necessary for high-quality tomographic images to be acquired in the therapy setting. Concerns of detector lag, additive noise, and x-ray scatter have been addressed and are not prohibitive factors in the development of a cone-beam computed tomography system for image-guided radiotherapy of the prostate or other sites. With this new technology, we have embarked in the construction of a new type of radiation therapy system that allows the radiation oncologist to guide the placement of radiation dose with a precision that has never before been possible. These developments will not only impact therapy of the prostate, but will also have significant implications for the entire field of radiation therapy.

In addition to the development of a new imaging technology for radiation therapy, it has become clear that this technology is well-suited to a variety of image-guidance applications ranging from brachytherapy to vertebroplasty (see Appendix J). Furthermore, the development of imaging information in the therapeutic setting challenges the existing model and tools employed in these procedures. It is becoming clear that performing therapy in an image-guided environment is a great deal different from conventional procedures, requiring a tight integration between the imaging procedure, the imaging data, and the therapeutic agent.

As outlined in this report, the pursuit of a high-precision system for radiation therapy of the prostate is underway, promising to bring a dramatic increase in dose conformity and therefore dose escalation for early and mid-stage prostate cancer without a corresponding increase in the occurrence of rectal complications.

Appendices

**Appendix A: Cone-Beam Tomographic Guidance of Radiation
Field Placement for Radiotherapy of the Prostate**

CONEBEAM TOMOGRAPHIC GUIDANCE OF RADIATION FIELD PLACEMENT FOR RADIOTHERAPY OF THE PROSTATE

D.A. Jaffray Ph.D.^(a,b), D.G. Drake, B.S.^(a,b), D. Yan, D.Sc.^(a,b)
L. Pisani, M.Sc.^(a,b), J.W. Wong, Ph.D.^(a,b)

a) Department of Radiation Oncology
William Beaumont Hospital, Royal Oak, Michigan 48073

b) Department of Physics
Oakland University, Rochester, Michigan 48309

Oral Presentation at the 1998 ASTRO Meeting
Pheonix, AZ - October 1998

Reprint requests to:

D.Jaffray, Ph.D.,
Dept. of Radiation Oncology
William Beaumont Hospital
Royal Oak, MI 48073
Ph: (248) 551-7024
Fax: (248) 551-0089
e-mail: djaffray@beaumont.edu

*Manuscript accepted for publication in the International Journal of Radiation
Oncology, Biology, and Physics (in press).*

Introduction: Involuntary movement of the prostate gland and rectal wall constrains the radiation dose that can be confidently delivered to the entire gland by external beam irradiation. Conventionally, a prescribed coverage dose is achieved in the presence of these targeting uncertainties by irradiating a planning target volume (PTV) determined from the clinical target volume (CTV) plus a margin (typically > 8mm). This coverage dose is limited by the inclusion of the rectum and bladder in the PTV. In this study, we (i) examine the relationship between achievable coverage dose and targeting precision for intensity modulated external beam irradiation of the prostate, and (ii) report the targeting precision of an on-line tomographic guidance system, indicating the coverage dose that can be delivered safely with such a system.

Materials and Methods: A cone-beam tomographic imaging system is installed on an Elekta SL-20 to explore on-line tomographic guidance of field placement. Multiple (180) kV exposures (120 kVp) are produced over 360° of continuous gantry rotation. The images are collected using a CCD-based fluoroscopic imaging system that is mounted on the accelerator opposite an x-ray tube. The images are corrected for flex in the detector assembly and a filtered back-projection technique is used to reconstruct 100 slices (each 2mm thick). The resulting volumetric dataset is imported into a 3D treatment planning system for contouring the target and for automated field-shaping. The resulting fields are exported to the multi-leaf collimator (MLC) field shaping system and transferred to the linear accelerator for delivery. The fields are then delivered to the targeted volume. The process is demonstrated on a prostate phantom constructed to simulate the computed tomography imaging characteristics of a prostate. Radiographic film is located at the central transverse slice within the phantom to verify

the geometric placement of the planned dose distribution. A simple four-field beam arrangement is delivered and the relative position of the dose distribution and the target boundary are compared.

Results and Discussion: The relationship between targeting precision and minimum dose for a fixed rectal wall dose and volume (<72 Gy rectal wall) indicates that a covering dose of 85 Gy could be achieved with a margin of 0.4 cm. The entire on-line guidance process has been demonstrated on the prostate phantom. The total time was 111 min., due largely to the reconstruction; the scanning procedure required 11 min. The targeting accuracy of the system is demonstrated by comparing the location of the measured dose distribution to the desired coverage volume at the central slice. Measurements indicate that the dose distribution can be placed within 0.2 cm of the specified location soft-tissue structure.

Conclusions: The relationship between targeting precision and coverage dose (minimum) has been determined for a specific beam configuration as applied to the prostate. On-line tomographic guidance has been demonstrated on a medical linear accelerator equipped with a kV imaging system. These feasibility studies suggest that significant dose escalation could be safely pursued with an on-line tomographic guidance approach for radiotherapy of the prostate and that technology exists to make such an approach feasible.

Keywords: conebeam tomography, guidance, on-line, prostate, radiotherapy

Acknowledgments

The authors would like to thank the National Cancer Institute (CA-66074, CA-71785) and the U.S. Army (PCRP-970201) for supporting this work. The inverse planning system used in the study was provided by MRC Systems, their assistance is appreciated. The support of Elekta Oncology Systems is also greatly appreciated.

1. Introduction

Dose escalation in radiotherapy of the prostate is constrained by the presence of adjacent structures, most strongly by the rectal wall, *and* by the targeting imprecision due to setup error and organ motion. Because adjacency is a key factor, field generation techniques that can increase dose gradients and create conforming shapes, such as intensity-modulated radiation therapy (IMRT), can play an important role in attempting to escalate dose.⁵ The gains in using IMRT depend on the targeting precision that can be achieved for treatment, and likewise, the converse is true; increasing targeting precision will not necessarily prove advantageous unless highly conformal distributions, like that generated through IMRT, can be employed.

An example that demonstrates this inter-relationship is occasionally found in radiotherapy of the prostate, in which, the prostate has a concave posterior surface and the rectal wall forms the corresponding convex surface. The use of a complex IMRT scheme to produce a concave dose distribution is only of value if the margins used for setup uncertainty and organ motion are not so large that the concavity has been eroded. This inter-relationship requires that planning studies of treatment techniques must consider both the conformity of the three-dimensional (3D) dose distribution that can be generated and the targeting precision that can be achieved in placing the distribution.

In this article, we (1) report on a planning study that explores the dosimetric advantage of improved targeting precision on radiotherapy of the prostate, (2) illustrate the capability of an on-line tomographic imaging system for localization of the prostate, and, (3) demonstrates the feasibility of achieving high targeting precision for soft-tissue targets based on a conebeam tomographic guidance system installed on our

accelerator. This device, combined with an IMRT capable micro-multileaf collimator (micro-MLC)⁷, is to ultimately form the basis of a system for on-line tomographic guidance of radiation field placement in treatment of the prostate.

II. Materials and Methods

A. Minimum Coverage Dose vs CTV-PTV Margin: A Treatment Planning Study

Treatment planning computed tomography (CT) datasets from 4 patients receiving radiotherapy of the prostate were used in the study. The prostate, rectal wall, bladder, seminal vesicles, and external contour were defined using the Pinnacle³ treatment planning system. The Konrad inverse planning system (MRC Systems GmbH, Heidelberg) was used to perform inverse planning⁶. The parameters used in the inverse planning are listed in Table I

For each of the four cases studied, an inverse plan was generated for 0, 2, 4, 6, 8, and 10 mm margins. These margins were applied as a full 3D expansion of the CTV (taken to be the GTV, i.e. the prostate gland as defined on CT) using the Pinnacle³ planning system. The inverse solution was constrained by the DVH for the rectal wall as produced by a conventional 4-field plan for a PTV constructed from the CTV (prostate bound) and a 10 mm uniform margin to accommodate setup uncertainty and organ motion. The coverage dose in the 4-field plan was 72 Gy. The minimum dose in the PTV was recorded for each combination of margin and case. The average of these minimum doses was calculated for each margin to demonstrate the relationship between coverage dose and margin.

B. On-line Tomographic Guidance: A Feasibility Study

i) Tomographic Guidance System

In a previous study, the components of a system with radiographic and tomographic guidance were described in detail.² Briefly, an Elekta SL-20 medical linear accelerator (Elekta Inc., Atlanta, GA 30329) has been modified to perform kilovoltage (kV) radiographic exposures. This is achieved through the installation of a conventional x-ray tube at 90 degrees with respect to the treatment beam. Opposite the x-ray tube is a CCD-based fluoroscopic detector that is used to capture the transmitted x-rays.

Figure 1 shows a photo of the system. The radiographic system has been employed to generate multiple exposures through a 360 degree rotation of the gantry. These multiple images are used to generate a conebeam tomographic image of any object in the detector's field-of-view (cylinder 20cm long x 25cm in diameter).

The tomographic acquisition produces 180 radiographs through 360 degrees of gantry rotation in an 11 minute period. Sufficient information is acquired in a single revolution of the gantry to allow reconstruction of a volumetric image series. The projection images are filtered and back-projected into the reconstruction volume using Feldkamp's algorithm.¹ A modification to the algorithm has been made to compensate for detector and source flex. The algorithm adjusts the sampling of the back-projection ray in the reference frame of each projection image.

In a separate calibration session, the detector and source flex are characterized by measuring the centroid of a shadow cast by a large steel ball (~0.8 cm in diameter) in images acquired through 360 degrees. The ball is located at a known position with respect to the treatment isocenter of the linear accelerator. The method used for the correction assumes that the source travels in a circular orbit and all the variations in shadow position are due to displacements in the sampling grid of the detector system.

Repeat measurements of these flex corrections indicate that the corrections are stable over very long periods (months) with sub-millimeter precision. This calibration data is also used to reference the reconstructed dataset to the treatment isocenter of the accelerator. This is achieved by placing the steel ball at a known location with respect to the treatment isocenter. With this calibration performed, the multiple CT slices reconstructed by the conebeam algorithm can be drawn into the planning system (Pinnacle³, ADAC Laboratories, Milpitas, CA 95035) without the need for isocenter identifying fiducial marks. The rotation of the image set is controlled by setting the gantry starting angle to -180 degrees (± 0.05 degrees) with a digital level.

The treatment planning system is used to define the contours of the target and to automatically shape the treatment fields. The beam's-eye-view for each image is transferred to the MLC field shaping workstation for transfer to the MLC of the linear accelerator.

ii) Soft-tissue Contrast Sensitivity of the Conebeam System

On-line tomographic guidance of radiation field placement will only prove useful if the prostate bound can be clearly delineated in the reference frame of the accelerator. The ability to detect the prostate gland is demonstrated in a conebeam CT scan of an anesthetized dog. In this study, the dog was placed on a wooden couch extension. A total of 181 projections were acquired over 360 degrees. Upon completion of reconstruction, it was evident that the dog moved after approximately 180 degrees of rotation. A final CT dataset was reconstructed using only the first 90 projections. The reconstruction was performed on 0.1 cm slices. After reconstruction the dataset was compressed to 0.6 cm slices by simple averaging. The structures of interest in this

dataset are the dog's prostate and rectum. It should be noted that the dog scanned in the study was neutered. This results in a significant reduction in the size of the dog's prostate gland.

iii). Demonstration of Tomographic Guidance on a Prostate Phantom

The use of the system for tomographic guidance was demonstrated using a phantom that simulates the shape and CT contrast of the prostate gland (Figure 2). The phantom is constructed of 13 polyethylene sheets (5" x 5.5" x 3/16" thick), in which, the negative of an actual prostate has been milled to a depth of 5/32". For each sheet, the negative is filled with a lard and barium mixture that produced a 50 Hounsfield Unit elevation in CT number with respect to the polyethylene sheets; the 50 HU elevation is verified on a conventional scanner at 120 kVp. These sheets are constructed to fit within the Nomos "battery" phantom (NOMOS Corporation, Sewickley, PA 15143). The sheets can be used with or without the light-tight container. In the experiments reported here, the container was not used, but rather, the sheets were fixed in rigid relation with respect to each other. A small gap (~1cm) was left in the middle of the phantom's layers to allow reproducible insertion of a light-tight polyethylene cassette which contained Kodak XV-2 radiographic film (Eastman-Kodak Corporation, Rochester, NY 14650).

The phantom was scanned on a wooden couch extension with the conebeam scanning technique described in the previous section (181 projections, 360 degrees, 3.75 mAs/projection, 120 kVp). For this scan, a dummy film cassette was positioned in the phantom. After the scan was complete, a one-hundred slice CT dataset was reconstructed with 0.2 cm thick slices and a 0.084 cm resolution (281 x 281 matrix). The CT dataset was drawn into the planning system and the prostate contour was

outlined. For the slices corresponding to the film cassette, the planning system was used to interpolate contours in this region. This volume was used as the target volume with no additional margin. A four-field beam arrangement (6 MV x-rays, Elekta SL-20) was applied to the 3D volume with automatic MLC field shaping. The monitor units for the delivery were calculated. A density over-ride of the CT numbers is necessary for the conebeam dataset, as accurate CT numbers are not reported by the system. These MLC field shapes were transferred to the accelerator for treatment. Before delivery, the dummy cassette was carefully exchanged with a cassette containing unexposed film. A cassette is constructed of two polyethylene sheets sandwiching a sheet of XV-2 film (Figure 2). The cassette was inserted into the phantom such that the edges of the film, edges of the two sheets and the edges of the phantom are aligned to within 0.05 cm. The four treatment fields were delivered using 6 MV x-rays. Care was taken not to disturb the position of the phantom between the start of scanning and the completion of delivery.

Following delivery, the XV-2 film was removed from the phantom and inserted into a larger film for scanning in a 12-bit film digitizer (Vidar VXR-12, Herndon, VA 20170). The resulting matrix of values was converted to a dose map using a previously measured dose response curve. This measured dose matrix was converted to a format compatible with the Pinnacle planning system and imported as a secondary dataset. Within the planning system, the matrix was registered to the outer bounds of the phantom using the 3D registration tools of the planning system. The accuracy of registration is estimated to be 0.05 cm. The dose levels contained in the measured dose matrix were contoured using the auto-contouring tool of the planning system. These levels were compared directly with the prostate contours used in the planning

step. The location of these dose lines with respect to the target is measured in the AP (anterio-posterior) and LAT (lateral) dimensions. The time required for each step in the procedure was recorded (see Table II).

III. Results and Discussion

A. Minimum Coverage Dose vs CTV-PTV Margin

The DVHs and distributions for one of the cases planned is shown in Figure 3. The DVHs for the PTVs and rectal wall volumes illustrate the constraints on rectal wall dose and volume. A large increase in minimum dose to the PTV is made possible by the reduction in proximity of the PTV bound to the rectal wall, the DVH for the rectal wall stays within the constraint. The averaged results from the four cases at each margin is shown in Figure 4. An expected trend is revealed, the achievable minimum dose in the PTV increases with decreasing margins. The magnitude of dose escalation is dramatic, a 15% increase is possible if targeting precision could be reduced to a level where 0.4 cm margins could be applied with confidence. Achieving a targeting precision which would permit a 0.4 cm margin requires a method to control internal organ motion. This is very difficult in a treatment site like the prostate. An alternative to controlling organ motion is to re-locate the prostate on a daily basis using an on-line tomographic guidance system.

When interpreting these results, one must keep in mind the parameters used in the planning exercise will strongly affect the results. Furthermore, the limited number of patients included in the study inevitably introduces some small-sample bias in the results.

B. On-line Tomographic Guidance

The ability of the conebeam system to detect structures of interest in radiotherapy is illustrated in Figure 5. The figure shows three tomographic slices through the conebeam CT dataset of an anesthetized dog, reconstructed with only 90 projections over 180 degrees (voxel size: 0.05 cm x 0.05 cm x 0.6 cm). In each image, the dog's rectum is clearly visible. The dog's prostate is clearly visible in the central slice. As this dog has been neutered, the size of the prostate is quite small (~ 0.6 cm in diameter).

The results of the tomographic guidance procedure are shown in the images of Figure 6a. The mock prostate is clearly visible in the reconstructed slices of the conebeam dataset. Figure 6b shows the contour of the prostate and the 75% line of the measured dose distribution. The plan was not designed to provide 100% coverage, rather the MLC leaves were set to contact the contoured volume. A slight discrepancy between the two curves is visible. The displacement is measured to be 0.1 cm in the LAT dimension and 0.15 cm in the AP dimension. This discrepancy includes all sources of error in the entire image guidance and delivery process.

Sources of error that could lead to this magnitude of discrepancy include: systematic errors from the calibration procedure of the guidance system, errors in transferring MLC leaf positions from the planning system, errors in the calibration of the MLC leaf banks, and errors in the experiment itself; these would include uncertainty in positioning the film in the phantom and errors in registering the measured dose distribution to the bounds of the phantom within the planning system. Given the discrepancy, the results are overall very encouraging. It would appear that even this experimental system would be capable of achieving a targeting and delivery precision

that would allow a margin of 4 mm to be delivered with a sufficient level of confidence.

The entrance exposure delivered to the phantom during the scanning procedure was estimated to be 3.1R. The total elapsed time for the imaging and delivery was nearly 5 hours. This time included the time to assemble the film cassette and transfer data between the various computer systems. A breakdown of the time required for the critical steps is shown in Table II; also included is an estimate of the times that will be achieved in the near future.

The implementation of this system for treatment of the prostate is not yet feasible, as the field-of-view of the scanner is only 20 cm. We are currently developing a second generation detector system which employs a large area flat-panel detector based on amorphous silicon technology. A 41 cm x 41 cm detector that is mounted with an offset would provide sufficient field of view to scan patients with up to a 45 cm diameter. The imaging performance of the flat panel detector will also be superior to the CCD-based system used in this study. The efficiency (quantum detective) of the new detector is estimated to be ~4 times (45% vs 11 %) than the CCD; this is largely due to the increased optical collection efficiency of the panel. Other advantages include reduced optical glare and better mechanical stability.

There are additional factors that have not been discussed that may limit the precision of this or any other tomographic guidance system^{4,9}. These are 1) the importance of respiratory motion in sites like the prostate⁸, 2) the tolerance of the patient for a prolonged treatment for which even the smallest of voluntary movements may possibly require beginning the procedure over, 3) the potential for prostate motion due to changes in bowel gas between scanning and delivery, and, 4) the magnitude of inter-observer variability in the definition of the prostate bound and in the definition of

the adjacent rectal wall.

Respiratory motion can be a significant factor. In a conventional CT scanner, respiratory motion results in adjacent slices that have inconsistent anatomy. Fortunately, the scan times are fast enough in a single slice to provide a reasonably consistent dataset for reconstruction. Depending on the speed of acquisition, conebeam CT scans may have large inconsistencies which prevent accurate reconstruction of any slices. Ideally scan times could be reduced to a short enough time interval that a breath-hold maneuver, or a breath-hold device¹⁰ could be employed. Such devices have been employed to hold a patient's breath for periods beyond 30 seconds.

Involuntary motion or motion due to discomfort is a very difficult factor to manage. Immobilization devices can be applied to reduce the magnitude and frequency of this type of motion. An attempt to immobilize the patient completely may be met with considerable resistance. One of the best approaches to this problem is to perform the guidance and treatment procedure as fast as possible. Considering that involuntary motion may be an issue, a secondary check of patient position should be made on a continuous basis to alert the staff. Internal motion is particularly difficult to detect. For motion due to bowel gas, it may be possible to provide a prescription of simethicone or equivalent to reduce the amount of gas present in the bowel over the course of treatment. Fortunately, gas has a very high radiographic contrast, and could be monitored by frequent low-dose radiographs.

Inter-observer variability in the definition of the prostate and rectum is expected. It may be difficult to reduce this uncertainty as the prostate and rectum are relatively low contrast structures with occasionally unclear boundaries. The magnitude of the

uncertainty will depend on many factors such as the contrast of the object being contoured, the noise present in the image, and the time taken in the contouring process. It can be expected that this uncertainty will be managed through the use of margins. It is interesting to note that conebeam CT may assist in reducing inter-observer uncertainty in regions of the prostate where slice thickness plays a role (base and apex). The flexibility of the conebeam CT algorithm allows reconstruction of virtually any slice within the volume with equivalent image quality.

We have illustrated that through tomographic guidance, it is technologically feasible to attempt high precision radiotherapy of the prostate. This raises the question of: "How should one employ such an approach in the context of current radiation therapy?".³ There are several strategies that could be pursued. These range from 1) daily on-line tomographic guidance with daily inverse planning and delivery, to, 2) daily tomographic localization and automated re-positioning, and, finally, to 3) passive off-line review of the tomographic information to assist the oncologist in re-designing or re-optimizing the treatment plan to accommodate the detected variations in target and normal tissue location.^{11,12} Regardless of the exact mechanism, it could be expected that the increased amount and quality of information available to the physician and technical staff would result in dramatic changes in the roles of the radiation therapy team.

Another question that can be raised is: "How will this potential increase in precision affect the future of radiation therapy?", or posed a different way, "What new directions could be pursued because of the added precision." Due to the interventional nature of an on-line approach, it may be prohibitively costly to strive for such high precision for the length of a conventional treatment course. For it to become cost

effective, it may be necessary to explore alternative fractionation schemes comparable to the achievements that have been made in fractionated high-dose-rate brachytherapy boost treatments for the prostate; very large dose fractions (2 X 10.5 Gy) are being delivered in our facility as a boost to conventional external. This is made possible by on-line ultrasound guidance and the conformal dose distributions formed by the Iridium-192 implants. It is exciting to consider the pursuit of large fraction treatments with an on-line tomographic guidance procedure and intensity-modulated beam delivery.

IV. Summary and Conclusions

This report examines the relationship between margins and minimum coverage dose for radiotherapy of disease confined to the prostate. The results demonstrate that significant dose escalation is possible with reduced margins on the order of 0.4 mm, while maintaining a dose-volume performance for the rectal wall equal to a 4-field box with a prescription dose of 72 Gy. Based on current approaches to treatment setup and organ motion, it is not possible to achieve a precision in target location that corresponds to a 0.4 cm margin; a new treatment approach is necessary.

We have proposed an on-line tomographic guidance approach to deliver highly conformal fields with a precision sufficient to employ PTVs that are generated from with a 0.4 cm margin. Such an approach has been demonstrated using a conebeam tomographic guidance system constructed on an Elekta SL-20 linear accelerator. Investigations indicate that a planned dose distribution can be placed to within 0.2 cm of a tomographically localized target. The margin that should be employed with this level of precision depends on the dose gradients that can be achieved and our ability to control other uncertain factors. The results of this study suggest that a 0.4 cm margin

maybe pursuable. The construction of an improved tomographic imaging chain and the integration of the acquisition, planning and delivery steps is the area of on-going investigation.

References

1. Feldkamp, L. A.; Davis, L. C.; Kress, J. W. Practical cone-beam tomography. *J. Opt. Soc. Amer. A*, 1:612-619; 1984.
2. D.A. Jaffray, D.G. Drake, M. Moreau, J.W. Wong, "A radiographic and tomographic imaging system integrated into a medical linear accelerator for localization of bone and soft tissue targets," *Int. J. Radiat. Oncol. Biol. Phys.* (accepted for publication) 1999
3. D.A. Jaffray, J.W. Wong, "Exploring 'Target of the Day' strategies for a medical linear accelerator with conebeam-CT scanning capabilities," *Proceedings of the XII ICCR*, pg. 172-175, Salt Lake City, Utah, USA 1997
4. T.R. Mackie, T. Holmes, S. Swerdloff, P. Reckwerdt, J.O. Deasy, J. Yang, B. Paliwal, T. Kinsella, "Tomotherapy: a new concept for the delivery of dynamic conformal therapy," *Med. Phys.* 20: 1709-1719, 1993
5. R. Mohan, Q. Wu, X. Wang, J. Stein Intensity modulation optimization, lateral transport of radiation, and margins. *Med. Phys.* 23(12):2011-2021
6. K. Preiser, Th. Bortfeld, K. Hartwig, W. Schlegel, J. Stein, "A new program for inverse radiotherapy planning," *Proceedings of the XII ICCR*, pg. 425-428, Salt Lake City, Utah, USA 1997

7. W. Schlegel, O. Pastyr, R. Kubesch, J. Stein, T. Diemer, K-H. Hover, and B. Rhein,
" A computer controlled micro-multileaf-collimator for stereotactic conformal
radiotherapy," Proceedings of the XII ICCR, pg. 79-82, Salt Lake City, Utah, USA
1997
8. J. Szanto, L. Gerig, J. Crook, S. Malone, "Respiratory variation in prostate position:
considerations for conformal radiotherapy treatment planning," Int. J. Radiat. Oncol.
Biol. Phys. 42(1) Suppl. pg. 367 (1998)
9. Uematsu, M.; Fukui, T.; Shioda, A.; Tokumitsu, H.; Takai, K.; Asai, Y.; Kusano, S.
A dual computed tomography linear accelerator unit for stereotactic radiation
therapy: a new approach without cranially fixated stereotactic frames. Int. J. Radiat.
Oncol. Biol. Phys. 35:587-92; 1996.
10. J. Wong, M.B. Sharpe, D.A. Jaffray, V.R. Kini, J.M. Robertson, J.S. Stromberg, A.A.
Martinez, "The use of active breathing control (ABC) to reduce margin for breathing
motion," Int. J. Radiat. Oncol. Biol. Phys. (accepted for publication) 1999.
11. D. Yan, F. Vicini, J. Wong, and A. Martinez, "Adaptive radiation therapy," Phys.
Med. Biol., 42, 123-132, 1997.
12. D. Yan, D. Lockman, and D. Brabbins, "A prediction model for defining a proactive
planning target volume in external beam treatment of prostate cancer," Int. J.
Radiat. Oncol. Biol. Phys. 42(1) Suppl. pg. 216 (1998)

Figure Captions

Figure 1: Photograph of the tomographic guidance system on an Elekta SL-20 accelerator. The system consists of a 600,000 HU x-ray tube mounted at 90 degrees to the treatment head and a CCD-based fluoroscopic imaging system. The field-of-view of the system is restricted by the small area of the detector.

Figure 2: The soft-tissue contrast phantom used to test tomographic guidance of field placement. Photograph of the prostate phantom and removable film cassette.

Figure 3: Potential for increase in minimum target dose as a function of decreasing margins used in the generation of the PTV (1mm bixel IMRT, 5 equispaced beams over 360 degrees). The dose increase is illustrated in the dose-volume histograms (DVHs) for the PTV. The DVHs for the rectal wall are constrained to that delivered by a four-field arrangement (1 cm margin, non-IMRT, 72 Gy). The relationship between dose and margin depend on the relative position of rectal wall and prostate; this will vary between patients and from day-to-day for a given patient.

Figure 4: The relationship between uniform 3D margin and minimum dose in the PTV. These data are the average of the results from four patients. Points on the curve that correspond to current conformal practice and the margins that would be possible in an on-line tomographic guidance approach (0.4 cm) are indicated. Relating a 0.4 cm margin to a targeting precision requires knowledge of the penumbra and a specification of the amount of dose variation that would be tolerated in the CTV.

Figure 5: The ability of the system to detect soft-tissue structures relevant to radiotherapy of the prostate is illustrated in these CT images of an anesthetized dog. The dog's rectum and prostate are clearly visible. The entrance exposure was estimated to be 3.1R for the full scan. Unfortunately, the dog began to move midway through the scanning procedure allowing only 90 images over 180 degrees to be used for the reconstruction (slice thickness = 0.6 cm, pixel size = 0.05 cm x 0.05 cm).

Figure 6: Results of tomographic guidance. (a) Conebeam CT images of the phantom acquired on the modified Elekta SL-20. Unfortunately, air pockets around the prostate model increases visibility in some slices. (b) Comparison of target position and measured dose distribution in the phantom. The desired and measured dose distributions are within 2 mm in the anterior-posterior (AP) and lateral (LAT) dimensions. No verification of the positioning accuracy was performed in the (superior-inferior) SI dimension.

Table Captions

Table I: Parameters used in the MRC inverse planning system for the simulations reported in this article.

Table II: Time required for critical components of the on-line tomographic guidance procedure as executed on a mock prostate phantom. The elapsed time was larger than the total time in the table due to the dosimetry component of the test. Improvements are being made to achieve the times reported in the second column.

Tables

Table I

Parameter	Value	Comment
Bixel dimension at isocenter	1mm x 1mm	
Iterations	10	5 min. on 150 MHz MIPS processor
Number of beams	5	-144, -72, 0, 72, 144 degrees
Beam Energy	15 MV	
Constraining OAR	Rectal Wall	5-point DVH from 4-field plan for 72 Gy
Inhomogeneity Corrections	None	

Table II

Procedure	Time Required (mins.)	
	Current	Possible
Acquisition (181 images, 512x512, every 2 degrees)	11	2
Reconstruction (filter and back-projection) 250 MHz UltraSparc 281 x 281, 100 slices	48	10
Contouring (prostate only on 30 slices)	15	10
Planning/MLC Field Shaping	30	< 30?
Delivery	2	2
Total	111 (1:51 hrs)	< 54 (< 0:54 hr)

Figure 1

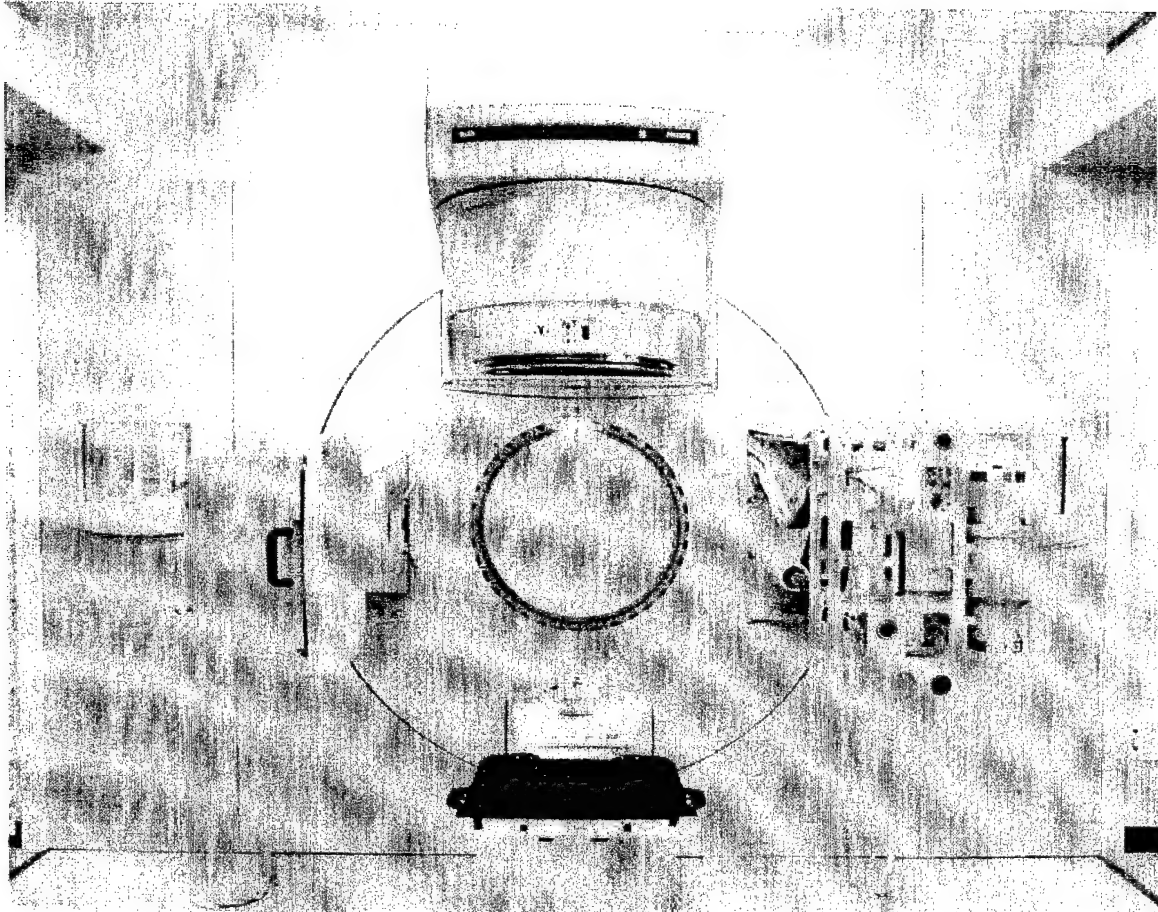


Figure 2

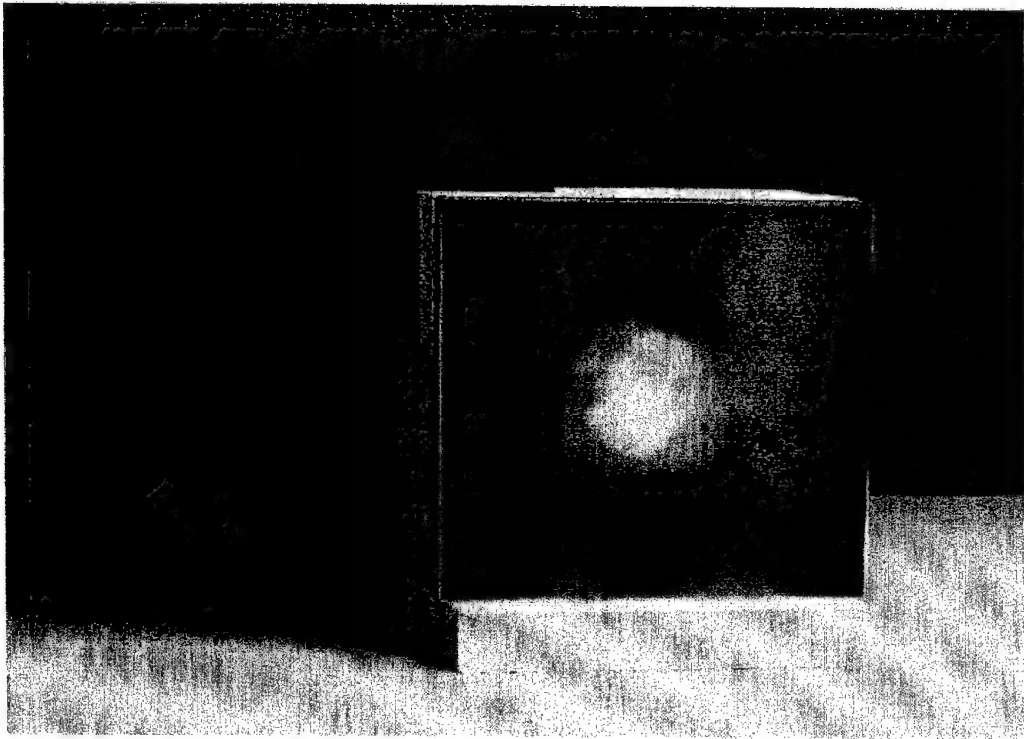
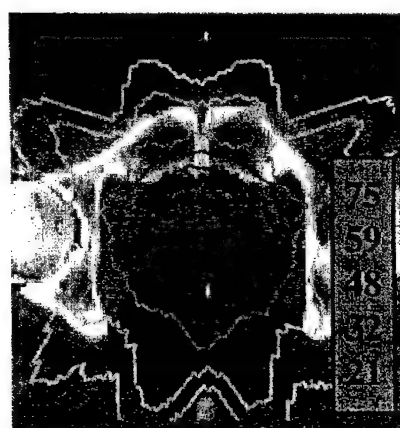
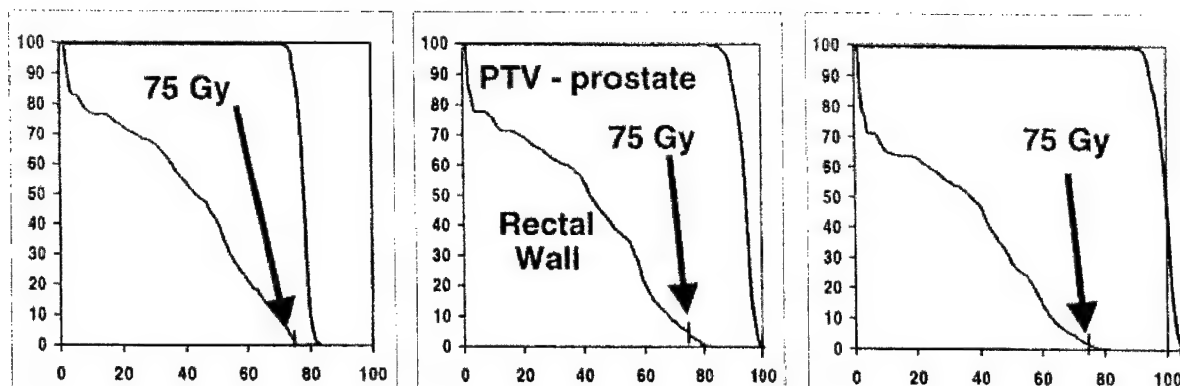


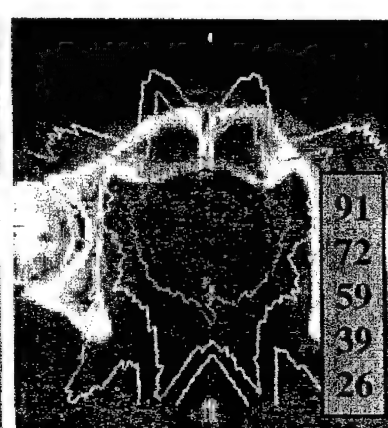
Figure 3



8 mm



4 mm



0 mm

Margin

Figure 4

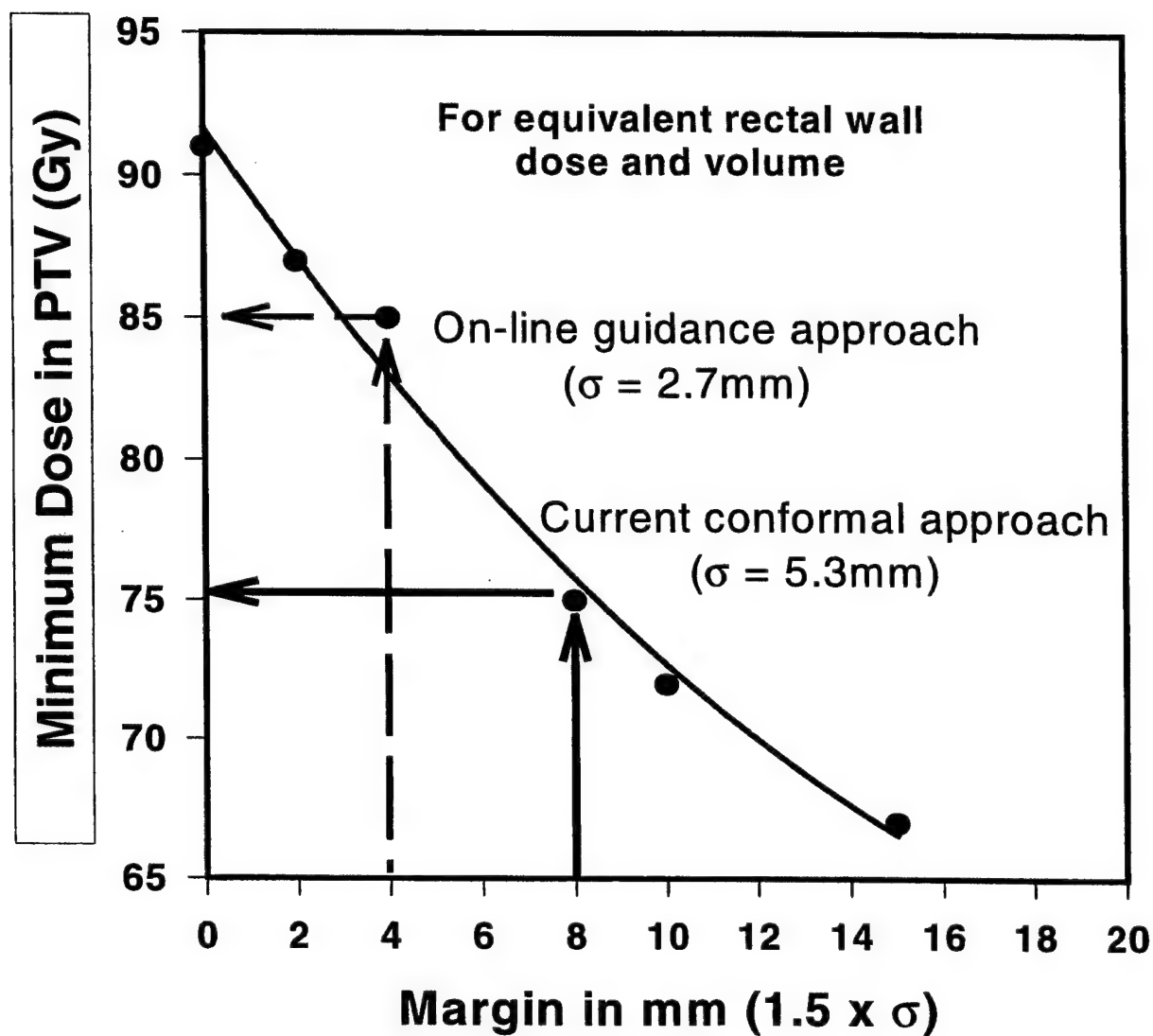


Figure 5

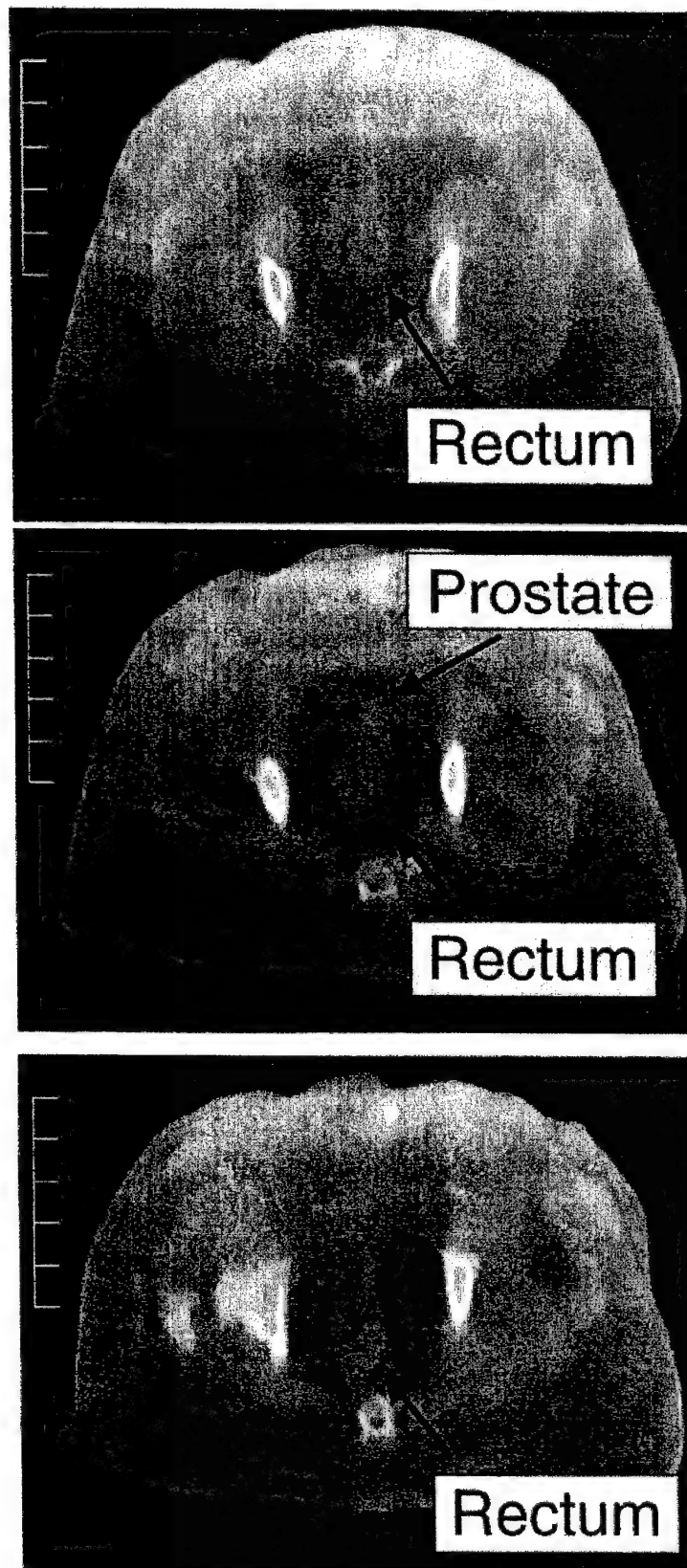


Figure 6a

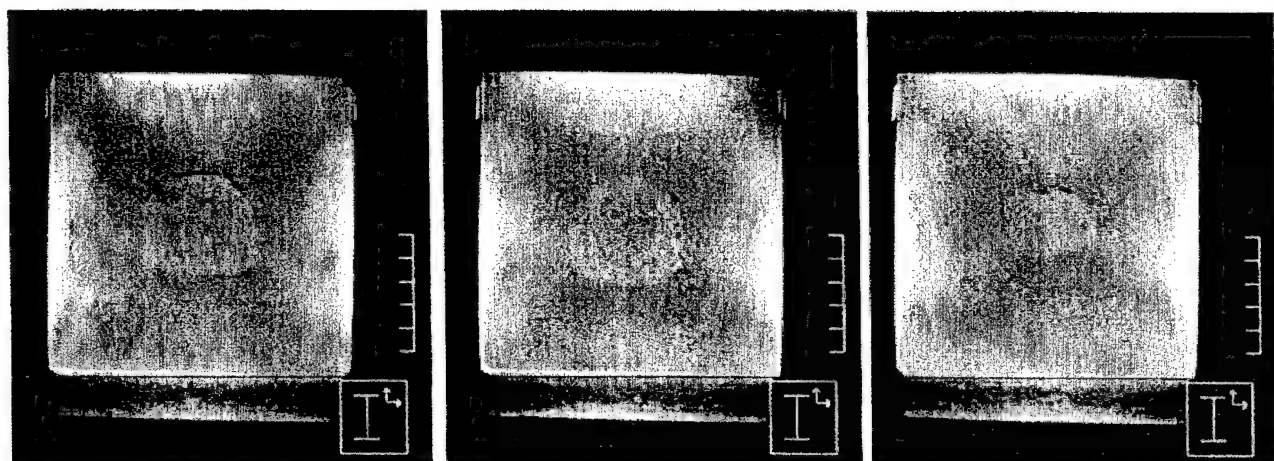
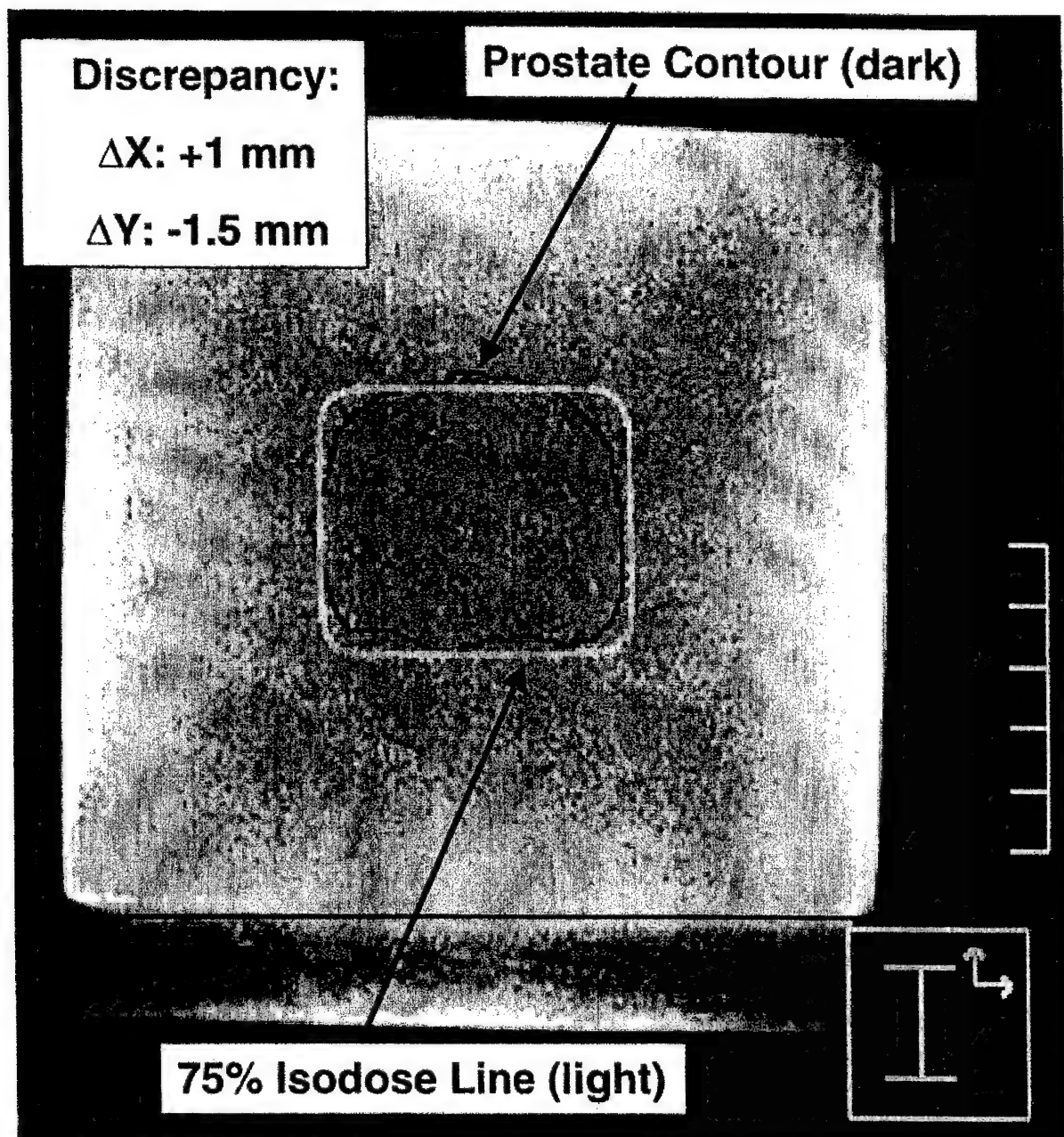


Figure 6b



**Appendix B: Spatio-temporal Response Characteristics of an
Indirect-detection Flat-panel Imager**

A ghost story: Spatio-temporal response characteristics of an indirect-detection flat-panel imager

J. H. Siewerdsen^{a)} and D. A. Jaffray

Department of Radiation Oncology, William Beaumont Hospital, Royal Oak, Michigan 48073-6769

(Received 20 January 1999; accepted for publication 27 April 1999)

Spatial and temporal imaging characteristics of an amorphous silicon flat-panel imager (FPI) were investigated in terms relevant to the application of such devices in cone-beam computed tomography (CBCT) and other x-ray imaging modalities, including general radiography, fluoroscopy, mammography, radiotherapy portal imaging, and nondestructive testing. Specifically, issues of image lag (including the magnitude, spatial uniformity, temporal-frequency characteristics, and dependence upon exposure and frame time) and long-term image persistence ("ghosts") were investigated. As part of the basic characterization of the FPI, pixel dark signal and noise (magnitude, temporal stability, and spatial uniformity) as well as radiation response (signal size, linearity, gain, and reciprocity) were also measured. Image lag was analyzed as a function of frame time and incident exposure. First-frame lag (i.e., the relative residual signal in the first frame following readout of an exposure) was ~2–10%, depending upon incident exposure and was spatially nonuniform to a slight degree across the FPI; second-, third-, and fourth-frame lag were ~0.7%, 0.4%, and 0.3%, respectively (at 25% sensor saturation). Image lag was also analyzed in terms of the temporal-frequency-dependent transfer function derived from the radiation response, allowing a quantitative description of system components contributing to lag. Finally, the contrast of objects as a function of time following an exposure was measured in order to examine long-term image persistence ("ghosts"). Ghosts were found to persist up to 30 min or longer, depending upon the exposure and frame time. Two means of reducing the apparent contrast of ghost images were tested: (i) rapid scanning of the FPI at maximum frame rate, and (ii) flood-field exposure of the FPI; neither was entirely satisfactory. These results pose important considerations for application of FPIs in CBCT as well as other x-ray imaging modalities. For example in CBCT, the magnitude of image lag is such that significant artifacts in tomographic reconstructions may result if strategies are not adopted either to reduce or correct the lag between successive projections (e.g., rapid scanning between projections or iterative correction algorithms, respectively). Similarly, long-term image persistence may necessitate frequent recalibration of offset corrections. © 1999 American Association of Physicists in Medicine. [S0094-2405(99)00608-2]

Key words: digital x-ray imaging, flat-panel imager, amorphous silicon, image lag, image persistence, cone-beam computed tomography

I. INTRODUCTION

Flat-panel imagers (FPIs) based upon arrays of hydrogenated amorphous silicon (*a*-Si:H) thin-film transistors (TFTs) in combination with either *a*-Si:H photodiodes and an overlying phosphor (to provide "indirect" detection of x rays) or with a continuous photoconductive layer (e.g., *a*-Se or PbI₂, to provide "direct" detection of x rays) are being developed for application in medical x-ray imaging (e.g., Refs. 1 and 2) and industrial nondestructive testing and evaluation (NDTE). Such devices are available in large area format (e.g., 30 × 40 cm²), may be packaged compactly (e.g., ~3 cm thick), and provide digital, real-time images. FPIs may operate in a single-shot, radiographic mode (e.g., in chest radiography or mammography), can be read continuously (e.g., at 30 fps in fluoroscopy), or can switch between these modes dynamically (e.g., momentarily interrupting fluoroscopic acquisition to obtain a radiograph). Furthermore, since such devices demonstrate relatively high resistance to radiation damage,³ they are an attractive technology for the field of radiotherapy

portal imaging.^{4,5} In this paper, an experimental setup developed specifically to investigate the performance of (indirect-detection) FPIs in cone-beam computed tomography (CBCT)^{6–8} is described, and a number of imager performance parameters relevant to CBCT (and other applications) are examined.

The imaging performance of a FPI is affected by a multitude of characteristics, including: the behavior of pixel dark signal;⁹ the linearity and gain of pixel signal response;⁹ the effects of charge trapping, release, and image lag;^{4,9–27} the spatial-frequency-dependent modulation transfer function (MTF),^{5,15,28–31} noise power spectrum (NPS),³² and detective quantum efficiency (DQE),^{15,32–35} as well as contrast-detail performance.⁴ This paper focuses specifically upon the subject of image lag, i.e., signal present in frames subsequent to the frame in which it was generated.

Image lag is a concern in CBCT, since image information carried over between successive x-ray projections causes artifacts in reconstructed tomographic images. In fact, the issue

TABLE I. Summary of several studies reporting upon the topic of image lag in FPIs. The top portion shows results reported for *a*-Si:H photodiodes in combination with either an *a*-Si:H TFT (denoted PD+TFT), dual switching diodes (denoted PD+2D), or a single switching diode (denoted PD+1D). The bottom contains results reported for FPIs based upon the direct-detection technology of a continuous *a*-Se photoconductor in combination with an *a*-Si:H TFT (denoted *a*-Se+TFT). The "Source" column identifies whether measurements were performed using an optical (denoted LED) or x-ray (denoted x ray) source of irradiation. The "Method" column identifies whether the measurement involved the step response to irradiation (denoted SRF), the impulse response (denoted IRF), or the response in the presence of moving objects (denoted Objects). The notation $Lag|_n$ refers to the *n*th-frame lag, as defined in Eq. (1).

Reference	Year	Detector	Source	Method	Image lag and long-term persistence
Street <i>et al.</i> (10)	1992	PD+TFT	LED	SRF	Estimated $Lag _1 < 1\%$ achievable
Powell <i>et al.</i> (11)	1992	PD+TFT	LED	SRF	$Lag _1 \sim 2\%$; $Lag _2 \sim 1\%$
Antonuk <i>et al.</i> (12)	1992	PD+TFT	LED	SRF	$Lag _1 \sim 2\% - 5\%$
Fujieda <i>et al.</i> (13)	1993	PD+TFT	LED	IRF	Showed dependence of lag on input light level
Antonuk <i>et al.</i> (14)	1993	PD+TFT	LED	SRF	$Lag _1 < \sim 5\%$
Schiebel <i>et al.</i> (15)	1994	PD+TFT	x ray	Objects	$Lag _1 \sim 5\%$; Observe persistence at $t \sim 10$ s
Graeve <i>et al.</i> (16)	1995	PD+2D	LED	IRF	$Lag _1 \sim 5\%$; $Lag _2 \sim 1\%$; $Lag _3 \sim 0.4\%$
Graeve <i>et al.</i> (17)	1996	PD+2D	LED	IRF	$Lag _1 \sim 5\% - 8\%$
Chabbal <i>et al.</i> (18)	1996	PD+1D	LED	...	$Lag _1 < \sim \text{"a few"}\%$
Weisfield <i>et al.</i> (19)	1997	PD	LED	SRF	Photodiode current decay $\sim 0.5\%$ after 30 ms
Antonuk <i>et al.</i> (9)	1997	PD+TFT	LED	SRF	$Lag _1 \sim 5\%$
Antonuk <i>et al.</i> (4)	1998	PD+TFT	LED	SRF	$Lag _1 \sim 10\%$
Bruijns <i>et al.</i> (20)	1998	PD+TFT	x ray	...	Observe long-term "memory effect"
Jung <i>et al.</i> (21)	1998	PD+TFT	x ray	IRF	$Lag _1 \sim 10\%$; long-term residual signal $\sim 0.1\% - 1\%$
Weisfield <i>et al.</i> (25)	1999	PD+TFT	x ray	SRF	$Lag _1 \sim 2\%$; Observe persistence at $t \sim 10$ s
Granfors <i>et al.</i> (26)	1999	PD+TFT	x ray	SRF	$Lag _1 \sim 2\%$; $Lag _2 \sim 0.7\%$; $Lag _3 \sim 0.5\%$
Polischuk <i>et al.</i> (22)	1998	<i>a</i> -Se+TFT	x ray	IRF	$Lag _1 \sim 0.4\%$; persistence \sim electronics noise
Tsukamoto <i>et al.</i> (23)	1998	<i>a</i> -Se+TFT	x ray	IRF	$Lag _1 \sim 1.5\%$; $Lag _2 \sim 0.8\%$; $Lag _3 \sim 0.5\%$
Lee <i>et al.</i> (24)	1998	<i>a</i> -Se+TFT	x ray	...	Persistent images eliminated by imager reset

of image lag is a consideration for all of the imaging applications mentioned above. In "single shot" radiographic modalities (e.g., chest radiography, mammography, and radiotherapy portal localization), the image lag represents an inefficiency in signal collection due to charge lost to traps (although trapped charge is released in subsequent frames). Depending upon the magnitude of charge trapping and the noise of the acquisition electronics, it might even prove beneficial to utilize the trapped charge through addition of the initial image with subsequent dark images. In fluoroscopy, of course, image lag causes spatial blurring of objects that are moving in the radiation field;³⁶ however, it has been shown³⁷ that a certain amount of image lag actually improves the signal-to-noise ratio by correlating information between frames. In fact, Wright *et al.* and Colbeth *et al.*^{27,38,39} purposely implement a recursive filter to introduce lag during fluoroscopic acquisition. In dual-mode imaging, where the FPI is switched momentarily from fluoroscopic acquisition to obtain a high-quality radiograph, image lag causes the radiographic signal to persist in the first few frames of subsequent fluoroscopic acquisition. Thus, in applications involving single-shot radiography, continuous fluoroscopy, dual-mode imaging, and/or multiple successive projections of a changing scene (e.g., CBCT), knowledge of and/or minimization of image lag is important.

The results reported in this paper were obtained using a commercially available prototype FPI (RID 512-400 A0 from EG&G Heimann⁴⁰) and are reported in three sections: fundamental properties, image lag, and image ghosting. First, a number of properties considered prerequisite to a thorough investigation of image lag are presented, including the dark

signal characteristics and radiation response of individual pixels.

Second, the magnitude, exposure and frame time dependence, temporal-frequency behavior, and spatial uniformity of the image lag is characterized through measurements under x-ray exposure. As shown in Table I, a number of studies have reported on image lag for FPIs, but only recently has the effect been characterized under x-ray irradiation. Moreover, the experimental methods employed in the studies vary considerably. Often, measurements are made of either the rising or falling edge of the signal response to a step function of incident radiation (called the step response function, SRF). Often, the response to an impulse of radiation (i.e., a radiographic exposure between frames) is considered (called the impulse response function, IRF). Still other studies have examined the signal response under constant irradiation in the presence of high-contrast, rapidly moving objects. Finally, the manner in which lag is defined and the terminology employed vary among the studies. The chronological listing in Table I suggests that (for indirect-detection FPIs) despite the low image lag demonstrated in early results (e.g., 1992–1993), later results (e.g., 1996–1998) showed higher levels of lag ($\sim 5\% - 10\%$). Most recently, improvements in array technology have demonstrated reduced image lag ($\sim 2\%$ or less), comparable to that reported for direct-detection FPIs.

Herein and as described in Sec. II, image lag is investigated through measurement of the IRF under x-ray irradiation as a function of exposure and imager frame time (i.e., the period, T_{frame} , between successive readout of a given row of pixels). Image lag is described in terms of the *n*th-frame lag, $Lag|_n$, given by the ratio of the (offset-

subtracted) pixel signal in frame n , $\text{Sig}|_n$, to that in the frame immediately following a radiographic exposure (frame zero):

$$\text{Lag}|_n \equiv \frac{\text{Sig}|_n}{\text{Sig}|_0}, \quad (1)$$

where n is a non-negative integer. Thus, $\text{Lag}|_0$, the zeroth-frame lag, is unity, and $\text{Lag}|_1$, the first-frame lag, is that which is typically reported, although a number of studies (Table I) have reported lag for frames beyond $n=1$. Direct comparison between results summarized in Table I should be done with a degree of caution, since the lag measured using different experimental methods (e.g., falling or rising edge SRF versus IRF measurements) can (and should) give different results.

Three sources of image lag in indirect-detection FPIs are generally regarded: (1) incomplete charge transfer between the capacitance of the sensor elements and that of the readout electronics; (2) finite decay time in optical emission from the x-ray converter; and (3) trapping and release of charge in the sensor elements. The first source depends upon the design of the array and amplifier electronics, but is typically small given that the time which the TFT is conducting during each readout cycle is much greater than the RC time constant of the pixel, and that charge-integrating amplifiers (and not voltage-sensitive amplifiers) are used in readout.^{11,13}

A second source of image lag is the decay and afterglow in optical emission from the phosphor. For the case of $\text{Gd}_2\text{O}_2\text{S:Tb}$, Shepherd *et al.*⁴¹ report that the phosphor decays to $1/e$ intensity in ~ 0.7 ms and to 10^{-4} intensity in less than 10 ms. Similarly, Rudin *et al.*⁴² reported $\text{Gd}_2\text{O}_2\text{S:Tb}$ decay to 10^{-2} intensity in 2.4 ms, consistent with the results of Mainprize and Yaffe,^{43,44} who showed decay to 10^{-1} , 10^{-2} , and 10^{-3} , intensity in ~ 1.2 , ~ 2.5 , and ~ 3.7 ms, respectively. Faster decay times may be achieved through use of different activators (e.g., $\text{Gd}_2\text{O}_2\text{S:Pr}$), possibly at the cost of increased long-term afterglow.⁴¹ For the case of CsI:Tl , Blasse⁴⁵ reported a 1 μs decay time, and Mainprize and Yaffe^{43,44} showed that the decay is dominated by an exponential component with lifetime ~ 3 μs . Since typical values of T_{frame} for FPIs in medical imaging range from ~ 30 ms (e.g., in fluoroscopy) to ~ 1 s (e.g., in radiographic applications), the contribution of phosphor decay to the total image lag is fairly small. For the measurements reported herein, the frame time was varied from $T_{\text{frame}} = 200$ ms up to 25.6 s, time scales at which phosphor decay contributes negligibly to image lag.

The third effect (trapping and release of charge in the sensor elements) is typically recognized as the dominant source of image lag for indirect-detection FPIs. Trapping may occur as a result of bulk effects⁴⁶ (in the i layer of the photodiode) or surface effects (at interfaces between materials in the sensor elements).⁴⁶⁻⁴⁸ Bulk effects include direct capture of charge at defect energy levels in the gap, followed by slow release over a broad range of time constants. Considering the density of defect states in high-quality $a\text{-Si:H}$ ($\sim 3 \times 10^{15} \text{ cm}^{-3}$),⁴⁶ the capacity for trapped charge is enormous (e.g., ~ 100 pC in a 400 μm photodiode, which is

about twice its parallel plate capacitance). Surface effects too could contribute to image lag, since the high density of dangling bonds at layer interfaces may be satisfied by constituents other than Si, such as oxides, resulting in a high density of defect states at surfaces. Trapping at layer interfaces is more significant for thin, multilayer structures, such as the TFT. Thus, both the photodiode (through bulk effects) and the TFT (through surface effects) are potential sources of charge trapping; however, the former is typically identified as the dominant source.^{25,46} As reported elsewhere,^{10,11,14} image lag is reduced by: (1) illuminating the photodiode through the p layer; (2) operating the photodiode at a high bias voltage (e.g., $V_{\text{bias}} \sim -5$ V); and (3) operating at signal levels far below sensor saturation.

Finally, in Sec. III, long-term persistence (up to 1 h following an exposure) of images of high-contrast objects is reported. Sometimes referred to as "ghosting," this long-term persistence has been observed by several investigators,^{15,20} but the effect and its clinical implications have yet to be quantified. Ghosts of high-contrast objects (e.g., collimator edges, skin line, metal prosthetics, surgical instruments, etc.) could have detrimental effects in any of the x-ray imaging applications mentioned above if present at a perceptible level of contrast. Similar to the sources governing image lag, the source of long-term ghosting could include (1) slow release of charge from deep trapping states in the $a\text{-Si:H}$ and/or (2) afterglow from the phosphor.

II. METHODS AND MATERIALS

A. Experimental setup

A laboratory bench consisting of an x-ray tube, object stage, and imager stage was constructed to investigate the performance of FPIs in CBCT. The x-ray tube was a General Electric Maxiray 75 powered by a 100 kW General Electric MSI-850 generator at a measured potential of 120 kVp. The x-ray tube was operated under computer control and had the following characteristics: a target angle of 11° ; a focal spot size of 0.6 mm; inherent filtration of 1.0 mm Al (specified equivalent at 150 kVp); added filtration of 1.5 mm Al plus 0.129 mm Cu; and first and second HVLs of 6.1 mm Al (measured) and 15.6 mm Al (calculated), respectively, at 120 kVp. As shown in Fig. 1, the tube was mounted on a rigid frame attached to the laboratory bench, with the x-ray beam directed horizontally. An object stage consisting of Daedal translation and rotation tables was positioned at a distance of 100 cm from the x-ray source and was computer controlled by means of a National Instruments PC-LPM-16 I/O board. All values of exposure ($\pm 3\%$), and kVp (± 2 kVp) were measured using an RTI Electronics PMX-III x-ray multimeter with an R25 diode placed at the surface of the FPI.

The flat-panel imager (RID 512-400 A0) was constructed by EG & G Heimann Optoelectronics and consists of an $a\text{-Si:H}$ imaging array in combination with a luminescent phosphor (Lanex Fast-B; $133 \text{ mg/cm}^2 \text{ Gd}_2\text{O}_2\text{S:Tb}$) along with a system of acquisition electronics.⁴⁰ The FPI was designed as a prototype for investigation of the imaging performance of such devices at diagnostic energies, with a sum-

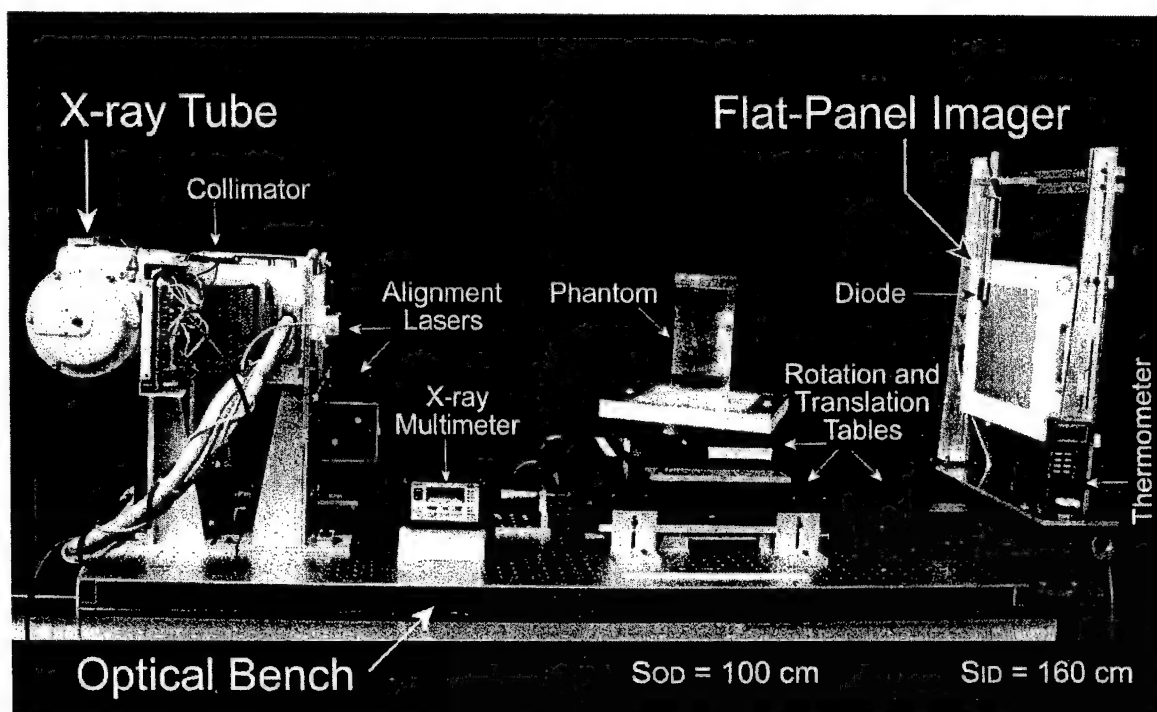


FIG. 1. Photograph of the experimental setup. The x-ray tube, object and imager stages, FPI, exposure meter, and relevant distances are labeled. A computer (not shown) provides synchrony of the x-ray tube, translation and rotation stages, and the FPI. This system was designed to provide a well-known, highly reproducible geometry for investigation of the performance of FPIs in cone-beam tomography.

mary of specifications given in Table II. The imaging array comprises a 512×512 matrix of a -Si:H TFTs coupled to n -i- p a -Si:H photodiodes at $400 \mu\text{m}$ pixel-to-pixel pitch, giving an active area of $\sim 20.5 \times 20.5 \text{ cm}^2$. Directed by a PC, the FPI operates asynchronously of the host computer and could be addressed at frame rates of 0.04–5 fps; i.e., at frame times ranging from 200 ms to 25.6 s. The frame time is

TABLE II. Summary of the design specifications for the FPI employed in the measurements. Designed as a prototype for investigation of FPI performance in diagnostic x-ray imaging, the RID 512-400 A0 is among a number of FPIs to be made commercially available for academic research and testing.

FPI design parameter	Value ^a
Array format	512×512
Pixel pitch	$400 \mu\text{m}$
Area	$\sim 20.5 \times 20.5 \text{ cm}^2$
Pixel fill factor	0.80
Photodiode bias voltage	-6 V
TFT off/on voltage	-10/+5 V
Photodiode charge capacity	$\sim 62 \text{ pC}$
ASIC amplifier charge capacity	$\sim 23 \text{ pC}$
ADC bit depth	16 bit
Dark current	$< 3 \text{ pA/mm}^2$
TFT thermal noise (on)	$\sim 1800 \text{ e}$
Photodiode shot noise (1 fps)	$\sim 1200 \text{ e}$
Digitization noise	$\sim 630 \text{ e}$
ASIC amplifier noise	$\sim 12\,700 \text{ e}$
Maximum frame rate	5 fps
X-ray converter	$133 \text{ mg/cm}^2 \text{ Gd}_2\text{O}_3\text{:Tb}$

^aReference 40.

varied by means of a variable-length pause imposed after scanning all rows in a given frame, i.e., the time that the TFTs are held conducting and the time interval between switching successive rows is held constant. The photodiode bias voltage (-6 V), TFT switching voltages (-10 and +5 V for TFT "off" and "on," respectively), and ASIC amplifier integration time ($\sim 80 \mu\text{s}$) were held fixed at the default values set by the manufacturer. The FPI was mounted on a vertical frame at a source-to-imager distance of 160 cm. The Fluke 52 K/J thermocouple placed inside the FPI enclosure monitored the temperature during operation.

This experimental setup was constructed specifically to provide a system for investigation of the performance of the FPI in CBCT. Measurements reported herein are part of the fundamental, empirical characterization of the FPI requisite to understanding and optimizing its performance in CBCT and other x-ray imaging applications.

B. Fundamental pixel performance properties: Dark signal, noise, and signal response

1. Temporal characteristics of pixel dark signal

The temporal stability ("drift") of the pixel dark signal was evaluated by operating the FPI in the absence of x rays (i.e., in the dark) and reading the pixel values as a function of elapsed time. Prior to each measurement, the FPI was left unpowered overnight, and measurements commenced from a time, $t = 0$ (corresponding to the time at which power was supplied to the FPI) and extending over 6 h. The FPI was operated at frame times from 0.2 to 25.6 s, and the tempera-

ture inside the FPI enclosure was monitored continuously. The average dark signal value (for an ensemble of 10 pixels) was plotted as a function of time. Furthermore, in order to examine the spatial uniformity of the dark signal drift, an image obtained immediately following imager startup, $I(t=0)$, was subtracted from images obtained at later times, $I(t>0)$, to yield a drift image, $I_{\text{drift}}(t) = I(t) - I(0)$. Inspection of the resulting drift images and image histograms allowed identification of regions exhibiting anomalous dark signal drift. As shown in Sec. III, the FPI generally exhibited significant drift over the first ~ 2 h of operation. Thus, all measurements below were performed following a warm-up period of at least 2 h.

2. Pixel dark noise

Fluctuations in pixel dark signal (the "pixel dark noise") were measured for values of T_{frame} ranging from 0.2 to 25.6 s by acquiring realizations of 200 consecutive samples from 48 pixels. The analysis was equivalent to that reported previously,³³ with slight modifications to identify various components of the pixel dark noise. From the ensemble of measurements, three values of pixel dark noise were determined: (1) the noise from a single pixel sampled repeatedly, $\sigma_{1\text{pix}}$; (2) the noise calculated from the difference between two pixels lying along the same row, $\sigma_{2\text{pix-row}}$; and (3) the noise calculated from the difference between two pixels in the same frame (but not lying along the same row or column), $\sigma_{2\text{pix-frame}}$. The noise analysis divides each realization into N groups in order to reduce possible effects arising from dark signal drift during the course of the measurement; however, comparison of results with and without such grouping were identical, suggesting that drift during the measurements was negligible.

As reported in a number of publications,^{2-4,33} the total pixel dark noise is modeled as the sum in quadrature of various independent noise components, including the TFT thermal noise (in the conducting state), $\sigma_{\text{TFT therm}}$, the photodiode shot noise, $\sigma_{\text{PD shot}}$, the noise of the readout and amplifier electronics, σ_{amp} , and the digitization noise of the analog-to-digital conversion process, σ_{ADC} . Other sources of additive noise include row-correlated noise arising from fluctuations in the TFT gate voltage, σ_{row} , and frame flicker noise, σ_{frame} , arising from fluctuations in the photodiode bias voltage applied across the entire array. Thus, the total pixel dark noise can be represented as:

$$\sigma_{1\text{pix}}^2 = \sigma_{\text{TFT therm}}^2 + \sigma_{\text{PD shot}}^2 + \sigma_{\text{amp}}^2 + \sigma_{\text{ADC}}^2 + \sigma_{\text{row}}^2 + \sigma_{\text{frame}}^2 \quad (2)$$

Reduction of the row-correlated component, σ_{row} , can be achieved by subtracting the values of pixels lying along the same gate line,³³ as in the row-subtracted noise realizations discussed above:

$$\sigma_{2\text{pix-row}}^2 = \sigma_{\text{TFT therm}}^2 + \sigma_{\text{PD shot}}^2 + \sigma_{\text{amp}}^2 + \sigma_{\text{ADC}}^2 \quad (3)$$

which also reduces the frame-correlated component, σ_{frame} . The frame-correlated component alone can be reduced (with-

out affecting the row-correlated noise) by subtracting the values of pixels from the same frame (but lying along different rows and columns):

$$\sigma_{2\text{pix-frame}}^2 = \sigma_{\text{TFT therm}}^2 + \sigma_{\text{PD shot}}^2 + \sigma_{\text{amp}}^2 + \sigma_{\text{ADC}}^2 + \sigma_{\text{row}}^2 \quad (4)$$

Thus, from the measurements described above, the magnitude of the row noise, frame flicker noise, and amplifier noise can be estimated:

$$\sigma_{\text{row}}^2 = \sigma_{2\text{pix-frame}}^2 - \sigma_{2\text{pix-row}}^2 \quad (5)$$

$$\sigma_{\text{frame}}^2 = \sigma_{1\text{pix}}^2 - \sigma_{2\text{pix-frame}}^2 \quad (6)$$

$$\sigma_{\text{amp}}^2 = \sigma_{2\text{pix-row}}^2 - \sigma_{\text{TFT therm}}^2 - \sigma_{\text{PD shot}}^2 - \sigma_{\text{ADC}}^2 \quad (7)$$

In order to examine the spatial uniformity of the pixel dark noise, 24 consecutive images at various settings of T_{frame} were acquired, and the standard deviation for each pixel was computed. The resulting data provided a map of $\sigma_{1\text{pix}}$ across the FPI.

3. Pixel signal response, linearity, gain, and reciprocity

The mean signal size for FPI pixels under x-ray irradiation was measured in a manner reported previously,⁹ where the signal from an ensemble of 20 pixels was recorded following exposure to the radiographic x-ray beam. Three basic measurements of signal response were performed: (1) measurement of the mean pixel signal as a function of exposure; (2) measurement of the slope of the signal response (termed the system gain, Γ , with units of e/mR/pixel); and (3) measurement of the system gain as a function of incident exposure rate, varied through adjustment of the radiographic mA setting. The first measurement indicates the degree of linearity of system response and shows the exposure that results in saturation of the FPI. Note from Table II that for the FPI under investigation, it is the charge capacity of the ASIC amplifier (and not the photodiode) that determines the saturation signal. The second measurement characterizes the system gain (i.e., the amount of signal collected per unit exposure to the FPI). The third measurement demonstrates the degree to which the signal response satisfies reciprocity, i.e., the degree to which the signal resulting from a given exposure is independent of the exposure rate. Operated in radiographic mode, the lowest and highest exposure rates allowed by the MSI-800 were (15.3 ± 0.6) mR/s and (916.6 ± 10.1) mR/s, thereby allowing investigation of reciprocity over a factor of ~ 60 in exposure rate and building upon earlier results⁴⁹ which demonstrated reciprocity over a factor of ~ 5 in exposure rate (4.8–22.4 mR/s).

C. Impulse response characteristics: Image lag

Image lag was characterized through measurement of the temporal response of the FPI to a radiographic exposure, called the IRF. The synchronization between the radiographic x-ray source and readout of the FPI is the same as described elsewhere,⁹ in which radiographic x-ray pulses were delivered between image frames. The frame immedi-

ately following the x-ray pulse (frame 0) contains the radiographic image, and subsequent frames (frames 1, 2, and so on) contain signal attributable to lag.

In order to examine the magnitude, exposure dependence, and frame-time dependence of the image lag, IRFs were measured for an ensemble of 20 pixels. Each IRF was 100 samples in length. The first 49 samples were used to estimate the pixel dark signal (to be subtracted); a radiographic exposure was made just prior to the 50th frame (called frame zero); and the n th frame lag was computed using Eq. (1) from the remaining 50 samples. Each measurement was repeated five times, and the results were averaged (over the five repeat IRFs and over the 20 pixels) to yield the reported values of $\text{Lag}|_n$.

A relevant concern is *whether it is primarily the number of reads or the amount of elapsed time following the initial exposure that determines the amount of residual signal present in subsequent frames*. To address this issue, measurements were performed at values of T_{frame} of 0.2, 0.4, 0.8, 1.6, 3.2, and 6.4 s, and the resulting IRFs and $\text{Lag}|_n$ were plotted as a function of both frame number and elapsed time. To examine the dependence of image lag on signal size, measurements were performed at exposures spanning the sensitive range of the detector.

The temporal-frequency characteristics of the image lag were analyzed by Fourier transform of the IRF, yielding the temporal-frequency-dependent transfer function, $T_{\text{lag}}(\omega)$ (similar to the transfer function common to digital signal processing, e.g., as in Ref. 50):

$$T_{\text{lag}}(\omega) = |\mathcal{F}[\text{IRF}_{\text{norm}}(t;n)]|, \quad (8)$$

where ω is the temporal-frequency (units s^{-1} or frame^{-1}) Fourier pair coordinate to time, t , or frame number, n . $\text{IRF}_{\text{norm}}(t;n)$ is the area-normalized impulse response function, and \mathcal{F} represents the Fourier transform operation, computed using a fast-Fourier algorithm in MATLAB.⁵¹ Clearly, a detector with $\text{Lag}|_{n>0} = 0$ has $T_{\text{lag}}(\omega) = 1$ up to the Nyquist frequency ($\omega_{\text{Nyq}} = 1/2T_{\text{frame}}$). Analysis of the image lag in this manner is insightful for a number of reasons. First, it provides a straightforward temporal analog to the spatial concepts widely employed in image science; that is, in the same sense that the MTF describes the transfer of signal at various spatial frequencies and provides a quantitative description of spatial blur, $T_{\text{lag}}(\omega)$ describes the transfer of information at various temporal frequencies and provides a quantitative description of "temporal blurring" that results from image lag. In a similar manner to MTF reducing the individual pixel noise³³ and noise-power spectrum through correlation of signal in space, $T_{\text{lag}}(\omega)$ reduces the noise in successive samplings of a given pixel through correlation of signal between frames.^{33,34} Furthermore, analysis of $T_{\text{lag}}(\omega)$ provides a "systems" description of the processes resulting in image lag. Hence, just as the MTF for an imaging system is given by the product of the MTFs of its various components (e.g., focal spot, phosphor blur, and sampling aperture), $T_{\text{lag}}(\omega)$ is the product of the temporal transfer functions of components responsible for image lag (e.g., radiation

wave form, phosphor decay and afterglow, and trapping and release of charge in $\alpha\text{-Si:H}$). Thus, $T_{\text{lag}}(\omega)$ allows identification of the system component that dominates the temporal response. Finally, analysis of $T_{\text{lag}}(\omega)$ allows identification of various temporal-frequency characteristics of the image lag. For example, degradation of $T_{\text{lag}}(\omega)$ at frequencies close to the Nyquist frequency corresponds to image lag between successive frames (e.g., between frame 0 and frame 1), whereas degradation near $\omega = 0$ corresponds to longer term signal retention.

To investigate the spatial uniformity of the image lag, IRFs for the 512×512 pixels were examined, and the resulting $\text{Lag}|_n$ were plotted as a function of spatial position. An exposure level of ~ 2 mR ($\sim 20\%$ saturation) and a frame time of 3.2 s were used. For these measurements, each IRF consisted of 30 samples: the first 10 samples were used to estimate the pixel dark signal; and the radiographic exposure was delivered just prior to the 11th frame. The measurement was repeated ten times, and the results were averaged.

Finally, the visual impression of image lag in successive radiographs was examined by acquiring images of moving objects placed at 100 cm from the source. Two types of objects were considered: a linear array of Pb BBs and a strongly attenuating edge (a Bi-Pb slab), each translated laterally across the field of view (FOV) while successive radiographs were acquired. For the moving edge, two sets of measurements were performed: one with the slab moving out of the FOV and one with the slab moving into the FOV. Such measurements illustrate the effect of image lag under conditions where subsequent frames experience a high exposure compared to conditions where such frames are in the shadow of the slab.

D. Long-term image persistence: Ghosts

The persistence of images up to 1 h following an exposure was examined at various settings of T_{frame} and at exposures up to and exceeding sensor saturation. A Pb slab with a ~ 2 cm hole was placed in a rigid mount at 100 cm from the source. With the imager operating at a given value of T_{frame} , an initial image of the object was obtained (at time $t = 0$), and the local contrast of the hole was analyzed as a function of elapsed time for up to 1 h. Local contrast was analyzed from the (ensemble average) pixel signal in the region of the hole, $\text{Sig}|_{\text{hole}}$, relative to the (ensemble average) pixel signal behind the Pb slab, $\text{Sig}|_{\text{Pb}}$:

$$C_{\text{local}} = \frac{\text{Sig}|_{\text{hole}} - \text{Sig}|_{\text{Pb}}}{\text{Sig}|_{\text{hole}}}. \quad (9)$$

Measurements were performed at T_{frame} settings of 0.2, 1.6, 6.4, and 25.6 s and at exposures of $\sim 20\%$, 50%, 100%, and 300% saturation. These measurements illustrate the magnitude of ghosting for the simple case of a single high-contrast object following a single exposure. The effect was observed to be smaller for objects of low contrast; furthermore, the effect is expected to depend on the history of FPI exposure and operation, e.g., upon the number of exposures delivered,

the cumulative exposure, the intensity of irradiation, etc. Such issues are beyond the scope of this study.

Finally, two methods of reducing the contrast of ghosts were examined. The first method involved rapid scanning of the FPI at maximum frame rate in an attempt to "flush" the ghost signal out of the imager. In this case, a relatively strong ghost was induced by forming an image of the hole (at an exposure $\sim 300\%$ saturation) with the FPI operated at $T_{\text{frame}} = 6.4$ s. Then, at $t \sim 30$ s, the FPI was switched to its highest frame rate setting ($T_{\text{frame}} = 200$ ms) and cycled for 600 frames before being switched back to $T_{\text{frame}} = 6.4$ s. The local contrast of the hole was measured, and at time $t \sim 3$ min, the FPI was switched again to $T_{\text{frame}} = 200$ ms this time for 1500 frames. Finally, the FPI was switched back to $T_{\text{frame}} = 6.4$ s, and the local contrast of the hole was measured for 1 h. The plot of C_{local} versus time for the rapid-scanning method was compared to the case where the FPI was operated at constant frame time.

The second strategy for reduction of ghost images involved flood-field exposures delivered following the initial exposure. An image of the hole was obtained (with exposure $\sim 300\%$ saturation and $T_{\text{frame}} = 6.4$ s), and C_{local} was measured as a function of elapsed time. Immediately following the initial exposure, the Pb slab was removed from the FOV, and at times $t \sim 30$ s and $t \sim 3$ min, a flood-field exposure (exposure $\sim 100\%$ saturation) was delivered. The local contrast for the case of the flood-fielding method was compared to the case in which the imager was operated continuously in the dark.

III. RESULTS AND DISCUSSION

A. Fundamental pixel performance properties

1. Temporal stability and spatial uniformity of pixel dark signal

Figure 2 plots the pixel dark signal as a function of elapsed time for the FPI operated at T_{frame} settings from 0.2 to 25.6 s. The magnitude and trend in the dark signal drift is seen to depend strongly on the selected frame time. For T_{frame} less than ~ 6.4 s, the dark signal exhibits an initial decrease, which stabilizes asymptotically within 1–2 h. At larger frame times, the dark signal initially decreases, then increases sharply before stabilizing. In each case, however, the pixel dark signal is seen to be fairly stable after a "warm-up" period of ~ 2 h. Superimposed in Fig. 2 is a plot of the temperature measured inside the FPI enclosure during the measurements. Starting from an ambient temperature of $\sim 18^\circ\text{C}$, the temperature increases rapidly after the FPI is switched on, rising to a stable temperature of $\sim 33^\circ\text{C}$ within ~ 1.5 h. The change in temperature is strongly correlated with the observed drift in pixel dark signal, and it is likely that the dark signal drift is at least partly the result of temperature-induced changes in the leakage currents of the TFT and photodiode. Furthermore, it should be noted that the pixel dark signal does not "reset" simply by changing the frame time. Rather, pixel dark signal appears strictly corre-

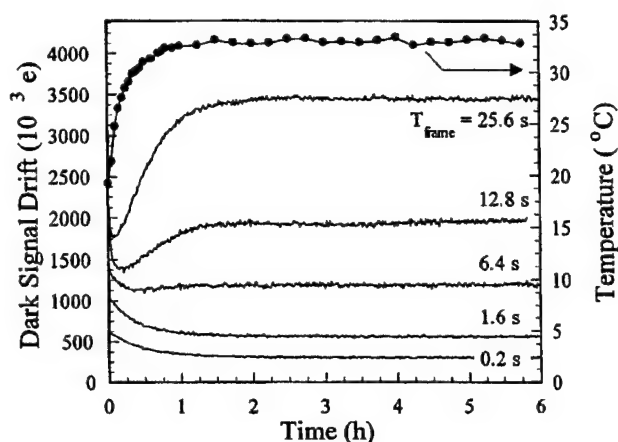


FIG. 2. Temporal stability of pixel dark signal. The dark signal drift was characterized by measuring the pixel dark signal over a period of 6 h at various settings of imager frame time. An arbitrary offset has been applied to each curve for purposes of presentation; thus, each curve indicates the change in pixel dark signal relative to an initial, arbitrary value at the time which power was supplied to the FPI. Superimposed is a plot of the temperature measured inside the FPI enclosure.

lated with the temperature of the FPI and, even during the "warm-up" period, switching between settings of T_{frame} simply switches between the drift curves.

The spatial uniformity of dark signal drift was analyzed by computing difference images relative to an image obtained at time $t = 0$. Shown in Fig. 3 are difference images at $t = 1, 2$, and 6 h for frame times of 0.2, 0.8, 3.2, and 25.6 s. For the lowest setting of T_{frame} , the drift is fairly uniform across the array, and the histograms of pixel dark signal shift downward as implied by Fig. 2, but do not broaden significantly. Close examination (e.g., in the circular, histogram-equalized areas of each image) reveals a number of regions that exhibit higher drift. At larger values of T_{frame} , these irregularly shaped regions become quite apparent, exhibiting dark signal drift ~ 2 –3 times greater than surrounding regions. Furthermore, pixels about the perimeter of such regions exhibit dark signal that did not stabilize even within 6 h but increased in a monotonic fashion over the course of the measurements. Thus, the spatial uniformity of the pixel dark signal is poor; however, such nonuniformities can be efficiently eliminated from x-ray images by means of a simple offset correction, provided that the dark signal is spatially stationary. The fact that certain regions exhibit dark signal drift that does not perfectly stabilize, however, suggests that the offset image used in gain-offset corrections should be obtained as close as possible (e.g., immediately prior) to the image to be corrected.

2. Pixel dark noise

Pixel dark noise measured as a function of frame time is plotted in Fig. 4. The pixel noise is nearly the same (~ 13 100 e) for the cases of row-subtracted and frame-subtracted sampling, suggesting that the row-correlated noise is small. This is likely due to the implementation of correlated double sampling (CDS) circuitry in the readout electronics, which forms

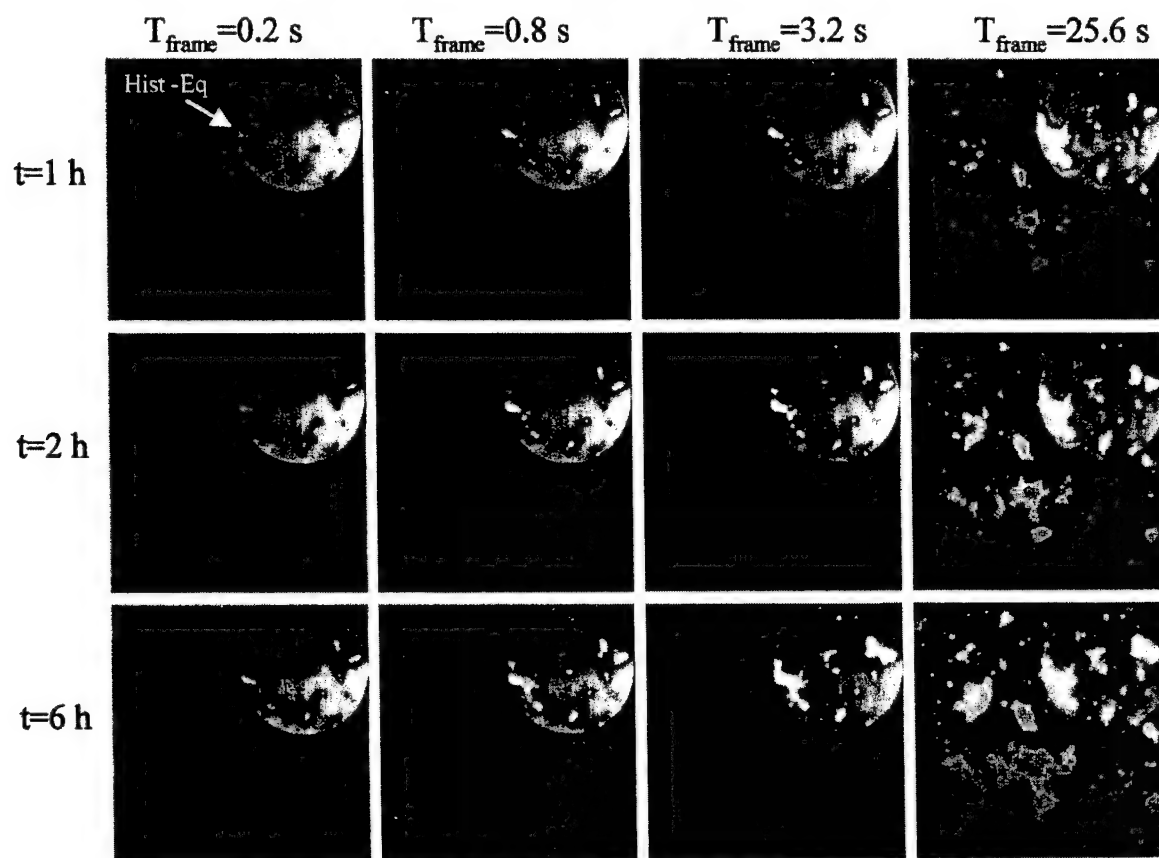


FIG. 3. Spatial uniformity of dark signal drift. Each image represents the difference between dark-field images acquired at a given time and time zero. The grayscale chosen for each plot was separated into two regions: (1) a common grayscale applied across each image, with lighter shades corresponding to positive drift; and (2) a circular region in the upper-right quadrant of each image that has been independently histogram equalized. The former choice of grayscale allows quantitative comparison of the dark signal drift between all conditions; the latter illustrates nonuniformities that are too subtle to be visualized through a single choice of grayscale.

an efficient high-pass filter of correlated noise. The single-pixel noise exhibits significant frame time dependence, increasing from $\sim 13\,300$ e at $T_{\text{frame}} = 200$ ms to $\sim 22\,500$ e at $T_{\text{frame}} = 25.6$ s. From Eqs. (5) to (7), it is concluded that the row-correlated noise is negligible, and that two components dominate the total pixel noise: the amplifier noise, σ_{amp} , and the frame flicker noise, σ_{frame} . The amplifier noise is estimated at $\sim 12\,700$ e and is the dominant component at low frame times. The frame flicker noise is apparently dependent upon the frame time, becoming the dominant noise source for T_{frame} greater than ~ 3 s.

The spatial uniformity of the pixel dark noise is shown in Fig. 5, where σ_{lpix} is plotted as a function of position for four settings of T_{frame} . At the lowest frame time, the pixel noise is fairly uniform across the FPI, with slight differences between eight rectangular sections that are addressed by separate banks of readout electronics. At higher values of T_{frame} , a number of irregularly shaped regions (coinciding with the regions of anomalous drift) are evident, with anomalous pixels exhibiting dark noise approximately 2–5 times larger than “normal” pixels. Two corners of the FPI demonstrate similarly increased pixel dark noise. The cause for the anomalous behavior in these regions is unclear, al-

though it may be related to increased leakage current, possibly due to nonuniform quality of processing and/or passivation. The variation in pixel dark noise across the FPI [standard deviation $\sim (2-5) \times 10^3$ e] is small relative to the mean pixel dark noise ($\sim 13 \times 10^3$ e) and is negligible compared to the x-ray quantum noise (e.g., $\sim 100 \times 10^3$ e/pixel at 1 mR) for this FPI system configuration.³⁴

3. Signal response, linearity, gain, and reciprocity

Figure 6 shows the signal response characteristics under x-ray irradiation. The FPI exhibits a linear response at exposures up to ~ 5 mR, beyond which the linearity degrades and the system (i.e., the amplifier) reaches saturation at ~ 10 mR. The system gain, Γ (calculated from the slope of the signal response curve below ~ 2 mR) is $\sim 18 \times 10^6$ e/mR. Figure 6(b) plots the slope of the signal response as a function of exposure and shows that the FPI maintains a linear response to within 5% across $\sim 50\%$ of its sensitive range. The system Γ measured as a function of kVp exhibits a spectral energy dependence similar to that reported previously for a different design of FPI:⁹ $\Gamma_{(80 \text{ kVp})} = (14.5 \pm 0.8) \times 10^6$ e/mR; $\Gamma_{(90 \text{ kVp})} = (16.5 \pm 0.9) \times 10^6$ e/mR; $\Gamma_{(100 \text{ kVp})} = (17.8 \pm 0.7) \times 10^6$ e/mR;

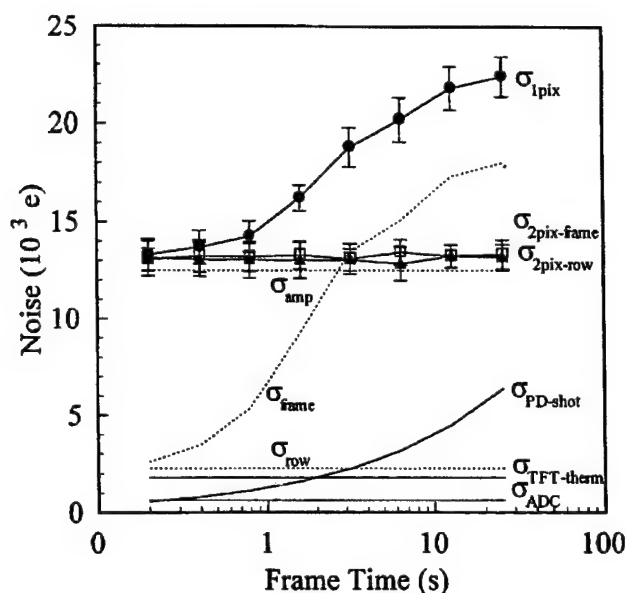


FIG. 4. Pixel dark noise vs frame time. Data labeled $\sigma_{1\text{pix}}$, $\sigma_{2\text{pix-frame}}$, and $\sigma_{2\text{pix-row}}$ are from measurements of the pixel noise from a single pixel sampled repeatedly, from a pixel pair within the same frame (but not along the same row or column), and from a pixel pair along the same row, respectively. (See the text for details). Lines connecting the data points (in this and subsequent figures) are provided merely for clarity. Superimposed are calculations of the TFT thermal noise, the photodiode shot noise, and the digitization noise, all of which are found to be small in comparison to the total measured noise.

$\Gamma_{(110\text{ kVp})} = (18.3 \pm 1.0) \times 10^6 \text{ e/mR}$; $\Gamma_{(120\text{ kVp})} = (18.3 \pm 0.7) \times 10^6 \text{ e/mR}$; and $\Gamma_{(130\text{ kVp})} = (18.4 \pm 0.6) \times 10^6 \text{ e/mR}$. The increase in Γ with kVp is well explained by a cascaded linear systems model that describes the tradeoffs in phosphor quantum detection efficiency and optical gain as a function of x-ray energy.³²⁻³⁴

The dependence of signal size upon the intensity of incident radiation (the so-called ‘reciprocity’ of the signal) was investigated by measuring Γ as a function of exposure rate. It is a well-known effect with screen-film systems that the optical density can depend upon the particular combination of exposure rate and exposure time; however, such a phenomenon has been investigated little for FPIs.⁴⁹ As shown in Fig. 6(c), over the range of exposure rates examined, no dependence of Γ on exposure rate was observed; therefore, for a given exposure, the FPI signal is independent of the exposure rate.

B. Impulse response characteristics: Image lag

Image lag was investigated in terms of: (1) its dependence upon frame time and signal size; (2) its temporal-frequency transfer function; (3) its spatial uniformity across the FPI; and (4) the visual impression of image lag in successive radiographs of moving objects.

1. Image lag: Impulse response functions

It is reasonable to consider whether the amount of residual signal (in frame n) following an exposure depends primarily upon n or upon elapsed time. That is, *is it the*

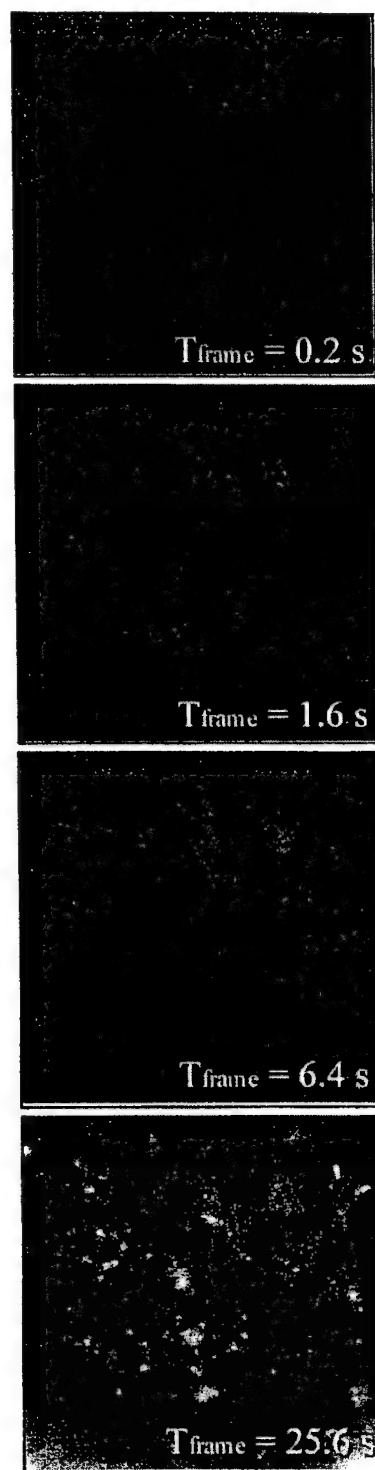


FIG. 5. Spatial uniformity of the pixel dark noise. Each image shows the individual pixel noise, $\sigma_{1\text{pix}}$, as a function of spatial position across the FPI. The grayscale was independently adjusted in each plot to maximize contrast. Histograms for each plot give some quantification of the spatial uniformity of pixel dark noise: at $T_{\text{frame}} = 0.2 \text{ s}$, the mean (mode) value of the noise is 12 900 (13 000 e) with a standard deviation of 2160 e, at $T_{\text{frame}} = 1.6 \text{ s}$, the mean (mode) value of the noise is 16 500 e (16 100 e) with a standard deviation of 3240 e, for $T_{\text{frame}} = 6.4 \text{ s}$, the mean (mode) value of the noise is 22 100 e (21 800 e) with a standard deviation of 3960 e, finally, for $T_{\text{frame}} = 25.6 \text{ s}$, the mean (mode) value of the noise is 22 300 e (21 500 e) with a standard deviation of 5340 e. These results are consistent with the measurements plotted in Fig. 4.

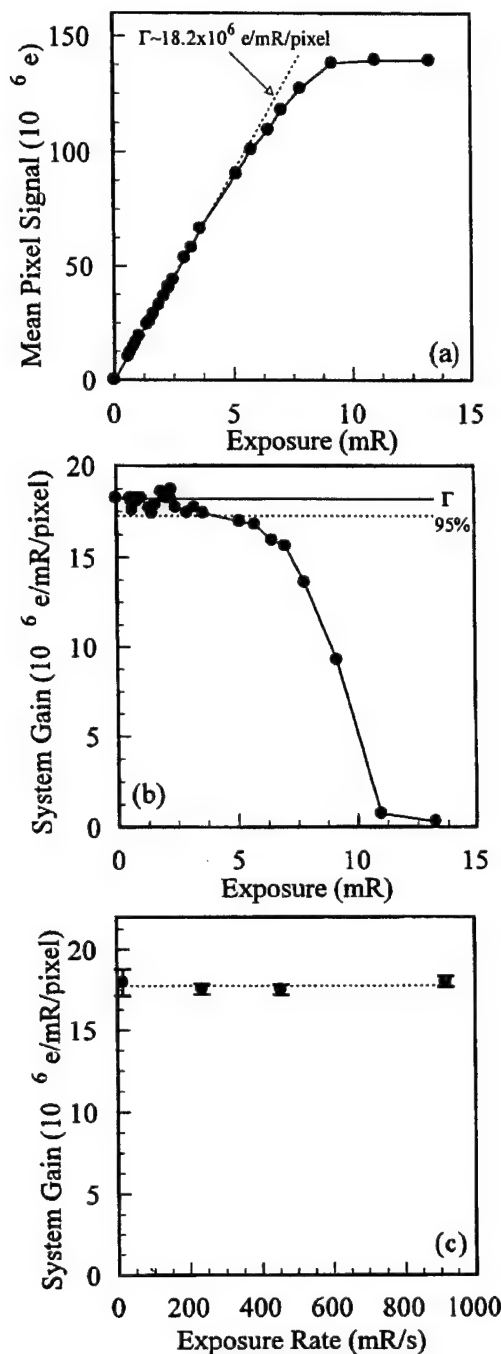


FIG. 6. Radiation response characteristics of the FPI. (a) Mean signal size as a function of exposure to the detector across the sensitive range of the FPI. (b) Slope of the signal response curve, i.e., gain, across the sensitive range of the detector. (c) The dependence of the system gain, Γ , upon exposure rate, measured from ~ 15 to ~ 900 mR/s (a factor of 60 in intensity). All values of exposure and exposure rate reported herein were measured at the surface of the FPI.

number of reads, n , or the amount of time, t , that primarily determines the magnitude of residual signal in subsequent frames? To answer this question, IRFs were analyzed both as a function of n and elapsed time. Figure 7(a) shows six IRFs plotted as a function of the number of reads, and it is seen

that the IRFs are nearly identical for all settings of T_{frame} . This strongly suggests that the n th frame lag (at least for $1 \leq n \leq 20$ and across a factor of 32 in frame time) is dependent primarily upon the number of reads, rather than the time since the exposure. The results plotted in the time domain [Fig. 7(b)] suggest the same conclusion, where each IRF is seen to separate, with $\text{Lag}|_{n=1} \sim (2.8 \pm 0.7)\%$, $\text{Lag}|_{n=2} \sim (0.74 \pm 0.06)\%$, and so on across all settings of frame time. The degree of dependence upon frame time is small in comparison to that upon frame number, but is evident nonetheless, as seen in the dashed lines connecting the data points in Fig. 7(b) and in the plot of Fig. 7(c). Still, the fractional signal level is determined primarily by the number of reads. This point is reiterated in the plot of Fig. 7(c), which shows the n th-frame lag as a function of T_{frame} . For $\text{Lag}|_{n=1}$ there is a measurable increase in image lag with increasing frame time, ranging from $(2.01 \pm 0.67)\%$ at $T_{\text{frame}} = 200$ ms to $(3.78 \pm 0.28)\%$ at $T_{\text{frame}} = 6.4$ s. This is consistent with the common notion that, for an amorphous semiconductor with a high density of deep trapping states, the longer one waits, the more charge is released from traps. The effect is clearly dominated by the number of reads, however (i.e., by the number of times that the pixel is reinitialized), and within experimental error the $\text{Lag}|_n$ curves for $n > 1$ are flat.

A valid interpretation of these results (e.g., in the context of CBCT) is that for a given time interval between successive projections (e.g., 1–10 s), it may be advantageous to scan the FPI at maximum frame rate in order to “flush” the lag signal between projections. For example, if the nominal T_{frame} for image acquisition is 1.6 s, and the interval between successive projections is 3.2 s, then the amount of residual signal could be reduced from $\text{Lag}|_{n=2} (\sim 0.7\%)$ to $\text{Lag}|_{n=16}$ (negligible) by switching temporarily to $T_{\text{frame}} = 200$ ms between projections. Alternatively, the FPI could be operated continuously at high frame rate, allowing residual signal to be “flushed” between projections. Exploration of such lag suppression procedures and determination of their effects upon CBCT reconstructions are the subject of ongoing investigation.

The dependence of image lag on signal size was examined by measuring IRFs as a function of exposure to the detector across the latitude of the FPI (at $T_{\text{frame}} = 3.2$ s). As shown in Fig. 8, $\text{Lag}|_n$ increases significantly as a function of signal size. For example, the first-frame lag at exposures of 10%, 25%, 50%, and 75% saturation is $\sim 3\%$, 3.6% , 5.2% , and 9% , respectively, and $\text{Lag}|_n$ for higher n exhibit a similar trend. Figure 8(b) plots the n th-frame lag versus exposure. $\text{Lag}|_{n=1}$ is as low as $\sim 2.5\%$ (at 5% saturation) and as high as $\sim 13.5\%$ (at 90% saturation), a factor of 5.4 across the latitude of the detector.

One implication of the exposure dependence of the lag concerns implementation of image lag correction algorithms that have been proposed for CBCT to reduce the effect of lag on tomographic reconstructions. One possible means by which such algorithms could reduce the effect of lag in successive projections is to correct the i th projection by subtracting the $(i-1)$ th projection weighted by $\text{Lag}|_{n=1}$ [and

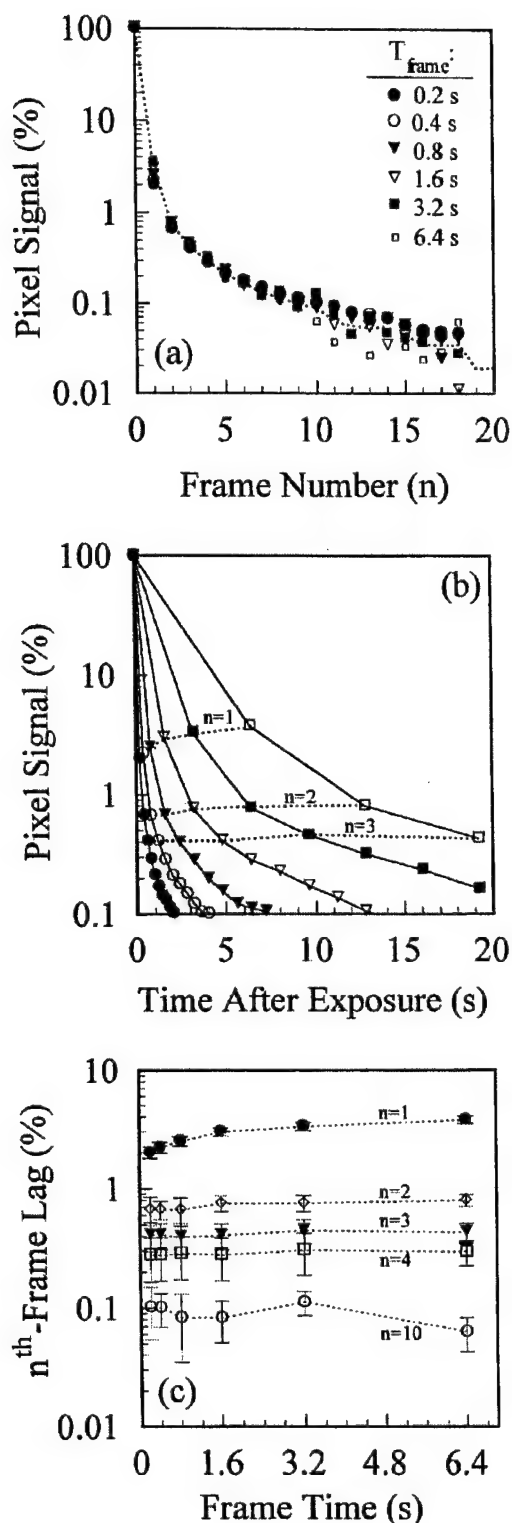


FIG. 7. Dependence of image lag upon frame time and number of readout cycles. (a) IRFs plotted as a function of readout cycle for six settings of T_{frame} . (b) The same IRFs plotted as a function of time. The dashed lines join values measured at various settings of T_{frame} . (c) Plot of the n^{th} -frame lag vs frame time. These illustrate that the residual signal level depends primarily upon frame number, although there is a measurable dependence upon time for $\text{Lag}|_{n=1}$ (increasing from 2.0% to 3.7% across a factor of 32 in frame time). Within experimental error, the curves for higher-order lag are nearly flat, with values of $\text{Lag}|_{n=2} \sim 0.74\%$, $\text{Lag}|_{n=3} \sim 0.42\%$, $\text{Lag}|_{n=4} \sim 0.29\%$, and $\text{Lag}|_{n=10} \sim 0.09\%$, for example.

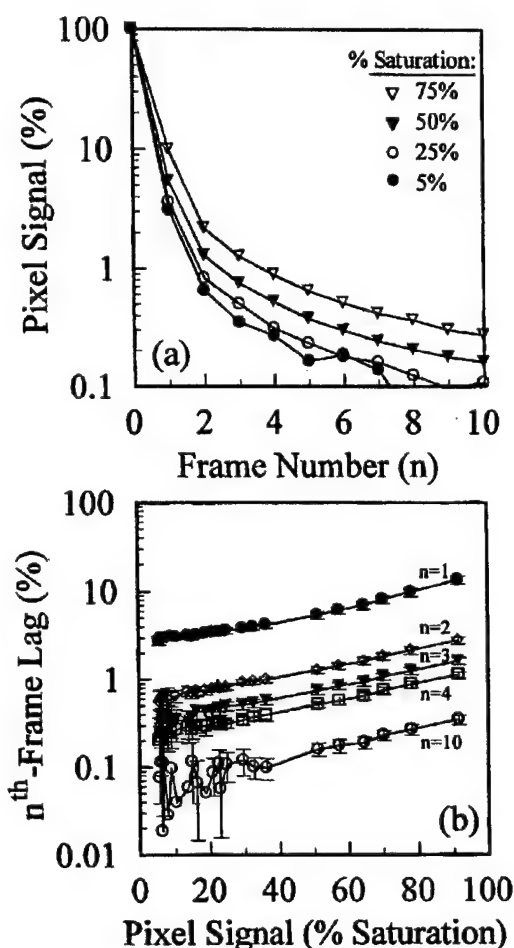


FIG. 8. Dependence of image lag upon exposure to the detector. (a) IRFs measured at exposures corresponding to 10%, 25%, 50%, and 75% of the saturation signal. In all cases, the saturation exposure was taken to be 10 mR. (b) Plot of the n^{th} frame lag vs exposure to the detector, expressed as a percent of the saturation exposure. For all n ($1 \leq n \leq 10$), the image lag increases by a factor of ~ 5 over the latitude of the detector (from 5% to 90% saturation).

the $(i-2)^{\text{th}}$ projection by $\text{Lag}|_{n=2}$ and so on]. The results of Fig. 8(b), however, suggest that a single value of $\text{Lag}|_{n=1}$, $\text{Lag}|_{n=2}$, etc., may be insufficient for such corrections; rather, an algorithm may provide better results if the i^{th} projection is corrected by subtracting the $(i-1)^{\text{th}}$ projection weighted by the values of $\text{Lag}|_{n=1}$ appropriate to the exposure to each pixel in the $(i-1)^{\text{th}}$ exposure [which may be obtained from the pixel value in the $(i-1)^{\text{th}}$ exposure]. The performance of such correction algorithms, the benefits of including exposure dependence in corrections, and investigation of the optimal number of recursive subtractions is the subject of future work.

2. Image lag: Temporal-frequency-dependent transfer functions, $T_{\text{lag}}(\omega)$

The temporal-frequency-dependent transfer function was determined by Fourier transform of the IRFs measured as a function of exposure. From the IRFs plotted in Fig. 9(a) (obtained at $T_{\text{frame}} = 3.2$ s), the temporal transfer functions,

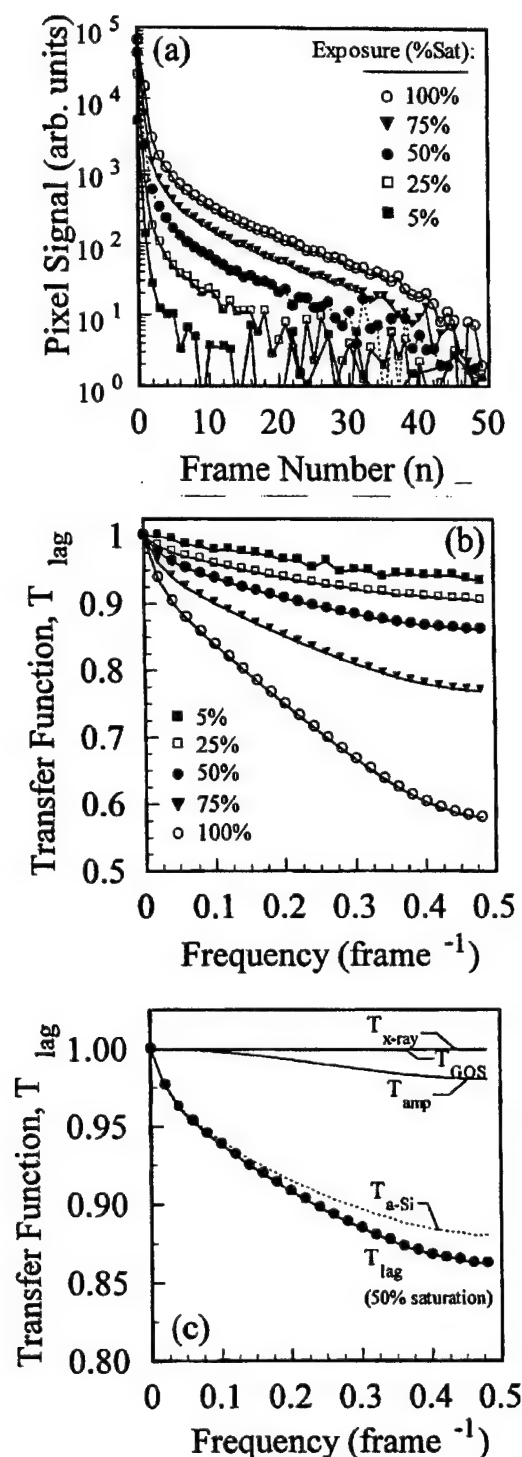


FIG. 9. Temporal-frequency characteristics of the image lag. (a) IRFs acquired at exposures corresponding to 5%–100% of signal saturation. Each IRF consists of 50 samples following the radiographic exposure and exhibits exposure-dependence consistent with the results of Fig. 8. (b) Temporal transfer functions, $T_{lag}(\omega)$, derived from the normalized IRFs by Fourier transform. (c) Temporal transfer functions (at 50% saturation) of the various system components contributing to image lag. The solid curves correspond to the transfer functions of the x-ray source (T_{x-ray}), the x-ray converter (T_{GOS}), and charge transfer between the sensor and the amplifier (T_{amp}); the dashed curve corresponds to the effect of trapping and release in the sensor (T_{a-Si}), derived from the other transfer functions.

$T_{lag}(\omega)$, were derived and plotted in Fig. 9(b). The temporal-frequency domain can be expressed either in terms of cycles per frame (with units of frame⁻¹ and Nyquist frequency, $\omega_{Nyq}=0.5$ frame⁻¹) or cycles per second (with units of s⁻¹ and $\omega_{Nyq}=1/2T_{frame}$). However, since the image lag depends primarily upon frame number rather than time (Fig. 7), the former choice for the frequency domain is employed. For exposures less than ~50% of saturation, $T_{lag}(\omega)$ is greater than ~85% out to the Nyquist frequency. At higher exposures the transfer function degrades (e.g., as low as ~55% near the Nyquist frequency for signal near saturation). As exposure increases, the degradation in $T_{lag}(\omega)$ at all temporal frequencies suggests that the exposure dependence of $Lag|_n$ is similar for all n (at least for $1 \leq n \leq 50$), consistent with Fig. 8(b). Even at the lowest frequency measured ($\omega = 0.02$ frame⁻¹, corresponding to $n = 50$), there is slight degradation in $T_{lag}(\omega)$, suggesting slight signal retention out to the 50th frame (160 s). Accurate IRF measurements over longer time scales are complicated by drift in the pixel dark signal; therefore, signal retention over extended time scales [corresponding to a low-frequency drop in $T_{lag}(\omega)$] is investigated in terms of “ghosts” (discussed below).

Analysis of the temporal transfer function, $T_{lag}(\omega)$, allows a “systems” view of the FPI components contributing to image lag. In the temporal domain [or the frame number domain—Fig. 9(a)] the total, measured IRF is given by convolution of the IRFs of the individual components; in the temporal-frequency domain [Fig. 9(b)] $T_{lag}(\omega)$ is given by multiplication of the transfer functions of each component. At least four temporal components can be identified: (1) temporal decay in the incident x-ray fluence; (2) decay and afterglow in the converting medium; (3) charge trapping and release in the sensor elements; and (4) signal transfer between the sensor elements and the readout electronics. This is illustrated in Fig. 9(c), which plots $T_{lag}(\omega)$ in comparison to the transfer functions of these four components: T_{x-ray} , T_{GOS} , T_{a-Si} , and T_{amp} , respectively. T_{x-ray} was derived from the measured x-ray radiation wave form (obtained using the PMX-III multimeter and an oscilloscope). Given the synchronization between the radiographic x-ray pulse and imager readout, the integrated intensity of the x-ray source was essentially a delta function in the frame number domain; hence, T_{x-ray} is unity. T_{GOS} was estimated based upon the phosphor decay measurements of Shepherd *et al.*⁴¹ and Mainprize and Yaffe.^{43,44} Two components of phosphor afterglow were assumed in the estimation: decay (at a level of 0.01% for $n=1$) and afterglow (at a level of 0.0001% for $n \geq 2$). Again, for the integration times achievable with the FPI, the IRF was nearly a delta function in the frame number domain; hence T_{GOS} is near unity. Signal retention due to incomplete charge transfer between the sensor and the external electronics was conservatively estimated at a level of 1% for all n ; hence, T_{amp} is greater than 98% out to ω_{Nyq} . Finally, the component corresponding to trapping and release of charge, T_{a-Si} , was obtained by dividing the measured $T_{lag}(\omega)$ by the product of T_{x-ray} , T_{GOS} , and T_{amp} . The result is that the total image lag for the FPI is strongly dominated

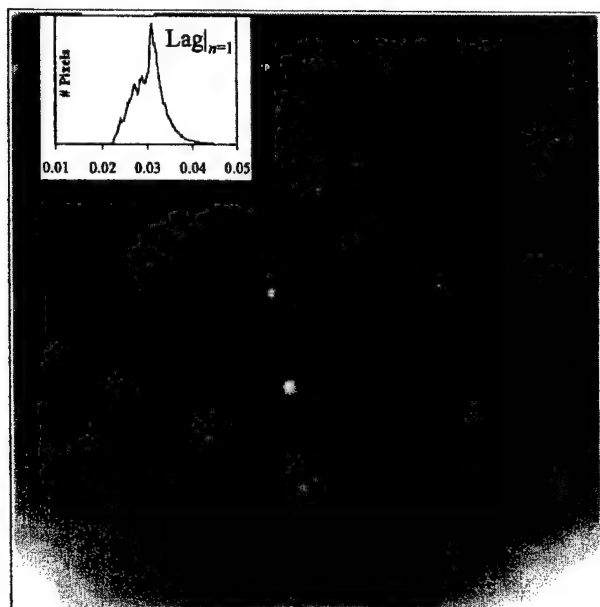


FIG. 10. Spatial uniformity of the (first-frame) image lag. The image shows $\text{Lag}|_{n=1}$ for all 512×512 pixels plotted as a function of spatial position across the FPI (for an exposure of ~ 2 mR and a T_{frame} setting of 3.2 s). The grayscale was adjusted to maximize the displayed contrast, and a histogram of lag values is superimposed.

by the effect of charge trapping and release in the α -Si:H sensor elements.

3. Image lag: Spatial uniformity

The spatial uniformity of the image lag was measured by acquiring IRFs for all pixels on the array. As shown in Fig. 10, the image lag is uniform to within $\sim 1\%$ (ranging from $\sim 2.5\%$ to 3.5%) across most of the FPI, although there is evidence of increased lag (by a factor of 2–3) in several regions (corresponding to the regions of anomalous pixel dark noise in Fig. 5). The cause for this variation in $\text{Lag}|_{n=1}$ is likely the result of nonuniform processing/quality of α -Si:H in the array. Its presence suggests, among other things, that lag correction algorithms for CBCT (mentioned above) should consider not only the magnitude of $\text{Lag}|_n$ and its dependence upon exposure, but also the (stationary) spatial dependence of $\text{Lag}|_n$ across the FPI. That is, $\text{Lag}|_n$ depends upon n [Fig. 7(a)], exposure [Fig. 8(b)], and to some extent upon position (Fig. 10).

4. Image lag: Visual impression in successive projections

Finally, the visual impression resulting from image lag between successive radiographs was examined by acquiring images of moving objects, including a linear array of Pb BBs and an angled Bi–Pb edge. The image in Fig. 11(a) clearly shows the position of the BBs at the time of the exposure (labeled “0”); however, image lag (at a level of $\text{Lag}|_{n=1} \sim 3.3\%$) results in the presence of a clearly visible artifact from the previous exposure (labeled “1”). Artifacts from the image obtained two frames prior (at a level of $\text{Lag}|_{n=2}$

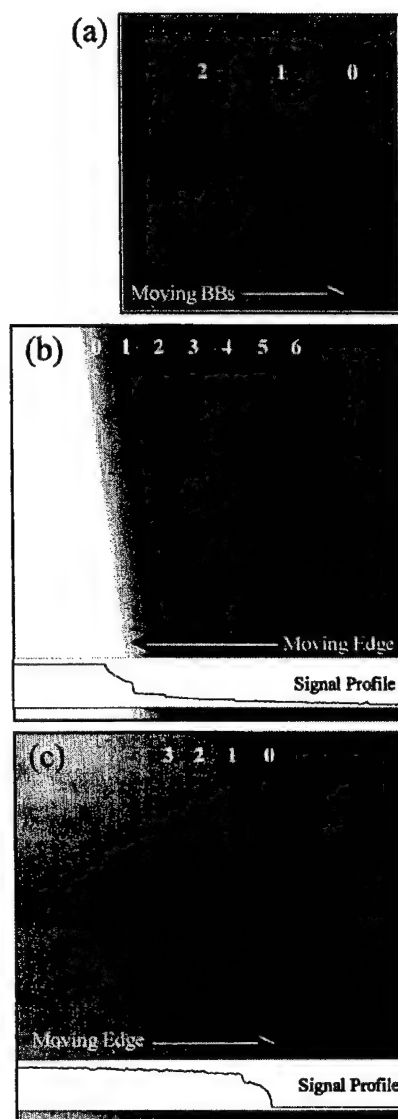


FIG. 11. Visual impression of image lag in successive radiographs. (a) A portion of a single image from a series of radiographs acquired (with an exposure of ~ 2 mR/frame and a frame time of 6.4 s) as a line of BBs was translated across the FOV, from left to right as indicated by the arrow. (b) and (c) Images from a series of successive radiographs during which the edge of a Bi–Pb alloy slab was translated into [to the left (b)] and out of [to the right (c)] the detector FOV. The relative signal along a row in the center of the image is illustrated in the signal profiles superimposed in (b) and (c).

$\sim 0.74\%$) are barely visible (labeled “2”), and artifacts from previous frames are imperceptible. Presumably, the visibility of such artifacts increases for higher exposures and for larger objects.

Figures 11(b) and 11(c) show images of a Bi–Pb alloy slab moving into (b) and out of (c) the FOV. The image in Fig. 11(b) exhibits step artifacts from not only the previous frame (labeled “1”) but from the previous three or four frames as well (or more, depending upon the choice of grayscale window). In Fig. 11(c), step artifacts from the previous two or three images are discernible. The fact that fewer step artifacts are discernible in the case of Fig. 11(c) than in Fig.

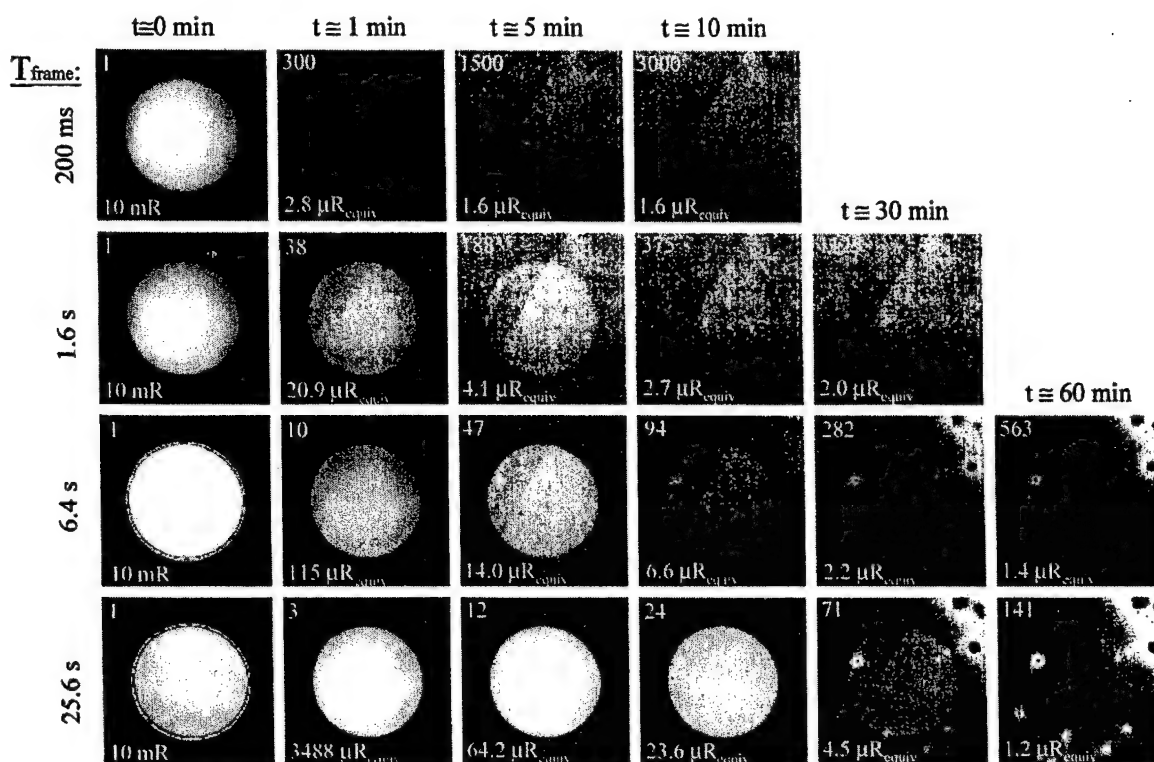


FIG. 12. A ghost in the machine. Images (of a 2 cm hole in a Pb slab) acquired at times 0, 1, 5, 10, 30, and 60 min following an exposure (at ~ 10 mR) are shown for continuous FPI operation at frame times of 0.2, 1.6, 6.4, and 25.6 s. Each image represents a small region (120×120 pixels) in the lower left of the FPI. All images at $t > 0$ were obtained without x-ray irradiation (i.e., in the dark). In the upper left of each image, the number of frames read following the exposure is indicated. In the lower-left of each image, the contrast of the hole is expressed in terms of the exposure that would produce an equivalent difference in signal level (expressed in units of μR and denoted $\mu\text{R}_{\text{equiv}}$).

11(b) points out an interesting consideration concerning the effect of image lag on clinical images: The visibility of lag artifacts is greater in regions of lower signal; and, the appearance of such artifacts is reduced in regions of high signal. This is due to at least two effects: (1) the contribution of lag signal relative to the signal generated on the current frame is large (small) in regions of low (high) exposure; and (2) the electric field across the photodiode is higher for regions of low signal, resulting in greater extraction of trapped charge from previous frames. This difference also points out an important caveat in interpreting lag results measured using various IRF, SRF, and moving object techniques (as in Table 1): The case of Fig. 11(b) is analogous to a falling-edge SRF measurement, whereas that of Fig. 11(c) is analogous to a rising-edge SRF measurement; a moving slit would be analogous to an IRF measurement. The implications of these results for applications involving high-contrast moving edges are obvious. For example, on-line verification imaging in radiotherapy regimens employing dynamic collimation (e.g., dynamic multileaf collimation) may exhibit such artifacts at field edges, which are often the regions of interest for portal localization.

C. Ghosts

The long-term persistence of "ghost" images was investigated by acquiring images of a hole drilled in a Pb slab as

a function of time following exposure. At time $t = 0$, an exposure was made, and images were acquired continuously for up to 1 h at various settings of T_{frame} . Figure 12 shows example images that demonstrate the "ghosting" effect (120×120 pixel region in the lower left-hand side of the FPI). For $T_{\text{frame}} = 200$ ms, the ghost image is barely perceptible at $t = 1$ min, and it is imperceptible at $t = 5$ min. At higher settings of T_{frame} , the ghost image persists longer. For example, at $T_{\text{frame}} = 25.6$ s, the ghost image is clearly visible at $t = 30$ min and barely visible at $t = 60$ min. Typically, the ghost image becomes imperceptible at a contrast equivalent to $\sim 2 \mu\text{R}$ (within the hole), corresponding to a signal difference of $\sim (18 \times 10^6 \text{ e/mR}) \times (0.002 \text{ mR}) \sim 36\,000\text{e}$ (which is ~ 2 – 3 times the pixel dark noise).

At first glance, one might conclude that the contrast of the ghost is simply a function of the number of frames [such as demonstrated for image lag in Fig. 7(a)] and that by reading out many frames, the ghost is made imperceptible; however, that is not entirely the case. For example, considering the image at ($t = 30$ min, $T_{\text{frame}} = 25.6$ s), the contrast corresponds to $4.5 \mu\text{R}_{\text{equiv}}$ after ~ 71 readout cycles; on the other hand, the image at ($t = 10$ min; $T_{\text{frame}} = 6.4$ s) exhibits $6.6 \mu\text{R}_{\text{equiv}}$ following ~ 94 about readout cycles. Therefore, the contrast is greater in the latter case despite a greater number of reads. This implies a mechanism for ghosting that depends not upon the number of readout cycles, but upon

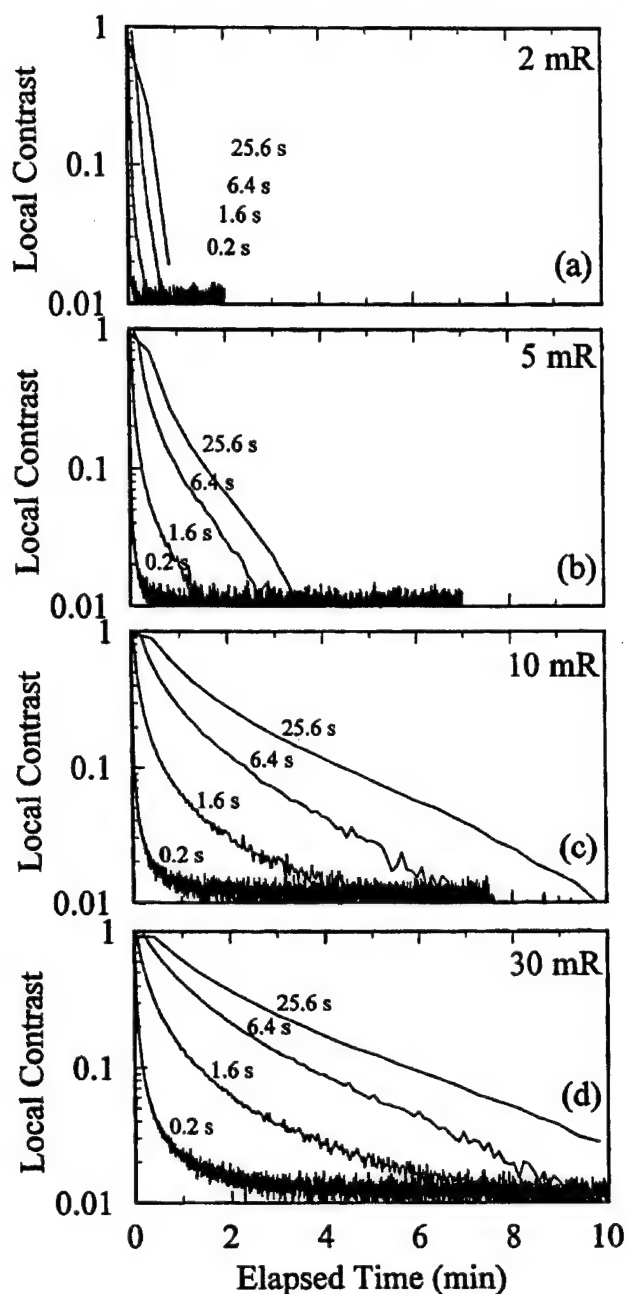


FIG. 13. Long-term persistence ("ghosting") of the image of a hole in a Pb slab. The local contrast of the hole is plotted vs time for T_{frame} settings of 0.2, 1.6, 6.4, and 25.6 s for exposures of ~2, 5, 10, and 30 mR [(a), (b), (c), and (d), respectively]. Typically, the ghost image of the hole is imperceptible at local contrast values of ~0.01–0.02.

time. To illustrate this point further, consider the three images at $[(t=60 \text{ min}; T_{\text{frame}}=25.6 \text{ s})]$, $[(t=30 \text{ min}; T_{\text{frame}}=6.4 \text{ s})]$, and $[(t=10 \text{ min}; T_{\text{frame}}=1.6 \text{ s})]$. For these three images, the number of readouts is 141, 282, and 375, respectively; however, the contrast corresponds to 1.2, 2.2, and $2.7 \mu\text{R}_{\text{equiv}}$, respectively, which follows a trend contradictory to a frame-dependent ghosting mechanism. Rather, it strongly suggests a long-term mechanism that depends not upon the number of reads, but upon the amount of time fol-

lowing the initial x-ray exposure. This mechanism is quite distinct from that governing image lag (which was shown to depend primarily on the number of reads over the first ~10–20 frames following exposure).

Figure 13 shows plots of the local contrast computed from ghost images of the hole at various exposures and T_{frame} versus time following the x-ray exposure. At the lowest exposure [2 mR, as in Fig. 13(a)], ghosting appears negligible, and the level of contrast exhibited in the first minute following the exposure is consistent simply with the image lag. At higher exposures, however, and especially beyond sensor saturation, the contrast of ghost images at $t > 1 \text{ min}$ is large for high settings of T_{frame} . Furthermore, it should be noted that at a given time following the exposure (say, $t = 10 \text{ min}$), the ghost image may be imperceptible at low T_{frame} , but if the imager is switched to large T_{frame} , the ghost is readily apparent. For example, an experiment was performed in which an image of the hole was formed at 10 mR and with $T_{\text{frame}} = 200 \text{ ms}$. Following the exposure, the FPI was cycled continuously in the dark at this same frame rate, and the ghost was imperceptible following ~1 min, as suggested by the lowest curve in Fig. 13(c). At $t = 30 \text{ min}$, however, the FPI was switched to $T_{\text{frame}} = 25.6 \text{ s}$, and the ghost image was readily apparent. Switching back to $T_{\text{frame}} = 200 \text{ ms}$ caused the ghost to vanish, and switching back to $T_{\text{frame}} = 25.6 \text{ s}$ caused it to reappear in the image. Obviously, this behavior suggests a low intensity source of the ghost signal, i.e., one that produces a small amount of signal electrons per unit time (compared to the pixel dark noise, and independent of T_{frame}), so that the integrated ghost signal is only appreciable at long integration times. Specifically, from the levels of contrast exhibited in Fig. 12, a signal source the intensity of which decays over time is suggested, with equivalent exposures rates of ~14, ~2.5, 1.0, and $0.3 \mu\text{R}_{\text{equiv}}/\text{s}$ (i.e., 252, 45, 18, and $5.4 \times 10^3 \text{ e/s}$) at $t = 1, 5, 10$, and 30 min, respectively. At least two such sources of ghosting may be hypothesized: (1) low intensity afterglow from the $\text{Gd}_2\text{O}_2\text{S:Tb}$ phosphor; and (2) very slow release of charge from deep trapping states in the $a\text{-Si:H}$ sensor. In light of the phosphor persistence data of Shepherd *et al.*⁴¹ and Mainprize *et al.*^{43,44} it is difficult to justify the former explanation. Considering the capacitance and broad spectrum of time constants⁴⁶ corresponding to trapping states in $a\text{-Si:H}$, the latter explanation may be more likely.

Finally, two methods of reducing the apparent contrast of ghost images were examined. The first involved rapid scanning of the FPI at maximum frame rate following the exposure (in an attempt to "flush out" the ghost image, a technique which might seem viable in the context of the image lag data, described in Sec. III D). As shown in Fig. 14(a), however, this approach proved ineffective at reducing the local contrast of the ghost image below that measured without rapid scanning. These results are consistent with the findings above—namely, that the long-term ghosting effect depends primarily upon elapsed time and not upon the number of readout cycles.

A second method was examined in which flood-field exposures were made at times following the original exposure

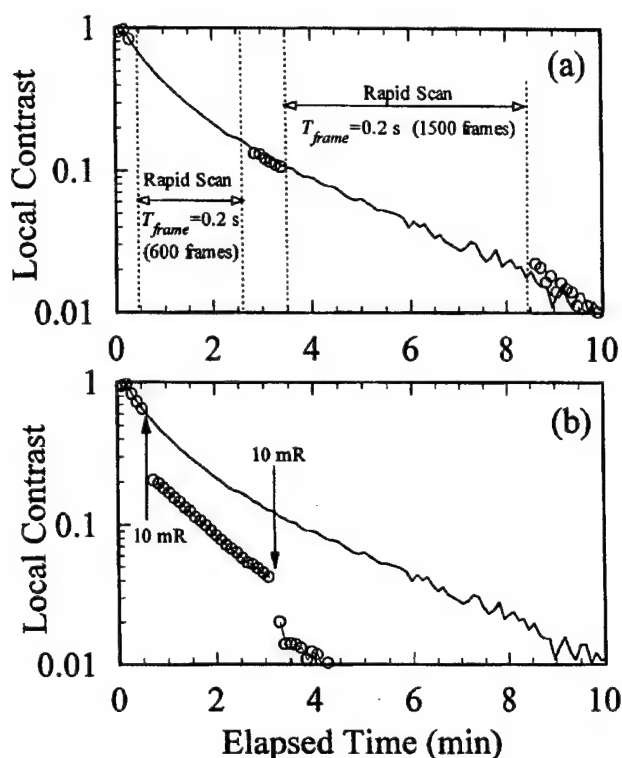


FIG. 14. Ghost-busters? Local contrast of the image of a hole (as in Figs. 12 and 13) is plotted vs time following the exposure [solid curves in both (a) and (b)]. In each case a fairly strong ghost image was induced by delivering a high exposure (~ 30 mR; nominal $T_{\text{frame}} = 6.4$ s), and the local contrast was monitored for 1 h. In (a), the measurement was repeated, except that at time $t = 30$ s, the FPI was switched to its fastest frame rate for 600 frames (~ 2 min), indicated by the bracketed region of the graph labeled "Rapid Scan." The imager was then switched back to the nominal frame time, and the local contrast was recorded, as shown by the open circles plotted at $t \sim 3$ min. The FPI was switched again to its highest frame rate (for 1500 frames, or 5 min), shown by the second "Rapid-Scan" region of the graph. In (b) flood-field exposures (10 mR each) were delivered at $t = 30$ s and $t = 3$ min, and the local contrast of the ghost image was recorded continuously (with T_{frame} held constant at 6.4 s). Neither technique represents an ideal means of eliminating ghost images: method (a) is ineffective, and method (b) is impractical.

(in an attempt to "wash out" the ghost image). The results are shown in Fig. 14(b). Delivery of the first flood field was found to significantly reduce the local contrast of the ghost, from ~ 0.6 to ~ 0.2 . The subsequent flood field at $t = 3$ min had a similar effect. These results suggest that flood-field exposures succeed to some extent in "washing out" the ghost image; however, this is likely accomplished by inducing a source of low intensity signal (i.e., a ghost) uniformly across the FPI. Thus, reduction of the ghost image might come at the cost of increased "dark" signal. The effect of this procedure upon image quality in subsequent images is beyond the scope of this investigation. Furthermore, the practice of delivering a flood-field exposure between radiographs may not be clinically practical. The same effect might be achieved, however, through incorporation of an optical reset mechanism (such as that employed in FPIs utilizing a single-diode switch¹⁸) to provide an optical flood field. Such a mechanism might not only aid in the reduction of ghost

artifacts, but might also reduce image lag in general by keeping deep and shallow trapping states full, so that charge generated from the x-ray exposure has a lower probability of being trapped.

IV. SUMMARY AND CONCLUSIONS

The prototype flat-panel imager under investigation for CBCT was characterized in terms of its pixel dark signal and noise, radiation response, image lag, and ghosting effects. For most pixels on the array, pixel dark signal is stable within ~ 5 – 10 fC following a 2 h warm-up period. A number of regions, however, exhibit increased dark signal drift which does not stabilize even after ~ 2 h. The pixel dark noise is typically ~ 13 100 e and is dominated by the noise of the amplifier and readout electronics. The radiation response of the FPI provides a system gain of $\sim 18 \times 10^6$ e/mR/pixel (at 120 kVp), saturates at an exposure of ~ 10 mR (limited by the charge capacity of the amplifier electronics), is linear within $\sim 5\%$ across 50% of the FPI latitude, and is independent of exposure rate. The reproducibility of the results was tested by repeating measurements of dark pixel noise (versus frame time) and image lag (versus frame time and exposure level) approximately four months after the measurements reported herein, and excellent agreement (well within statistical error) was achieved in all cases.

The image lag characteristics were quantified through measurements of pixel IRFs. First, second, and third-frame lag is $\sim 2.8\%$, $\sim 0.7\%$, and $\sim 0.4\%$ (at exposures corresponding to $\sim 20\%$ saturation), and tenth-frame lag is $\sim 0.1\%$. Image lag was found to increase significantly with exposure and to depend primarily upon the number of reads, rather than the amount of time between successive frames. Lag is largely uniform across the FPI; however, a number of anomalous regions exhibit first-frame lag ~ 2 – 5 times higher than "normal" pixels. The visual impact of image lag is such that artifacts of high-contrast, moving objects are clearly visible in successive frames, depending upon exposure. This suggests that, in the context of the CBCT application, strategies to minimize or account for such artifacts should be adopted. Such strategies include: (1) "flushing" the lag signal by reading several (e.g., ~ 1 – 10) frames between successive projections; and (2) implementation of a correction algorithm to subtract the lag signal from each projection. The first strategy is likely the easier to implement and possibly the more effective, although it may slow CBCT acquisition. By switching to the highest frame rate between projections, for example, 10 frames could be "flushed" within 2 s. Alternatively, a special readout mode (not currently implemented) could be utilized in which all rows of the FPI are activated simultaneously. Of course, such a mode provides no imaging information, but it could allow very fast "flushing" between CBCT projections. The latter strategy (a correction algorithm) necessarily introduces noise in corrected images and should account for the magnitude, exposure dependence, and spatial nonuniformity of the image lag. Each strategy in flat-panel CBCT is the subject of future work.

Measurements of the spatial uniformity of pixel dark signal, dark signal drift, pixel dark noise, and image lag not only demonstrate the degree of uniformity attained by a state of the art, commercially available FPI, but also provide insight into the physical mechanisms responsible for such phenomena. Nonuniformity in these phenomena exhibited strong spatial correlation, and typically occurred about numerous, irregularly shaped regions and/or in two corners of the FPI. The periphery of the irregularly shaped regions exhibited elevated dark signal and dark signal drift (Fig. 3), whereas the interior of such regions, in addition to the corner regions, exhibited elevated pixel dark noise (at extended frame time; Fig. 5) and image lag (Fig. 10). The degraded performance of pixels in such regions may be the result of nonuniform quality of the α -Si:H⁵² and/or the passivation layer.⁹ The fact that regions of elevated pixel dark noise are strongly correlated with regions exhibiting increased image lag suggests that these effects share a common physical mechanism (which is distinct from the mechanism governing drift), e.g., increased density of trapping states and/or increased device resistance. The fact that these regions seem "bounded" by regions of high drift is intriguing.

Long-term persistence ("ghosting") was observed for images of high-contrast objects obtained at high exposures. Ghosts were found to persist for 30 min or longer and were more apparent at higher settings of T_{frame} , suggesting a low-intensity source of the ghost signal (e.g., increased leakage current in regions of high exposure, slow release of charge from deep trapping states, or phosphor afterglow). The intensity of the ghost signal source was small but easily detected, equivalent to $\sim 2\text{--}3 \mu\text{R/s}$ at an elapsed time of 5 min following the exposure. Rapid scanning was ineffective in removing persistent ghosts; flood-field exposures succeeded to some degree in reducing the visibility of ghosts, but it is doubtful that this represents a practical solution. These results are most relevant to imaging applications in which high-contrast edges (e.g., collimators, skin line, prosthetics, or any number of objects in industrial NDTE) are routinely imaged. In order to inhibit strong ghosting effects, it is clearly advantageous to avoid delivering a saturating exposure to the FPI; similarly, it is beneficial to avoid repeated imaging of high-contrast objects placed in the same region of the FOV. Frequent recalibration of the dark signal offset image required for gain-offset correction (e.g., acquisition of offset images immediately prior to imaging) may be the most efficient means of reducing the visibility of ghosts. Such a procedure is prudent also in that it allows better correction of pixels exhibiting anomalous dark signal drift.

ACKNOWLEDGMENTS

The authors extend their gratitude to D. G. Drake (Oakland University) for assistance with the measurements, W. Jendhoff (Beaumont Services Corp.) for instrumentation of numerous components employed on the laboratory bench, Elekta Oncology Systems, Inc. for supplying the flat-panel imaging system, and M. K. Gauer (EG&G Heimann) for technical information concerning the imaging array. This re-

search was funded in part by the Prostate Cancer Research Program Grant No. DAMD-17-98-1-8497 from the U. S. Army Medical Research and Materiel Command.

¹⁾ Author to whom all correspondence should be addressed; electronic mail: jsiewerd@beaumont.edu

¹L. E. Antonuk, J. Boudry, W. Huang, D. L. McShan, E. J. Morton, J. Yorkston, M. J. Longo, and R. A. Street, "Demonstration of megavoltage and diagnostic x-ray imaging with hydrogenated amorphous silicon arrays," *Med. Phys.* **19**, 1455–1466 (1992).

²W. Zhao and J. A. Rowlands, "X-ray imaging using amorphous selenium: Feasibility of a flat panel self-scanned detector for digital radiology," *Med. Phys.* **22**, 1595–1604 (1995).

³J. M. Boudry, *Evaluation of Hydrogenated Amorphous Silicon Photodiodes and Field-Effect Transistors for Use as Elements of Two-Dimensional X-ray Imaging Arrays* (UMI Dissertation Services, Ann Arbor, MI, 1996).

⁴L. E. Antonuk *et al.*, "Initial performance evaluation of an indirect-detection, active matrix flat-panel imager (AMFPI) prototype for megavoltage imaging," *Int. J. Radiat. Oncol., Biol., Phys.* **42**, 437–452 (1998).

⁵P. Munro and D. C. Bouius, "X-ray quantum limited portal imaging using amorphous silicon flat-panel arrays," *Med. Phys.* **25**, 689–702 (1998).

⁶D. A. Jaffray, J. H. Siewerdsen, and D. G. Drake, "Performance of a volumetric CT scanner based upon a flat-panel imaging array," *Proc. SPIE* **3659**, 204–214 (1999).

⁷R. Ning, D. Lee, X. Wang, Y. Zhang, D. Conover, D. Zhang, and C. Williams, "Selenium flat panel detector-based volume tomographic angiography imaging: Phantom studies," *Proc. SPIE* **3336**, 316–324 (1998).

⁸R. Ning, X. Tang, R. Yu, D. Zhang, and D. Conover, "Flat panel detector-based cone beam volume CT imaging: Detector evaluation," *Proc. SPIE* **3659**, 192–203 (1999).

⁹L. E. Antonuk, Y. El-Mohri, J. H. Siewerdsen, J. Yorkston, W. Huang, V. E. Scarpine, and R. A. Street, "Empirical investigation of the signal performance of a high-resolution, indirect detection, active matrix flat-panel imager (AMFPI) for fluoroscopic and radiographic operation," *Med. Phys.* **24**, 51–70 (1997).

¹⁰R. A. Street, I. Fujieda, R. Weisfield, S. Nelson, and P. Nysten, "Large area 2-dimensional α -Si:H imaging arrays," *Mater. Res. Soc. Symp. Proc.* **258**, 1145–1150 (1992).

¹¹M. J. Powell, I. D. French, J. R. Hughes, N. C. Bird, O. S. Davies, C. Glasse, and J. E. Curran, "Amorphous silicon image sensor arrays," *Mater. Res. Soc. Symp. Proc.* **258**, 1127–1137 (1992).

¹²L. E. Antonuk, J. Yorkston, W. Huang, J. Boudry, E. J. Morton, M. J. Longo, and R. A. Street, "Factors affecting image quality for megavoltage and diagnostic x-ray α -Si:H imaging arrays," *Mater. Res. Soc. Symp. Proc.* **258**, 1069–1074 (1992).

¹³I. Fujieda, R. A. Street, R. L. Weisfield, S. Nelson, P. Nysten, V. Perez-Mendez, and G. Cho, "High sensitivity readout of 2D α -Si image sensors," *Jpn. J. Appl. Phys., Part 1* **32**, 198–204 (1993).

¹⁴L. E. Antonuk, J. Yorkston, W. Huang, J. Siewerdsen, and R. A. Street, "Considerations for high frame rate operation of two-dimensional α -Si:H imaging arrays," *Mater. Res. Soc. Symp. Proc.* **297**, 945–950 (1993).

¹⁵U. Schiebel *et al.*, "Fluoroscopic x-ray imaging with amorphous silicon thin-film arrays," *Proc. SPIE* **2163**, 129–140 (1994).

¹⁶T. Graeve, W. Huang, S. M. Alexander, and Y. Li, "Amorphous silicon image sensor for x-ray applications," *Proc. SPIE* **2415** (1995).

¹⁷T. Graeve, Y. Li, A. Fabians, and W. Huang, "High-resolution amorphous silicon image sensor," *Proc. SPIE* **2708**, 494–498 (1996).

¹⁸J. Chabbal *et al.*, "Amorphous silicon x-ray image sensor," *Proc. SPIE* **2708**, 499–510 (1996).

¹⁹R. L. Weisfield, R. A. Street, R. Apte, and A. Moore, "An improved page-size 127 μm pixel amorphous-silicon image sensor for x-ray diagnostic medical imaging applications," *Proc. SPIE* **3032**, 14–21 (1997).

²⁰T. J. C. Bruijns *et al.*, "Technical and clinical results of an experimental flat dynamic (digital) x-ray image detector (FDXD) system with real-time corrections," *Proc. SPIE* **3336**, 33–44 (1998).

²¹N. Jung *et al.*, "Dynamic x-ray imaging system based on an amorphous silicon thin-film array," *Proc. SPIE* **3336**, 396–407 (1998).

²²B. Polischuk, Z. Shukri, A. Legros, and H. Rougeot, "Selenium direct

- converter structure for static and dynamic x-ray detection in medical imaging applications," *Proc. SPIE* **3336**, 494–504 (1998).
- ²³A. Tsukamoto, S. Yamada, T. Tomisaki, M. Tanaka, and T. Sakaguchi, "Development of a selenium-based flat-panel detector for real-time radiography and fluoroscopy," *Proc. SPIE* **3336**, 388–395 (1998).
 - ²⁴D. L. Lee, L. K. Cheung, B. Rodricks, and G. F. Powell, "Improved imaging performance of a 14×17-inch direct radiography system using Se/TFT detector," *Proc. SPIE* **3336**, 14–23 (1998).
 - ²⁵R. L. Weisfield, M. Hartney, R. Schneider, K. Aflatooni, and R. Lujan, "High performance amorphous silicon image sensor for x-ray diagnostic medical imaging applications," *Proc. SPIE* **3659**, 307–317 (1999).
 - ²⁶P. R. Granfors, "Performance characteristics of an amorphous silicon flat panel x-ray imaging detector," *Proc. SPIE* **3659**, 480–490 (1999).
 - ²⁷R. E. Colbeth *et al.*, "Characterization of a third generation, multi-mode sensor panel," *Proc. SPIE* **3659**, 491–500 (1999).
 - ²⁸J. Yorkston, L. E. Antonuk, Y. El-Mohri, K. W. Jee, W. Huang, M. Maolinbay, X. Rong, and J. H. Siewerdsen, "Improved spatial resolution in flat-panel imaging systems," *Proc. SPIE* **3336**, 556–563 (1998).
 - ²⁹J. Yorkston, L. E. Antonuk, N. Seraji, W. Huang, J. Siewerdsen, and Y. El-Mohri, "Evaluation of the MTF for a-Si:H imaging arrays," *Proc. SPIE* **2163**, 141–148 (1994).
 - ³⁰J. Yorkston, L. E. Antonuk, N. Seraji, W. Huang, J. Siewerdsen, and Y. El-Mohri, "MTF measurements with high resolution a-Si:H imaging arrays," *Proc. SPIE* **2432**, 260–269 (1995).
 - ³¹J. Earnhart and E. Chaney, "Modulation transfer function for a large area amorphous silicon image receptor," *Phys. Med. Biol.* **42**, 2531–2540 (1997).
 - ³²J. H. Siewerdsen, L. E. Antonuk, Y. El-Mohri, J. Yorkston, W. Huang, and I. A. Cunningham, "Signal, noise power spectrum, and detective quantum efficiency of indirect-detection flat-panel imagers for diagnostic radiology," *Med. Phys.* **25**, 614–628 (1998).
 - ³³J. H. Siewerdsen, L. E. Antonuk, Y. El-Mohri, J. Yorkston, W. Huang, J. M. Boudry, and I. A. Cunningham, "Empirical and theoretical investigation of the noise performance of indirect detection, active matrix flat-panel imagers (AMFPIs) for diagnostic radiology," *Med. Phys.* **24**, 71–89 (1997).
 - ³⁴J. H. Siewerdsen, *Signal, Noise, and Detective Quantum Efficiency of a-Si:H Flat-Panel Imagers* (UMI Dissertation Services, Ann Arbor, MI, 1998).
 - ³⁵D. G. Drake, D. A. Jaffray, and J. W. Wong, "A prototype amorphous silicon array based radiotherapy portal imager," *Proc. SPIE* **3032**, 32–41 (3032)
 - ³⁶P. Xue and D. L. Wilson, "Effects of motion blurring in x-ray fluoroscopy," *Med. Phys.* **25**, 587–599 (1998).
 - ³⁷Y. Matsunaga, F. Hatori, T. Hiroyuki, and O. Yoshida, "Analysis of signal to noise ratio of photoconductive layered solid-state imaging device," *IEEE Trans. Electron Devices* **42**, 38–42 (1995).
 - ³⁸M. D. Wright *et al.*, "Amorphous silicon dual mode medical imaging system," *Proc. SPIE* **3336**, 505–514 (1998).
 - ³⁹R. E. Colbeth *et al.*, "Flat panel imaging system for fluoroscopy applications," *Proc. SPIE* **3336**, 376–387 (1998).
 - ⁴⁰EG&G Heimann Optoelectronics GmbH, Germany, Weher Koppel 3, D-65199 Wiesbaden (product information).
 - ⁴¹J. A. Shepherd, S. M. Gruner, M. W. Tate, and M. Tecotzky, "Study of afterglow in x-ray phosphors for use on fast-framing charge-coupled device detectors," *Opt. Eng. (Bellingham)* **36**, 3212–3222 (1997).
 - ⁴²S. Rudin, J. J. Patel, and D. R. Bednarek, "Decay time measurements of imaging phosphor materials," *Med. Phys.* (submitted).
 - ⁴³J. G. Mainprize and M. J. Yaffe, "The effect of phosphor persistence on image quality in digital x-ray scanning systems," *Proc. SPIE* **2708**, 85–94 (1996).
 - ⁴⁴J. G. Mainprize and M. J. Yaffe, "The effect of phosphor persistence on image quality in digital x-ray scanning systems," *Med. Phys.* **25**, 2440–2454 (1998).
 - ⁴⁵G. Blasse, "Scintillator materials," *Chem. Mater.* **6**, 1465–1475 (1994).
 - ⁴⁶R. A. Street, *Hydrogenated Amorphous Silicon* (Cambridge University Press, New York, 1991).
 - ⁴⁷S. M. Sze, *Physics of Semiconductor Devices* (Wiley, New York, 1990).
 - ⁴⁸P. Bhattacharya, *Semiconductor Optoelectronic Devices* (Prentice-Hall, Englewood Cliffs, NJ, 1994).
 - ⁴⁹L. E. Antonuk, J. H. Siewerdsen, J. Yorkston, and W. Huang, "Radiation response of amorphous silicon imaging arrays at diagnostic energies," *IEEE Trans. Nucl. Sci.* **41**, 1500–1505 (1994).
 - ⁵⁰J. G. Proakis and D. G. Manolakis, *Digital Signal Processing: Principles, Algorithms, and Applications*, 2nd ed. (Macmillan, New York, 1992).
 - ⁵¹*Signal Processing Toolbox for Use with Matlab* (The MathWorks Inc., Natick, MA, 1988).
 - ⁵²E. A. Schiff, R. A. Street, and R. L. Weisfield, "Reverse bias currents in amorphous silicon nip sensors," *J. Non-Cryst. Solids* **198–200**, 1155–1158 (1996).

**Appendix C: Cone-beam Computed Tomography with a Flat-panel
Imager: Effects of Image Lag**

Cone-beam computed tomography with a flat-panel imager: Effects of image lag

J. H. Siewerdsen^{a)} and D. A. Jaffray

Department of Radiation Oncology, William Beaumont Hospital, Royal Oak, Michigan 48073

(Received 12 May 1999; accepted for publication 29 September 1999)

A system for cone-beam computed tomography (CBCT) has been developed based upon the technology of active matrix flat-panel imagers (FPIs), and the system has demonstrated the potential for fully three-dimensional volumetric imaging with high spatial and contrast resolution. This paper investigates the effects of image lag (arising from charge trapping and release in the FPI pixels) upon CBCT reconstructions. Hypotheses were derived based upon a simple, geometrical/physical model, suggesting that image lag in the projection data results primarily in two artifacts: a spatial blurring artifact in the direction opposite to the direction of rotation (called a "comet") and a line artifact along the direction of the first few projections (called a "streak"). The hypotheses were tested by means of computer simulations and experimental measurements that yielded CBCT images of a simple cylindrical water phantom containing an attenuating rod of varying size and composition. The computer simulations generated projection images based upon analysis of the system geometry and a simple model of the FPI that allowed free adjustment of the image lag. Experimental measurements involved CBCT scans of the phantom under various conditions and modes of acquisition followed by examination of the resulting CBCT axial slices for lag artifacts. Measurements were performed as a function of exposure level, position and contrast of the rod, and for three modes of acquisition designed to isolate and/or minimize the two hypothesized artifacts. The results clearly illustrate the comet and streak artifacts, particularly in relation to high-contrast objects imaged at high exposure levels. The significance of such artifacts under clinical conditions is expected to be small, considering the magnitude of the effect relative to the morphology and composition of typical anatomy. The artifacts may become appreciable, however, in the presence of high-contrast objects, such as marker BBs, dental fillings, and metal prosthetics. A procedural method of reducing lag artifacts is demonstrated. © 1999 American Association of Physicists in Medicine. [S0094-2405(99)02012-X]

Key words: flat-panel imager, amorphous silicon, cone-beam computed tomography, image lag, artifacts

I. INTRODUCTION

Active matrix flat-panel imagers (FPIs) have become subjects of widespread research and development in every major field of medical x-ray imaging. Based upon the technology of large area, active matrix arrays of thin-film hydrogenated amorphous silicon (a-Si:H) thin-film transistors (TFTs), such devices offer a number of potential advantages over existing clinical technologies. Originally developed for electronic portal imaging (e.g., Refs. 1 and 2), the large area, compact design, real-time readout, and inherent radiation damage resistance of FPIs made them an attractive technology for radiotherapy localization and verification imaging. Soon thereafter, the potential of FPIs in diagnostic imaging was recognized as well.³ For example, in chest radiography, FPIs offer the potential of improved detective quantum efficiency (DQE) compared to screen-film and storage phosphor systems (e.g., Ref. 4). In fluoroscopy, FPIs offer a compact technology free from the effects of image distortion and veiling glare (e.g., Ref. 5), and can be operated in a dual radiographic/fluoroscopic mode (e.g., Refs. 6 and 7). FPIs are also under development for full-field digital mammogra-

phy (e.g., Ref. 8). Most recently, application of FPIs in cone-beam computed tomography (CBCT) has been reported.⁹⁻¹²

The device performance requirements posed by the various fields of projection radiography have motivated a continuing evolution in the design of FPIs. For example, in chest radiography the desire for improved DQE has resulted in the use of enhanced x-ray converters (e.g., Ref. 13). Similarly in fluoroscopy, the additional requirement of high-speed, real-time readout has necessitated the development of high-performance electronics (e.g., Ref. 14). In mammography, the requirements of high DQE and spatial resolution pose a challenge to develop arrays offering fine pixel pitch while maintaining high fill factor (e.g., Ref. 15). These are but a few of the considerations that motivate the continuing evolution in FPI technology. Application of FPIs in CBCT is comparatively new, and as yet no FPIs have been designed specifically for the demands of tomography. However, the performance of FPIs in CBCT clearly benefits from the significant advances accomplished in the context of projection imaging, particularly in terms of high DQE, rapid readout, and low-noise electronics.

In CBCT, the imager acquires numerous, successive pro-

jections of an object from multiple views (e.g., 300 projections obtained at equiangular rotations of 1.2° across 360°). The trajectory of the x-ray source and imager with respect to the object may be circular, but a number of innovative trajectories have been proposed in order to improve the accuracy of cone-beam reconstructions and reduce artifacts associated with violation of Tuy's condition.¹⁶⁻¹⁸ Also, the source and imager may be operated in a step-and-shoot mode, wherein a radiographic x-ray pulse is delivered at each angular increment, or in a continuous fluoroscopic mode. In either case, the imager acquires a series of projection images that form the basis for reconstructing a three-dimensional volume image of the object. An important consideration, therefore, is the degree to which image lag (i.e., signal carried over between projections) affects imager performance and the quality of the volume reconstructions.

Temporal correlation in the projection data is known to give rise to reconstruction artifacts for conventional CT scanners, since even slight inconsistency in detector response can result in a multitude of distinct and significant artifacts.^{19,20} Specifically, for CT systems in which the rate of change in the projection scene is comparable to the response time of the detector (e.g., in CT fluoroscopy or for systems employing multiple or wobbling x-ray sources),²¹⁻²⁴ temporal correlation causes artifacts that have been the subject of considerable investigation.²⁵⁻³⁰ For example, afterglow in the detector can cause ring artifacts near objects of high contrast, where the intensity impinging on the detector varies rapidly between projections.²⁵ These results are particularly relevant to consideration of image lag effects for FPIs in CBCT, since the temporal response of these detectors is known to suffer from the effects of charge trapping and release in the a-Si:H detector elements.³¹

Image lag is defined broadly as signal present in image frames subsequent to the frame in which it was generated. Since FPIs are known to exhibit image lag (e.g., at levels of a few percent; see the Table in Ref. 32), it is worthwhile to consider to what extent image lag affects CBCT performance, and to investigate how image lag is manifest in volume reconstructions. A previous paper³² presented a detailed examination of the image lag properties of the FPI under consideration, including the dependence upon signal size and readout rate, spatial uniformity, temporal-frequency transfer function, and visual impression in successive projections. For example, Fig. 1 shows the measured temporal and signal-size dependence of the residual signal following a radiographic exposure (i.e., the impulse response function, IRF). The IRFs are described well by a double-exponential fit in the time domain [Fig. 1(a)], and the residual signal is found to increase exponentially with exposure level [Fig. 1(b)]. Another study¹⁰ involved FPI-CBCT imaging of a small animal, and preliminary examination of the resulting images [e.g., Fig. 1(c)] revealed no obvious artifacts attributable to image lag. Hence, the effects of image lag are expected to be fairly subtle.

This paper examines the effects of image lag in FPI-CBCT reconstructions by means of tests specifically de-

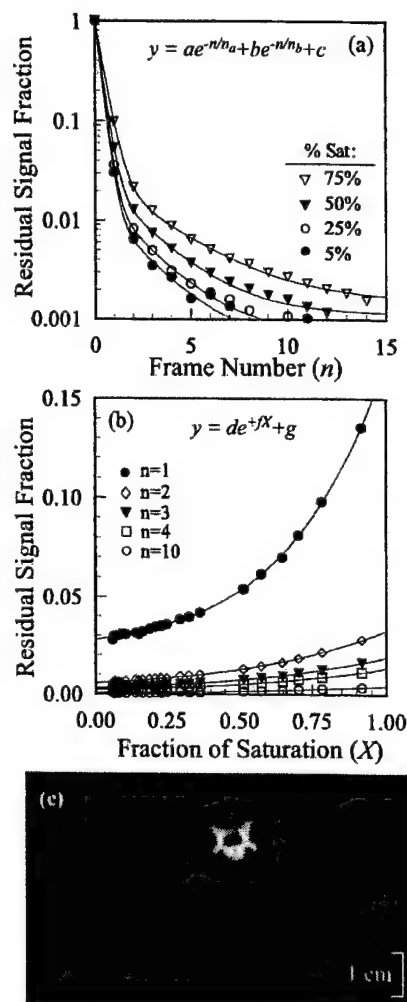


FIG. 1. Summary of image lag results for the FPI under consideration for CBCT. (See Refs. 10 and 32 for experimental details.) (a) Impulse response functions (IRFs) measured for the FPI under investigation. Results show the decay in detector signal following a radiographic exposure for signal sizes of 5%, 25%, 50%, and 75% of sensor saturation. The time interval between successive frames was 3.2 s. The solid curves are least-square fits to the double-exponential form shown, characterized in part by the two decay parameters, n_a and n_b . For the four curves shown, in order of increasing exposure level, n_a is 2.06, 2.08, 2.26, and 2.97, respectively; n_b is 0.262, 0.270, 0.306, and 0.394, respectively. Thus, the time constant for signal decay increases significantly with exposure. (b) Residual signal in the 1st, 2nd, 3rd, 4th, and 10th frames following a radiographic exposure measured as a function of exposure level. The solid curves are fits to the exponential form shown, characterized in part by the parameter f , which decreases from a value of 3.06 to 2.29 from the 1st to the 10th frame, respectively. Thus, the exposure dependence of residual signal is greatest for the 1st frame following the exposure, and decreases significantly for higher-order frame numbers. (c) Axial image slice through the abdomen of a rat obtained with the FPI-CBCT system. Preliminary results exhibited no obvious artifacts resulting from image lag.

signed to accentuate possible image lag artifacts. First, the experimental setup^{10,12} is described, and two hypotheses are derived concerning the effects of image lag upon x-ray projections and CBCT reconstructions. Second, the hypotheses are tested by means of computer simulations and experimental CBCT measurements. The computer simulations model

the FPI-CBCT system and calculate projection images that are then volume reconstructed. The experimental measurements involved numerous CBCT scans under conditions selected to illustrate artifacts that are the result of image lag and that are conspicuous in volume reconstructions. These studies illustrate the qualitative nature of image lag artifacts in FPI-CBCT, based quantitatively on previous investigation of the image lag characteristics and processes of image formation in the FPI. Finally, procedural and algorithmic methods of managing effects of image lag are discussed.

II. METHODS AND MATERIALS

A. General experimental design and geometry

1. Experimental setup

As described previously,^{10,12,32} a laboratory bench was constructed to test the performance of FPIs in CBCT under a precise, reproducible geometry that mimics the implementation of the system on a radiotherapy treatment gantry for image-guidance and soft-tissue localization.^{10,12} Mounted on an optical bench, the setup consists of three primary components: an x-ray tube (General Electric Maxiray 75 powered by a 100 kW MSI-800 generator), an object stage (Daedal 20000 Series rotary table mounted on a Daedal 30000 Series open frame linear table), and the FPI (RID 512-400-A0 from EG&G Heimann Optoelectronics). Each component is computer controlled, providing synchrony between x-ray exposure, object rotation, and imager readout. CBCT acquisition generally consisted of rotating a phantom at angular increments of 1.2 across 360°, delivering a radiographic exposure (100 kVp, 0.25–2.5 mAs) at each increment, and reading the projection image at each increment. The resulting 300 projection images were flat-field corrected for stationary gain and offset variations,³³ and a small number of defective pixels were 3×3 median-filtered. Each projection was normalized relative to the signal in the bare beam to account for variations in tube output. Finally, the volumetric data set was reconstructed using the Feldkamp algorithm³⁴ for cone-beam filtered backprojection.

The design, operation, and basic performance of the FPI employed in these studies have been detailed previously.³² The imaging array incorporates a 512×512 matrix of pixels at 400 μm pitch, giving a total area of $\sim 20.5 \times 20.5 \text{ cm}^2$. Each pixel is composed of an optically sensitive a-Si:H n-i-p photodiode in combination with an a-Si:H TFT, and the x-ray converter is composed of 133 $\text{mg}/\text{cm}^2 \text{ Gd}_2\text{O}_2\text{S:Tb}$. Images may be read at frame rates up to five frames per second (i.e., frame times down to 200 ms), but for all results reported herein, a frame time of 3.2 s was employed. Therefore, a typical CBCT acquisition took 16 min. All measurements were performed following a “warm-up” period of at least two hours,³² beyond which the effects of dark signal drift are minimized. Immediately prior to each CBCT acquisition, a set of 20 dark-fields (i.e., images acquired in the absence of x-rays) and 20 flood-fields (i.e., images acquired under uniform irradiation at the same exposure level as the ensuing acquisition) were obtained for flat-field corrections.

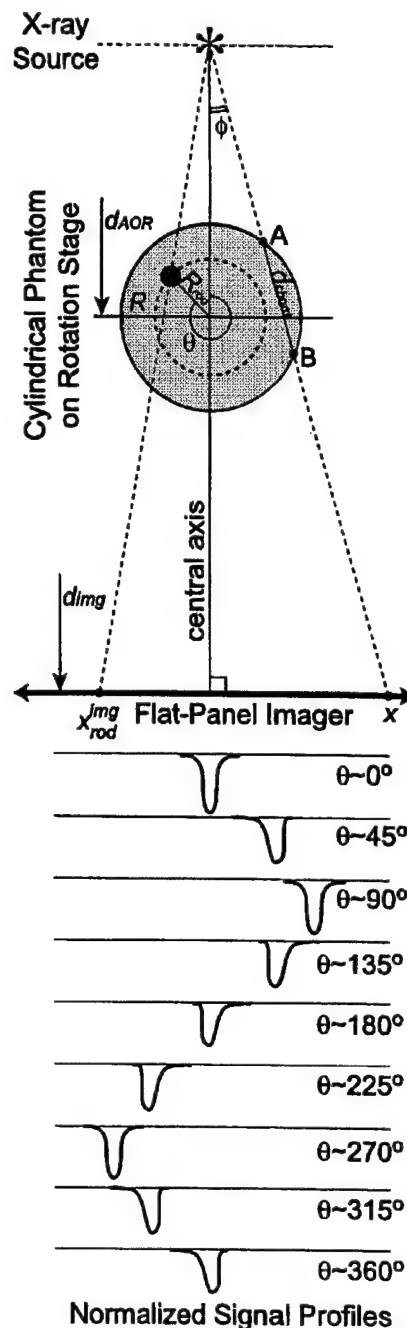


FIG. 2. Illustration of the imaging geometry used in both the experimental measurements and the computer simulations. Cone-beam filtered back-projection reconstruction (Ref. 34) of projection images of the rod phantom allowed investigation of lag artifacts in the axial plane. The lower portion of the figure represents normalized signal profiles of the rod at various projection angles.

The imaging geometry is illustrated in Fig. 2, which shows the x-ray source, rotating object, and image plane as viewed from above. The cone angle was fixed at $\sim 7.1^\circ$, the distance from the source to the axis of rotation was $d_{\text{AOR}} = 103.3 \text{ cm}$, and the distance from the source to the image plane was $d_{\text{img}} = 165.0 \text{ cm}$. A simple phantom was con-

TABLE I. Summary of system parameters used in the studies of image lag in flat-panel cone-beam CT. The first column represents the various system parameters discussed in the text and shown in Figs. 2 and 3. The second and third columns show the values of the parameters used in the computer simulations and in the CBCT measurements, respectively. Items denoted “(nom)” are the nominal settings.

System parameter	Computer simulations	CBCT measurements
d_{AOR}		103.3 cm
d_{img}		165.0 cm
R		5.5 cm
$\Delta\theta$		1.2°
# projections		300
Rod material		Stainless steel (nom) Aluminum
Radius of rod	0.25 mm	
(r_{rod})	1.25 mm	1.25 mm (nom)
	5.0 mm	
Rod displacement		0.5 cm
(R_{rod})		2.0 cm
		4.0 cm (nom)
X-ray spectrum	50 keV	100 kVp
Exposure	0.25, 0.75, 1.5, and	
(per projection)	2.5 mAs (nom)	
Image lag	“No Lag” “Nominal” “High”	See Ref. 32
Pixel pitch		400 μ m
X-ray converter		133 mg/cm ² Gd ₂ O ₂ S:Tb
Frame time	...	3.2 s
Acquisition time	~1 min	~16 min
Reconstruction time		~1 min

structed in order to examine the effects of image lag in CBCT, consisting of an 11 cm diameter, water-filled cylinder in which a rod was placed vertically. The rod had a diameter of 2.5 mm ($r_{rod}=1.25$ mm), was placed at varying radii within the cylinder (i.e., at $R_{rod}=0.5, 2.0$, or 4.0 cm), and was made of stainless steel (high contrast) or aluminum (lower contrast). The phantom was placed in a rigid, reproducible mount on the rotation stage and was centered on the axis of rotation to within ~1 mm using a dial calipers. Images of this cylindrical phantom formed the basis for characterizing the effects of image lag in CBCT. Parameters related to the phantom, the system geometry, and image acquisition/reconstruction are summarized in Table I.

2. Hypotheses

Previous investigations^{25–30} in conventional (slice-based) CT have demonstrated the existence of ring, radial blur, and streak artifacts resulting from temporal correlation in the projection data. In considering how these effects might be manifest in CBCT using an FPI, the following simple gedanken was entertained and led to the formation of two hypotheses. Herein, we are concerned with “step-and-shoot” projections of an object where the effects of motion blur^{35–37} are negligible. Consider an object traveling in a plane orthogonal to the detector; for example, a mass following the path of the rod as shown in Fig. 2. Now consider the i th projection image of the object, or simply the one-dimensional signal pro-

file, $I_i(x)$, where the position of the object in the image plane is x_i at the i th exposure. For a detector without lag, the signal profile is given simply by

$$I_i(x) = [O'_i(x) * \delta(x - x_i)] * \text{PSF}(x) \\ = O_i(x) * \delta(x - x_i), \quad (1a)$$

where $O'_i(x)$ is the physical object function (in the i th projection), $\text{PSF}(x)$ is the point-spread function of the detector (due to spatial spreading processes such as optical blur), and $O_i(x)$ is the (blurred) image object function. Convolution with the delta function simply locates the object at its position in the image plane for the i th projection. If one now considers a case in which a fraction, $\text{Lag}|_1$, of the signal from the previous projection contributes to the current projection, we have

$$I_i(x) = [O_i(x) * \delta(x - x_i)] + \text{Lag}|_1 [O_{i-1}(x) * \delta(x - x_{i-1})]. \quad (1b)$$

Extending this argument indefinitely to consider signal contribution from all previous frames, and taking $\text{Lag}|_j$ as the fraction contributed from the $(i-j)$ th projection, we have

$$I_i(x) = \sum_{j=0}^{\infty} [\text{Lag}|_j \cdot O_{i-j}(x) * \delta(x - x_{i-j})], \quad (1c)$$

where $\text{Lag}|_0$ is taken as unity. For a circularly symmetric object, such as the cylindrical rod, the object function is the same in each projection [i.e., $O_i(x) = O(x) \forall i$], so that the relation simplifies to

$$I_i(x) = O(x) * \sum_{j=0}^{\infty} \text{Lag}|_j \cdot \delta(x - x_{i-j}). \quad (1d)$$

Thus, the i th projection is given by the object function for the current projection convolved with a weighted sum of all previous projections. The contribution of signal from previous projections (i.e., image lag) causes the image of the object to be “blurred” in the direction opposite to the direction of motion. This is consistent with the common experience of how moving objects appear blurred, e.g., in x-ray fluoroscopy, under conditions of appreciable image lag. Furthermore, it is consistent with results²⁵ for conventional CT.

This argument is illustrated in Fig. 2, where signal profiles from normalized projections of the rod are shown for various projection angles. For the first exposure ($\theta=0^\circ$), the signal profile is simply the image object function [as in Eq. (1a)], since there are no previous projections from which image lag may contribute. As the object rotates, however (as shown for $\theta>0^\circ$), the object is blurred in the direction opposite to its motion, and the signal profile forms a tail attributable to image lag. At $\theta=90$ and $\theta=270^\circ$, of course, no tail is evident because the object is moving toward or away from the detector. Thus, in terms of the axial tomographic reconstruction, the projections would suggest that the object—rather than having a circular shape—possesses a diffusely attenuating tail. This leads to the first hypothesis, associated with the equilibrium of charge trapping and release throughout the majority of the projections: *image lag results in a*

diffuse tomographic artifact, called a "comet," extending in the direction opposite to the direction of rotation.

A clue to another possible artifact is evident in Fig. 2, however. Considering the first projection ($\theta=0^\circ$) in comparison to the fifth and final projections ($\theta=180$ and 360°), one finds that image lag results in an inconsistency in the projection data. Since each projection is normalized, the first signal profile suggests a strongly attenuating object without a diffuse tail, whereas the fifth suggests a less strongly attenuating object with a tail. Thus, views along the direction of the first projection are inconsistent in both shape and magnitude. This leads to a second hypothesis, associated with the non-equilibrium of charge trapping and release in the first few frames relative to subsequent frames: *image lag results in a "streak" artifact along the direction of the first few projections.*

The artifacts, therefore, are related to the notion of signal equilibrium, i.e., equilibrium in the amount of charge that is captured and released from trapping states during a given frame. With regard to CBCT acquisition, the mean signal (e.g., in the unattenuated beam) "builds up" over the first several projections in accordance with the detector step-response function. During these first few frames (typically ~ 2 – 10 frames), the system is in nonequilibrium in that more signal is lost to traps than is released. Gradually (e.g., by the ~ 10 th frame), the amount of charge released from traps during a given frame equals the amount that is captured, and the mean signal approaches a constant, equilibrium value. Of course, equilibrium is not maintained locally under conditions of a changing radiographic scene, as in the case of CBCT. Objects (e.g., the off-axis rod in Fig. 2) perturb local signal equilibrium in successive projections; hence, pixels about the region of the object are not in signal equilibrium. Therefore, "equilibrium" herein refers to the global state of the system (e.g., in the unattenuated beam or in regions distant from the rod) rather than local states (e.g., for pixels proximal to the rod). It describes the mean signal in frames following the "build-up" over the first several projections.

B. Computer simulations

Computer simulations were performed to calculate projection images of the phantom as a function of the rotation angle, θ . Then, the same cone-beam reconstruction algorithm as used with the CBCT measurements was used to reconstruct tomographic data from these simulated images. The purpose of the computer simulations was not to model or replicate the image quality of the physical system. Rather, the simulations simply allow investigation of the effects of image lag upon CBCT reconstructions in a manner that permitted free variation of all system parameters.

Figure 3 illustrates the computational processes involved in the simulations. First, the system geometry (as in Fig. 2) is defined. Second, the exposure conditions are specified (i.e., x-ray energy and magnitude of exposure for each projection). Finally, the imager configuration is defined, including the pixel pitch, system gain, screen thickness, etc., as well as the magnitude of the image lag. Given these input parameters,

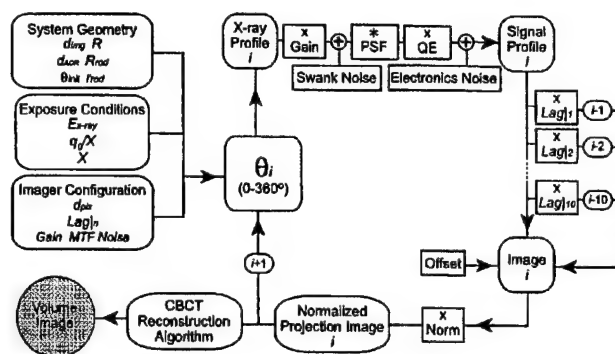


FIG. 3. Flow diagram for computer simulations of the FPI-CBCT system. The system geometry, exposure conditions, and imager configuration are specified, and the simulation computes projection images of the cylindrical phantom. These projection images are then operated upon by the same CBCT reconstruction algorithm as used with the CBCT measurements. For purposes of studying the effects of image lag on the reconstructions, the noise parameters of the simulation were set to zero. (See text for details.) This allowed examination of the image lag artifacts free from the confounding effects of quantum noise, x-ray conversion (Swank) noise, and additive electronics noise. The values of $Lag_{i(1:10)}$ were freely varied in the simulations, from zero up through arbitrarily large settings.

the simulation computes projection images of the rod phantom as a function of the rotation angle, θ .

All parameters of the system geometry were set nominally to the values in Table I. The x-ray fluence was monoenergetic ($E = 50$ keV), and effects of x-ray scatter and attenuation in air were neglected. Only the central slice was considered in the simulations (i.e., the plane containing the central axis and perpendicular to the axis of rotation). For each simulation, 300 images were computed at increments of 1.2° . The imager gain, blur, and noise properties were based upon a cascaded systems model that has demonstrated excellent agreement with measured signal, noise-power spectrum, and DQE.^{38–40} All parameters could be freely varied, e.g., to examine the effects upon image quality due to the number of views, system gain, blur, and additive noise. For purposes of investigating the effects of image lag, however, all noise sources (including Poisson variations in the x-ray quanta, conversion noise in the phosphor, and additive electronics noise) were set to zero. The system modulation transfer function (MTF) was approximated by that of the phosphor (Lanex Fast-B)⁴¹ in combination with the $400\text{ }\mu\text{m}$ pitch (80% fill factor) pixels [described by a two-dimensional (2D) sinc function]. The fluence distribution at each projection angle was convolved with the point-spread function (PSF) of the converting screen as shown in the diagram. Then, the fluence was integrated over the pixel area and sampled at locations corresponding to the pixel centers. Therefore, the simulated projections are noiseless idealizations of the empirical data and are intended to illustrate only those effects arising from image lag.

Each projection, I_i , is the sum of the x-ray generated signal and a weighted sum from previous projections attributable to image lag. The image lag was modeled as a freely adjustable, ten-element vector, $Lag_{i(1:10)}$, where the value $Lag_{i=1}$ represents the fraction of projection I_{i-1} that is added into the current projection, the value $Lag_{i=2}$ is the

fraction from projection I_{i-2} , and so on, accounting for contributions from up to ten previous projections. The image lag could be set to values approximating that measured for the device,³² or it could be freely varied from zero to arbitrarily large values. Furthermore, the effect of object size and average object velocity could be varied by adjustment of r_{rod} and R_{rod} , respectively. For a given simulation, the values in $\text{Lag}|_{i(1:10)}$ were held constant; therefore, the simulations do not account for the fact that the image lag is dependent upon the exposure to the detector. Thus, the simulations are an oversimplification of the physical system, which is known to exhibit image lag with significant exposure-dependence,³² and are intended merely to illustrate artifacts that arise from (constant) charge trapping and release.

C. Cone-beam CT lag measurements

The FPI-CBCT system has previously demonstrated^{10,12} volumetric images with contrast performance comparable to a commercial CT scanner [objects visible at 0.2% contrast; see also Fig. 1(c)] and high spatial resolution (50% MTF at $\sim 0.75 \text{ mm}^{-1}$ in the axial plane). Since preliminary analysis of those results revealed no obvious evidence of image lag artifacts, the effects of image lag on CBCT reconstructions are expected to be subtle. The experiments described below were designed specifically to examine and aggressively accentuate the effects of image lag in CBCT, and they are not necessarily representative of conditions under which FPI-CBCT might be implemented clinically. Specifically, the tests involved imaging small, high-contrast objects obtained at high exposure.

Four sets of experiments were designed to test the above hypotheses, all involving CBCT imaging of the cylindrical phantom shown in Fig. 2. First, the dependence of artifacts upon FPI signal size was tested by acquiring volume images at four exposure levels. Second, the dependence of artifacts upon the average rotational velocity of the object was tested by placing the rod at various positions within the cylinder. Third, the dependence of artifacts upon object contrast was tested by acquiring scans in which the cylinder contained a stainless steel or aluminum rod. Finally, a set of experiments was designed that involved three different modes of CBCT acquisition in order to separately investigate and/or minimize the comet and streak artifacts.

1. Exposure dependence

The dependence of artifacts upon the magnitude of the x-ray exposure was tested by acquiring volume images at 0.25, 0.75, 1.5, and 2.5 mAs per projection. These exposures correspond to FPI signal levels spanning the sensitive latitude of the detector, from $\sim 8\%$ to $\sim 75\%$ of system saturation (in the bare, unattenuated beam; i.e., $\sim 0.8\text{--}7.5 \text{ mR}$ measured at the surface of the FPI). In each case, the stainless steel rod was used, placed at $R_{\text{rod}}=4.0 \text{ cm}$ within the cylinder. The mode of acquisition was as described above, where a radiographic exposure was delivered between each image frame. Referred to as the "fast" mode for CBCT acquisition, this readout scheme is illustrated in the timing diagram of



Fig. 4. Timing diagram showing three step-and-shoot acquisition modes. The arrow symbolizes delivery of an x-ray exposure, the $\Delta\theta$ symbol represents an incremental rotation, and the I_i symbol represents readout of the i th frame. For each timing sequence, the pulses drawn in solid lines indicate recorded frames (i.e., projection data that are written to file and used in the CBCT reconstruction), whereas dashed lines indicate frames that are discarded. Furthermore, the height of each pulse is intended to illustrate the pixel signal magnitude (e.g., in the unattenuated beam). The nominal acquisition mode is the "fast" mode (a), in which an exposure is delivered between each image frame. In "lag-suppression" mode (b), n frames are flushed between projections. In "priming" mode, the system is brought closer to signal equilibrium before the actual scan by means of m exposures, rotations, and readouts carried out prior to the first recorded projection. The hypotheses suggest that reconstructed images from "fast" mode should exhibit both the comet and streak artifacts, those from "lag-suppression" mode should exhibit reduced comet and streak, and those from "priming" mode should exhibit reduced streak.

Fig. 4(a). The hypotheses suggest that artifacts resulting from image lag will increase with exposure in a manner concomitant with that of the image lag.³²

2. Speed/position dependence

Equation (1d) suggests that the comet artifact depends not only upon the magnitude of the image lag, but also upon the size of the object and its position in each projection relative to previous projections. That is, the artifact depends upon the average rotational velocity of the object during the CBCT scan. This parameter was varied experimentally (without affecting the total number of projections) by locating the rod at various positions of R_{rod} . In these studies, the stainless steel rod was used, the exposure per projection was 2.5 mAs (purposely large in order to accentuate artifacts), and the rod was placed at positions of $R_{\text{rod}} \sim 0.5, 2.0$, and 4.0 cm within the cylinder. All other parameters were as described above and shown in Table I, and the "fast" acquisition mode was used. The hypotheses suggest that the artifacts will increase for increasing values of R_{rod} (i.e., for higher average velocity).

3. Contrast dependence

Related to the dependence upon exposure level and signal size, the dependence of artifacts upon object contrast was investigated by obtaining images of both a stainless steel and aluminum rod of equal size ($r_{\text{rod}}=1.25 \text{ mm}$). In each case, the rod was placed at $R_{\text{rod}} \sim 4.0 \text{ cm}$, the highest exposure level (2.5 mAs per projection) was delivered, and the "fast" acquisition mode was used. The hypotheses suggest that the artifacts will be stronger for the higher contrast object.

4. Acquisition modes

Finally, a set of CBCT scans was performed using alternative acquisition modes that varied the orchestration of the x-ray exposure, object rotation, and FPI readout. Timing diagrams for each mode are illustrated in Fig. 4. In the "fast" mode [Fig. 4(a)] explained above, an exposure is made between each image frame. The hypotheses suggest that both the comet and streak artifacts will be present.

The second mode is referred to as the "lag-suppression" mode [Fig. 4(b)], because it was specifically designed to flush the image lag signal from the FPI pixels between each exposure. In this mode, n frames are read from the FPI between each exposure in order to flush out the image lag, and only the frame that immediately follows an exposure is recorded among the projection data. Since the frame rate was held constant throughout, the total acquisition time correspondingly increased by a factor of $(n+1)$. The "lag-suppression" mode hypothetically reduces or eliminates both artifacts. The comet is reduced, since the image lag signal is flushed during the n frames between each projection; the streak is reduced, since there is reduced inconsistency in the projections.

The "priming" mode [Fig. 4(c)] brings the imager closer to signal equilibrium prior to recording the projection data by priming for m frames prior to the actual scan. The acquisition mode begins with the object rotated backward m times the rotational increment so that the first projection image, I_0 , corresponds to the same nominal starting position as the other modes. During the m "priming" frames, an exposure is made, the object is rotated, and the image is read from the FPI (but not recorded), thus bringing the system closer to signal equilibrium at the first recorded projection [called I_0 in Fig. 4(c)]. From there, acquisition proceeds in a manner identical to "fast" mode. The "priming" mode hypothetically diminishes the streak artifact by reducing inconsistencies from the projection data that arise from nonequilibrium during the first few frames. The comet, however, is preserved.

Measurements were performed in each of the three modes, using the nominal system parameters in each case (stainless steel rod; $r_{\text{rod}}=1.25$ mm; $R_{\text{rod}}\sim 4.0$ cm; 2.5 mAs per projection). The "fast" mode was performed as described above, with the resulting tomographic data denoted I_{fast} . For the "lag-suppression" mode, scans were performed using several values of n flushed frames. Taking $n=1, 2$, and 9 (i.e., flushing one, two, and nine frames between projections, respectively) yielded tomographic images denoted I_{flush1} , I_{flush2} , and I_{flush9} , respectively. For the "priming" mode, a value of $m=30$ frames was used, resulting in data denoted I_{prime30} .

Computing the difference between tomographic images obtained in various modes allowed further investigation of image lag artifacts. Such difference images reduce effects that are common between modes, such as cupping (resulting from x-ray scatter)^{42,43} and beam-hardening (resulting from the polyenergetic x-ray spectrum and energy-dependent detector response).⁴⁴⁻⁴⁶ Hypothetically, I_{fast} contains both the

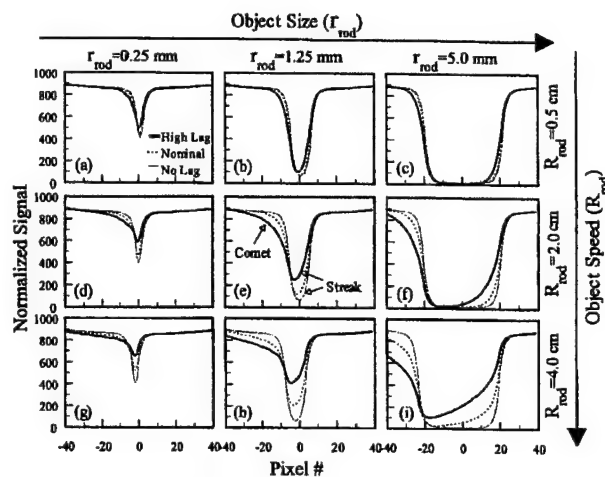


FIG. 5. Normalized signal profiles resulting from the computer simulations for various settings of object size (r_{rod}), object speed (i.e., displacement per angular increment, determined by R_{rod}), and image lag (three settings—"No Lag," "Nominal," and "High Lag"—corresponding to the three curves in each plot). In each case, the signal profile in a small region (± 40 pixels) about the position of the rod is shown, taken from the 300th simulated projection image where the rod was in the center of the field and moving toward the right. (See text for details.)

comet and streak artifacts, I_{flush9} contains neither, and I_{prime30} contains only the comet. Therefore, an image of the comet and streak alone is obtained from the difference tomogram,

$$I_{(\text{comet}+\text{streak})} = I_{\text{fast}} - I_{\text{flush9}}. \quad (2a)$$

The reduction of the comet and streak in "lag-suppression" mode should be evident in the images,

$$I_{(\text{comet}+\text{streak})}' = I_{\text{flush1}} - I_{\text{flush9}} \quad (2b)$$

and

$$I_{(\text{comet}+\text{streak})}'' = I_{\text{flush2}} - I_{\text{flush9}}, \quad (2c)$$

where the apostrophes designate reduction in the artifact. The comet alone should be exhibited in

$$I_{(\text{comet})} = I_{\text{prime30}} - I_{\text{flush9}}, \quad (2d)$$

and the streak alone should be manifest in

$$I_{(\text{streak})} = I_{\text{fast}} - I_{\text{prime30}}. \quad (2e)$$

Finally, the reproducibility of the measurements is evident in the difference tomograms (along the perimeter of the plastic cylinder) and was tested further by repeating the scan in "fast" mode and computing the difference between the original and repeated results.

III. RESULTS

A. Computer simulations

1. Signal profiles from simulated images

Figure 5 shows normalized signal profiles of the rotating rod from computer simulations performed for various settings of object size (r_{rod}), object speed (determined by R_{rod}), and image lag ($\text{Lag}|_{i(1:10)}$). Object size is constant for each

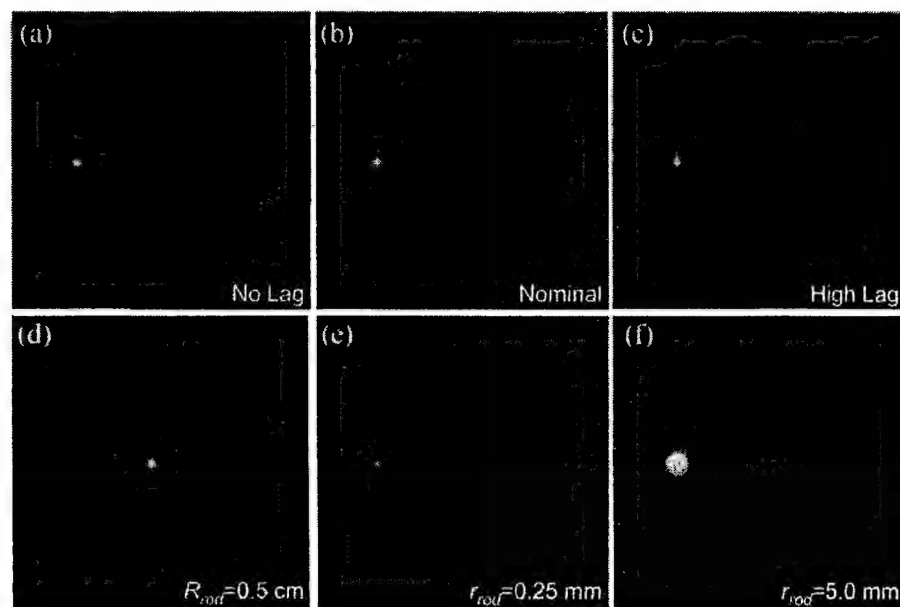


FIG. 6. Tomographic reconstructions of projections generated by the computer simulation. Reconstructions of the simulated phantom are shown for the cases of the (a) "No Lag," (b) "Nominal," and (c) "High Lag" settings, demonstrating increase in the comet and streak artifacts for increasing levels of image lag. In (d), the rod is located near the center of the cylinder, showing that the lag artifact depends upon the object path of motion, as expected. In (e) and (f), reconstructions of a small ($r_{\text{rod}}=0.25$ mm) and large ($r_{\text{rod}}=5.0$ mm) rod are shown, illustrating the comet and streak in addition to an artifact along the direction of motion and within the object (a "ramp," particularly evident for the large object). The plastic wall of the cylinder was not modeled in the computer simulations.

column of figures: a small rod ($r_{\text{rod}}=0.25$ mm) is simulated in the first column [Figs. 5(a),(d),(g)]; a rod equal to that used in the CBCT measurements ($r_{\text{rod}}=1.25$ mm) is simulated in the middle column [Figs. 5(b),(e),(h)]; and a large rod ($r_{\text{rod}}=5.0$ mm) is simulated in the third column [Figs. 5(c),(f),(i)]. Object speed (i.e., position in the cylinder) is constant for each row of figures: the rod is near the center of the cylinder ($R_{\text{rod}}=0.5$ cm) in the first row [Figs. 5(a),(b),(c)]; the rod is displaced a bit more ($R_{\text{rod}}=2.0$ cm) in the second row [Figs. 5(d),(e),(f)]; and the rod is in the same position as in the CBCT measurements ($R_{\text{rod}}=4.0$ cm) in the last row [Figs. 5(g),(h),(i)]. In each plot, signal profiles are shown for three settings of $\text{Lag}|_{i(1:10)}$, referred to as "No Lag," "Nominal," and "High Lag." For the "No Lag" setting, the image lag vector was set to zero (i.e., $\text{Lag}|_{i(1:10)}=0 \forall i$). For the "Nominal" setting, the image lag vector was set to values comparable to the image lag of the CBCT system (i.e., $\text{Lag}|_{i(1:10)}=[0.15 \ 0.05 \ 0.035 \ 0.025 \ 0.015 \ 0.01 \ 0.0075 \ 0.004 \ 0.003 \ 0.0025]$). For the "High Lag" setting, the image lag vector was set to arbitrarily large values in order to accentuate the effect; specifically, the image lag vector for the "High Lag" setting was double that of the "Nominal" setting.

These results clearly illustrate the effect of image lag in producing a tail in the signal profiles opposite to the direction of rotation. (Note that the tail is not due to motion blur during the exposure, since the object is at rest when each exposure is made; rather, the tail is purely the result of image lag. All results herein—both simulations and experiments—were performed using "step-and-shoot" acquisition.) As seen in Fig. 5, the signal profile for the "No Lag" case is simply the blurred image of the object, with no distortion associated with image lag. For the "Nominal" and "High Lag" cases, the profiles are progressively distorted. In addition to the formation of a tail "behind" the object, the

"front" edge of the object is distorted as well, due to the gradual buildup of signal associated with image lag. This suggests that in addition to the hypothesized comet, the resulting tomographic image will exhibit nonuniformity within the object due to signal buildup. This is especially evident for the large object ($r_{\text{rod}}=5.0$ mm) moving with high average velocity ($R_{\text{rod}}=4.0$ cm), as in Fig. 5(i).

The signal profiles of Fig. 5 support the argument regarding the comet artifact, and they suggest another effect (non-uniformity within the object due to signal build-up). However, they do not illustrate the mechanism for the streak, since they only show a single frame. The streak effect (which arises from inconsistency between the 1st and latter frames) is suggested by way of illustration, however, in Fig. 5(e). There, a tail associated with the "High Lag" condition is evident and is labeled in the plot by the term "comet." The undistorted profile corresponding to the "No Lag" case is, in fact, equivalent to the 1st frame profile computed for the "High Lag" case. Therefore, the discrepancy between the "No Lag" and "High Lag" profiles is similar to the inconsistency associated with the streak artifact. Thus, the discrepancy between the two is labeled by the term "streak" for purposes of illustration.

2. Tomographic reconstructions from simulated images

The simulated projection images were operated upon by the same CBCT reconstruction algorithm used for the real projection data, and example results are shown in Fig. 6. Each image in Fig. 6 represents a single axial slice in the central plane, computed from the simulations described above. In Figs. 6(a)–6(c), reconstructions are shown for the "No Lag," "Nominal," and "High Lag" settings, respectively, using the nominal size and displacement of the rod.

For the "No Lag" case [Fig. 6(a)] there are faint streaks extending radially from the rod, but there are no artifacts associated with image lag. These radial streaks were due to rounding errors in the computer simulation in placing the central position of the rod, x_{rod}^{img} (at each rotational increment), at the position corresponding to the center of the nearest pixel. For the "Nominal" case [Fig. 6(b)], two artifacts become immediately apparent—a diffuse region of high attenuation behind the rod, and a stripe along the direction of the first projection—consistent with the hypothesized comet and streak, respectively. As expected, the two artifacts become stronger for the "High Lag" case of Fig. 6(c). The simulations were repeated for various settings of initial rod position [i.e., 0 (as shown in Fig. 6), 45, and 90°], and in each case the streak corresponded precisely with the direction of the first few projections.

Besides the comet extending behind the rod along the path of its orbit, there also appears to be anomalously high attenuation extending vertically "in front of" and "behind" the rod as well. This may be attributed to another inconsistency in the projections arising from image lag, explained as follows. Consider the system near signal equilibrium, with the rod object moving across the field of view (FOV) and exhibiting a tail in its wake. When the object rotates about so that it is moving toward or away from the image plane (i.e., $\theta=90$ or 270° , respectively), the projection signal is not necessarily consistent with that for the object when near the center of the FOV (i.e., around 0 or 180°). That is, the transmission of the object (e.g., at 90°) is inconsistent with that of a real 3D object suggested by other projections (e.g., at 0°).

As a result, when the object moves toward or away from the detector, image lag may cause the attenuation to be overestimated along the direction of motion. The magnitude of this effect was found to be highly sensitive to the selection of the lag values in $Lag|_{i(1:10)}$.

Figures 6(d)–6(f) show reconstructions of simulated projections for objects at various positions within the cylinder and for objects of various size for the "Nominal" lag setting. Figure 6(d) shows the nominal-size rod [as in Fig. 6(b)] placed near the center of the cylinder ($R_{rod}=0.5$ cm). As suggested by the signal profiles in Fig. 5(b), the object shows little or no distortion. Figures 6(e) and 6(f) show reconstructions for the small ($r_{rod}=0.25$ mm) and large ($r_{rod}=5.0$ mm) rods, respectively, at nominal displacement. In each case, both a comet and streak are clearly evident, with the size of the artifact related to the size of the object. For the case of the large object [Fig. 6(f)], the above-mentioned artifact related to signal build-up along the direction of motion is particularly evident, as is the nonuniformity within the object suggested by the signal profile of Fig. 5(f).

B. CBCT lag measurements

Volume images of the rod phantom were acquired with the FPI-CBCT system as described above. First, measurements were performed in order to examine the dependence of image lag artifacts on exposure level, object speed, and object contrast. Second, three acquisition modes ("fast," "lag-suppression," and "priming") were employed to further examine the nature of such artifacts. Unless otherwise stated,

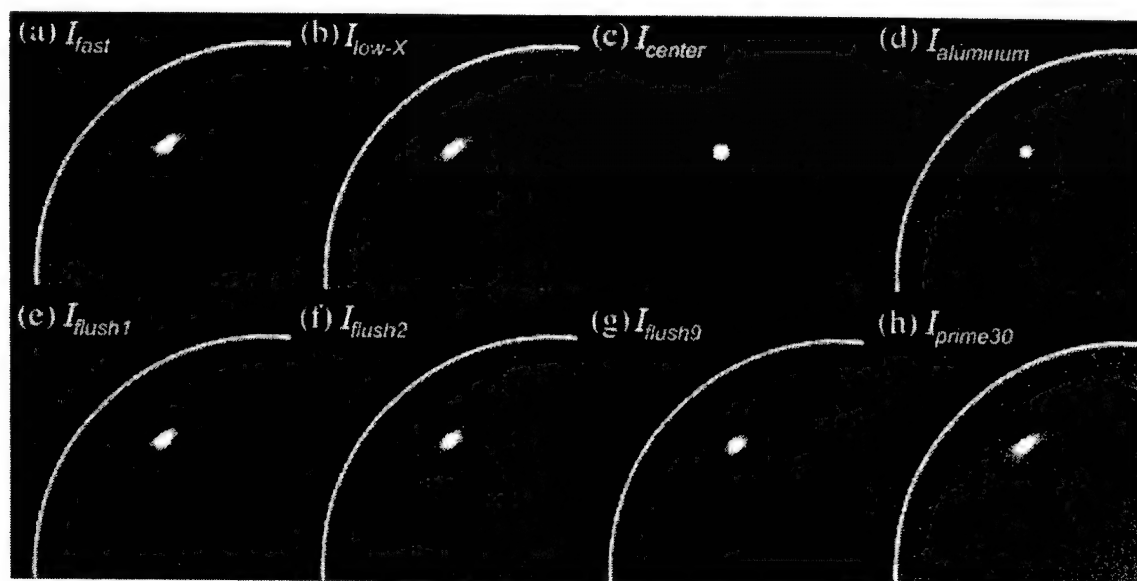


FIG. 7. Cone-beam CT reconstructions of the cylindrical phantom obtained with the flat-panel-imager-based CBCT system. Each figure shows a single quadrant of an axial slice from the volume data (281×281 voxels averaged over seven slices about the central plane). (a) Image of the stainless steel rod acquired in "fast" mode at high exposure. (b) Image of the same, obtained at lower exposure. (c) Image of the rod located near the center of the phantom, where the displayed "quadrant" was cropped from the center of the axial slice to allow comparison with other figures. (d) Image of a lower-contrast aluminum rod, exhibiting reduced lag artifacts. (e)–(g) Images acquired in "lag-suppression" mode, with (e) one frame, (f) two frames, and (g) nine frames flushed between projections. (h) Image of the rod acquired in "priming" mode, showing the full comet artifact but somewhat reduced streak. The gray scale for all images was consistently windowed and leveled to allow intercomparison. The results are consistent with the hypotheses developed in relation to Fig. 2.

the stainless steel rod was used ($r_{\text{rod}}=1.25$ mm), placed at $R_{\text{rod}}=4.0$ cm, and scanned at an exposure level of 2.5 mAs per projection in "fast" mode. Results are summarized in Fig. 7.

1. Artifacts: dependence upon exposure, speed, and contrast

Figures 7(a) and 7(b) show the effect of exposure level upon the image lag artifacts. The hypotheses suggest that such artifacts will be reduced at lower exposures. The image in Fig. 7(a) was acquired at the high exposure setting of 2.5 mAs per projection and exhibits a significant comet and streak. The image in Fig. 7(b) was acquired at the lowest exposure level (0.25 mAs per projection). Careful examination suggests that the streak is significantly reduced in the latter image but that the comet is only marginally reduced. This suggests that the streak (associated with reduced signal in the first few projections relative to subsequent projections) is dominated by the first-order lag characteristics of the system (i.e., the "first-frame" lag, $\text{Lag}|_1$), which has been shown³² to have a stronger dependence upon exposure than the higher-order lag terms (i.e., $\text{Lag}|_2$, $\text{Lag}|_3$, ..., $\text{Lag}|_{10}$ and so on). On the other hand, the extent of the comet depends more upon the higher-order lag terms (e.g., out to $\sim \text{Lag}|_{10}$ and so forth), which have a smaller dependence upon exposure.³² Therefore, reducing the exposure reduces the streak but has a smaller effect upon the comet. Images acquired at intermediate exposure levels (see Table I) exhibited levels of artifact between those of Figs. 7(a) and 7(b). Furthermore, images acquired with the phantom rotated to a different starting angle confirmed that the streak artifact lies along the direction of the first few projections. The artifact along the direction of motion, which was demonstrated in the simulations but found to depend strongly upon the lag characteristics, is less pronounced in the empirical results. The origins of the black "bow-tie" artifact along the radial direction and the reduced attenuation on one side of the streak artifact are unclear. Since such effects were not evident in the simulations, they may be the result of beam-hardening, x-ray scatter, and/or slight misalignment of the axis of rotation (AOR) with the reconstruction matrix.

Figure 7(c) shows the effect of object speed upon artifacts in the reconstruction, where the rod was placed near the center of the cylinder ($R_{\text{rod}}=0.5$ cm). As expected, reducing the average object rotational speed (i.e., displacement per projection) reduces the effects of image lag. Rather than a spatially extended comet and streak, the object is blurred out over the region of its smaller orbit. Of course, this effect is fundamentally the same as that of the comet, simply convolved over a smaller region. Images obtained with the intermediate value of $R_{\text{rod}}=2.0$ cm exhibited comet and streak artifacts somewhat reduced from the case with $R_{\text{rod}}=4.0$ cm.

The effect of object contrast is illustrated in Fig. 7(d), where the aluminum rod was used in place of the stainless steel. As expected, the artifacts associated with image lag are greatly reduced. This result explains why previous studies^{10,12} involving the visibility of low-contrast objects

and anatomical soft tissue in FPI-CBCT images exhibited no obvious lag artifacts. Furthermore, it suggests that lag artifacts may only be clinically significant for anatomy containing high-contrast objects, such as marker BBs, dental fillings, metal prosthetics, and such.

2. Artifacts: Dependence upon acquisition mode

Images acquired in "fast," "lag-suppression," and "priming" modes are shown in Figs. 7(a) and 7(e)–7(h), respectively. As previously discussed, the image acquired in "fast" mode [I_{fast} in Fig. 7(a)] contains a significant comet and streak, consistent with expectations.

Images acquired in "lag-suppression" mode [I_{flush1} , I_{flush2} , and I_{flush9} in Figs. 7(e)–7(g), respectively] show significant reduction of both comet and streak artifacts. Taking $n=1$ (I_{flush1}) strongly reduces the streak but has less effect upon the comet. This is similar to the effect discussed above in relation to exposure dependence: the streak is primarily dependent upon the first-frame lag ($\text{Lag}|_1$), whereas the comet results from higher-order lag terms. Therefore, flushing one frame between projections (as in I_{flush1}) does much to reduce the streak, but less to reduce the comet. Accordingly, taking $n=2$ or $n=9$ (I_{flush2} and I_{flush9}) largely eliminates the streak and progressively reduces the comet.

The image acquired in "priming" mode [I_{prime80} in Fig. 7(b)] exhibits the full comet artifact and a reduced streak compared to I_{fast} . The hypotheses suggest that "priming" mode could completely eliminate the streak while retaining the comet. That the streak persists to a slight degree suggests that the system was not in full charge trapping and release equilibrium following the m "priming" frames, so that a slight inconsistency in the projection data persisted along the direction of the first view.

Finally, the lag artifacts in and of themselves were examined in difference tomograms, as defined in Eqs. (2) and illustrated in Fig. 8. (Note that the calculation of difference tomograms is *not* intended to suggest an image-processing means of reducing lag artifacts; rather, they are computed herein simply as a means of analyzing the lag artifacts.) Figure 8(a) represents the difference between I_{fast} and I_{flush9} and therefore should contain only the full comet and streak [to the extent that both artifacts are eliminated in I_{flush9} ; see Fig. 7(g)]. The difference image supports this hypothesis. For these experimental conditions, both the comet and streak exhibit CT number approximately 3%–6% of the CT number of the rod. Since the CT number for the steel object is very high relative to water, the comet and streak are appreciable above the level of system noise;¹⁰ conversely, for the lower contrast aluminum rod, the CT number is such that the comet and streak are imperceptible.

Figures 8(b) and 8(c) show the extent to which the comet persists after flushing $n=1$ and $n=2$ frames, respectively, in "lag-suppression" mode (relative to flushing nine frames). As mentioned above, the former case reduces the streak more so than the comet. From Fig. 8(c), it is clear that flushing two frames between projections (I_{flush2}) largely eliminates the streak and exhibits only slight retention of the comet. Fur-

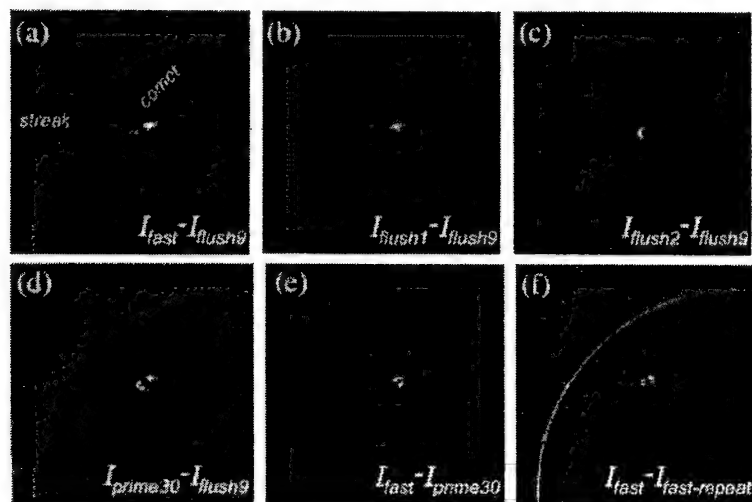


FIG. 8. Difference images between tomographic slices shown in Fig. 7, as defined in Eq. (2). As in Fig. 7, only a single quadrant of the axial slice is shown in order to "zoom in" on the object. (a) The difference between images acquired in "fast" and "lag-suppression" modes clearly illustrates the comet and streak. (b) and (c) Progressive reduction of the comet and streak artifacts using $n=1$ and $n=2$ flushed frames in "lag-suppression" mode. The lack of artifacts in (c) suggests that flushing two frames is nearly as effective in reducing the artifacts as flushing nine frames, and entails considerably shorter acquisition time. (d) and (e) Difference images based upon the "priming" mode of acquisition, showing (d) the full comet artifact, with somewhat reduced streak, and (e) the streak alone.

thermore, I_{flush2} and I_{flush9} are nearly identical but entailed an increase in CBCT acquisition times by a factor of 3 and 10, respectively. Since the difference between the resulting images is slight, the implication is that with regard to the tradeoff between lag-suppression and total acquisition time, flushing only two frames is preferable.

Figures 8(d) and 8(e) show the difference between the "priming" mode image ($I_{prime30}$) and the I_{flush9} and I_{fast} images, respectively. The first case [Fig. 8(d)] exhibits the comet artifact fully (as expected) but retains the streak somewhat as discussed above. The second case [Fig. 8(e)] suggests nearly complete elimination of the comet artifact, with stronger presence of the streak, as expected. The "priming" mode provides an interesting experimental technique, but because it involves delivering an extra dose (during the priming frames), it is not a practical technique where dose to the patient is an issue. Furthermore, at least for $m=30$ as shown herein, it fails to completely remove the streak artifact.

Finally, the reproducibility of the experiments was examined by repeating the "fast" mode acquisition of Fig. 7(a). Clearly, in order for difference tomograms to be precise and meaningful, the reproducibility of the measurements and the precision in aligning the phantom for each acquisition should be high. The difference between the original I_{fast} image [Fig. 7(a)] and the repeat measurement is shown in Fig. 8(f). From the difference exhibited along the perimeter of the plastic cylinder and in the region of the rod, it is clear that the phantom was shifted slightly down and to the right in the repeat scan. Correspondingly, the streak characteristic of the original I_{fast} image is not completely eliminated. As evident in the other difference tomograms [Figs. 8(a)–8(e)], this example represents a worst-case in the reproducibility of the measurement. From the small difference exhibited along the perimeter of the cylinder in Figs. 8(a)–8(e) [especially in Fig. 8(e), where realignment is seen to be near perfect], we conclude that the reproducibility and precision in realignment were sufficient to allow qualitative examination of the artifacts as discussed above.

IV. DISCUSSION AND CONCLUSIONS

Image lag results in measurable artifacts in reconstructions obtained using a flat-panel imager in cone-beam CT. Two effects include: (1) a "comet" artifact resulting from charge trapping and release throughout the majority of the projection data; and (2) a "streak" artifact along the direction of the first few views resulting from inconsistencies between the first projections (in signal nonequilibrium) and subsequent projections (near signal equilibrium). In addition, and particularly for large, high-contrast objects displaced from the axis-of-rotation, image lag may result in nonuniform signal (i.e., a "ramp" or "build-up") within the image of the object [e.g., Fig. 6(f)]. Also, inconsistency between projections obtained for an object moving laterally across the FOV and those obtained when the object is moving toward or away from the detector may result in an artifact (increased attenuation) along the direction of object motion. The above investigation suggests that the former two (the comet and streak) are the more significant, and that the comet is related primarily to higher-order lag characteristics (i.e., Lag_i where $i > 1$), whereas the streak is dominated by first-order lag characteristics (i.e., Lag_1 and Lag_2). As a result, the comet artifact is more difficult to reduce using the methods described in this article.

The experimental conditions and the object used in these studies were selected specifically to illustrate and accentuate the effects of image lag on CBCT reconstructions, and they do not necessarily correspond to typical clinical conditions. Specifically, the object examined consisted of a small, high-contrast object, for which the terms "comet" and "streak" seem appropriate and descriptive of the observed artifacts. The basic concepts presented in this paper still apply with regard to more complex objects (i.e., objects of various size, shape, and composition, with significant and/or irregular spatial extent), even though the observed artifacts (if any) may not resemble the comet or streak demonstrated herein. Rather, the resulting artifact may be described by a convolu-

tion of these effects over the extent of the object and its path of motion (relative to the source and imager, e.g., for non-circular trajectories). For example, based on the above results, one might reason that replacing the rod with a vertical slab would result in reconstructions where the edge of the slab appears blurred opposite to the direction of rotation, and more so at greater distances from the axis of rotation. Clearly, the effect with regard to complex anatomy is significantly more complicated but can be similarly explained. Furthermore, lag artifacts may be somewhat reduced in relation to objects that are complex in shape and composition, since the effects of image lag would not be reinforced in successive projections to the extent that they are for a simple, high-contrast object such as a steel rod.

Previous results¹⁰ showing FPI-CBCT images of low-contrast objects and real anatomy (a Wistar rat) exhibited no obvious artifacts attributable to image lag. This is, in fact, consistent with the above results, which show that lag artifacts are significant only for high-contrast objects at high exposure levels. For example, reconstruction of an aluminum rod [Fig. 7(d)] exhibited little or no artifact relative to that of a stainless steel rod [Fig. 7(a)]. Thus, manifestation of lag artifacts in CBCT images of soft-tissue and even bony anatomy is likely to be small. Such effects may become significant, however, for cases in which the volume contains high-contrast objects, such as marker BBs and metal prosthetics. In nonmedical applications, such as x-ray cone-beam CT for industrial nondestructive testing and evaluation (NDTE), where subjects often include high-contrast objects (often imaged at high exposures in air), artifacts resulting from image lag are likely to be more conspicuous. Furthermore, the results presented above were obtained using various "step-and-shoot" modes of CBCT acquisition, which largely eliminate effects of motion blur. Of course, CBCT acquisition may utilize fluoroscopic acquisition, in which the x-ray beam is on continuously during rotation and imager readout. Such operation introduces the additional effect of motion blur, which is beyond the context of the present paper.

In the event that lag artifacts are sufficiently deleterious to warrant effort toward their reduction, such artifacts may be reduced either procedurally or algorithmically. For example, the simple "lag-suppression" mode shown in Fig. 4(b), with $n=2$ frames flushed between projections, proved to be a fairly effective procedural means of managing both the comet and streak artifacts. (The "priming" mode—developed simply to test the hypotheses—is impractical, since it requires delivery of extra dose and only addresses the streak artifact.) Since the FPI frame rate was held constant in the above measurements, use of the "lag-suppression" mode entailed an increase in the acquisition time [by a factor of $(n+1)$]. However, a variation of this mode in which intermediate frames are flushed at a higher frame rate may provide similar artifact reduction with less tradeoff in acquisition time. Previous results³² support this idea in that the level of image lag was shown to depend more upon the number of times the pixel was reinitialized (i.e., upon the number of frames) than upon the elapsed time. Of course, one needs to

verify that such variation of the frame rate during acquisition does not introduce other undesirable effects, such as additional noise or degradation of gain-offset corrections.

Alternatively, lag artifacts can be reduced by means of algorithmic correction of the projection images, either offline or as the data are acquired. For example, each projection could be corrected for image lag effects by subtracting previous projections weighted by the magnitude of image lag in those projections. Since each projection contains uncorrelated noise, however, subtraction necessarily introduces noise to the projection data. Toth *et al.*²⁹ show that artifacts resulting from temporal correlation in a CT scanner can be managed by deconvolution of the projection data with the temporal response function of the detectors. Alternatively, Hsieh²⁸ developed a method for CT scanning in which projections are arithmetically compensated by the measured signal decay in order to reduce effects of detector afterglow. Furthermore, Hsieh³⁰ demonstrated that selective weighting of the projections in CT fluoroscopy can improve speed while maintaining an acceptable level of artifacts.

Based upon the above results, it is concluded that the effects of image lag in flat-panel CBCT under conditions typical of medical imaging are small, given the image lag performance of state-of-the-art FPIs.³² For cases in which lag artifacts may be significant (e.g., in the presence of high-contrast markers or dental fillings, for FPIs exhibiting particularly high image lag, or possibly in NDTE), simple procedures such as the "lag-suppression" mode appear to be effective in suppressing lag artifacts.

ACKNOWLEDGMENTS

We extend our sincere thanks to W. Jendhoff (Beaumont Services Corp.) for assistance with the experimental setup, to Elekta Oncology Systems, Inc. for supplying the flat-panel imager employed in this work, and to M. K. Gauer, Ph.D. (EG&G Heimann Optoelectronics) for technical information concerning the imaging array. This research was funded in part by the Prostate Cancer Research Program Grant DAMD17-98-1-8497 from the U.S. Army Medical Research and Materiel Command.

^a Author to whom correspondence should be addressed; electronic mail: jsiewerd@beaumont.edu

¹ L. E. Antonuk, J. Yorkston, J. Boudry, M. J. Longo, and J. Jimenez, "Development of hydrogenated amorphous silicon sensors for high energy photon radiotherapy imaging," *IEEE Trans. Nucl. Sci.* **37**, 165–170 (1990).

² P. Munro and D. C. Bouius, "X-ray quantum limited portal imaging using amorphous silicon flat-panel arrays," *Med. Phys.* **25**, 689–702 (1998).

³ Recent proceedings from the SPIE Physics of Medical Imaging Conference (e.g., Vols. 2708, 3032, 3336, and 3659) contain numerous articles from commercial and academic endeavors investigating flat-panel-imaging technology for diagnostic radiology.

⁴ R. L. Weisfield, M. A. Hartney, R. A. Street, and R. B. Apte, "New amorphous-silicon image sensor for x-ray diagnostic medical imaging applications," *SPIE Phys. Med. Imaging* **3336**, 444–452 (1998).

⁵ U. Schiebel, N. Conrads, N. Jung, M. Weibrecht, H. Wiczorek, T. Zaengel, M. J. Powell, I. D. French, and C. Glaske, "Fluoroscopic x-ray imaging with amorphous silicon thin-film arrays," *SPIE Phys. Med. Imaging* **2163**, 129–140 (1994).

- ⁶M. D. Wright *et al.*, "Amorphous silicon dual mode medical imaging system," *SPIE Phys. Med. Imaging* **3336**, 505–514 (1998).
- ⁷N. Jung, P. L. Alving, F. Busse, N. Contrads, H. M. Meulenbrugge, W. Rutten, U. Schiebel, M. Weibrecht, and H. Wiecezorek, "Dynamic x-ray imaging system based on an amorphous silicon thin-film array," *SPIE Phys. Med. Imaging* **3336**, 396–407 (1998).
- ⁸V. Venkatakrishnan, M. Yavuz, L. T. Niklason, B. Opsahl-Ong, S. Han, C. Landberg, R. Nevin, L. Hamberg, and D. B. Kopans, "Experimental and theoretical spectral optimization for digital mammography," *SPIE Phys. Med. Imaging* **3659**, 142–149 (1999).
- ⁹R. Ning, D. Lee, X. Wang, Y. Zhang, D. Conover, D. Zhang, and C. Williams, "Selenium flat panel detector-based volume tomographic angiography imaging: Phantom studies," *SPIE Phys. Med. Imaging* **3336**, 316–324 (1998).
- ¹⁰D. A. Jaffray, J. H. Siewerdsen, and D. G. Drake, "Performance of a volumetric CT scanner based upon a flat-panel imaging array," *SPIE Phys. Med. Imaging* **3659**, 204–214 (1999).
- ¹¹R. Ning, X. Tang, R. Yu, D. Zhang, and D. Conover, "Flat panel detector-based cone beam volume CT imaging: Detector evaluation," *SPIE Phys. Med. Imaging* **3659**, 192–203 (1999).
- ¹²D. A. Jaffray, J. H. Siewerdsen, and D. G. Drake, "Cone-beam computed tomography with a flat-panel imager: Initial performance characterization," *Med. Phys.* (submitted).
- ¹³H. Wiecezorek, G. Frings, P. Quadflieg, and U. Schiebel, "CsI:Tl for solid state x-ray detectors," *Proceedings of the International Conference on Inorganic Scintillators and their Applications*, Delft, Netherlands, 1995.
- ¹⁴R. E. Colbeth, V. N. Cooper III, D. L. Gilblom, R. Harris, I. D. Job, M. E. Klausmeier-Brown, M. Marc, J. Pavlovich, E. J. Seppi, E. G. Shaprio, M. D. Wright, and J. M. Yu, "Characterization of a third generation, multi-mode sensor panel," *SPIE Phys. Med. Imaging* **3659**, 491–500 (1999).
- ¹⁵J. T. Rahn, R. Lemmi, R. L. Weisfield, R. Lujan, P. Mei, J. P. Lu, J. Ho, S. E. Ready, R. E. Apte, P. Nylén, J. Boyce, and R. A. Street, "High resolution, high fill factor a-Si:H sensor arrays for medical imaging," *SPIE Phys. Med. Imaging* **3659**, 510–517 (1999).
- ¹⁶B. D. Smith, "Cone-beam tomography: Recent advances and a tutorial review," *Opt. Eng.* **29**, 524–534 (1990).
- ¹⁷R. Clack and M. DeFrise, "Overview of reconstruction algorithms for exact cone-beam tomography," *SPIE Mathematical Methods in Medical Imaging III* **2299**, 230–241 (1994).
- ¹⁸H. Kudo and T. Saito, "Feasible cone beam scanning methods for exact reconstruction in three-dimensional tomography," *J. Opt. Soc. Am. A* **7**, 2169–2183 (1990).
- ¹⁹P. M. Joseph, "Artifacts in computed tomography," in *Radiology of the Skull and Brain: Technical Aspects of Computed Tomography*, edited by T. H. Newton and D. G. Potts (C. V. Mosby, St. Louis, 1981), Chap. 114, pp. 3956–3992.
- ²⁰J. Hsieh, "Image artifacts: Causes and correction," in *Medical CT and Ultrasound: Current Technology and Applications*, *Proceedings of the 1995 Summer School of the AAPM*, edited by L. W. Goldman and J. B. Fowlkes (Advanced Medical Publishing, Madison, 1995), Chap. 26, pp. 487–518.
- ²¹J. Hsieh, M. F. Gard, and S. Gravelle, "A reconstruction technique for focal spot wobbling," *Proceedings of SPIE Medical Imaging VI*, 1992, pp. 175–182.
- ²²A. H. Lonn, "Computed tomography system with translatable focal spot," U.S. Patent 5173852 (1990).
- ²³E. Dolazza and H. Weedon, "Optimal channel filter for CT system with wobbling focal spot," U.S. Patent 5841829 (1998).
- ²⁴R. A. Sohval and D. Freundlich, "Plural source computerized tomography device with improved spatial resolution," U.S. Patent 4637040 (1987).
- ²⁵D. L. Parker, J. L. Couch, K. R. Peschmann, V. Smith, M. Jimbo, and E. C. Wang, "Design constraints in computed tomography: A theoretical review," *Med. Phys.* **9**, 531–539 (1982).
- ²⁶C. R. Crawford and N. J. Pelc, "Angular integration and inter-projection correlation effects in CT reconstructions," *Proc. IEEE Eng. Med. Biol. Soc.* **9**, 1670–1671 (1987).
- ²⁷J. Hsieh, "Compensation of computed tomography data for detector afterglow," U.S. Patent 5265142 (1993).
- ²⁸J. Hsieh, "Radiation detector offset and afterglow compensation technique," U.S. Patent 5331682 (1994).
- ²⁹T. L. Toth, C. R. Crawford, and K. F. King, "Deconvolution filter for CT system," U.S. Patent 5361291 (1994).
- ³⁰J. Hsieh, "Improving the temporal response of computed tomography fluoroscopy," *SPIE Phys. of Med. Imaging* **3336**, 296–304 (1998).
- ³¹R. A. Street, *Hydrogenated Amorphous Silicon* (Cambridge University Press, New York, 1991).
- ³²J. H. Siewerdsen and D. A. Jaffray, "A ghost story: Spatio-temporal response characteristics of an indirect-detection flat-panel imager," *Med. Phys.* **26**, 1624–1641 (1999).
- ³³J. A. Seibert, J. M. Boone, and K. K. Lindfors, "Flat-field correction technique for digital detectors," *SPIE Phys. Med. Imaging* **3336**, 348–363.
- ³⁴L. A. Feldkamp, L. C. Davis, and J. W. Kress, "Practical cone-beam algorithm," *J. Opt. Soc. Am. A* **1**, 612–619 (1984).
- ³⁵C. R. Crawford, J. D. Godwin, and N. J. Pelc, "Reduction of motion artifacts in computed tomography," *Proc. IEEE Eng. Med. Biol. Soc.* **11**, 485–486 (1989).
- ³⁶C. R. Crawford and N. J. Pelc, "Method for reducing motion artifacts in projection imaging," U.S. Patent 4994965 (1991).
- ³⁷J. Hsieh, M. F. Gard, and C. J. Ritchie, "Methods for reducing motion induced artifacts in a projection imaging system," U.S. Patent 5271055 (1993).
- ³⁸I. A. Cunningham and R. Shaw, "Signal-to-noise optimization of medical imaging systems," *J. Opt. Soc. Am. A* **16**, 621–632 (1999).
- ³⁹J. H. Siewerdsen, L. E. Antonuk, Y. El-Mohri, J. Yorkston, W. Huang, J. M. Boudry, and I. A. Cunningham, "Empirical and theoretical investigation of the noise performance of indirect detection, active matrix flat-panel imagers (AMFPIs) for diagnostic radiology," *Med. Phys.* **24**, 71–89 (1997).
- ⁴⁰J. H. Siewerdsen, L. E. Antonuk, Y. El-Mohri, J. Yorkston, W. Huang, and I. A. Cunningham, "Signal, noise power spectrum, and detective quantum efficiency of indirect-detection flat-panel imagers for diagnostic radiology," *Med. Phys.* **25**, 614–628 (1998).
- ⁴¹MTF data for Lanex screens provided by P. C. Bunch, Ph.D., Eastman Kodak Co., Rochester NY (private communication).
- ⁴²P. M. Joseph and R. D. Spital, "The effects of scatter in x-ray computed tomography," *Med. Phys.* **9**, 464–472 (1982).
- ⁴³G. H. Glover, "Compton scatter effects in CT reconstructions," *Med. Phys.* **9**, 860–867 (1982).
- ⁴⁴R. A. Brooks and G. DiChiro, "Beam hardening in reconstructive tomography," *Phys. Med. Biol.* **21**, 390–398 (1976).
- ⁴⁵P. K. Kijewski and B. E. Bjarnagard, "Correction for beam hardening in computed tomography," *Med. Phys.* **5**, 209–214 (1978).
- ⁴⁶A. J. Duerinckx and A. Macovski, "Nonlinear polychromatic and noise artifacts in x-ray computed tomography images," *J. Comput. Assist. Tomogr.* **3**, 519–526 (1979).

**Appendix D: Cone-beam Computed Tomography with a Flat-panel
Imager: Initial Performance Characterization**

Cone-beam computed tomography with a flat-panel imager: Initial performance characterization

D. A. Jaffray^{a)} and J. H. Siewerdsen

Department of Radiation Oncology, William Beaumont Hospital, Royal Oak, Michigan 48073

(Received 15 September 1999; accepted for publication 29 March 2000)

The development and performance of a system for x-ray cone-beam computed tomography (CBCT) using an indirect-detection flat-panel imager (FPI) is presented. Developed as a bench-top prototype for initial investigation of FPI-based CBCT for bone and soft-tissue localization in radiotherapy, the system provides fully three-dimensional volumetric image data from projections acquired during a single rotation. The system employs a 512×512 active matrix of *a*-Si:H thin-film transistors and photodiodes in combination with a luminescent phosphor. Tomographic imaging performance is quantified in terms of response uniformity, response linearity, voxel noise, noise-power spectrum (NPS), and modulation transfer function (MTF), each in comparison to the performance measured on a conventional CT scanner. For the geometry employed and the objects considered, response is uniform to within 2% and linear within 1%. Voxel noise, at a level of ~ 20 HU, is comparable to the conventional CT scanner. NPS and MTF results highlight the frequency-dependent transfer characteristics, confirming that the CBCT system can provide high spatial resolution and does not suffer greatly from additive noise levels. For larger objects and/or low exposures, additive noise levels must be reduced to maintain high performance. Imaging studies of a low-contrast phantom and a small animal (a euthanized rat) qualitatively demonstrate excellent soft-tissue visibility and high spatial resolution. Image quality appears comparable or superior to that of the conventional scanner. These quantitative and qualitative results clearly demonstrate the potential of CBCT systems based upon flat-panel imagers. Advances in FPI technology (e.g., improved x-ray converters and enhanced electronics) are anticipated to allow high-performance FPI-based CBCT for medical imaging. General and specific requirements of kilovoltage CBCT systems are discussed, and the applicability of FPI-based CBCT systems to tomographic localization and image-guidance for radiotherapy is considered. © 2000 American Association of Physicists in Medicine. [S0094-2405(00)01306-7]

Key words: cone-beam computed tomography, flat-panel imager, amorphous silicon, volume imaging, image-guided therapy, radiotherapy

I. BACKGROUND AND INTRODUCTION

The relationship between radiation treatment dose and tumor control has spurred numerous protocols aimed at escalation of radiation dose for management of prostate cancer. Accordingly, such activities have focused the radiotherapy community on the tradeoffs between dose escalation and induced normal tissue complication. These tradeoffs are, for the most part, governed by the margins used to accommodate the geometric uncertainties in treatment. Investigators have demonstrated the potential for significant dose escalation, if geometric uncertainties can be reduced from current levels of 5–10 mm to the 3 mm level.¹ In sites where organ motion is a significant factor, such as the prostate, this level of precision can only be achieved through on-line image guidance available at the time of treatment.

An imaging system for guidance has several requirements if it is to be applied in radiotherapy of the prostate. These include: (i) contrast sensitivity sufficient to discern soft-tissue; (ii) high spatial resolution and low geometric distortion for precise localization of soft-tissue boundaries; (iii) operation within the environment of a radiation treatment machine; (iv) large field-of-view (FOV), capable of imaging

patients up to 40 cm in diameter; (v) short image acquisition time (within a few minutes); (vi) negligible harm to the patient from the imaging procedure (e.g., dose much less than the treatment dose); and (vii) compatibility with integration into an external beam radiotherapy treatment machine. A strong candidate technology to satisfy these requirements is kilovoltage (kV) cone-beam computed tomography (CBCT).^{2–4} CBCT operates on the same principle as conventional CT, with the exception that an entire volumetric image is acquired through a single rotation of the source and detector. This is made possible by the use of a two-dimensional (2D) detector, as opposed to the 1D detectors used in conventional CT. There are constraints associated with image reconstruction under a cone-beam geometry; however, these can be addressed through innovative source and detector trajectories.^{5–7}

In a previous article, the development of a kV cone-beam CT imaging system for on-line tomographic guidance was reported.⁸ The system consisted of a kV x-ray tube and a radiographic detector mounted on the gantry of a medical linear accelerator. The imaging detector was based on a low-noise CCD optically coupled to a phosphor screen. The poor

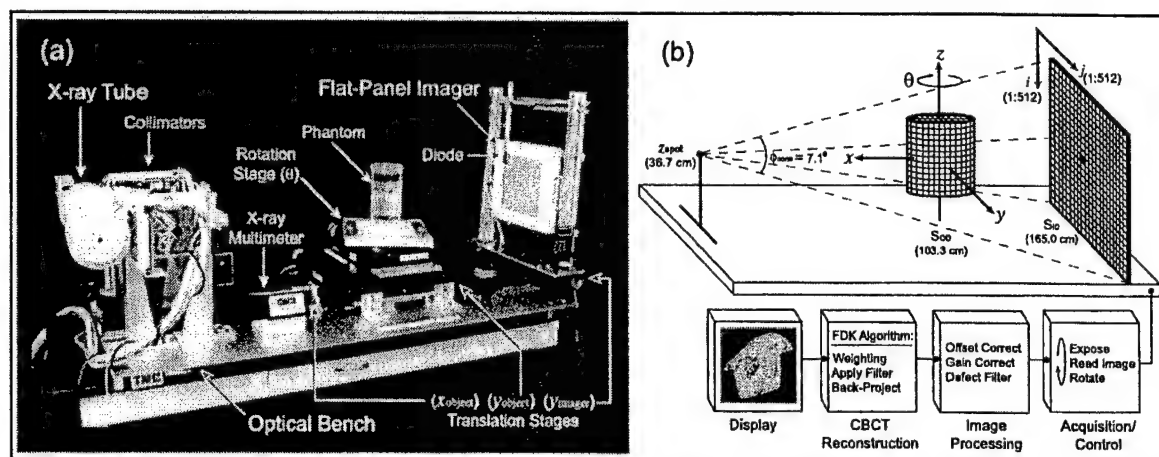


FIG. 1. (a) Photograph of the FPI-based CBCT prototype system and (b) schematic illustration of the geometry and procedures within the CBCT system. The flat-panel imager acquires 2D projections at incremental rotations of the object, and fully 3D volume reconstructions are obtained by cone-beam filtered back-projection. The prototype was constructed to provide a precise, reproducible geometry that corresponds closely with that of a tomographic system for image-guided radiotherapy on a linear accelerator.

optical coupling efficiency ($\sim 10^{-4}$) between the phosphor and the CCD significantly reduced the detective quantum efficiency (DQE) of the system. While this system was capable of producing CBCT images of sufficient quality to visualize soft-tissues relevant to radiotherapy of the prostate, the low DQE required imaging doses a factor of 3–4 times larger than would be required for a system with an efficient coupling (e.g., $\sim 50\%$ or better) between the screen and detector.⁹

Recently developed flat-panel imaging technology offers an ideal replacement for the CCD-based imager. This technology is based upon thin-film hydrogenated amorphous silicon (*a*-Si:H) electronics fabricated on large area panels (e.g., $\sim 40 \times 40$ cm²). A two-dimensional matrix of *a*-Si:H thin-film transistors (TFTs) and optically sensitive photodiodes collect the image emitted from the phosphor screen. Such panels demonstrate excellent optical coupling efficiency ($> 50\%$) and possess high tolerance to radiation damage ($> 2 \times 10^4$ Gy).¹⁰ Their spatial resolution and noise characteristics are compatible with computed tomography, and the devices appear overall well-suited to CBCT.^{11–13} Images may be read at rates up to ~ 30 frames per second, making rapid acquisition of CBCT data feasible. Moreover, the compact form of the x-ray converter, imaging array, and readout electronics makes these devices robust in the rotating geometry of a CBCT system.

We propose the construction of a CBCT system for radiotherapy guidance on a treatment-by-treatment basis using CT data obtained with a kV x-ray source and a large-area, indirect detection flat-panel imager (FPI). Ultimately, an imaging system based on this technology will be installed on a conventional radiotherapy linear accelerator in our clinic for application to image-guided radiation therapy. In this article, we report on the construction, operation, and performance of a small-volume prototype CBCT imaging system and examine the feasibility of employing FPI technology in the clinical system for image-guided radiotherapy. The system com-

ponents, the imaging geometry, and the methods of image acquisition and reconstruction are described. The performance of the system is quantified in terms of objective measures of signal and noise transfer characteristics. Finally, a more qualitative examination of performance involves comparison of images produced with the prototype FPI-based CBCT system to those produced with a conventional third generation CT scanner (Tomoscan SR7000, Philips Medical Systems, Shelton, CT).

II. MATERIALS AND METHODS

A. Prototype CBCT system

1. Overview and system geometry

A bench-top system was constructed to mimic the geometry of the CCD-based CBCT scanner currently installed on a linear accelerator, with a source-to-axis distance of 1000 mm and a source-detector distance of 1600 mm. Figure 1 contains a photograph of the CBCT prototype and illustrates the geometry and acquisition processes for the bench-top system for all experiments described in this article. Care was taken in the construction and assembly of all components to guarantee precision and reproducibility in the imaging geometry.

The primary components of the system are the x-ray tube, the rotation stage, and the flat-panel imager. These three components are mounted rigidly to an optical bench [Fig. 1(a)]. The relative position of these components is controlled by means of computer-controlled translation and rotation stages, which are used during initial setup to accurately determine and control the imaging geometry. Each motorized stage contains a home or limit switch, and the imaging geometry is referenced to the location of these switches with a reproducibility of ± 0.01 mm. The specific geometry used in these studies is shown in Fig. 1(b). A set of alignment lasers allows visualization of the axis of rotation (AOR) and the

source plane (that which is perpendicular to the axis of rotation and intersects the x-ray source). The AOR is positioned such that it intersects the central ray between the source and detector plane (± 0.1 mm). The FPI is positioned such that the piercing point (i.e., the intersection of the central ray and the image plane) is centered on the imaging array (i.e., between columns #256 and #257, ± 0.1 mm), with a quarter-pixel offset applied to give improved view sampling for CBCT acquisitions in which the object is rotated through 360° .¹⁴ The x_{object} stage is controlled manually by means of a positioning micrometer. The source-to-object (S_{OD}) and source-to-image (S_{ID}) distances were measured to within ± 0.5 mm and give an object magnification of 1.60, equal to that of the imaging system on the linear accelerator. The cone angle for this geometry is $\sim 7.1^\circ$.

2. X-ray source

Radiographic exposures used in the acquisition procedure are produced under computer control with a 300 kHU x-ray tube (General Electric Maxi-ray 75) and a 100 kW generator (General Electric MSI-800). The tube has a total minimum filtration of 2.5 mm Al, with an additional filtration of 0.129 mm Cu to further harden the beam, and a nominal focal spot size of 0.6 mm. The 100 kVp beam is characterized by first and second HVLs of 5.9 and 13.4 mm Al, respectively. The accelerating potential of the generator was monitored over a one-week period and was found to be stable to within $\pm 1\%$. All exposures were measured using the x-ray multimeter (RTI Electronics, Model PMX-III with silicon diode detector) shown in Fig. 1(a). The exposures for the CBCT acquisitions are reported in terms of exposure to air at the AOR in the absence of the object. The same method of reporting exposure was used for the images acquired on the conventional scanner. For the conventional scanner, the exposure per unit charge was measured with the gantry rotation disabled and the collimators set for a 10 mm slice thickness, thereby guaranteeing complete coverage of the silicon diode. The exposure per unit charge at 100 kVp was 9.9 mR/mAs and 14.9 mR/mAs for the bench-top and conventional scanners, respectively.

3. Flat-panel imager

The FPI used in these investigations was manufactured by EG&G Heimann Optoelectronics (RID 512-400 A0) and incorporates a 512×512 array of α -Si:H photodiodes and thin-film transistors. The electromechanical characteristics of the imager are shown in Table I. The array is read out at one of eight present frame rates (up to 5 frames per second) and operates asynchronously of the host computer. The analog signal from each pixel is integrated by ASIC amplifiers featuring correlated double-sampling noise reduction circuitry. Digitization is performed at 16 bit resolution. The values are transferred via an RS-422 bus to a hardware buffer in the host computer. The processor on the host computer is interrupted when a complete frame is ready for transfer to host memory.

TABLE I. Summary of characteristics of the prototype flat-panel CBCT system.

CBCT characteristics	Value
Acquisition Geometry	
Source-axis-distance (S_{AD})	103.3 cm
Source-imager-distance (S_{ID})	165.0 cm
Cone angle	7.1°
Field of view (FOV)	12.8 cm
X-ray Beam/Exposure Characteristics	
Beam energy	100 kVp
Added filtration	1.5 mm Al + 0.129 mm Cu
Beam quality	HVL ₁ = 5.9 mm Al HVL ₂ = 13.4 mm Al
Scatter-to-primary ratio ^a	0.18
Tube output (at S_{AD})	9.34 mR/mAs
Flat-Panel Imager	
Designation	RID 512-400 A0
Array format	512×512 pixels
Pixel pitch	400 μm
Area	$\sim 20.5 \times 20.5 \text{ cm}^2$
Pixel fill factor	0.80
Photodiode charge capacity	$\sim 62 \text{ pC}$
ASIC amplifier charge capacity	$\sim 23 \text{ pC}$
ASIC amplifier noise	$\sim 12\,700 \text{ e}$
ADC bit-depth	16 bit
Nominal frame rate	0.16 fps
Maximum frame rate	5 fps
X-ray converter	133 mg/cm ² Gd ₂ O ₂ S:Tb
Acquisition Procedure	
Number of projections	300
Angular increment	1.2°
Total rotation angle	360°
Maximum angular rotation rate	$0.5^\circ/\text{s}$
Reconstruction Parameters	
Reconstruction matrix	$561 \times 561 \times (1-512)$
Voxel size	$0.25 \times 0.25 \times 0.25 \text{ mm}^3$
W , parameter for cutoff frequency	1.60
γ , cutoff frequency modification	1.0
α , modified Hamming filter parameter	0.50
Range of convolution	$\pm 25 \text{ mm}$

^aRatio of scatter-to-primary signal as measured with the flat-panel imager for the cylindrical water phantom [Fig. 2(a)] and a 7.1° cone-angle. Measurements of scatter and total signal were performed on the central axis using small lead blockers.

4. CBCT acquisition procedure

The cone-beam scanning procedure consists of a repeated sequence of radiographic exposure, array readout, and object rotation. The timing of this procedure is driven by the asynchronous frame clock of the FPI readout electronics. A conservative frame time of 6.4 s was used for all scans reported in this study unless otherwise specified. Between the periodic frame transfers from the FPI, the host computer (Pentium 350 MHz, Windows NT) advances the motorized rotation stage and triggers the x-ray generator. The rotor of the x-ray tube remains spinning throughout the scanning procedure. The control software allows the operator to specify the number of frames between exposures; this was designed as a mechanism to investigate methods of reducing the amount of lag in sequential projections.^{15,16} In the investigations reported here no lag suppression schemes were employed, i.e., an exposure was delivered prior to each frame. The detector

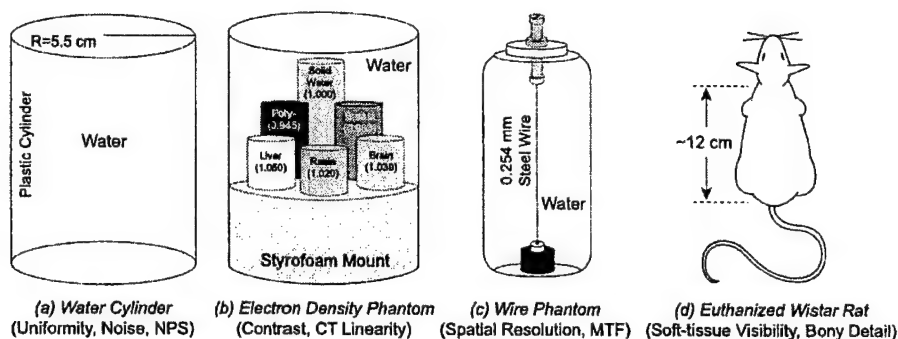


FIG. 2. Objects employed in the battery of tests performed to investigate the performance of the FPI-based CBCT system. (a) Uniformity of response, voxel noise, and noise-power spectrum were analyzed from images of a uniform water cylinder. (b) Six low-contrast inserts in the water bath allowed characterization of contrast sensitivity and response linearity. Parenthetical values specify electron density relative to water. (c) The spatial resolution (MTF) was analyzed from images of a steel wire under tension within a water bath. (d) Images of a euthanized rat provided qualitative examination of soft-tissue visibility and detail in fine structures.

signal from a group of nine pixels in the bare-beam region of the array is monitored to measure and verify the stability of each radiographic exposure. Exposures outside tolerance are trapped and repeated at the same projection angle. Each projection image is written to hard disk between frame transfer and motor rotation; all scans reported in this study involved 300 projections over 360° of rotation. After the projections are acquired, a set of flood and dark field images (20 each) are collected to construct gain and offset images for flat-field processing of the projection images.

5. Processing of the projection data

Prior to reconstruction, the projections are corrected for stationary pixel-to-pixel variations in offset and gain. Defective pixels with significant variations in dark field signal or with aberrant signal response are median filtered. The resulting projections are padded by an additional 128 columns prior to reconstruction; the value of the padded pixels is set row-by-row to the average of the 7 pixels at the periphery of the array. Finally, to account for small variations in x-ray tube output, the signal in each projection is normalized using signal measured from the bare-beam monitor pixels mentioned above (nine pixels). The pre-reconstruction processing was performed on a 300 MHz UltraSparc processor (Enterprise 450, Sun Microsystems, Sunnyvale, CA).

6. Reconstruction

Feldkamp's filtered back-projection algorithm is used to reconstruct the data set.^{17,18} Images are reconstructed on a Cartesian matrix of voxels $561 \times 561 \times N$, where the number of slices, N , depends on the object of interest. The voxel size used in these reconstructions was typically $0.25 \times 0.25 \times 0.25$ mm³. The filtering used in the reconstructions follows the formalism of Webb.¹⁸ Table I contains the three parameters that specify the filter used in these investigations. Upon completion of the reconstruction, an offset and scale adjustment is applied to set the CT number of air to 0 (-1000 HU) and that of water to 1000 (0 HU); the offset and scale parameters are constant for a given set of reconstruction and

acquisition parameters. The reconstruction of the volumetric CBCT data sets is also performed on the UltraSparc system.

B. CBCT imaging performance

1. Uniformity of response

The uniformity of response of the imaging system over the three-dimensional (3D) field of view (FOV) was studied by imaging a cylindrical water bath [110 mm diam; see Fig. 2(a)]. Scans of the same phantom were also acquired on the conventional scanner. The response was examined along both radial and vertical profiles through the reconstructed volume.

2. Noise characteristics

The noise in reconstructed images of the water bath was studied as a function of x-ray exposure. Images were acquired at exposures of 131, 261, 653, 1310, 3260, and 6530 mR. The images were reconstructed on a $561 \times 561 \times 20$ matrix with voxel dimensions of 0.25 mm on a side. For all reconstructions, the reconstruction filter was fixed at the parameters specified in Table I; varying these parameters is known to have a significant effect on the noise characteristics of the reconstructed images.

The noise characteristics of these image sets were analyzed by (i) analysis of the standard deviation in CT number in $5 \times 5 \times 1$ regions throughout the data set, and by (ii) calculation of the noise power spectrum (NPS) from the 3D data sets. Both methods of analysis were performed as a function of exposure. The relative stationarity of the noise was assessed by examining the uniformity of the noise over the entire 3D data set. These results indicated that the noise characteristics of the data set vary only slightly with location, as expected.¹⁹ These initial results lend support to the application of noise power analysis, since stationarity is a necessary condition for proper interpretation of noise power results. The NPS was analyzed from the volumetric data by extension of methods employed for analysis of 2D projection images.²⁰⁻²² The volume data were normalized such that the mean CT number within the water cylinder was 1000. A

tetragonal region ($256 \times 256 \times 20$ voxels) within the water cylinder was cropped from the volume, and a small number of voxel defects (always $< 1\%$) were 3×3 median-filtered. In order to obtain a convergent 2D central slice of the 3D Fourier transform, the 20 slices were averaged along the z -direction, and it was found that averaging more slices did not affect the NPS; i.e., the data were convergent. A background slice formed from the average of 81 slices in a separate scan was subtracted in order to reduce background trends. Low-frequency trends were further reduced by subtraction of a planar fit to the data, yielding a 2D zero-mean realization. The two-dimensional FFT was computed from ensembles of sixteen 64×64 nonoverlapping regions within the realization, and the results were averaged. The results were normalized to account for voxel size and for averaging in z , and the volume under the NPS was compared to (and, as expected, found to agree with) the square of the standard deviation. The resulting NPS represents a central profile through the (u_x, u_y) domain, i.e., the Fourier counterpart to the (x, y) domain. Following Dobbins,²⁰ and for simplicity of presentation, strips along the u_x axis were extracted in order to show 1D power spectra, $NPS(u_x)$, e.g., at various exposure levels.

The noise characteristics of the CBCT system were compared to those of the conventional CT scanner. To allow meaningful comparison, the two systems must demonstrate similar response over the range of signal variation. The response was tested by scanning an electron density phantom [Fig. 2(b)] with the two systems. Seven inserts with coefficients near that of water were inserted into a 110 mm diam water bath. The inserts are taken from the RMI electron density phantom²³ having nominal CT numbers [Fig. 2(b), clockwise from the top]: CT solid water (CT# 1001), BR-SR1 breast (CT# 945), BRN-SR2 brain (CT# 1005), CB3 resin mix (CT# 1002), LV1 liver (CT# 1082), and polyethylene (CT# 897). This phantom was imaged at equivalent exposure and kVp with both the CBCT system and the conventional scanner. The attenuation coefficients (relative to water) reported by the CBCT system were compared to those reported by the conventional scanner. A first-order fit was generated using the least-squares technique. The noise characteristics of the conventional scanner were also measured using the water cylinder test phantom described above. Images were acquired at 100 kVp with a slice thickness of 1 mm at four different exposure levels (743, 1490, 2970, and 5940 mR). Three images were acquired at each exposure level. Reconstructions were performed on the conventional scanner using the "High Res Head (#1H)," "Standard Head (#2)," and "Smooth Abdomen (#3)" filters. The noise analysis was identical to that applied to the CBCT data sets. In order to compare noise results measured on each system, analysis of the CBCT data sets was repeated wherein the CBCT data were first averaged over $2 \times 2 \times 4$ voxels to yield an equivalent voxel size ($0.5 \times 0.5 \times 1$ mm³) to that given by the conventional scanner.

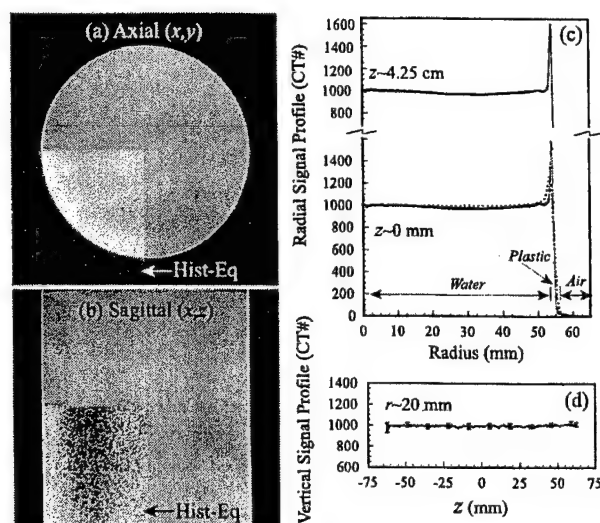


FIG. 3. Uniformity of response. (a) Axial and (b) sagittal slices through volume images of a uniform water bath illustrate the relative uniformity in CT number reported by the CBCT system. The lower-left region of each image has been histogram-equalized to maximize displayed contrast. (c) Radial profiles shown at $z = 0$ mm and $z = 4.25$ cm indicate that response is uniform to within 2% throughout the volume. Superimposed in the lower plot of (c) is a radial profile from a scan of the same phantom on a conventional scanner (dotted line). (d) A vertical signal profile at $r = 20$ mm from the axis of rotation shows excellent uniformity in the z -direction. The aspect ratio of the graphs in (c) and (d) was chosen to facilitate intercomparison of the vertical scales.

3. Spatial resolution

The spatial frequency transfer characteristics of the CBCT system were measured using a wire test object [Fig. 2(c)]. The test object consists of a 0.254 mm diam steel wire suspended in a 50 mm diam water bath. The phantom was imaged on the CBCT system (at 100 kVp) with the wire centered on the AOR and with the wire located ~ 30 mm off-axis. The resulting images were reconstructed on a high resolution reconstruction grid of $0.1 \times 0.1 \times 0.25$ mm³ using the filter described in Table I. Six adjacent slices (each 0.25 mm thick) were averaged to generate a low noise point spread function (PSF). Orthogonal slices through the 2D modulation transfer function (MTF) were calculated by computing the Radon transform of the PSF (i.e., integrating along either the x or y axis)²⁴ calculating the 1D Fourier transform, and dividing by the spatial frequency spectrum described by the steel wire. The latter was determined from the Radon transform of a circular disk and is shown in Fig. 7(b). For purposes of comparison, the same tests were performed on the conventional scanner at 100 kVp for a slice thickness of 1.5 mm. Images were reconstructed using three different reconstruction filters ["High Res Head (#1H)," "Standard Head (#2)," and "Smooth Abdomen (#3)"].

4. Phantom and small animal study

The relative imaging performance of the CBCT system and the conventional scanner were compared using phantoms and small animals. A simple comparison in soft-tissue de-

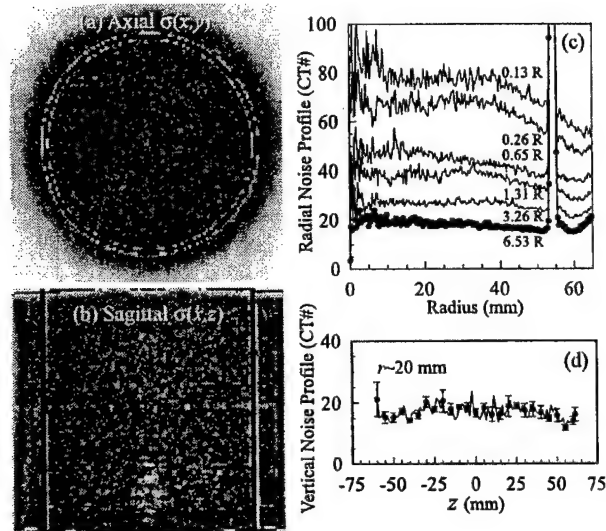


FIG. 4. Noise characteristics. (a) Axial and (b) sagittal noise images from volume reconstructions of a uniform water bath, where each point displayed represents the standard deviation in voxel values over a $5 \times 5 \times 1$ neighborhood. The increased noise in the central region of the lower portion of (b) is due to ring artifacts arising from defective pixels. As seen in (a) and in the radial noise profiles of (c), the noise is fairly uniform in a given axial slice, with somewhat reduced noise values at extended radius consistent with expectations. As seen in (b) and in the vertical noise profile of (d), the variation of the noise in the z -direction is very small. The curves in (c) represent radial noise profiles measured at various exposures. The aspect ratio of the graphs in (c) and (d) were chosen to facilitate intercomparison of the vertical scales.

tectability was performed with the phantom shown in Fig. 2(b). The proximity in CT number between each of the six cylinders makes this phantom a useful test object for examining contrast sensitivity and soft-tissue detectability. Images were acquired of the phantom with both the CBCT and conventional scanners. Multiple high-resolution CBCT slices were averaged to produce an equivalent slice thickness to that used on the conventional scanner (1.5 mm). Equivalent exposure (2980 mR) and kVp were used in the two different scans.

A second test of soft-tissue sensitivity was performed by imaging a laboratory rat that had been euthanized for other purposes. A scanning procedure identical to that described in the previous section was used, delivering an in-air, on-axis exposure of 2980 mR at 100 kVp for both systems. The subject was also scanned on the conventional CT scanner at a slice thickness of 1.5 mm. This scan delivered the same imaging dose as was delivered by the CBCT system. For purposes of intercomparison, six slices from the CBCT data set were averaged to produce a slice thickness equivalent to that of the conventional scan. The images were displayed at comparable window and level to allow comparison.

III. RESULTS

A. CBCT imaging performance

1. Uniformity of response

The uniformity of response of the CBCT scanner is presented in Fig. 3. Axial and sagittal slices through the CBCT

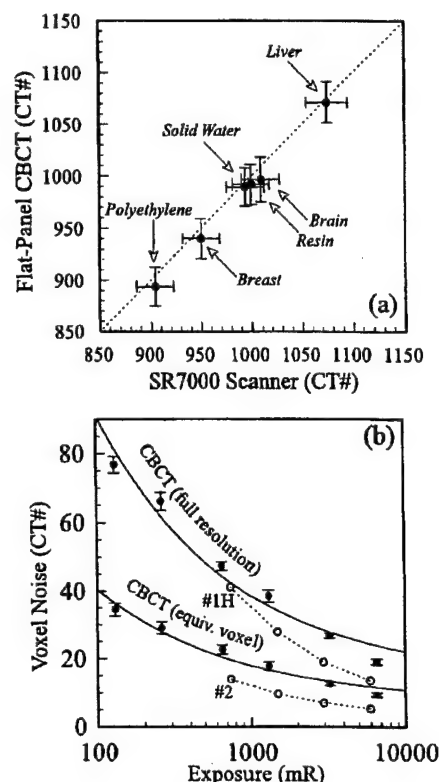


FIG. 5. Comparison of (a) response linearity and (b) voxel noise for the FPI-based CBCT prototype and a conventional CT scanner. (a) The CT# reported by the CBCT system is plotted for various materials as a function of the CT# reported by the conventional scanner (taken to provide linear response to electron density). Throughout this work, CT values of air and water are normalized to 0 and 1000, respectively. Within experimental error, the CBCT prototype provides response that is linear and consistent (within $\sim 1\%$) with the response of the conventional CT scanner. (b) Voxel noise measured as a function of exposure. The solid circles (solid lines) correspond to the CBCT prototype, whereas the open circles (dotted lines) correspond to the conventional CT scanner. The solid curves represent least-square fits to the CBCT data by a form proportional to the inverse square-root of the exposure. The top curve shows results for the CBCT system for full-resolution reconstruction ($0.25 \times 0.25 \times 0.25$ mm³ voxels), and the lower solid curve shows results for the CBCT system averaged to give voxel size equivalent to the conventional scanner ($0.5 \times 0.5 \times 1$ mm³ voxels). Results for the conventional scanner were obtained using two reconstruction filters—"High-Res Head (#1H)" and "Standard Head (#2)."

3D data set are shown. The images demonstrate a relatively uniform response over the entire FOV of the system. A slight non-uniformity of approximately 20 CT numbers (2%) is visible in the histogram equalized regions of the images. This nonuniformity appears as a combined cupping and capping artifact; the radial profile [Fig. 3(c)] illustrates this point further by comparing to the results obtained from the conventional scanner (dotted line). The source of this cupping and capping artifact was investigated using simulated projection data and using an alternative reconstruction library on the measured data. Both investigations demonstrate that the capping artifact in these results is an artifact of the current reconstruction engine. Apart from the axial nonuniformity

inherent to the reconstruction engine, the response of the CBCT system is highly uniform, particularly along the z -dimension.

2. Noise characteristics

In addition to demonstrating uniformity of system response, the images in Fig. 3 also demonstrate uniform noise characteristics with few artifacts. This is the case for the full range of exposures studied. The magnitude and uniformity of the noise is demonstrated in Fig. 4. The noise varies to a slight degree along the radial axis and to a negligible degree along the vertical axis. A slight dependence on radial position is expected^{19,25} due to the differences in transmission across the cylindrical water bath. Figure 4(c) also presents the measured dependence of noise on exposure [also shown below, in relation to Fig. 5(b)]. Overall, the CBCT system was capable of achieving a noise level of approximately 20 CT numbers for an in-air exposure of 6560 mR at isocenter.

The noise measured for the CBCT system as a function of exposure is shown in the top curve of Fig. 5(b). The noise is seen to decrease from ~ 80 units at the lowest exposure examined down to ~ 20 units at the highest. Superimposed is a least-squares fit of the form $\sigma = a + b/\sqrt{X}$, where σ is the noise in voxel values, X is the exposure at isocenter, and a and b are constants obtained from the numerical fit. This inverse-square-root dependence upon exposure is consistent with basic noise transfer theory for x-ray tomographic reconstructions.^{19,25}

In order to examine the linearity and accuracy of system response, the CT numbers reported by the CBCT system for a variety of materials [Fig. 2(b)] were compared to those reported by the conventional scanner. As shown in Fig. 5(a), the CT numbers of the CBCT system agree well with those of the conventional scanner. The largest discrepancy over the range of CT numbers was 8 units, with an average discrepancy of 5.7. The high coefficient of correlation indicates that, over the range examined, the values reported by the CBCT system are proportional to attenuation coefficient.

The voxel noise of the CBCT system and the conventional scanner was compared as a function of exposure, shown in Fig. 5(b). Shown by the open circles and dashed lines are the results for the conventional scanner using the "High-Res Head (#1H)" and "Standard Head (#2)" reconstruction filters. In each case, the noise decreases as expected with exposure. An exact comparison between the two systems requires that both data sets be reconstructed at equivalent voxel size and with the same reconstruction filter. The requirement for equivalent voxel size was achieved by repeating the noise analysis for the CBCT system, with voxel size equivalent to that of the scanner. In order to illustrate the effect of the reconstruction filter upon the voxel noise, reconstructions were performed with both the "High-Res Head" and "Standard Head" reconstruction filters. The noise for the CBCT system at equivalent voxel size is shown by the lower solid curve with a least-squares fit superimposed. At equivalent voxel size, it is clear that the CBCT system has higher noise at lower exposures than the "Standard Head"

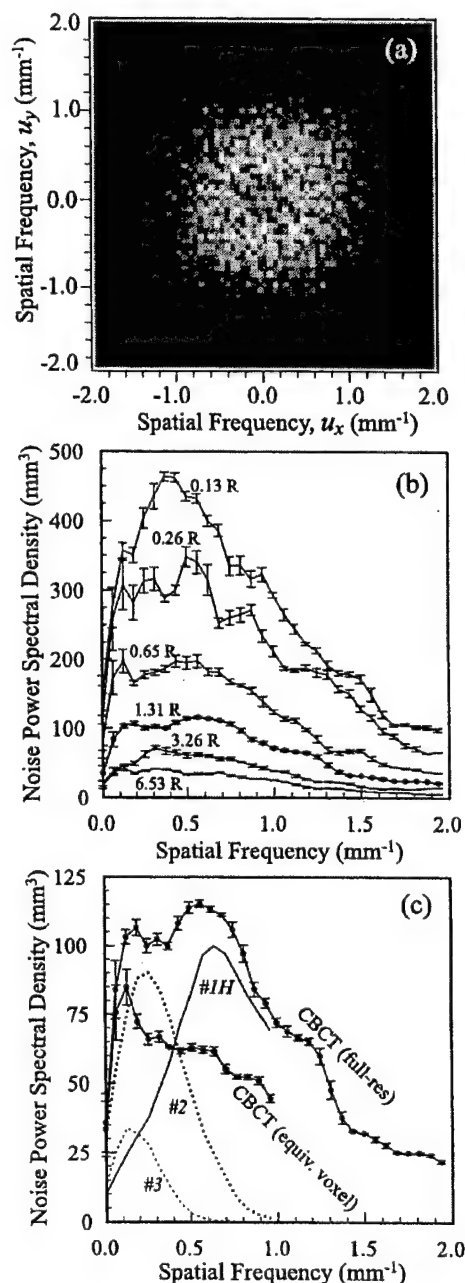


Fig. 6. Noise-power spectrum. (a) Grayscale plot of the axial $NPS(u_x, u_y)$, with brighter shades corresponding to higher spectral density. The overall shape of the axial NPS is typical of systems employing filtered back-projection reconstruction. (b) NPS measured at various exposures. Spectral density increases at low and mid-frequencies due to the ramp filter, and decreases at higher frequencies due to blur and apodisation. The spectral density decreases with increasing exposure, since the mean signal value (i.e., CT value for water=1000) is fixed. (c) NPS for the CBCT system in comparison to the conventional scanner. As in Fig. 5(b), the top curve represents results for the CBCT system at full-resolution, whereas the lower curve is for the CBCT system averaged to give voxel size equivalent to the conventional scanner. Results for the conventional scanner are shown for three choices of reconstruction filter ["High-Res Head (#1H)," "Standard Head (#2)," and "Smooth Abdomen (#3)," also shown in Fig. 7(b)]. Careful consideration of the reconstruction parameters is essential for quantitative comparison of noise and spatial resolution.

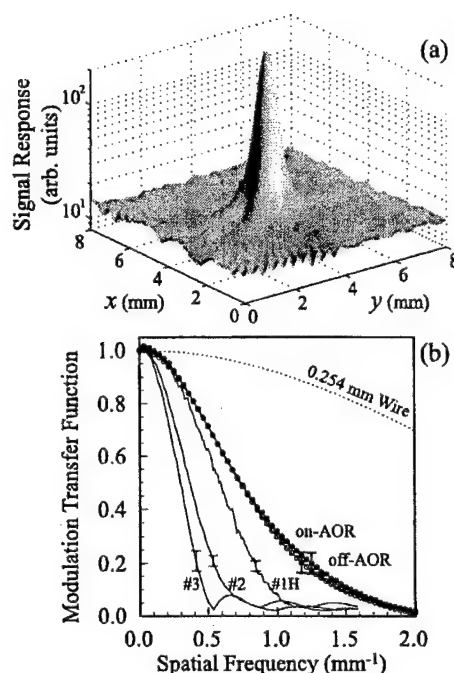


FIG. 7. Spatial resolution. (a) Surface plot of an axial slice image of a thin steel wire (0.254 mm diam). The full-width at half-maximum is ~ 0.6 mm. (b) MTF measured for the CBCT prototype and for a conventional scanner. The dotted line represents the frequency function of the circular wire, which was divided out of the measured results. The solid and open circles represent the MTF of the CBCT prototype measured on and off the axis of rotation, respectively. The solid lines represent the MTF of the conventional scanner, measured for three selections of reconstruction filter ["Smooth Abdomen (#3)," "Standard Head (#2)," and "High-Res Head (#1H)"]. Sample error bars, computed from repeated MTF analysis in adjacent slices and representing $\pm 1\sigma$, are shown at values near $\sim 20\%$ MTF. Note that the MTFs shown here were analyzed from images in the axial plane. For the CBCT prototype, the spatial resolution is expected to be isotropic, whereas that of the conventional scanner in the z -direction is limited by the choice of slice thickness (typically ≥ 1 mm).

CT scanner results. Compared to the "High-Res Head" results for the conventional scanner, however, the CBCT system actually provides lower noise at all but the very highest exposures. Clearly, careful matching of reconstruction filters and reconstruction matrix is required to permit exact intercomparison of the two systems. Nonetheless, the results obtained using the CBCT system are encouraging, since the early prototype flat-panel detector used in this system is known to exhibit a fairly high level of additive electronics noise,¹⁶ a factor of ~ 5 – 10 higher than that achieved by more recent electronics designs.

Results of the NPS measurements are summarized in Fig. 6. The 2D NPS in the axial plane [Fig. 6(a)] exhibits a spectral shape typical of systems employing filtered back-projection reconstruction.²⁶ The spectral density is reduced (but nonzero) near zero-frequency, increases at mid-frequencies due to the ramp filter (e.g., peaking around ~ 0.5 mm^{-1}), and declines at higher frequencies by virtue of the low-pass noise characteristics of the system (e.g., 2D image blur and choice of apodisation window).²⁷ Slices of the NPS along the u_x -dimension are shown in Fig. 6(b) for various

exposure levels. Since the mean signal level is fixed for each case (i.e., $\text{CT}\# = 1000$ within the water phantom), the NPS decreases with increasing exposure. Specifically, the NPS appears inversely proportional to exposure in a fashion consistent with the form of the numerical fits in Fig. 5(b). As shown in Fig. 6(c), the NPS measured at $\sim 1.3 R$ (in air at isocenter) is $\sim 30 \text{ mm}^3$ near zero-frequency, increases by a factor of ~ 4 at mid-frequencies, and then descends to about the initial level of spectral density at the Nyquist frequency. Superimposed in Fig. 6(c) are the results measured for the conventional scanner using three reconstruction filters, and to facilitate intercomparison, NPS results for the CBCT system are shown for an equivalent voxel size. For the #2 and #3 filters, the conventional scanner exhibits NPS with the characteristic shape described above; however, the high-resolution #1H filter is seen to significantly amplify high-frequency noise. The CBCT system appears to exhibit low-frequency NPS comparable to the conventional scanner using the #2 filter, and high-frequency NPS intermediate to the cases of the conventional scanner using the #2 and #1H filters. Given that the choice of reconstruction filter can significantly affect noise and spatial resolution, and considering the two cases that seem most closely matched [CBCT at equivalent voxel size compared to the conventional scanner (#1H); see also Fig. 7(b), below], the CBCT system—even in its initial, unoptimized configuration—appears to provide noise performance comparable to the conventional scanner. As evident in Fig. 5(b), the CBCT system exhibits lower voxel noise than the conventional scanner (#1H) at low exposures. Similarly, the CBCT exhibits reduced high-frequency NPS. These initial results are especially promising considering the on-going improvements in FPI design and readout electronics.^{28,29}

3. Spatial resolution

The response of the CBCT system to the wire test object is presented in Fig. 7(a). Overall, the PSF is symmetric (aside from a small streak artifact believed associated with the image lag characteristics of the system)¹⁵ and has a full-width at half-maximum (FWHM) of 0.6 mm. The system MTF is shown in Fig. 7(b) for both the on- and off-axis wire results. These results suggest that the frequency pass of the system in the $z=0$ plane does not change significantly over the relatively small (~ 30 mm) range examined. The strong influence of the reconstruction filter is demonstrated in the MTF results for the conventional scanner, also shown in Fig. 7(b). The "Standard Head (#2)" filter significantly reduces the signal pass of the system compared to the "High-Res Head (#1H)" filter. The results demonstrate that the MTF of the conventional scanner is comparable to that of the CBCT system when the "High-Res Head (#1H)" filter is used. This observation is consistent with the noise results presented in Fig. 5(b). The resolution of the CBCT and conventional scanner have not been compared in the z -dimension. It is expected, however, that the spatial resolution of the CBCT system in the z -dimension will be comparable to that measured in the axial plane. Of course, the spatial resolution of

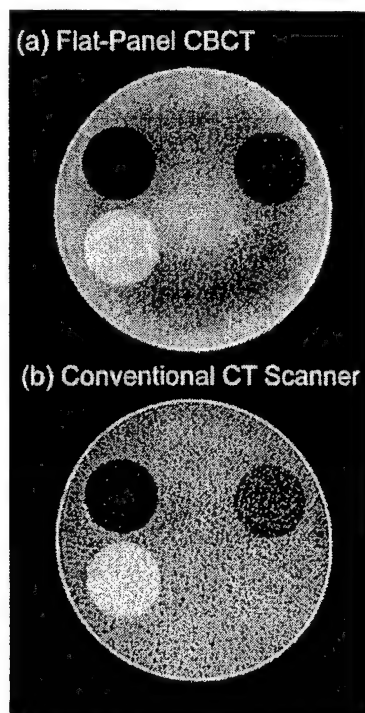


FIG. 8. Images of a low-contrast phantom obtained using (a) the CBCT prototype system and (b) a conventional CT scanner. Cylindrical inserts are as shown in Fig. 2(b), clockwise from top: CT solid water, breast, brain, CB-3 resin, liver, and polyethylene. For purposes of comparison, the image in (b) was obtained using the "High-Res Head (#1H)" filter, for which the MTF and NPS most closely match those of the CBCT prototype. While the filter selection affected the apparent texture of the image, it did not significantly affect the visibility of the inserts from what is shown in (b).

the conventional scanner will be limited by the selected slice thickness, which is typically 1 mm or greater. The nearly isotropic resolution of the CBCT system is expected to be a significant advantage for detection and localization.

B. Imaging studies: A low-contrast phantom and a small animal

Shown in Fig. 8 are axial image slices of the low-contrast phantom obtained on (a) the CBCT prototype system and (b) the conventional CT scanner at equivalent kVp and exposure. The grayscale window in each case is quite narrow in order to maximize the displayed contrast, and despite the slight signal nonuniformity evident for the CBCT image (cupping/capping artifact discussed above) the visibility of each insert is comparable to the conventional scanner. The mean signal values for each material are as shown in Fig. 5(a). Slight differences in system response (e.g., due to detector response, x-ray spectrum, etc.) can result in contrast reversal for materials with CT# very close to that of water. For example in the case of the brain insert (lower right), even the slight (~ 5 CT#) difference between the mean value reported by the CBCT prototype and the conventional scanner is sufficient to give an apparent inversion in the density of the material relative to water. The minimum detectable contrast is arguably superior for the CBCT prototype (e.g., vis-

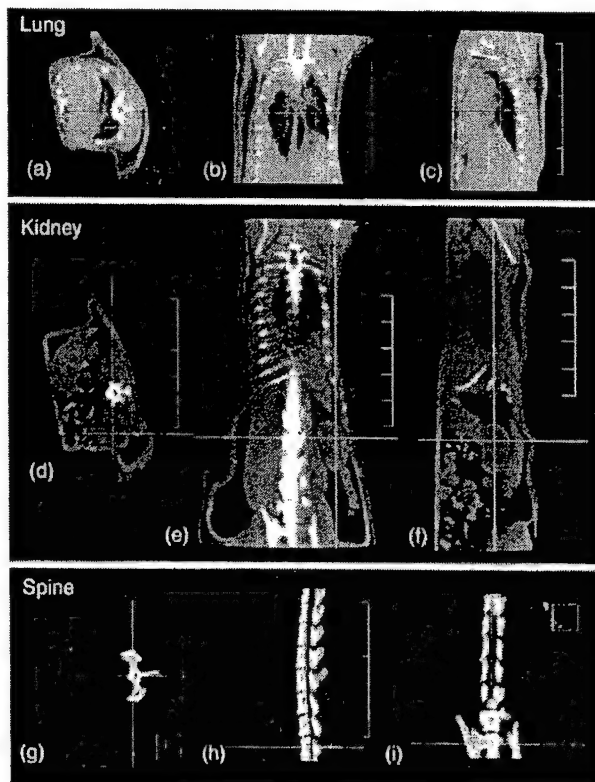


FIG. 9. CBCT images of a euthanized rat in regions of (a,b,c) the lungs, (d,e,f) the kidney, and (g,h,i) the lower spine. The window and level settings were varied in each image to allow visualization of the structures of interest. Axial (a,d,g), coronal (b,e,h), and sagittal (c,f,i) slices qualitatively demonstrate isotropic spatial resolution, with excellent soft-tissue contrast in each case. Bronchial structure within the lungs is clearly identifiable, the kidney is well delineated from surrounding muscle and fat, and fine detail in the vertebrae and intervertebral spaces is demonstrated. Voxel size in each case is $0.25 \times 0.25 \times 0.25$ mm³, and the vertical scale in the images shows 1 cm spacing.

ibility of the brain and CB-3 inserts), but this remains to be verified by a more quantitative observer study.

The overall performance of the CBCT system is demonstrated in the images of a volumetric data set illustrated in Fig. 9. These images of a euthanized rat demonstrate the soft tissue sensitivity and high spatial resolution of the system. Example images are shown from various regions throughout the volumetric set [e.g., in regions of the lungs (a,b,c), the kidney (d,e,f), and lower spine (g,h,i)] to illustrate the quantity and uniform quality of the data produced with the CBCT system. The clear visualization of soft-tissue structures demonstrates the soft-tissue contrast sensitivity of the scanner. In Figs. 9(a)–9(c), the window and level have been set to emphasize features in the lung of the rat. In addition to the lung detail, there are some streak artifacts evident, the origin of which is believed to be associated with detector lag effects¹⁵ and/or beam hardening. The soft tissue contrast sensitivity of the CBCT system is illustrated in Figs. 9(d)–9(f), in which the window and level have been set to delineate fat and muscle. The cross-hair in each image indicates the location of the rat's left kidney. These images illustrate the advantage

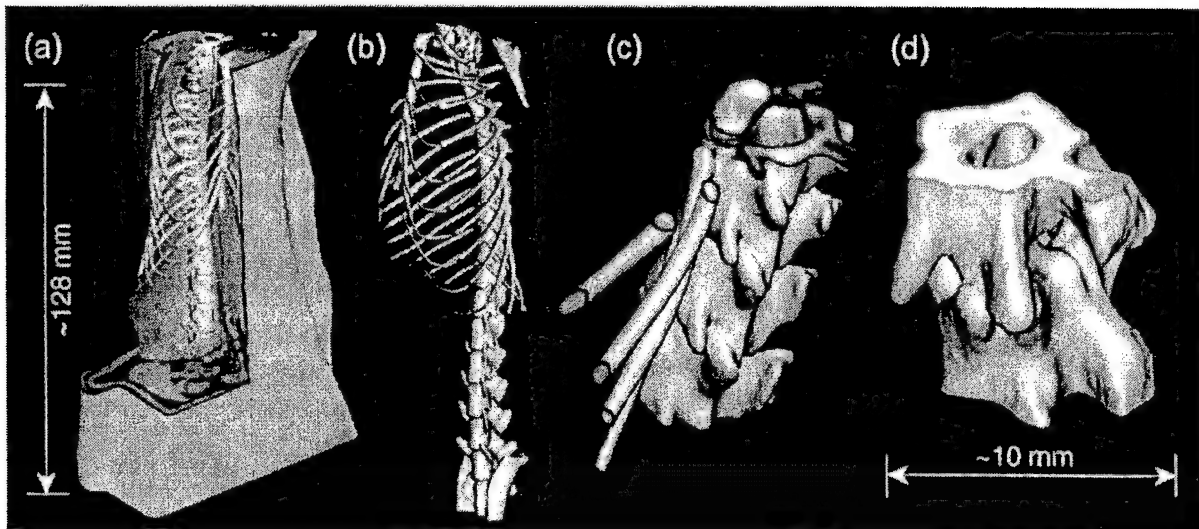


FIG. 10. Volume renderings of CBCT images of a euthanized rat, illustrating the degree of spatial resolution achieved in delineating structures of the vertebrae. (a) Volume renderings with axial and sagittal cut-planes, showing the skeletal anatomy along with soft-tissue structures of the abdomen. (b) A different view of (a), windowed to show skeletal features only. The scale in (a) and (b) is such that the entire vertical field of view (128 mm) is shown. (c) A magnified view of a region of the spine and ribs. Note the contrast in cortical and noncortical bone as well as the excellent delineation of spinal processes and ribs ($\sim 1\text{--}2$ mm diam). (d) A magnified view of part of two vertebrae. These images qualitatively suggest isotropic spatial resolution with sub-millimeter precision, consistent with the MTF results of Fig. 7.

of a nearly isotropic spatial resolution for delineation of a 3D structure such as the kidney. Other structures, such as the stomach, bowel, and liver are also clearly visible. The spatial resolution performance of the system is demonstrated in Figs. 9(g)–9(i), in which the same rat data set is displayed with window and level selected to display bony features. The clear visibility of the intervertebral spaces and the noncortical bone in the pelvis is stunning. It should be kept in mind that this level of detail was produced on a CBCT bench-top system that operates on a scale that mimics the geometry of the linear accelerator; therefore, this level of detail would be expected in the clinical implementation of the device, given accurate correction of mechanical flex.³⁰ The volumetric data

set is illustrated further in Fig. 10, in which volume renderings demonstrate the fully 3D nature of the data set and show the level of detail contained within the CBCT data. It is interesting to note that all the data presented in Figs. 9 and 10 were obtained from a single acquisition performed in a single rotation.

Finally, the quality of images produced by the CBCT system was assessed by comparison to images produced by the conventional scanner. Figure 11 shows an axial slice of the rat acquired on the two systems. At equivalent exposure, the images produced by the two systems are of comparable quality both in terms of spatial resolution and contrast sensitivity. The FPI-based CBCT image exhibits exquisite spatial reso-

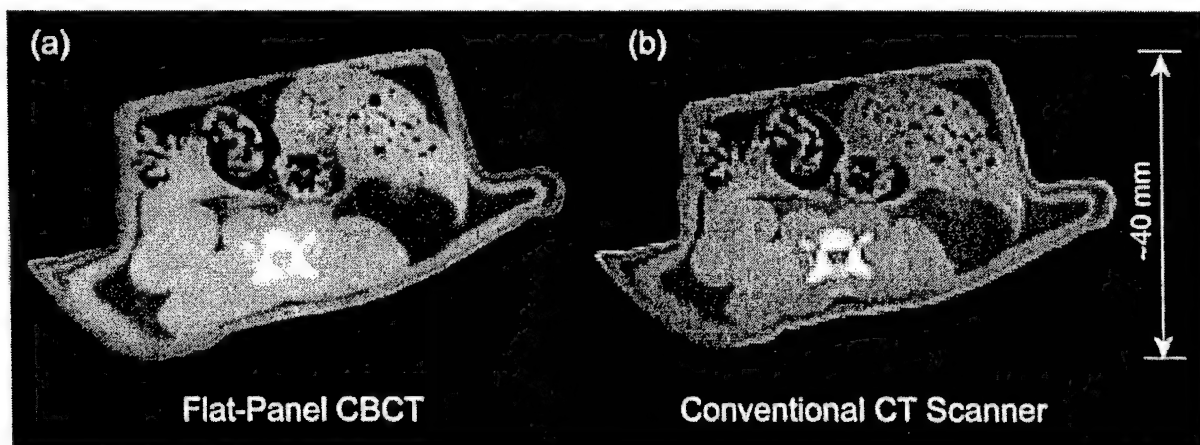


FIG. 11. Comparison of axial images of a euthanized rat obtained on (a) the CBCT prototype system and (b) a conventional CT scanner for equivalent kVp and exposure. Reconstruction matrix is $0.25 \times 0.25 \times 0.25$ mm³ and $0.5 \times 0.5 \times 1.5$ mm³, respectively. For the FPI-based CBCT image, six slices were averaged to give an equivalent slice thickness of 1.5 mm.

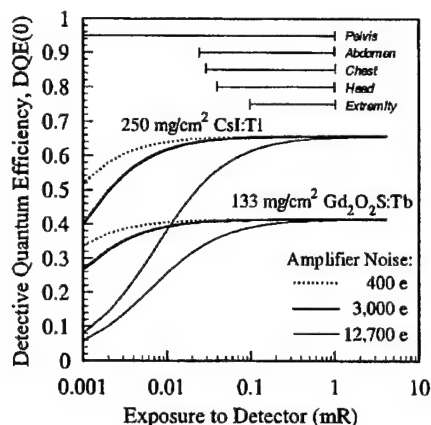


Fig. 12. DQE calculated as a function of exposure for existing and hypothetical FPI configurations. The horizontal brackets labeled "pelvis," "chest," etc. indicate the range of exposures typical of each anatomical site (expressed in terms of exposure at the detector, per projection, at 120 kVp). The FPI reported herein employs a $133 \text{ mg/cm}^2 \text{ Gd}_2\text{O}_2\text{S:Tb}$ x-ray converter, exhibits a high level of amplifier noise ($\sim 12\,700 \text{ e}$), and clearly suffers in DQE at exposures less than $\sim 0.1 \text{ mR}$. Incorporation of an improved x-ray converter ($250 \text{ mg/cm}^2 \text{ CsI:Tl}$) increases the DQE considerably by virtue of higher quantum detection efficiency and provides superior or equivalent DQE(0) down to $\sim 0.01 \text{ mR}$. Furthermore, improvement in the amplifier electronics noise level significantly extends the range of exposures over which the FPI is x-ray quantum limited. For example, reduction of amplifier noise to less than $\sim 3000 \text{ e}$ provides $\text{DQE}(0) > 40\%$ even at micro-Roentgen exposure levels, dramatically improving performance for the most challenging anatomical sites (e.g., the pelvis). Driven largely by the performance requirements of projection radiography and interventional fluoroscopy, recent improvements in FPI designs and technology have made such enhancements a reality.

lution and provides clear delineation of soft-tissue boundaries and detail in the gut. The spatial resolution of the CBCT system appears to exceed that of the conventional scanner; however, it must be noted that restrictions in available reconstruction matrices for the conventional CT scanner limited the voxel size to twice that of the CBCT image.

IV. DISCUSSION AND CONCLUSIONS

The objective of these investigations is to evaluate the applicability of flat-panel technology as a detector in a CBCT system—specifically, a tomographic imaging system for use in the guidance of radiation therapy on a medical linear accelerator. The results of these studies are overall very encouraging.

The quantitative and qualitative results of our studies suggest that a CBCT scanner based on flat panel detector technology is a viable means for high performance computed tomography. Initial studies of signal response uniformity demonstrated that the response of the system is uniform over the FOV to within $\pm 2\%$. The linearity of response was demonstrated using a range of soft-tissue test materials and was found to be linear to within $\pm 0.6\%$. Measurements of image noise versus exposure demonstrate that the prototype CBCT system performs comparably to the conventional scanner, demonstrating the inverse square root exposure dependence predicted by theory. Investigations of noise power spectrum and spatial frequency response for the two systems

reinforce these conclusions and illustrate the advantages of developing more extensive (empirical and theoretical) frequency-dependent characterization methods for volumetric computed tomography systems.²² In addition to the quantitative measures of performance, the images of low-contrast phantoms and small animal anatomy confirm the conclusions drawn from these measures, showing excellent detail and soft-tissue contrast, more than sufficient for tissue localization in radiation oncology.

The results presented here demonstrate the potential of this approach for volumetric imaging. However, this study has been performed under conditions of small object size and small cone angle. These conditions are imposed by the size of the detector used in this investigation. Imaging with larger detectors allows increased cone angle and, for CT, increased object thickness. The extrapolation of performance based on the results presented here to that for larger detectors must be done with some caution. Imaging larger objects with an increased FOV will result in increased scatter and reduced transmission. The increase in scatter can be expected to have a negative impact on CT imaging performance by introducing non-uniformities in the reconstructed image (e.g., cupping and/or streaks),^{31,32} and by adding x-ray quantum noise to the image signal. The magnitude of scatter reaching the detector will depend greatly on the cone-angle and air gap employed, and studies suggest that scatter at these distances may be reduced compared to conventional radiographic applications.^{33,34} Quantifying the magnitude of the x-ray scatter problem and developing methods to reduce it are areas of ongoing investigation.

In addition to concerns of x-ray scatter at large cone-angles, the scanning of larger objects will significantly reduce the fluence arriving at the detector. This reduced transmission will negatively impact the performance of the flat-panel detector. Additive noise causes the DQE of the imager to depend on the number of x rays forming an image.^{21,28} This dependence is illustrated in Fig. 12 for the flat-panel imager used in these investigations and for hypothetical detectors that embody the most recent advances in imager design,²⁸ including higher x-ray quantum detection efficiency through the use of CsI:Tl and a reduction in additive noise through improvements in readout electronics. The zero-frequency DQE was computed using a model for signal and noise transfer that has demonstrated excellent agreement with measurements.^{21,35} It is clear from Fig. 12 that improvements in the x-ray converter and electronics noise significantly reduce the exposure dependence of the DQE over the broad range of exposures required for CT. The magnitude of the reduction depends greatly on the amplifier noise in the system. For the prototype imager used in these studies, the amplifier noise is very high¹⁶ at $12\,700 \text{ e}$. For the low transmitted exposure levels in CT of pelvic anatomy, for example, this detector would achieve a zero-frequency DQE of less than 10%. In comparison, an imager that incorporates the recent advances in design listed above (e.g., a high-quality CsI:Tl converter and amplifier noise of 3000 e or better) would achieve a higher DQE ($\sim 65\%$) at full transmission and maintain a DQE of $> 40\%$ even at low exposure levels.

Such enhancements in imager design are within the current capabilities of FPI manufacturers and will greatly facilitate the medical application of FPIs in cone-beam CT. Furthermore, these improvements are largely driven by other forces in digital imaging that anticipate use of FPIs in place of conventional image-intensifier systems for interventional fluoroscopy. For this reason, it can be expected that imagers with such characteristics will be available within the next few years.

High performance imaging using a CBCT scanner based on a flat-panel imager has been demonstrated on a bench-top apparatus. Is it possible to build a clinical imaging system with such technology? The answer to this question is an unqualified, "yes." Overall, the operating characteristics of the flat-panel are highly compatible with acquisition in a CBCT scanning geometry. Unlike image-intensifier or lens based systems, flat-panel detectors are geometrically robust under a rotating geometry, eliminating concerns of image distortion. The high readout rate of these detectors allows for imaging sequences of 300 projection images to be acquired within 10 s (operating at 30 fps). This is more than sufficient to satisfy the allowable rotation rates for the gantry of a medical linear accelerator. In fact, while the International Electromechanical Commission (IEC) recommends less than 1 revolution per minute for linear accelerators, it would be reasonable to reconsider such constraints in light of the advantages of CBCT guidance in the treatment room. Currently, the detector size and aspect ratio are driven by the needs of digital radiography, producing detectors comparable in size to radiographic film. These sizes limit the field-of-view of the reconstruction if sufficient clearance is to be maintained between the detector and patient during gantry rotation. This problem can be addressed using offset-detector schemes that use 360° of gantry rotation.³ Ultimately, a specialized detector could be designed with a size and aspect ratio that match the requirements for CBCT (e.g., $\sim 25 \times 50$ cm² area panel).

Given the potential that this technology is demonstrating, the opportunities for new areas of application for computed tomography are significant. Imaging systems based on this technology can be constructed to address specific imaging problems, including nondestructive testing (at kilovoltage or megavoltage energies), early detection and monitoring of specific medical conditions, and, of course, navigational imaging for therapies. The compact nature of the panels allows FPI-based CBCT imagers to be applied in situations that would never be considered feasible for a conventional CT scanner. The CBCT approach offers two important features that dramatically reduce its cost in comparison to a conventional scanner. First, the cone-beam nature of the acquisition does not require an additional mechanism to move the patient (or object) during image acquisition. Second, the use of a cone-beam, as opposed to a fan-beam, significantly increases the x-ray utilization, lowering the x-ray tube heat capacity required for volumetric scanning. For the same source and detector geometry, the efficiency roughly scales with the slice thickness. For example, the x-ray utilization increases by a factor of 30 in going from a 3 mm slice in a

conventional scanner to a cone-angle corresponding to a 100 mm slice with a cone-beam system. This would decrease heat-load capacities dramatically. From our experience, a 5200 kHU x-ray tube costs approximately \$70 000, whereas a 600 kHU x-ray tube (a factor of ~ 10 lower in capacity) costs roughly \$6000.

Cone-beam computed tomography has been a topic of active research and development for over a decade in areas such as nuclear medicine and industrial testing; however, only recently has it begun to appear in the diagnostic CT arena. The developments in this area have been for the most part limited to multislice detectors.³⁶ In this investigation, the use of an alternative detector for high-quality CT has been studied. The results of the investigation suggest that there is a significant potential for the use of these detectors in CBCT systems for radiotherapy and quite possibly for diagnostic and interventional CT imaging tasks that will take advantage of the fully 3D nature of CBCT. Based upon the positive results presented here, we have begun to construct an FPI-based kilovoltage CBCT scanner for guiding radiation therapy on a medical linear accelerator. While the advantages of improved precision in radiotherapy are clear, it remains to be seen how this new and exciting technology alters clinical practice.

ACKNOWLEDGMENTS

The authors extend their sincere gratitude to J. W. Wong, Ph.D., and A. A. Martinez, M.D., for stimulating discussions in the initiation of this work and for their continued enthusiasm and support. Thanks also to D. G. Drake (Oakland University) and W. Jendhoff (Beaumont Services Corp.) for assistance with this project. The flat-panel imager employed in this work was provided by Elekta Oncology Systems Inc., and technical information was courtesy of M. K. Gauer, Ph.D. (Perkin-Elmer Optoelectronics—Heimann Opto). This research was funded in part by the Prostate Cancer Research Program Grant No. DAMD-17-98-1-8497 dispensed by the U. S. Army Medical Research and Materiel Command.

^aSend all correspondences to the following address: Department of Radiation Oncology, William Beaumont Hospital, 3601 W. Thirteenth Mile Road, Royal Oak, Michigan 48073. Phone: 248-551-7024; Fax: 248-551-0089; electronic mail: djaffray@beaumont.edu

¹D. A. Jaffray, D. G. Drake, D. Yan, L. Pisani, and J. W. Wong, "Cone-beam tomographic guidance of radiation field placement for radiotherapy of the prostate," *Int. J. Radiat. Oncol., Biol., Phys.* (2000) (accepted).

²W. Swindell, R. G. Simpson, J. R. Oleson, C. Chen, and E. A. Grubbs, "Computed tomography with a linear accelerator with radiotherapy applications," *Med. Phys.* **10**, 416–420 (1983).

³P. S. Cho, R. H. Johnson, and T. W. Griffin, "Cone-beam CT for radiotherapy applications," *Phys. Med. Biol.* **40**, 1863–1883 (1995).

⁴R. M. Harrison and F. T. Farmer, "Possible application of a radiotherapy simulator for imaging of body cross sections," *Br. J. Radiol.* **49**, 813 (1976).

⁵B. D. Smith, "Cone-beam tomography: Recent advances and a tutorial review," *Opt. Eng.* **29**, 524–534 (1990).

⁶R. Clack and M. DeFrise, "Overview of reconstruction algorithms for exact cone-beam tomography," *SPIE Mathematical Methods in Medical Imaging III* **2299**, 230–241 (1994).

⁷H. Kudo and T. Saito, "Feasible cone beam scanning methods for exact

- reconstruction in three-dimensional tomography," *J. Opt. Soc. Am. A* **7**, 2169–2183 (1990).
- ⁸ D. A. Jaffray, D. G. Drake, M. Moreau, A. A. Martinez, and J. W. Wong, "A radiographic and tomographic imaging system integrated into a medical linear accelerator for localization of bone and soft-tissue targets," *Int. J. Radiat. Oncol., Biol., Phys.* **44**, 773–789 (1999).
 - ⁹ D. G. Drake, D. A. Jaffray, and J. W. Wong, "Characterization of a fluoroscopic imaging system for kilovoltage and megavoltage radiography," *Med. Phys.* **27**, 898–905 (2000).
 - ¹⁰ L. E. Antonuk, J. Yorkston, W. Huang, H. Sandler, J. H. Siewerdsen, and Y. El-Mohri, "Megavoltage imaging with a large-area, flat-panel, amorphous silicon imager," *Int. J. Radiat. Oncol., Biol., Phys.* **36**, 661–672 (1996).
 - ¹¹ D. A. Jaffray, J. H. Siewerdsen, and D. G. Drake, "Performance of a volumetric CT scanner based upon a flat-panel imager," in *Medical Imaging 1999: Physics of Medical Imaging*, edited by J. M. Boone and J. T. Dobbins III, *Proc. SPIE* **3659**, 204–214 (1999).
 - ¹² R. Ning, D. Lee, X. Wang, Y. Zhang, D. Conover, D. Zhang, and C. Williams, "Selenium flat panel detector-based volume tomographic angiography imaging: Phantom studies," in *Medical Imaging 1998: Physics of Medical Imaging*, edited by J. M. Boone and J. T. Dobbins III, *Proc. SPIE* **3336**, 316–324 (1998).
 - ¹³ R. Ning, X. Tang, R. Yu, D. Zhang, and D. Conover, "Flat panel detector-based cone beam volume CT imaging: Detector evaluation," in *Medical Imaging 1999: Physics of Medical Imaging*, edited by J. M. Boone and J. T. Dobbins III, *Proc. SPIE* **3659**, 192–203 (1999).
 - ¹⁴ T. M. Peters and R. M. Lewitt, "Computed tomography with fan beam geometry," *J. Comput. Assist. Tomogr.* **1**, 429–436 (1977).
 - ¹⁵ J. H. Siewerdsen and D. A. Jaffray, "Cone-beam computed tomography with a flat-panel imager: Effects of image lag," *Med. Phys.* **26**, 2635–2647 (1999).
 - ¹⁶ J. H. Siewerdsen and D. A. Jaffray, "A ghost story: Spatio-temporal response characteristics of an indirect-detection flat-panel imager," *Med. Phys.* **26**, 1624–1641 (1999).
 - ¹⁷ L. A. Feldkamp, L. C. Davis, and J. W. Kress, "Practical cone-beam algorithm," *J. Opt. Soc. Am. A* **1**, 612–619 (1984).
 - ¹⁸ S. Webb, "A modified convolution reconstruction technique for divergent beams," *Phys. Med. Biol.* **27**, 419–423 (1982).
 - ¹⁹ D. A. Chesler, S. J. Riederer, and N. J. Pelc, "Noise due to photon counting statistics in computed x-ray tomography," *J. Comput. Assist. Tomogr.* **1**, 64–74 (1977).
 - ²⁰ J. T. Dobbins III, D. L. Ergun, L. Rutz, D. A. Hinshaw, H. Blume, and D. C. Clarke, "DQE(f) of four generations of computed radiography acquisition devices," *Med. Phys.* **22**, 1581–1593 (1995).
 - ²¹ J. H. Siewerdsen, L. E. Antonuk, Y. El-Mohri, J. Yorkston, W. Huang, and I. A. Cunningham, "Signal, noise power spectrum, and detective quantum efficiency of indirect-detection flat-panel imagers for diagnostic radiology," *Med. Phys.* **25**, 614–628 (1998).
 - ²² J. H. Siewerdsen and D. A. Jaffray, "Cone-beam CT with a flat-panel imager: Noise considerations for fully 3-D computed tomography," *SPIE Phys. Med. Imag.* **3977**, 408–416 (2000).
 - ²³ Electron density CT Phantom RMI 465, Gammex RMI, Madison, WI.
 - ²⁴ J. C. Dainty and R. Shaw, *Image Science: Principles, Analysis, and Evaluation of Photographic-Type Imaging Processes* (Academic, London, 1974).
 - ²⁵ R. A. Brooks and G. DiChiro, "Statistical limitations in x-ray reconstructive tomography," *Med. Phys.* **3**, 237–240 (1976).
 - ²⁶ K. M. Hanson, "Detectability in computed tomographic images," *Med. Phys.* **6**, 441–451 (1979).
 - ²⁷ M. F. Kijewski and P. F. Judy, "The noise power spectrum of CT images," *Phys. Med. Biol.* **32**, 565–575 (1987).
 - ²⁸ L. E. Antonuk, Y. El-Mohri, K. W. Jee, M. Maolinbay, S. C. Nassif, X. Rong, J. H. Siewerdsen, Q. Zhao, and R. A. Street, "Beyond the limits of present active matrix flat-panel imagers (AMFPIs) for diagnostic radiology," in *Medical Imaging 1999: Physics of Medical Imaging*, edited by J. M. Boone and J. T. Dobbins III, *Proc. SPIE* **3659**, 518–528 (1999).
 - ²⁹ N. Jung, P. L. Alving, F. Busse, N. Conrads, H. M. Meulenbrugge, W. Rutten, U. Schiebel, M. Weibrecht, and H. Wicczorek, "Dynamic x-ray imaging system based on an amorphous silicon thin-film array," in *Medical Imaging 1998: Physics of Medical Imaging*, edited by J. M. Boone and J. T. Dobbins III, *Proc. SPIE* **3336**, 396–407 (1998).
 - ³⁰ M. Moreau, D. Drake, and D. Jaffray, "A novel technique to characterize the complete motion of a medical linear accelerator," *Med. Phys.* **25**, A191 (1998).
 - ³¹ G. H. Glover, "Compton scatter effects in CT reconstructions," *Med. Phys.* **9**, 860–867 (1982).
 - ³² P. C. Johns and M. Yaffe, "Scattered radiation in fan beam imaging systems," *Med. Phys.* **9**, 231–239 (1982).
 - ³³ U. Neitzel, "Grids or air gaps for scatter rejection in digital radiography: A model calculation," *Med. Phys.* **19**, 475–481 (1992).
 - ³⁴ J. M. Boone and J. A. Seibert, "An analytical model of the scattered radiation distribution in diagnostic radiology," *Med. Phys.* **15**, 721–725 (1988).
 - ³⁵ J. H. Siewerdsen, L. E. Antonuk, Y. El-Mohri, J. Yorkston, W. Huang, J. M. Boudry, and I. A. Cunningham, "Empirical and theoretical investigation of the noise performance of indirect detection, active matrix flat-panel imagers (AMFPIs) for diagnostic radiology," *Med. Phys.* **24**, 71–89 (1997).
 - ³⁶ H. Hu, "Multi-slice helical CT: Scan and reconstruction," *Med. Phys.* **26**, 5–18 (1999).

**Appendix E: Optimization of X-ray Imaging Geometry (with
Specific Application to Flat-panel Cone-beam
Computed Tomography)**

Optimization of x-ray imaging geometry (with specific application to flat-panel cone-beam computed tomography)

Jeffrey H. Siewerdsen^{a)} and David A. Jaffray

Department of Radiation Oncology, William Beaumont Hospital, Royal Oak, Michigan 48073

(Received 12 January 2000; accepted for publication 25 April 2000)

A theoretical method is presented that allows identification of optimal x-ray imaging geometry, considering the effects of x-ray source distribution, imaging task, x-ray scatter, and imager detective quantum efficiency (DQE). Each of these factors is incorporated into the ICRU-recommended figure of merit for image quality, the detectability index, which is maximized to determine the optimal system configuration. Cascaded systems analysis of flat-panel imagers (FPIs) is extended to incorporate the effects of x-ray scatter directly in the DQE, showing that x-ray scatter degrades DQE as an additive noise source. Optimal magnification is computed for FPI configurations appropriate to (but not limited to) cone-beam computed tomography (CBCT). The sensitivity of the results is examined as a function of focal spot size, imaging task (e.g., ideal observer detection or discrimination tasks), x-ray scatter fraction, detector resolution, and additive noise. Nominal conditions for FPI-CBCT result in optimal magnification of ~ 1.4 – 1.6 , depending primarily on the magnitude of the x-ray scatter fraction. The methodology is sufficiently general that examination of optimal geometry for other FPI applications (e.g., chest radiography, fluoroscopy, and mammography) is possible. The degree to which increased exposure can be used to compensate for x-ray scatter degradation is quantified. © 2000 American Association of Physicists in Medicine. [S0094-2405(00)00708-2]

Key words: flat-panel imager, cone-beam computed tomography, detective quantum efficiency, x-ray scatter, cascaded systems analysis, optimization, magnification

I. INTRODUCTION

Active matrix flat-panel imagers (FPIs) are experiencing widespread proliferation in medical and nonmedical x-ray imaging applications, and the geometries employed in such venues are as varied in form as the applications themselves. Selection of imaging geometry (e.g., a contact image or use of an air gap) has largely been determined by extension of precedent (e.g., incorporating the FPI into a preexisting film cassette holder). However, it is worthwhile to consider whether this new imaging technology brings with it new considerations for optimal geometry.

The general aim of this article is to identify a theoretical framework for optimization of system performance, accounting for the effects of x-ray source distribution, imaging task, x-ray scatter, and detective quantum efficiency (DQE). The specific aim is to apply this framework to the case of FPI-based cone-beam computed tomography (CBCT) in order to identify optimal geometric magnification, and to examine the dependence of the optimum on various system parameters.

Within the context of the general aim, there are many parameters—including x-ray energy spectrum,¹ thickness of the x-ray converter,^{2,3} and geometric magnification⁴—that can be analyzed in order to identify an optimum. Specifically, this investigation considers only the last—i.e., what geometric magnification, M , is optimal, given the imaging task and spatial-frequency-dependent transfer characteristics of the imager. Ultimately, a multivariate analysis in which numerous system parameters are interdependently examined

could be used to identify an overall optimal system configuration for a given application.

Application of FPIs in CBCT is relatively new,^{5–11} and initial reports indicate that such systems could offer an attractive technology for volumetric imaging. As reported previously,^{7–11} a prototype FPI-CBCT system was constructed to examine the use of this technology in image-guided radiotherapy. The prototype consists of a kilovoltage x-ray tube, an object rotation stage, and a FPI within a precise, reproducible geometry on an optical bench. The geometry is illustrated schematically in Fig. 1, summarizing the imaging geometry considered throughout this article. Terms and symbols are defined in Table I. For the FPI-CBCT prototype, $S_{OD}=100$ cm and $S_{ID}=160$ cm, giving $M=1.6$. An example FPI-CBCT image is shown in Fig. 2, illustrating the spatial detail and volumetric nature of the data acquired with the prototype.

II. THEORETICAL METHODS

The classic description of medical x-ray imaging systems—i.e., source–object–detector–observer—is replete with factors that affect system performance. By encompassing relevant factors analytically in a manner that allows quantification of imaging performance under varying system geometry, specifically geometric magnification, an optimum geometry can be identified, and the relative tradeoffs of sub-optimal configurations can be examined. Four such factors—size of the x-ray focal spot, imaging task, magnitude of x-ray scatter, and imager DQE—are analyzed below. These factors

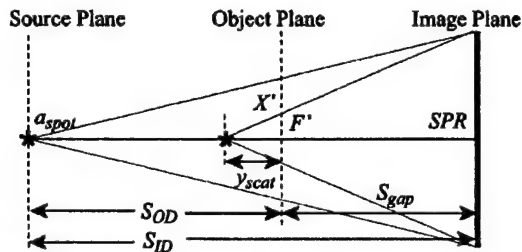


FIG. 1. Illustration of imaging geometry. The object and image planes are at distances S_{OD} and S_{ID} from the source plane, respectively. The x-ray focal spot is characterized by width, a_{spot} and an effective scatter point source is located at a distance y_{scat} (nominally 20 cm) (Ref. 18) from the object plane. The in-air entrance exposure at the object plane is X' , and the x-ray scatter fraction at the exit of the object plane is F' . The object plane is attenuative (nominally equivalent to 20 cm H_2O), and separated from the image plane by S_{gap} , which serves to reduce x-ray scatter to SPR at the image plane. All terms are described in Table I.

are then brought together in the figure of merit for image quality described by the International Commission on Radiation Units and Measurements (ICRU).¹²

A. Factors affecting geometric optimization

1. Spatial distribution of the x-ray focal spot

The size of the x-ray focal spot is a well-known source of geometric blur and is discussed in most x-ray imaging textbooks.^{13,14} Following Johns and Cunningham,¹³ and for a symmetric source distribution $\psi(x)$, the modulation transfer function, MTF, of the focal spot is given by the (normalized) cosine transform:

$$T_{spot}(u') = \frac{\int_{-\infty}^{+\infty} \cos(2\pi[(M-1)/M]u'x) \psi(x) dx}{\int_{-\infty}^{+\infty} \psi(x) dx}, \quad (1a)$$

where x is the spatial domain in the plane of the source, and u' is the spatial-frequency domain in the plane of the object. For simplicity, we restrict the present analysis to a single dimension x , with Fourier complement u' (in the object plane); extension to two dimensions is straightforward. Although the source distribution is rarely Gaussian,¹⁴ we assume such as a simple analytic case, characterized by width a_{spot} , yielding

$$T_{spot}(u') = e^{-\pi[(M-1)/M]a_{spot}u'}^2 \quad (1b)$$

in which $1/a_{spot}$ is precisely the "characteristic MTF width" of Barrett and Swindell.¹⁴

2. Imaging task

Essential to examining "optimal" spatial-frequency-dependent system performance is identification of the spatial frequencies of interest for a given detection task.¹² Ignoring such task dependence implicitly assumes that all spatial frequencies are equally weighted. Example elementary tasks include detection of a single object against a noisy background and discrimination between two objects, with the task function, $f_{task}(u')$, related to the Fourier transform of the object function. ICRU Report 54¹² illustrated detection and dis-

TABLE I. Glossary of symbols.

Symbol	Property
Imaging geometry	
S_{OD}	Source-to-object distance
S_{gap}	Object-to-detector gap
S_{ID}	Source-to-image distance
$M(M^*)$	Geometric magnification (optimal)
(u', u')	Spatial-frequency in object plane
X-ray source	
T_{spot}	MTF of focal spot
a_{spot}	Width of Gaussian focal spot distribution
$X'(X)$	Exposure incident on object (on detector)
X-ray scatter	
F'	X-ray scatter fraction at exit of object plane
y_{scat}	Position of effective scatter point source
$\bar{q}_0'(q_0)$	Total x-ray fluence at object (image) plane
$\bar{q}_0^{P'}(\bar{q}_0^P)$	Primary x-ray fluence at object (image) plane
$\bar{q}_0^{S'}(\bar{q}_0^S)$	Scatter x-ray fluence at object (image) plane
Σ	Selectivity of the air gap
SPR	Scatter-to-primary ratio at detector
Imaging task	
f_{task}	Task function
a_{task}	Width of object to detect (e.g., Gaussian cloud)
Detector	
DQE	Detective quantum efficiency
NEQ	Noise-equivalent quanta
\bar{g}_1	Quantum detection efficiency
\bar{g}_2	Quantum gain (optical photons/interacting x ray)
ϵ_{g2}	Poisson excess in \bar{g}_2
I	Swank factor
\bar{g}_4	Coupling efficiency of photodiode
T_3	MTF of x-ray converter
H	Lorentzian screen blur parameter in T_3
T_5	Pixel presampling MTF
$a_{pix}(a_{pd})$	Width of pixel (sensitive aperture)
σ_{amp}	Additive amplifier electronics noise
σ_{add}	Additive NPS due to electronics noise
Figures of merit	
S_{geo}	Geometric sharpness
d_{NEQ}	Detectability index (from NEQ)
d_{DQE}	Detectability index (from DQE)
d_{peak}	Peak value of d_{DQE}
α_{SCF}	Scatter compensation factor

crimination tasks for ideal and quasi-ideal (Hotelling and non-prewhitening matched filter) observers.¹² Siewerdsen and Antonuk³ used five simple detection tasks relevant to chest radiography, fluoroscopy, and mammography in examining optimal converter thickness for FPIs in projection radiography. Bissonnette, Cunningham, and Munro² used task functions based on point objects (i.e., uniform task) as well as on the frequency content of pelvis images in examining optimal converter thickness for portal imaging. We assume the simple case of an ideal observer and consider three task functions that broadly represent: (1) all spatial-frequencies equally weighted; (2) a low-frequency detection task; and (3) a high-frequency discrimination task:

$$f_{task}(u') = \begin{cases} k_1 & \text{(Task \#1),} \\ k_2 e^{-\pi a_{task}^2 u'^2} & \text{(Task \#2),} \\ k_3 (1 - e^{-\pi a_{task}^2 u'^2}) & \text{(Task \#3),} \end{cases} \quad (2a)$$

$$f_{task}(u') = k_2 e^{-\pi a_{task}^2 u'^2} \quad \text{(Task \#2),} \quad (2b)$$

$$f_{task}(u') = k_3 (1 - e^{-\pi a_{task}^2 u'^2}) \quad \text{(Task \#3),} \quad (2c)$$

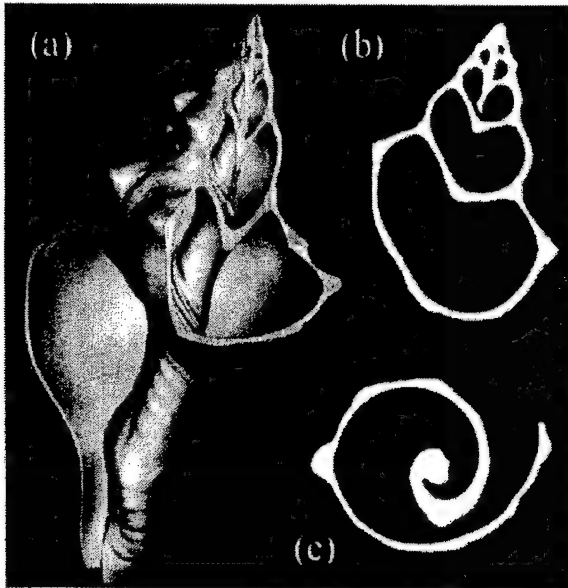


FIG. 2. (a) Volume rendering, (b) sagittal slice, and (c) transaxial slice of an FPI-CBCT image of a sea-shell. The scale is 5 cm in length (1 cm increments). The shell was imaged in air, using a 100 kVp beam (1.5 mm Al + 0.129 mm Cu added filtration), with 300 projections (1 mAs per projection) acquired at 1.2° rotational increments of the shell. The FPI (RID 512-400 A0 from EG&G Heimann Optoelectronics) incorporated a 512×512 matrix of *a*-Si:H photodiodes and TFTs at 400 μm pixel pitch, in combination with a 133 mg/cm² Gd₂O₂S:Tb x-ray converter. These images illustrate the quality of cone-beam reconstructions for the case of a high-contrast object (512×512×512 reconstruction with 250 μm voxels). The minute streaks and irregularities evident on the surface and interior of the shell are non-artifactual, real features of the object. More complete description of the prototype, along with quantitative characterization of the imaging performance, is given in Refs. 7–11.

where a_{task} is the width of a spherically symmetric Gaussian object, and k_i are area-normalization constants.

3. Efficiency of x-ray scatter rejection

The dominant interaction of kilovoltage x rays with tissue is Compton scattering,^{15–17} and an arsenal of methods for reducing its deleterious effects has evolved, including the use of air gaps and grids,^{18–22} and deconvolution techniques.^{23,24} For digital imagers, the loss in contrast associated with increased scatter can largely be overcome by adjusting window and level. Still, scatter rejection reduces the additional x-ray quantum noise associated with x-ray scatter. Furthermore, the presence of x-ray scatter in CBCT results in artifacts^{25–27} and contrast reduction that are not as easily overcome, although techniques for managing such effects have been proposed.²⁸

In examining the performance of air gaps compared to scatter-rejection grids, Neitzel¹⁸ treated the scatter reduction mechanism as a generalized transfer process and derived measures for scatter-rejection performance considering the simple geometry of Fig. 1. The primary and scatter fluence at the image plane are

$$q_0^P = q_0^{P'} \left(\frac{S_{\text{ID}} - S_{\text{gap}}}{S_{\text{ID}}} \right)^2, \quad (3a)$$

and

$$q_0^S = q_0^{S'} \left(\frac{y_{\text{scat}}}{y_{\text{scat}} + S_{\text{gap}}} \right)^2, \quad (3b)$$

respectively, where primed variables are at the object plane, e.g., scatter fraction, $F' = q_0^{S'} / (q_0^{P'} + q_0^{S'})$, and y_{scat} is the location of the effective scatter point source¹⁸ as in Fig. 1. Therefore, the scatter-to-primary ratio, SPR, at the image plane is

$$\begin{aligned} \text{SPR} &= \frac{q_0^S}{q_0^P} = \frac{F'}{1 - F'} \frac{1}{(1 - S_{\text{gap}}/S_{\text{ID}})^2 (1 + S_{\text{gap}}/y_{\text{scat}})^2} \\ &= \frac{F'}{1 - F'} \frac{1}{\Sigma} \end{aligned} \quad (3c)$$

where Σ is the selectivity of the gap, as derived by Neitzel:¹⁸

$$\Sigma = \left(1 - \frac{S_{\text{gap}}}{S_{\text{ID}}} \right)^2 \left(1 + \frac{S_{\text{gap}}}{y_{\text{scat}}} \right)^2. \quad (3d)$$

Here Σ is the ratio of the primary and scattered transmission factors, is independent of F' , and may be related to the DQE of the gap as defined by Wagner:²⁹

$$\text{DQE}_{\text{gap}} = \frac{(1 - F')\Sigma}{(1 - F')\Sigma + F'}. \quad (3e)$$

Note that F' is defined at the exit of the object plane and is independent of the gap, with typical values depending on field size and anatomical site:^{30–34} for small objects and fields, $F' \sim 0.3$, increasing to ~ 0.9 for larger objects. Furthermore, as reported by Niklason³⁴ for chest radiography, the scatter fraction can be significantly nonuniform within a single image—from ~ 0.5 in the region of the lungs to ~ 0.9 in the mediastinum.

4. Detective quantum efficiency

The spatial-frequency-dependent SNR transfer characteristics of the imaging system are described by the DQE and noise-equivalent quanta, NEQ, which may be determined empirically and/or analytically. As summarized in the Appendix, linear cascaded systems analysis^{35,36} provides a means of calculating imager DQE by modeling the imager as a series of gain and spatial spreading stages. As reported previously for indirect-detection FPIs,

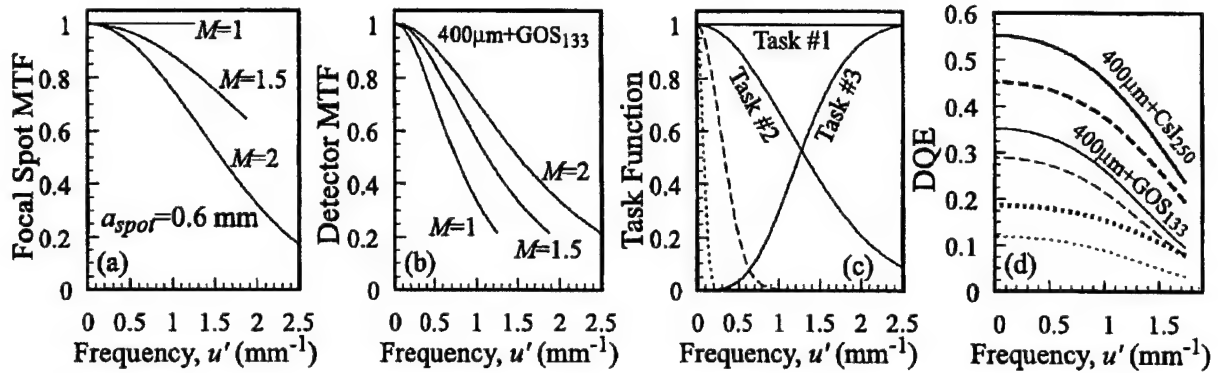


FIG. 3. Spatial-frequency-dependent factors affecting geometric optimization. (a) The MTF of the x-ray focal spot for three values of magnification. (b) The MTF of the FPI for three values of M . Imager configuration is abbreviated in terms of [pixel pitch+converter type and coverage (mg/cm^2)]. Therefore, as in (b) “400 μm +GOS₁₃₃” indicates an FPI incorporating a 400 μm pitch array in combination with 133 mg/cm^2 Gd₂O₂S:Tb. (c) Example task functions (normalized to unity height for presentation). Task #1 weights all spatial frequencies uniformly. Task #2 is a low-frequency detection task characterized by the width, a_{task} , of a Gaussian sphere (with a_{task} equal to 0.25, 1, and 4 mm for the solid, dashed, and dotted curves, respectively). Task #3 weights high frequencies preferentially. (d) The DQE for FPIs incorporating two imager configurations [400 μm +CsI₂₅₀ (bold curves) and 400 μm +GOS₁₃₃ (thin curves)] at various levels of x-ray scatter ($M=1.4$; $X=1$ μR at detector; and $\sigma_{\text{amp}}=3000$ e). $F'=0$ (solid curves) corresponds to the scatter-free case; higher levels of scatter [e.g., $F'=0.5$ (dashed curves) and $F'=0.9$ (dotted curves)] significantly degrade the DQE.

$$\text{DQE}(u') = \frac{\overline{g_1} \overline{g_2} \overline{g_4} T_3^2(u') T_5^2(u')}{[1 + \overline{g_4}(\overline{g_2} + \varepsilon_{g2}) T_3^2(u')] T_5^2(u') + S_{\text{add}}(u') / a_{\text{pd}}^4 \overline{q_0} \overline{g_1} \overline{g_2} \overline{g_4}}, \quad (4a)$$

where each term is defined in the Appendix and summarized in Table I, and NEQ is equal to the DQE times the incident fluence. This analytic form^{37–39} has demonstrated excellent agreement with empirical results for various FPI designs, x-ray converters, and exposure conditions—all acquired under conditions of low x-ray scatter. It is generally recognized that the effect of x-ray scatter is to introduce additional x-ray quantum noise; however, there is no accommodation for the effect in this simple linear cascaded systems model. As shown in the Appendix, the effect of x-ray scatter on DQE can be derived by considering the propagation of primary and scatter components separately in the imaging chain. Accounting for x-ray scatter, the DQE is then

$$\text{DQE}(u') = \frac{\overline{g_1} \overline{g_2} \overline{g_4} T_3^2(u') T_5^2(u')}{(1 + \text{SPR}) [1 + \overline{g_4}(\overline{g_2} + \varepsilon_{g2}) T_3^2(u')] T_5^2(u') + S_{\text{add}}(u') / a_{\text{pd}}^4 \overline{q_0} \overline{g_1} \overline{g_2} \overline{g_4}}. \quad (4b)$$

In addition to the usual assumptions required of such analysis (e.g., linearity and stationarity),³⁶ for the sake of clarity and simplicity as discussed in the Appendix, Eqs. (4) assume unity pixel fill-factor, lack of noise-power aliasing, and that the spectrum for scattered x rays is comparable to that of the primary. Accounting for these effects adds only a slight degree of complexity to the analysis but has been neglected in order to highlight the novel feature of this analysis—incorporation of x-ray scatter in the DQE. Degradation of the DQE can be understood by considering the terms in the denominator. For example, Eq. (4a) exhibits terms related to the Poisson excess (conversion noise, or Swank factor⁴⁰) and to the additive electronics noise (the S_{add} term, which governs the exposure dependence of the DQE). Equation 4(b) shows that x-ray scatter reduces the DQE by way of an additional term proportional to the SPR. For example, under conditions for which the imager is strongly input quantum limited (i.e., the S_{add} term is negligible), a SPR of 1 reduces the DQE by a factor of 2 relative to scatter-free conditions.

Furthermore, note that the reduction in DQE due to x-ray scatter cannot be restored by increased exposure; rather, increasing exposure simply increases NEQ. This is perfectly analogous to the dependence of DQE and NEQ on additive electronics noise and exposure: in the limit of zero electronics noise, DQE is independent of exposure, whereas NEQ is proportional.

5. Brief summary of frequency-dependent factors

Figure 3 summarizes the spatial-frequency-dependent factors affecting geometric optimization. As shown in Fig. 3(a), the MTF of the focal spot degrades significantly with increased magnification. The detector MTF, however (taken as the product of the x-ray converter MTF,⁴¹ T_3 , and pixel presampling MTF,^{42,43} T_5), improves with increased magnification as shown in Fig. 3(b). Obviously, an optimal magnification exists in terms of spatial resolution considerations alone. Figure 3(c) plots the various task functions described in Eq. (2). For Task #2—the low-frequency detection task—

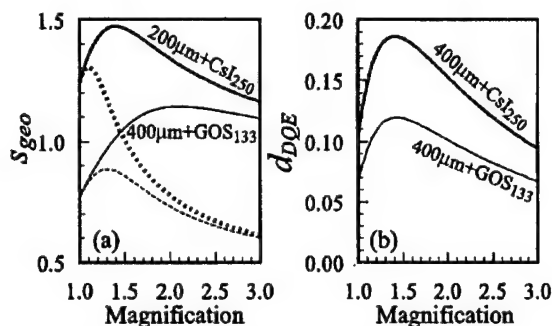


FIG. 4. Figures of merit as a function of geometric magnification. (a) Geometric sharpness [Eq. (5)] gives a measure of system spatial resolution and is shown for various configurations of focal spot size [$a_{spot} = 0.6$ mm (solid curves) and $a_{spot} = 1.2$ mm (dotted curves)], converter type, and pixel pitch [200 $\mu\text{m} + \text{CsI}_{250}$ (bold curves) and 400 $\mu\text{m} + \text{GOS}_{133}$ (thin curves)]. (b) The detectability index [Eq. 6(b)] gives a composite measure accounting for spatial resolution, noise characteristics, x-ray scatter, and imaging task. Two imager configurations are shown, with $a_{spot} = 0.6$ mm, Task #2 ($a_{task} = 1$ mm), $X' = 1$ mR, $F' = 0.8$, and $\sigma_{amp} = 3000$ e. Optimal magnification, M^* , is that at which detectability is maximized.

$f_{task}(u')$ is shown for Gaussian spheres of size ranging from 0.25 to 4 mm. Finally, Fig. 3(d) shows $DQE(u')$ for two FPI configurations (one employing a 250 mg/cm^2 CsI:Tl x-ray converter, the other 133 mg/cm^2 $\text{Gd}_2\text{O}_2\text{S:Tb}$) at various levels of x-ray scatter.

To identify an optimal geometric magnification, we consider the tradeoffs implied by all of the above factors. Geometric blur due to the nonzero size of the focal spot biases the optimum toward unity magnification (contact image). Finite detector resolution, on the other hand, biases the optimum toward infinity. In terms of DQE, higher magnification improves detector MTF and reduces x-ray scatter, but reduces the x-ray fluence impinging on the detector due to $1/r^2$ falloff. Thus, under conditions where additive electronics noise is significant [the S_{add} term in Eqs. (4)], the DQE will bias optimal magnification toward unity. The process of optimization, therefore, is a tug-of-war among the physical factors described by Eqs. (1)–(4).

B. System performance: Detectability index

A composite figure of merit for system performance is required to quantify the tradeoffs among these factors. Considering spatial resolution alone, the geometric sharpness may be defined as the integral over the product of the squares of the MTFs:

$$s_{geo} = \int_{-\infty}^{+\infty} T_{spot}^2(u') T_3^2(u') T_5^2(u') du'. \quad (5)$$

The MTFs are squared, and the symbol s_{geo} is used, in analog to the sharpness factor used in describing the effective aperture in propagation of individual pixel noise.^{37,44,45} Figure 4(a) plots the geometric sharpness versus magnification for four system configurations—a large and small focal spot, and a higher- and lower-resolution FPI. For the small focal spot ($a_{spot} = 0.6$ mm), the higher-resolution detector (200 $\mu\text{m} + \text{CsI}_{250}$) exhibits an optimum at $M = 1.4$, whereas

the lower-resolution detector (400 $\mu\text{m} + \text{GOS}_{133}$) increases slowly with M , peaking at $M = 2.1$, and then falling off only slightly at extended values. For the large focal spot ($a_{spot} = 1.2$ mm), the detector configurations exhibit more distinct optima at $M = 1.1$ and $M = 1.2$, respectively. Such analysis points out some of the intuitive trends expected in the following calculations, but geometric sharpness alone is clearly incomplete as a figure of merit where issues of x-ray scatter and additive noise are concerned.

For the case of an ideal observer performing a simple hypothesis-testing task under signal-known-exactly and background-known-exactly conditions, the figure of merit for system performance described in ICRU 54¹² is the detectability index:

$$d_{NEQ} = \int_0^{u'_{Nyq}} f_{in}^2(u') NEQ(u') du', \quad (6a)$$

where $f_{in}(u')$ is the product of the task function and focal spot MTF: $f_{in}(u') = f_{task}(u') T_{spot}(u')$. Thus each of the factors discussed above—geometric blur, imaging task, x-ray scatter, and detector SNR transfer characteristics—is incorporated in this figure of merit. Such representation separates imaging task from detector performance, can be extended to quasi-ideal observers, and may be related to the experimentally determined receiver operating characteristic (ROC) curve.¹² Since we are concerned with optimization within the constraint of finite dose, we consider the detectability index per unit dose (or fluence), which simply replaces NEQ with DQE in the integrand:

$$d_{DQE} = \int_0^{u'_{Nyq}} f_{in}^2(u') DQE(u') du'. \quad (6b)$$

Thus the optimal magnification, M^* , is that at which d_{DQE} is maximized (with the peak value in d_{DQE} termed d_{peak}). For example, Fig. 4(b) plots d_{DQE} as a function of magnification for the same imager configurations as in Fig. 3(d). The 400 $\mu\text{m} + \text{CsI}_{250}$ system exhibits a fairly sharp peak at $M = 1.4$, and the 400 $\mu\text{m} + \text{GOS}_{133}$ system exhibits a broader peak at $M = 1.45$. Moreover, detectability is higher for the former configuration (due to higher DQE) for equivalent M . However, note that for the conditions specified, suboptimal configuration of the superior imager (e.g., employing the 400 $\mu\text{m} + \text{CsI}_{250}$ FPI at $M = 1$) results in d_{DQE} that is actually less than that given by optimal configuration of the other (i.e., employing the 400 $\mu\text{m} + \text{GOS}_{133}$ FPI at $M = 1.45$). Thus, DQE alone does not guarantee superior system performance, and knowledgeable selection of the imaging geometry—considering imaging task and x-ray scatter—is essential to achieving maximum performance.

Numerous imager configurations were considered, with results shown for either the 400 $\mu\text{m} + \text{CsI}_{250}$ or 400 $\mu\text{m} + \text{GOS}_{133}$ configurations. Unless otherwise stated, other system parameters were set to the following nominal values: $a_{spot} = 0.6$ mm; 120 kVp spectrum⁴⁸ with 3 mm Al added filtration; $X' = 1$ mR; 20 cm H_2O object; $S_{OD} = 100$ cm; Task #2 ($a_{task} = 1$ mm); $F' = 0.8$; and $\sigma_{amp} = 3000$ e. S_{OD} was fixed at 100 cm to give geometry consistent with the proto-

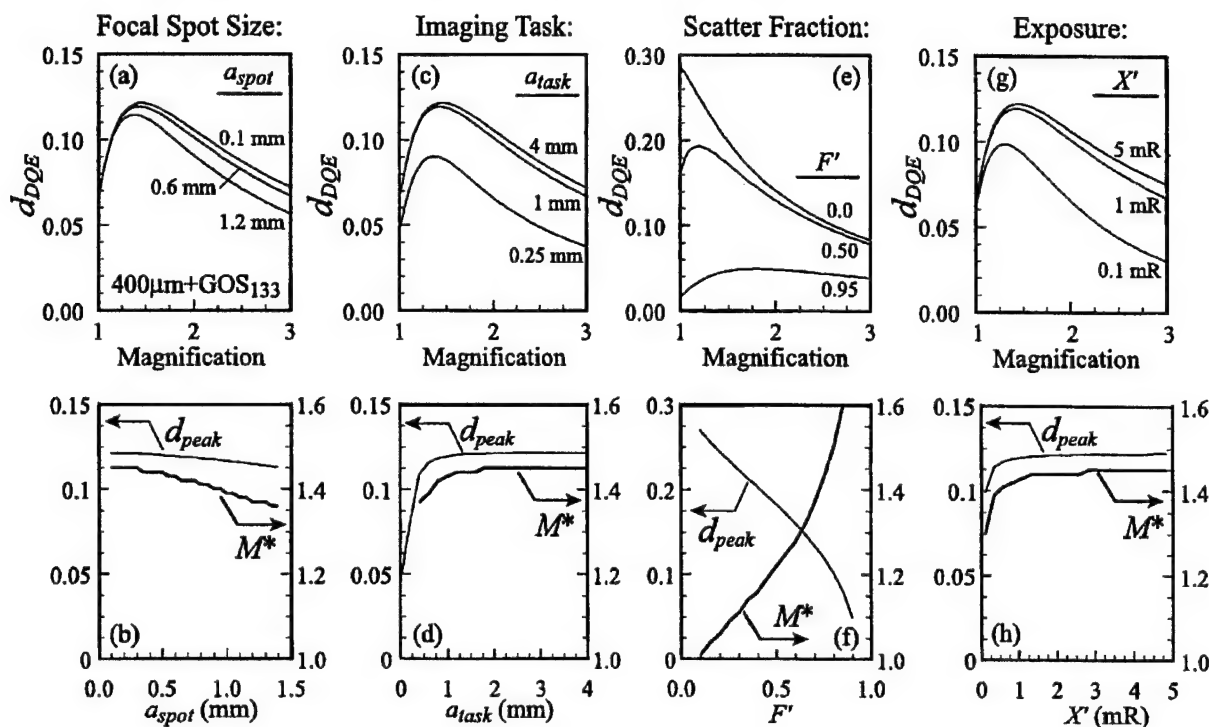


FIG. 5. Detectability and optimal magnification for various system parameters. The top row of figures plots d_{DQE} versus M at various values of (a) focal spot size ($a_{spot} = 0.1, 0.6$, and 1.2 mm); (c) imaging task (Task #2; $a_{task} = 0.25, 1$, and 4 mm); (e) scatter fraction ($F' = 0.0, 0.5$, and 0.95); and (g) exposure ($X' = 0.1, 1$, and 5 mR). The bottom row of figures plots d_{peak} (left-vertical axis) and M^* (right-vertical axis) as a function of a_{spot} , a_{task} , F' , and X' , respectively. In each case, results for the $400 \mu\text{m} + \text{GOS}_{133}$ imager configuration are shown.

type for image-guided radiotherapy^{8–11} and so that dose to the patient is held constant unless otherwise stated. The $1/r^2$ reduction in x-ray fluence at the image plane is implicit in calculations in which M is varied. Calculations were performed numerically using Matlab (the MathWorks, Natick MA), with quantization in the resulting M^* limited to a resolution of 0.01 .

III. RESULTS

The following sections analyze imaging performance in light of these geometrical/physical considerations. First, the optimal magnification for a number of system configurations is computed, and the sensitivity of the results is examined as a function of various system parameters—specifically focal spot size, imaging task, x-ray scatter fraction, detector blur, and exposure. Then, issues concerning the most dominant parameter (scatter fraction) are considered. We compute the scatter-rejection efficiency of the air gap, show the effects on DQE and NEQ, and quantify the degree to which degradation due to x-ray scatter can be compensated by increased exposure.

A. Optimal magnification

Optimal magnification was computed for a number of imager configurations as a function of focal spot size, imaging task, x-ray scatter fraction, detector blur, and exposure. In each case, the sensitivity of the optima (i.e., the degree to which variations in a given parameter affect M^*) was exam-

ined by plotting optimal magnification (M^*) and peak detectability (d_{peak}) as a function of each parameter.

1. Optimal magnification: Dependence on focal spot size

Figure 5(a) plots the detectability index as a function of M for the $400 \mu\text{m} + \text{GOS}_{133}$ configuration and three focal spot sizes ($0.1, 0.6$, and 1.2 mm). The peak in each curve corresponds to the optimal magnification. As shown in Fig. 5(b), the value of M^* (~ 1.4 in each case) is largely insensitive to the value of a_{spot} (for the conditions specified), and peak detectability decreases by only $\sim 5\%$ for the largest spot. This is not to say that spot size is irrelevant in general, but rather that for the specified nominal imaging task, scatter fraction, and detector configuration, other factors exhibit a stronger influence upon the value of M^* .

2. Optimal magnification: Dependence on imaging task

Figure 5(c) plots d_{DQE} versus M for three elementary detection tasks (Task #2; $a_{task} = 0.25, 1$, and 4 mm). In each case, detectability increases for larger objects (i.e., lower-frequency tasks). That the detectability decreases at larger M (i.e., that a peak exists at all) is indicative of the bias impelled by factors such as focal spot size and additive electronic noise. As shown in Fig. 5(d) peak detectability increases up to $a_{task} \sim 1$ mm, beyond which d_{peak} is nearly

insensitive. Similarly, the optimal magnification increases slightly with a_{task} (for the specified nominal conditions), with $M^* \sim 1.4$ for each case. Depending on conditions, e.g., for smaller focal spot, lower scatter fraction, and lower additive electronic noise, the opposite trend may be exhibited (i.e., M^* decreases for larger a_{task}), but in all cases examined the sensitivity of M^* to a_{task} was fairly small. For both the uniform task (Task #1) and high-frequency task (Task #3), the optimal magnification is again ~ 1.4 , reiterating the relative insensitivity to task for the nominal conditions. The relative insensitivity of the optimal magnification to imaging task is convenient, since one may want to accomplish multiple tasks given a single image. Optimal values for other system parameters, e.g., x-ray converter thickness,^{2,3} have been shown to exhibit significantly higher sensitivity to task.

3. Optimal magnification: Dependence on x-ray scatter fraction

Figure 5(e) shows d_{DQE} as a function of M for values of x-ray scatter fraction ranging from 0.1 to 0.95, and significantly greater sensitivities are observed. For both the $400\text{ }\mu\text{m} + \text{GOS}_{133}$ and $400\text{ }\mu\text{m} + \text{CsI}_{250}$ imager configurations, the shape and magnitude of the d_{DQE} curves depend greatly on F' . For $F' = 0.1$, the curves are monotonically decreasing—i.e., a contact image ($M^* \sim 1$) is optimal, since the scatter fraction is already fairly low, and the S_{add} term in the denominator of the DQE [Eq. (4b)] is dominant. For $F' = 0.5$, the detectability is biased toward higher magnification, and a peak appears ($M^* \sim 1.2$). For high scatter conditions ($F' = 0.95$) the detectability curve broadens significantly, with $M^* \sim 1.8$, beyond which d_{DQE} reduces only slightly. As shown in Fig. 5(f), the dependence of M^* and d_{peak} on the x-ray scatter fraction is significant. The $400\text{ }\mu\text{m} + \text{GOS}_{133}$ and $400\text{ }\mu\text{m} + \text{CsI}_{250}$ configurations yielded similar values for M^* , increasing asymptotically with F' as in Fig. 5(f).

4. Optimal magnification: Dependence on detector spatial resolution

The dependence of d_{DQE} and M^* on detector resolution was also analyzed. (Graphs not shown for space considerations.) For these calculations, the MTF of the x-ray converter was continually varied by adjusting the screen blur, H , from zero (perfect converter MTF) to arbitrarily large values [Eq. (A2)]. For reference, the values of H for three common $\text{Gd}_2\text{O}_2\text{S:Tb}$ (Lanex) screens are⁴¹ $H = 0.06$ (34 mg/cm^2 —Lanex Fine); $H = 0.43$ (70 mg/cm^2 —Lanex Regular); and $H = 1.25$ (133 mg/cm^2 —Lanex Fast-B). In order to examine the dependence on screen blur alone, other parameters of the x-ray converter (e.g., g_1 , g_2 , ϵ_{g2} , and g_4) were held fixed. Specifically, $g_1 = 0.56$, $g_2 = 1650$, $\epsilon_{g2} = 625$, and $g_4 = 0.75$ (which are the values for 133 mg/cm^2 $\text{Gd}_2\text{O}_2\text{S:Tb}$). Therefore, the calculations represent imager configurations incorporating a hypothetical x-ray converter that is immune to the usual gain-resolution tradeoff. A range of pixel pitch was considered ($100\text{ }\mu\text{m} < a_{\text{pix}} < 400\text{ }\mu\text{m}$) over separate ranges of screen blur ($0 < H < 1.5$) that represent reasonable

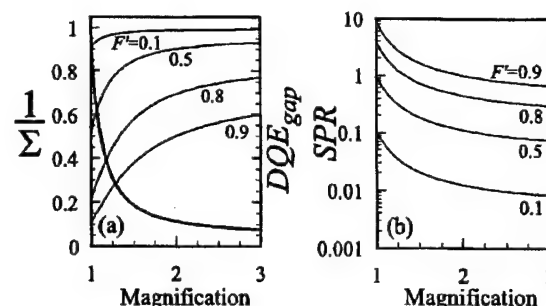


FIG. 6. X-ray scatter rejection by the air gap. (a) The inverse of the selectivity (bold curve; left axis) and the DQE of the gap (thin curves; right axis) provide measures of scatter-rejection for the air gap. (b) The SPR at the image plane is the term appearing in the denominator of the DQE [Eq. 4(b)] and degrades detector performance in a manner analogous to an "additive quantum noise." Values for DQE_{gap} and SPR are shown for F' ranging from 0.1 to 0.9.

match between screen and pixel MTFs. For a given pixel pitch, both optimal magnification and peak detectability were relatively insensitive to screen blur. As a function of pixel pitch, M^* increases from ~ 1.3 (for $a_{\text{pix}} = 100\text{ }\mu\text{m}$; $0 < H < 0.4$) to ~ 1.45 (for $a_{\text{pix}} = 400\text{ }\mu\text{m}$; $0.9 < H < 1.5$), relating the intuitive trend that a lower-resolution detector implies a larger optimal magnification. It should be noted that for low values of H the assumption that noise-power aliasing is negligible becomes less valid, and modification of Eq. 4(b) to include noise aliasing is required to give a more realistic analysis of imager DQE. Accounting for the gain-resolution tradeoff in the analysis would depend on the particular physical characteristics of the x-ray converter (e.g., a powder phosphor such as $\text{Gd}_2\text{O}_2\text{S:Tb}$ or a crystalline scintillator such as CsI:Tl) in a manner consistent with the trends illustrated in Figs. 3 and 4.

5. Optimal magnification: Dependence on exposure and additive noise

The dependence of d_{DQE} and M^* on exposure is shown in Figs. 5(g) and 5(h). As expected, d_{DQE} and d_{peak} improve with increasing exposure due to improved DQE. However, the increase in d_{peak} is significant ($\sim 20\%$) only across the lowest exposure levels (at which the imager is electronics noise limited). Conversely, for a fixed exposure, M^* and d_{DQE} decrease with increasing additive electronic noise. The trend is readily understood by considering the two "additive" terms in the denominator of the DQE [Eq. 4(b)]: the "additive electronic noise" term (containing S_{add}) affects the exposure dependence of the DQE and is important in analyzing the performance of FPIs in low-dose applications;⁴⁷ similarly, the "additive quantum noise" term (containing SPR) affects the scatter dependence of the DQE. Each is a dimensionless, spatial-frequency-dependent quantity for which nonzero values imply loss in DQE. Incorporating both additive electronic noise and x-ray scatter into the DQE formalizes the manner in which these effects conspire to degrade imager performance.

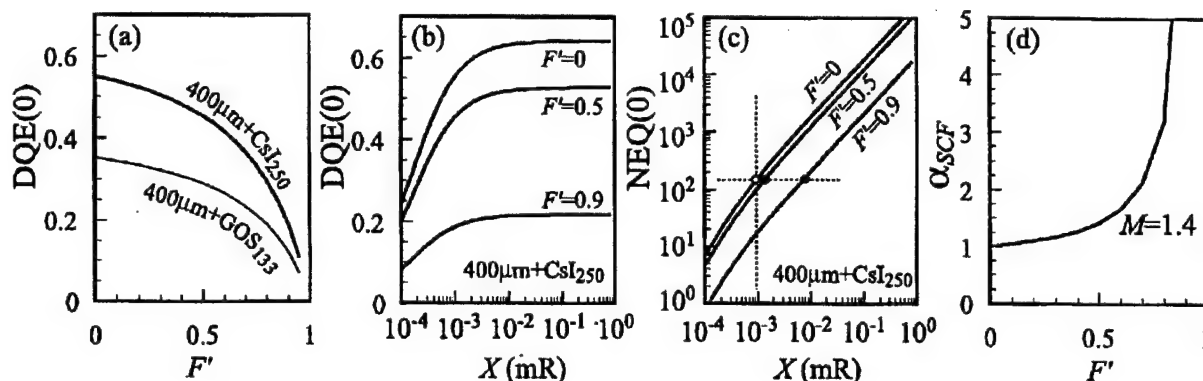


FIG. 7. Effect of x-ray scatter on DQE and NEQ. (a) Zero-frequency DQE [DQE(0)] versus F' for two imager configurations [$400\mu\text{m} + \text{CsI}_{250}$ and $400\mu\text{m} + \text{GOS}_{133}$] at $M = 1.4$ and $X = 1\mu\text{R}$. (b) DQE(0) for the $400\mu\text{m} + \text{CsI}_{250}$ configuration plotted as a function of exposure to the detector at various levels of scatter ($F' = 0, 0.5$, and 0.9). (c) Zero-frequency NEQ [NEQ(0)] for the $400\mu\text{m} + \text{CsI}_{250}$ configuration versus exposure to the detector. (d) Scatter compensation factor— α_{SCF} , the factor by which exposure must be increased to restore NEQ(0) to a value equal to the scatter-free case—plotted as a function of x-ray scatter fraction.

B. X-ray scatter considerations

Clearly, a significant parameter in identifying optimal imaging geometry is the x-ray scatter fraction. Below, we summarize the efficiency of scatter rejection using air gaps, comment on this efficiency in relation to scatter-rejection grids, and examine the effect on DQE and NEQ.

1. X-ray scatter rejection: Efficiency of the gap

Figure 6 illustrates the efficiency of x-ray scatter rejection imparted by the air gap. Reduction in scatter transmission [related to $1/\Sigma$, left axis of Fig. 6(a)] is a steep function of magnification; therefore, even a modest air gap can provide significant scatter rejection. Since the DQE of the gap²⁹ [Eq. 3(e), right axis of Fig. 6(a)] improves most rapidly for low scatter fractions, the benefits of an air gap are greatest for low to moderate levels of scatter (e.g., $F' < 0.5$), whereas for higher levels (e.g., $F' > 0.8$) the scatter rejection improves somewhat more slowly with M . Such results were well quantified by Neitzel,¹⁸ who examined the relative performance of air gaps and grids, concluding that (1) for high scatter conditions, gaps and grids give comparable improvement in SNR; (2) for low to moderate levels of scatter, gaps are clearly superior (and use of a grid can even degrade the SNR); and (3) the advantages of the gap are even greater if the application can physically/logistically accommodate larger gaps (e.g., $M > 1.4$).

In terms of detector DQE [Eq. 4(b)], the parameter of interest is the SPR at the detector, related to F' and Σ by Eq. 3(c). As shown in Fig. 6(b), SPR is a steeply descending function of M for $M < \sim 1.5$, falling by a factor of ~ 5 for $M = 1.5$, a factor of ~ 10 for $M = 2$, and a factor of ~ 13 for $M = 3$. This reduction in SPR should be considered in relation to the ratio of additive electronics noise and exposure level—i.e., the degradation in DQE due to the SPR term [Eq. 4(b)] should be considered relative to that of the S_{add} term. For conditions where the imager is strongly electronics noise limited (e.g., at low dose), reduction in SPR by increasing M may give negligible improvement (or even degradation) in

DQE. On the other hand, for conditions where the imager is strongly input-quantum-limited (i.e., negligible S_{add}), a modest air gap can significantly improve DQE.

2. X-ray scatter: Effect on DQE and NEQ

Figure 7(a) plots the zero-frequency DQE as a function of F' for two imager configurations, reiterating the trend of Fig. 2(d) and showing the significant degradation due to x-ray scatter. DQE(0) is plotted as a function of exposure in Fig. 7(b) for the $400\mu\text{m} + \text{CsI}_{250}$ configuration, showing the expected low-exposure falloff (e.g., for $X < \sim 1\mu\text{R}$) due to additive electronics noise.^{37–39,47} Considering the curves at various levels of F' , we see, furthermore, that degradation in DQE due to x-ray scatter cannot be restored by increased exposure. For example, considering the top curves of Fig. 7(b) ($F' = 0$ and $F' = 0.5$), it is clear that the DQE exhibited in the scatter-free case (~ 0.64 for $X > \sim 1\mu\text{R}$) cannot be achieved in the $F' = 0.5$ case by increasing exposure. This is because the SPR term is independent of exposure (whereas the S_{add} term is inversely proportional). This is similar to the manner in which x-ray conversion noise in the phosphor⁴⁰ (i.e., “Swank noise” included in ϵ_{g2} at stage 2) imposes an irrecoverable drop in DQE. In the limit of zero electronics noise, Swank noise degrades DQE by a multiplicative factor (the Swank factor, giving $\text{DQE} = g_1 I$);⁴⁰ similarly, x-ray scatter degrades DQE by a factor of $1/(1 + \text{SPR})$.

The NEQ of course increases in proportion to incident x-ray fluence, as shown in Fig. 7(c) at various levels of F' . The nonlinear reduction in NEQ(0) at low exposure is due to additive electronic noise. This plot illustrates a means of quantifying the degree to which degradation in NEQ due to x-ray scatter can be restored by increasing exposure. For scatter-free conditions ($F' = 0$) where the imager is input quantum limited [e.g., $X > \sim 1\mu\text{R}$, for which, as shown in Fig. 7(b), the DQE is maximized and constant] the system exhibits NEQ(0) shown by the horizontal dashed line. For increasing levels of x-ray scatter, the same NEQ(0) can be achieved by increasing exposure (small dots on $F' = 0.5$ and

$F' = 0.9$ curves). The scatter compensation factor, α_{SCF} , is the factor by which exposure must be increased to compensate for loss in NEQ(0) due to x-ray scatter and is shown in Fig. 7(d). For low-to-moderate scatter fraction ($0 < F' < 0.5$), α_{SCF} increases gradually compared to high scatter conditions ($F' > 0.8$) where the compensation factor diverges asymptotically. For example, restoration of NEQ(0) to the level achieved at $X = 1 \mu R$ in the scatter-free case requires exposure increase by a factor of ~ 1.4 for $F' = 0.5$ and ~ 3.2 for $F' = 0.8$ for the conditions shown. For higher magnifications, α_{SCF} reduces slightly due to improved scatter rejection. For example, for the FPI-CBCT prototype ($M = 1.6$), NEQ can be recovered by increasing exposure by $\alpha_{SCF} \sim 1.3$ (for $F' = 0.5$) and $\alpha_{SCF} \sim 2.5$ (for $F' = 0.8$). Results for α_{SCF} versus F' are identical for both $400 \mu m + CsI_{250}$ and $400 \mu m + GOS_{133}$ imager configurations.

IV. DISCUSSION AND CONCLUSIONS

The effects of geometric blur, imaging task, x-ray scatter, and imager DQE have been incorporated in a theoretical method for identifying optimal imaging geometry, specifically the geometric magnification that maximizes the detectability index. Incorporation of the SPR into the linear cascaded systems expression for DQE provides a straightforward means of quantifying the effects of x-ray scatter on imager performance. X-ray scatter reduces the DQE in a manner analogous to an "additive quantum noise," and the degree to which scatter and/or electronics noise degrade performance is evident in the relative magnitude of each term in the denominator of the DQE: for SPR and S_{add} negligible, the imager is input quantum limited (i.e., DQE equal to g_1 times the Swank factor); for SPR negligible, the DQE depends on the ratio of S_{add} and detector signal;^{37-39,47} for S_{add} negligible, the DQE is proportional to $1/(1 + SPR)$; for both SPR and S_{add} significant, the DQE suffers from additive quantum and electronics noise, and the above methodology identifies the geometry that optimizes imager performance.

Although any given factor (e.g., focal spot size, imaging task, scatter fraction, or DQE) can significantly affect the optimal geometry under certain conditions, for the nominal conditions specified above, the most dominant parameter is the x-ray scatter fraction. For low scatter conditions (e.g., $F' \sim 0.3$ as with small fields and thin objects, such as extremities) optimal magnification is ~ 1.1 (which for practical purposes is close to a contact image). For moderate-to-high scatter conditions (e.g., $F' \sim 0.8$ as in the retrocardiac region³⁴), $M^* \sim 1.4$. For high scatter conditions (e.g., $F' \sim 0.9$ as with large fields and thick objects, such as the pelvis), $M^* \sim 1.6$, which admittedly by coincidence, is precisely the magnification employed in the FPI-CBCT prototype. Degradation in NEQ due to x-ray scatter can be compensated by increasing exposure by a factor of ~ 1.2 – 1.5 (for low-to-moderate scatter; i.e., $F' = 0.3$ – 0.5) and by a factor of ~ 2 – 3 (for higher scatter; i.e., $F' = 0.7$ – 0.9). In FPI-CBCT, such compensation is not expected to reduce scatter artifacts (e.g.,

cupping and streaks²⁵⁻²⁷). For the immediate application envisioned for the prototype (i.e., CBCT image-guided radiotherapy of the prostate, in which quantitative accuracy in CT# is of secondary importance to contrast and spatial resolution), scatter compensation is proposed simply to alleviate limitations in NEQ.

Secondary to the x-ray scatter fraction are the dependencies on (1) the ratio of additive electronic noise to exposure and (2) detector spatial resolution. Lower levels of S_{add} lead to higher values of optimal magnification, since DQE is then less sensitive to $1/r^2$ falloff in fluence. Hence, besides the clear SNR incentive that has driven the quest for low electronic noise (e.g., in the context of FPI fluoroscopy⁴⁷), there is a SPR incentive as well: lower electronic noise affords larger gaps, lower SPR, and therefore improved DQE.

Typically, improved detector MTF leads to reduced optimal magnification, in agreement with intuition. Clearly, however, optimization based on spatial resolution considerations alone [as in Fig. 3(a)] is insufficient and may neglect the very parameters that are most significant. Using the analysis described herein for higher-resolution systems (e.g., direct-detection systems,⁴⁸⁻⁵² such as α -Se or PbI_2 , which typically lack a mechanism for presampling blur) should furthermore account for the effects of noise-power aliasing.

The results for M^* shown above are specific to the nominal conditions stated, but the methodology is sufficiently general to allow application to other systems. Particularly interesting would be analysis for systems that vary significantly from the above nominal specifications (which are appropriate for the case of FPI-CBCT). For example, (1) imagers for low-dose fluoroscopy (e.g., XRIIs or high-performance FPIs—typically lower-resolution, but offering low additive electronic noise and high DQE; trends herein suggest M^* comparable to or slightly greater than reported above); (2) FPIs and CCD-based imagers for radiotherapy (each of lower-resolution, but with the latter experiencing a secondary quantum sink at the optical coupling stage; trends herein suggest M^* larger than the above, consistent with the results of Bissonnette *et al.*⁴); and (3) systems for digital mammography (high-resolution, high DQE; analysis requires account of noise-power aliasing). Of course, mechanical/logistical/clinical considerations cannot be blindly sacrificed for the sake of optimal geometry, and certain clinical applications may simply not accommodate large air gaps (e.g., under-table radiography) or a contact image (e.g., CBCT). Furthermore, the field-of-view and imager area are obvious considerations in selecting S_{ID} . Still, in light of the ever-broadening spectrum of applications envisioned for FPIs—ranging from radiography and mammography, to C-arm systems, to CBCT, industrial radiography, and crystallography—it is only sensible to knowledgeably consider the numerous tradeoffs present in selection of imaging geometry.

ACKNOWLEDGMENTS

This work was supported in part by the Prostate Cancer Research Program Grant No. DAMD 17-98-1-8497.

APPENDIX: EFFECT OF X-RAY SCATTER ON DQE

We seek an expression for the spatial-frequency-dependent DQE that accounts for x-ray scatter, effectively combining the generalized scatter-reduction mechanism (e.g., gap or grid) with the imaging system. Cascaded systems analysis³⁶ provides a means of computing DQE by modeling the FPI as a series of amplification and spatial spreading stages³⁵ and has demonstrated reasonable agreement with empirical results^{7,37–39} for the scatter-free case. As detailed elsewhere,³⁹ the DQE may be defined as the ratio⁵³

$$\text{DQE}(u') = \frac{S_{\text{ideal}}(u')}{S_{\text{actual}}(u')} = \frac{\overline{g_1} \overline{g_2} \overline{g_4} T_3^2(u') T_5^2(u')}{[1 + \overline{g_4}(\overline{g_2} + \varepsilon_{g2}) T_3^2(u')] T_5^2(u') + S_{\text{add}}(u') / a_{\text{pd}}^4 \overline{q_0} \overline{g_1} \overline{g_2} \overline{g_4}} \quad (\text{A1c})$$

and

$$\text{NEQ}(u') = \overline{q_0} \text{DQE}(u'), \quad (\text{A1d})$$

where each parameter is defined in Table I and summarized below. The equations shown here neglect the effects of noise-power aliasing,^{54,55} but can be extended to include such in a straightforward manner;^{38,39} for indirect-detection FPIs, this effect is usually small. Furthermore, for simplicity, the pixel fill-factor is assumed equal to unity. Such is reasonable for large pixels (e.g., $a_{\text{pix}} > 200 \mu\text{m}$) or for advanced pixel designs.⁵⁶ Subunity fill-factor is known to degrade the DQE by reducing signal response and increasing noise-power aliasing.⁵⁴ The fundamental assumptions of cascaded systems analysis include linearity, stationarity, shift-invariance, and neglect of noise due to the polychromatic nature of the x-ray fluence—discussion of which is beyond the scope of this article.

The definition of DQE as the ratio of noise-power spectra is useful, because it highlights the fact that it is the stochastic components of the imaging chain that reduce DQE. To briefly summarize, $\overline{q_0}$ is the incident x-ray fluence; $\overline{g_1}$ is the quantum detection efficiency of the x-ray converter; $\overline{g_2}$ is the optical gain of the converter (photons emitted per interacting x-ray), and ε_{g2} is the Poisson excess in the optical gain; T_3 is the MTF of the x-ray converter; $\overline{g_4}$ is the optical coupling efficiency of the α -Si:H photodiodes; T_5 is the presampling MTF of the photodiode apertures, of width a_{pd} (equal to a_{pix} for unity fill-factor); and S_{add} is the NPS of the readout electronics. Each of these parameters is determined analytically or empirically, for example, using a common algorithm for computing x-ray spectra,⁴⁶ the known cross-sectional data of the converting material,⁵⁷ etc. For the MTF of the x-ray converter, T_3 was approximated by a Lorentzian fit to measured results.^{41,58–61}

$$T_3(u') = \frac{1}{1 + Hu'^2} \quad (\text{A2})$$

characterized by the screen blur, H . For extended S_{ID} , the spatial-frequency domain in the object plane, u' , scales as

of the noise-power spectrum (NPS) of an ideal, deterministic detector (i.e., a noiseless equivalent to the real system)

$$S_{\text{ideal}}(u') = a_{\text{pd}}^4 \overline{q_0} \overline{g_1}^2 \overline{g_2}^2 \overline{g_4}^2 T_3^2(u') T_5^2(u'), \quad (\text{A1a})$$

to that of the real system

$$S_{\text{actual}}(u') = a_{\text{pd}}^4 \overline{q_0} \overline{g_1} \overline{g_2} \overline{g_4} [1 + \overline{g_4}(\overline{g_2} + \varepsilon_{g2}) T_3^2(u')] T_5^2(u') + S_{\text{add}}(u'), \quad (\text{A1b})$$

yielding

u'/M . For the two nominal imager configurations considered in this article, an x-ray converter consisting of 133 mg/cm² Gd₂O₂S:Tb or 250 mg/cm² CsI:Tl is assumed. For the former, $\overline{g_1} = 0.56$; $\overline{g_2} = 1650$; $\varepsilon_{g2} = 625$; $H = 1.25$; and $\overline{g_4} = 0.75$. For the latter, $\overline{g_1} = 0.74$; $\overline{g_2} = 1750$; $\varepsilon_{g2} = 260$; $H = 0.69$; and $\overline{g_4} = 0.65$. Pixel presampling MTF is a sinc function, and electronic noise is taken as the sum in quadrature^{8,47} of TFT-thermal, photodiode shot, digitization, and amplifier noise—dominated by the last ($\sigma_{\text{amp}} = 3000 \text{ e}$, a conservative estimate^{47,62} comparable to typical reported values). All calculations were performed for a 120 kVp beam filtered by 3 mm Al and 20 cm H₂O.

This analysis can be extended to include the effects of x-ray scatter by considering the propagation of the primary, $\overline{q_0^P}$, and scatter, $\overline{q_0^S}$, fluence separately. We conceptualize a generalized scatter-reduction mechanism (e.g., an air gap) at stage 0 of the imaging chain and recompute the power spectra:

$$S_{\text{ideal}}(u') = a_{\text{pd}}^4 \overline{q_0^P} \overline{g_1}^2 \overline{g_2}^2 \overline{g_4}^2 T_3^2(u') T_5^2(u'), \quad (\text{A3a})$$

i.e., the “ideal” detector includes perfect scatter rejection, and

$$\begin{aligned} S_{\text{actual}}(u') &= S_{\text{primary}}(u') + S_{\text{scatter}}(u') + S_{\text{add}}(u') \\ &= a_{\text{pd}}^4 \overline{q_0^P} \overline{g_1} \overline{g_2} \overline{g_4} [1 + \overline{g_4}(\overline{g_2} + \varepsilon_{g2}) T_3^2(u')] \\ &\quad \times T_5^2(u') + a_{\text{pd}}^4 \overline{q_0^S} \overline{g_1} \overline{g_2} \overline{g_4} [1 + \overline{g_4}(\overline{g_2} + \varepsilon_{g2}) \\ &\quad \times T_3^2(u')] T_5^2(u') + S_{\text{add}}(u'), \end{aligned} \quad (\text{A3b})$$

where, for simplicity, we have used the same $\overline{g_1}$, $\overline{g_2}$, etc. in the S_{scatter} term as in the S_{primary} term, thus assuming that the shape of the spectrum for scattered x rays is comparable to that of the primary. A shift in the spectrum could be accommodated by taking the scattered x-ray spectrum and recomputing $\overline{g_1}$, $\overline{g_2}$, etc. for the S_{scatter} term; for present purposes, however, we assume that the spectral shift is small. The DQE then becomes

$$\text{DQE}(u') = \frac{\overline{g_1} \overline{g_2} \overline{g_4} T_3^2(u') T_5^2(u')}{(1 + \text{SPR}) [1 + \overline{g_4} (\overline{g_2} + \varepsilon_{g2}) T_3^2(u')] T_5^2(u') + S_{\text{add}}(u') / a_{\text{pd}}^4 \overline{q_0} \overline{g_1} \overline{g_2} \overline{g_4}} \quad (\text{A3c})$$

and

$$\text{NEQ}(u') = \overline{q_0^P} \text{DQE}(u') \quad (\text{A3d})$$

which, of course, are equivalent to Eqs. (A1) for the scatter-free case (i.e., $\overline{q_0} = \overline{q_0^P} + \overline{q_0^S} = \overline{q_0^P}$). Equation (A3c) is particularly interesting, since it conveys the fairly intuitive result that, for conditions under which the imager is input quantum limited, the DQE is reduced in proportion to $1/(1 + \text{SPR})$. This analytic form shows that x-ray scatter can be treated as an additive noise source—an “additive quantum noise” proportional to the SPR—that appears in the denominator of the DQE in a manner directly analogous to the additive electronics noise.

^aElectronic mail: jsiewerd@beaumont.edu

- ¹R. Fahrig, J. A. Rowlands, and M. J. Yaffe, “X-ray imaging with amorphous selenium: optimal spectra for digital mammography,” *Med. Phys.* **23**, 557–567 (1996).
- ²J. P. Bissonnette, I. A. Cunningham, and P. Munro, “Optimal phosphor thickness for portal imaging,” *Med. Phys.* **24**, 803–814 (1997).
- ³J. H. Siewerdsen and L. E. Antonuk, “DQE and system optimization for indirect-detection flat-panel imagers in diagnostic radiology,” *Proc. SPIE* **3336**, 546–554 (1998).
- ⁴J. P. Bissonnette, D. A. Jaffray, A. Fenster, and P. Munro, “Optimal radiographic magnification for portal imaging,” *Med. Phys.* **21**, 1435–1445 (1994).
- ⁵R. Ning, D. Lee, X. Wang, Y. Zhang, D. Conover, D. Zhang, and C. Williams, “Selenium flat panel detector-based volume tomographic angiography imaging: phantom studies,” *Proc. SPIE* **3336**, 316–324 (1998).
- ⁶R. Ning, X. Tang, R. Yu, D. Zhang, and D. Conover, “Flat panel detector-based cone beam volume CT imaging: detector evaluation,” *Proc. SPIE* **3659**, 192–203 (1999).
- ⁷J. H. Siewerdsen and D. A. Jaffray, “Cone-beam CT with a flat-panel imager: noise considerations for fully 3-D imaging,” *Proc. SPIE* **3336**, 546–554 (2000).
- ⁸J. H. Siewerdsen and D. A. Jaffray, “A ghost story: spatio-temporal response characteristics of an indirect-detection flat-panel imager,” *Med. Phys.* **26**, 1624–1641 (1999).
- ⁹J. H. Siewerdsen and D. A. Jaffray, “Cone-beam computed tomography with a flat-panel imager: effects of image lag,” *Med. Phys.* **26**, 2635–2647 (1999).
- ¹⁰D. A. Jaffray, J. H. Siewerdsen, and D. G. Drake, “Performance of a volumetric CT scanner based upon a flat-panel imaging array,” *Proc. SPIE* **3659**, 204–214 (1999).
- ¹¹D. A. Jaffray, J. H. Siewerdsen, and D. G. Drake, “Cone-beam computed tomography with a flat-panel imager: initial performance characterization,” *Med. Phys.* **27**, 1311–1323 (2000).
- ¹²International Commission on Radiation Units and Measurements Report No. 54, *Medical Imaging—the Assessment of Image Quality* (ICRU, Bethesda, MD, 1996).
- ¹³H. E. Johns and J. R. Cunningham, *The Physics of Radiology*, 4th ed. (Thomas, Springfield, IL, 1983).
- ¹⁴H. H. Barrett and W. Swindell, *Radiological Imaging: The Theory of Image Formation, Detection, and Processing, Volume I* (Academic, New York, 1981).
- ¹⁵J. M. Boone and J. A. Seibert, “An analytical model of the scattered radiation distribution in diagnostic radiology,” *Med. Phys.* **15**, 721–725 (1988).
- ¹⁶J. M. Boone and J. A. Seibert, “Monte Carlo simulation of the scattered

radiation distribution in diagnostic radiology,” *Med. Phys.* **15**, 713–720 (1988).

- ¹⁷M. Honda, K. Kikuchi, and K. Komatsu, “Method for estimating the intensity of scattered radiation using a scatter generation model,” *Med. Phys.* **18**, 219–226 (1991).
- ¹⁸U. Neitzel, “Grids or air gaps for scatter reduction in digital radiography: a model calculation,” *Med. Phys.* **19**, 475–481 (1992).
- ¹⁹M. Sandborg, D. R. Dance, G. A. Carlsson, and J. Persliden, “Monte Carlo study of grid performance in diagnostic radiology: factors which affect the selection of tube potential and grid ratio,” *Br. J. Radiol.* **66** (792), 1164–1176 (1993).
- ²⁰D. L. McDaniel, G. Cohen, L. K. Wagner, and L. H. Robinson, “Relative dose efficiencies of antiscatter grids and air gaps in pediatric radiography,” *Med. Phys.* **11**, 508–512 (1984).
- ²¹P. R. Maynard, “Space—the unknown accessory,” *Radiol. Technol.* **52** (6), 597–604 (1981).
- ²²J. Persliden and G. A. Carlsson, “Scatter rejection by air gaps in diagnostic radiology. Calculations using a Monte Carlo collision density method and consideration of molecular interference in coherent scattering,” *Phys. Med. Biol.* **42** (1), 155–175 (1997).
- ²³J. M. Boone, B. A. Arnold, and J. A. Seibert, “Characterization of the point spread function and modulation transfer function of scattered radiation using a digital imaging system,” *Med. Phys.* **13**, 254–256 (1986).
- ²⁴J. A. Seibert and J. M. Boone, “X-ray scatter removal by deconvolution,” *Med. Phys.* **15**, 567–575 (1988).
- ²⁵G. H. Glover, “Compton scatter effects in CT reconstructions,” *Med. Phys.* **9**, 860–867 (1982).
- ²⁶P. C. Johns and M. Yaffe, “Scattered radiation in fan beam imaging systems,” *Med. Phys.* **9**, 231–239 (1982).
- ²⁷P. M. Joseph and R. D. Spital, “The effects of scatter in x-ray computed tomography,” *Med. Phys.* **9**, 464–472 (1982).
- ²⁸J. Hsieh, “Image artifacts, causes, and corrections,” in *Medical CT and Ultrasound: Current Technology and Applications*, edited by L. W. Goldman and J. B. Fowlkes (Advanced Medical, Madison, WI, 1995).
- ²⁹R. F. Wagner, “Noise equivalent parameters in general medical radiography: the present picture and future pictures,” *Photograph. Sci. Eng.* **21**, 252–262 (1977).
- ³⁰J. W. Motz and C. E. Dick, “X-ray scatter background signals in transmission radiography,” *Med. Phys.* **2**, 259–267 (1975).
- ³¹C. E. Dick, C. G. Soares, and J. W. Motz, “X-ray scatter data for diagnostic radiology,” *Phys. Med. Biol.* **23**, 1076–1085 (1978).
- ³²W. Kalender, “Monte Carlo calculations of x-ray scatter data for diagnostic radiology,” *Phys. Med. Biol.* **26**, 835–849 (1981).
- ³³H. P. Chan and K. Doi, “Physical characteristics of scattered radiation in diagnostic radiology: Monte Carlo studies,” *Med. Phys.* **12**, 152–165 (1985).
- ³⁴L. T. Niklason, J. A. Sorenson, and J. A. Nelson, “Scattered radiation in chest radiography,” *Med. Phys.* **8**, 677–681 (1981).
- ³⁵M. Rabbani, R. Shaw, and R. Van Metter, “Detective quantum efficiency of imaging systems with amplifying and scattering mechanisms,” *J. Opt. Soc. Am. A* **4** (5), 895–901 (1987).
- ³⁶I. A. Cunningham, M. S. Westmore, and A. Fenster, “A spatial-frequency dependent quantum accounting diagram and detective quantum efficiency model of signal and noise propagation in cascaded imaging systems,” *Med. Phys.* **21**, 417–427 (1994).
- ³⁷J. H. Siewerdsen, L. E. Antonuk, Y. El-Mohri, J. Yorkston, W. Huang, J. M. Boudry, and I. A. Cunningham, “Empirical and theoretical investigation of the noise performance of indirect detection, active matrix flat-panel imagers (AMFPIs) for diagnostic radiology,” *Med. Phys.* **24**, 71–89 (1997).
- ³⁸J. H. Siewerdsen, L. E. Antonuk, Y. El-Mohri, J. Yorkston, W. Huang, and I. A. Cunningham, “Signal, noise power spectrum, and detective quantum efficiency of indirect-detection flat-panel imagers for diagnostic radiology,” *Med. Phys.* **25**, 614–628 (1998).
- ³⁹J. H. Siewerdsen, *Signal, Noise, and Detective Quantum Efficiency of*

- a-Si:H Flat-Panel Imagers*, Ph.D. thesis (Bell and Howell Publishing, Ann Arbor, MI, 1998).
- ⁴⁰ R. K. Swank, "Absorption and noise in x-ray phosphors," *J. Appl. Phys.* **44** (9), 4199–4203 (1973).
 - ⁴¹ MTF data for Lanex screens provided by P. C. Bunch, Ph.D., Eastman Kodak Co., Rochester, NY (private communication).
 - ⁴² J. Yorkston, L. E. Antonuk, N. Seraji, W. Huang, J. Siewerdsen, and Y. El-Mohri, "Evaluation of the MTF for *a-Si:H* imaging arrays," *Proc. SPIE* **2163**, 141–148 (1994).
 - ⁴³ J. Yorkston, L. E. Antonuk, Y. El-Mohri, K. W. Jee, W. Huang, M. Maolinbay, X. Rong, and J. H. Siewerdsen, "Improved spatial resolution in flat-panel imaging systems," *Proc. SPIE* **3336**, 556–563 (1998).
 - ⁴⁴ D. G. Drake, D. A. Jaffray, and J. W. Wong, "A prototype amorphous silicon array based radiotherapy portal imager," *Proc. SPIE* **3032**, 32–41 (1997).
 - ⁴⁵ L. E. Antonuk, Y. El-Mohri, W. Huang, K. W. Jee, J. H. Siewerdsen, M. Maolinbay, V. E. Scarpine, H. Sandler, and J. Yorkston, "Initial performance evaluation of an indirect-detection, active matrix flat-panel imager (AMFPI) prototype for megavoltage imaging," *Int. J. Radiat. Oncol., Biol., Phys.* **42** (2), 437–452 (1998).
 - ⁴⁶ D. M. Tucker, G. T. Barnes, and D. P. Chakraborty, "Semiempirical model for generating tungsten target x-ray spectra," *Med. Phys.* **18**, 211–218 (1991).
 - ⁴⁷ L. E. Antonuk, K. W. Jee, Y. El-Mohri, M. Maolinbay, S. Nassif, X. Rong, Q. Zhao, J. H. Siewerdsen, R. A. Street, and K. S. Shah, "Strategies to improve the signal and noise performance of active matrix, flat-panel imagers for diagnostic x-ray applications," *Med. Phys.* **27**, 289–306 (2000).
 - ⁴⁸ W. Zhao and J. A. Rowlands, "X-ray imaging using amorphous selenium: feasibility of a flat panel self-scanned detector for digital radiology," *Med. Phys.* **22**, 1595–1604 (1995).
 - ⁴⁹ D. L. Lee, L. K. Cheung, B. Rodricks, and G. F. Powell, "Improved imaging performance of a 14×17-inch direct radiography system using Se/TFT detector," *Proc. SPIE* **3336**, 14–23 (1998).
 - ⁵⁰ B. Polischuk, Z. Shukri, A. Legros, and H. Rougeot, "Selenium direct converter structure for static and dynamic x-ray detection in medical imaging applications," *Proc. SPIE* **3336**, 494–504 (1998).
 - ⁵¹ R. A. Street, J. T. Rahn, S. E. Ready, K. Shah, P. R. Bennett, Y. Dmi-
triyev, P. Mei, J. P. Lu, R. B. Apte, J. Ho, K. van Schuylenbergh, F. Lemmi, J. B. Boyce, and P. Nylen, "X-ray imaging using lead iodide as a semiconductor detector," *Proc. SPIE* **3659**, 36–47 (1999).
 - ⁵² K. S. Shah, P. Bennett, M. Klugerman, L. P. Moy, and G. Entine, "Lead iodide films for x-ray imaging," *Proc. SPIE* **3032**, 395–404 (1997).
 - ⁵³ I. A. Cunningham, "Analyzing system performance," in *The Expanding Role of Medical Physics in Diagnostic Imaging*, edited by G. D. Frey and P. Sprawls (Advanced Medical, Madison, WI, 1997), pp. 231–263.
 - ⁵⁴ I. A. Cunningham, "Degradation of the detective quantum efficiency due to a non-unity fill factor," *Proc. SPIE* **3032**, 22–31 (1997).
 - ⁵⁵ J. P. Moy, "Image quality of scintillator based x-ray electronic imagers," *Proc. SPIE* **3336**, 187–194 (1998).
 - ⁵⁶ J. T. Rahn, R. Lemmi, R. L. Weisfield, R. Lujan, P. Mei, J. P. Lu, J. Ho, S. E. Ready, R. E. Apte, P. Nylen, J. Boyce, and R. A. Street, "High resolution, high fill factor *a-Si:H* sensor arrays for medical imaging," *Proc. SPIE* **3659**, 510–517 (1999).
 - ⁵⁷ E. Storm and H. I. Israel, "Photon cross sections from 1 keV to 100 MeV for elements $Z=1$ to $Z=100$," *Nucl. Data Tables*, **A7**, 565–681 (1970).
 - ⁵⁸ U. Schiebel, N. Conrads, N. Jung, M. Weibrecht, H. Wiczorek, T. Zaengel, M. J. Powell, I. D. French, and C. Glasse, "Fluoroscopic x-ray imaging with amorphous silicon thin-film arrays," *Proc. SPIE* **2163**, 129–140 (1994).
 - ⁵⁹ H. Roehrig, L. L. Fajardo, T. Yu, and W. S. Schempp, "Signal, noise and detective quantum efficiency in CCD based x-ray imaging systems for use in mammography," *Proc. SPIE* **2163**, 320–332 (1994).
 - ⁶⁰ T. Graeve, Y. Li, A. Fabians, and W. Huang, "High-resolution amorphous silicon image sensor," *Proc. SPIE* **2708**, 494–498 (1996).
 - ⁶¹ J. Chabbal, C. Chaussat, T. Ducourant, L. Fritsch, J. Michailos, V. Spinner, G. Vieux, M. Arques, G. Hahm, M. Hoheisel, H. Horbachek, R. Schulz, and M. Spahn, "Amorphous silicon x-ray image sensor," *Proc. SPIE* **2708**, 499–510 (1996).
 - ⁶² T. J. C. Bruijns, P. L. Alving, E. L. Baker, R. Bury, A. R. Cowen, N. Jung, H. A. Luijendijk, H. J. Meulenbrugge, and H. J. Stouten, "Technical and clinical results of an experimental flat dynamic (digital) x-ray image detector (FDXD) system with real-time corrections," *Proc. SPIE* **3336**, 33–44 (1998).

**Appendix F: Cone-beam Computed Tomography with a Flat-panel
Imager: Magnitude and Effects of X-ray Scatter**

Cone-beam computed tomography with a flat-panel imager: Magnitude and effects of x-ray scatter

Jeffrey H. Siewerdsen^{a)} and David A. Jaffray

Department of Radiation Oncology, William Beaumont Hospital, Royal Oak, Michigan 48073

(Received 7 July 2000; accepted for publication 6 November 2000)

A system for cone-beam computed tomography (CBCT) based on a flat-panel imager (FPI) is used to examine the magnitude and effects of x-ray scatter in FPI-CBCT volume reconstructions. The system is being developed for application in image-guided therapies and has previously demonstrated spatial resolution and soft-tissue visibility comparable or superior to a conventional CT scanner under conditions of low x-ray scatter. For larger objects consistent with imaging of human anatomy (e.g., the pelvis) and for increased cone angle (i.e., larger volumetric reconstructions), however, the effects of x-ray scatter become significant. The magnitude of x-ray scatter with which the FPI-CBCT system must contend is quantified in terms of the scatter-to-primary energy fluence ratio (SPR) and scatter intensity profiles in the detector plane, each measured as a function of object size and cone angle. For large objects and cone angles (e.g., a pelvis imaged with a cone angle of 6°), SPR in excess of 100% is observed. Associated with such levels of x-ray scatter are cup and streak artifacts as well as reduced accuracy in reconstruction values, quantified herein across a range of SPR consistent with the clinical setting. The effect of x-ray scatter on the contrast, noise, and contrast-to-noise ratio (CNR) in FPI-CBCT reconstructions was measured as a function of SPR and compared to predictions of a simple analytical model. The results quantify the degree to which elevated SPR degrades the CNR. For example, FPI-CBCT images of a breast-equivalent insert in water were degraded in CNR by nearly a factor of 2 for SPR ranging from $\sim 2\%$ to 120%. The analytical model for CNR provides a quantitative understanding of the relationship between CNR, dose, and spatial resolution and allows knowledgeable selection of the acquisition and reconstruction parameters that, for a given SPR, are required to restore the CNR to values achieved under conditions of low x-ray scatter. For example, for SPR=100%, the CNR in FPI-CBCT images can be fully restored by: (1) increasing the dose by a factor of 4 (at full spatial resolution); (2) increasing dose and slice thickness by a factor of 2; or (3) increasing slice thickness by a factor of 4 (with no increase in dose). Other reconstruction parameters, such as transaxial resolution length and reconstruction filter, can be similarly adjusted to achieve CNR equal to that obtained in the scatter-free case. © 2001 American Association of Physicists in Medicine. [DOI: 10.1118/1.1339879]

Key words: flat-panel imager, cone-beam computed tomography, x-ray scatter, scatter-to-primary ratio, artifacts, contrast, noise, contrast-to-noise ratio

I. INTRODUCTION

The combination of active matrix flat-panel imagers (FPIs) and cone-beam computed tomography (CBCT) represents a promising technology for volumetric imaging,¹⁻⁸ capitalizing on continuing advances in FPI technology and cone-beam reconstruction techniques. FPIs provide efficient, distortionless, real-time detectors that are experiencing widespread proliferation in x-ray projection imaging, and cone-beam reconstruction⁹⁻¹² techniques have been accelerated from hours to seconds through the development of dedicated hardware. Capable of acquiring volumetric (i.e., multi-slice) images in an open geometry, from a single rotation about the patient, and without the need for a ring-based gantry or a mechanism for translating the patient, FPI-CBCT provides separation of the imaging system and patient support. These aspects appear particularly advantageous for image-guided therapies, such as radiation therapy, brachytherapy, and surgery, where the logistics of the treatment procedure largely dictate the geometry. Furthermore, such systems could pro-

vide the therapist with combined radiographic, fluoroscopic, and tomographic imaging. As described previously,^{1,13} an FPI-CBCT system is being developed for online tomographic guidance of radiation therapy procedures by incorporating a kilovoltage x-ray tube and an FPI on the gantry of a medical linear accelerator. This system is expected to provide soft-tissue visibility and spatial resolution sufficient for correction of patient setup errors and interfraction organ motion.^{1,13}

The FPI-CBCT system under development has demonstrated reasonable volumetric uniformity, noise, and spatial resolution characteristics, providing soft-tissue visibility comparable to that achieved with a conventional CT scanner.¹ Application of this technology, however, is not without its challenging aspects, including the effects of detector performance, image lag, and x-ray scatter. Analysis of FPI signal and noise performance^{1,5} suggests that in order to provide high-quality projections at very low exposures (e.g., on the order of a μR to the detector for lateral projections of

a large pelvis), high-performance FPIs are required (e.g., incorporating a CsI:Tl x-ray converter and low-noise amplifiers). Analysis of the magnitude³ and effects⁴ of image lag in FPI-CBCT suggests that image lag can result in subtle artifacts in regions of high-contrast objects at high exposures, and that such effects can be largely eliminated through simple procedural and/or algorithmic methods. This article is concerned with the magnitude and effects of x-ray scatter in flat-panel cone-beam CT and seeks to identify strategies for management of deleterious scatter effects.

Investigations of x-ray scatter in fan-beam CT have demonstrated experimentally and analytically that scatter results in artifacts (e.g., cup and streak artifacts) and quantitative inaccuracy in reconstructed CT number (CT#).^{14–16} Analytical and Monte Carlo methods have been employed to estimate the intensity of scattered radiation at diagnostic energies,^{17–21} demonstrating reasonable agreement with measured results. Based on the magnitude and shape of such intensity distributions, correction algorithms^{22,23} have been developed that largely remove scatter artifacts and restore CT# accuracy. Such methods are standard components of modern fan-beam CT systems. In cone-beam CT, the problem of x-ray scatter is expected to be significantly greater, due to the use of a large cone angle and 2D detector. A significant degree of scatter rejection can be achieved using conventional grids and focused collimators;²⁴ however, it is uncertain whether such strategies provide an advantage compared to a knowledgeably selected air gap.^{6,25} For digital imagers, Netizel²⁵ concluded that air gaps and grids perform comparably under high-scatter conditions, and for low-scatter conditions an air gap is clearly superior; moreover, the advantages of a gap are even stronger if the application, such as FPI-CBCT, can logistically accommodate large air gaps.

This article reports on the magnitude of x-ray scatter expected in the clinical environment and quantifies the effects on image artifacts, CT# inaccuracy, contrast, noise, and contrast-to-noise ratio (CNR) in FPI-CBCT reconstructions. Finally, the degree to which CNR can be restored to levels achieved under conditions of low x-ray scatter is examined using simple analytical forms for CT contrast¹⁴ and noise.²⁶

II. METHODS AND MATERIALS

A. Experimental setup

The magnitude and effects of x-ray scatter in flat-panel cone-beam CT were measured using the experimental setup illustrated in Fig. 1. The imaging geometry [i.e., source-to-axis distance (y_{AOR}), source-to-detector distance (y_{FPI}), and axis-to-detector distance (y_{ADD})] mimics that of a system for online tomographic guidance of radiotherapy procedures^{1,13} and, for conditions of high x-ray scatter, is close to the optimal configuration,⁶ considering the effects of geometric sharpness, imaging task, scatter rejection, and detector performance. As detailed elsewhere,^{1,3} the three main components of the system are an x-ray tube, a rotating object, and an FPI. For rectangular collimation and field of view, the angle subtended by the primary x-ray beam in the lateral (x)

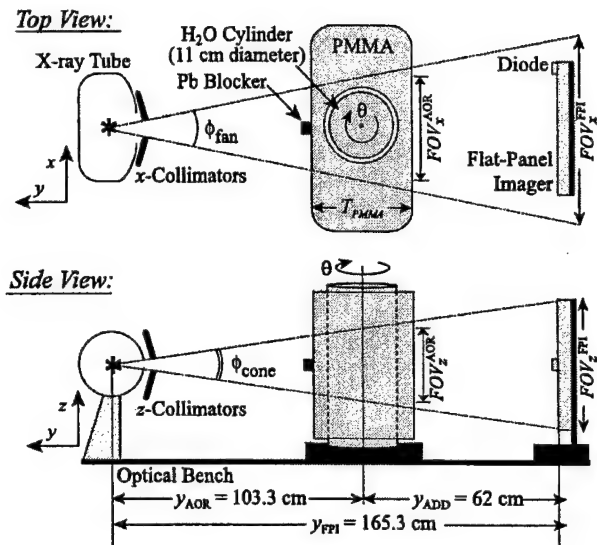


FIG. 1. Schematic illustration of the experimental setup used to measure the magnitude and effects of x-ray scatter in flat-panel cone-beam CT. The x-ray tube, rotating object, and FPI operate synchronously to acquire projection data for cone-beam reconstruction. The magnitude of x-ray scatter was varied through adjustment of the fan angle (ϕ_{fan}), the cone angle (ϕ_{cone}), and the thickness of PMMA (T_{PMMA}) surrounding a rotating water-filled cylinder. The Pb blocker was used for measurement of the SPR at the detector plane.

direction is the fan angle, ϕ_{fan} , and determines the lateral field of view, FOV_x^{AOR} and FOV_x^{FPI} at the axis and detector planes, respectively:

$$\phi_{fan} = 2 \tan^{-1} \left(\frac{FOV_x^{AOR}}{2y_{AOR}} \right) = 2 \tan^{-1} \left(\frac{FOV_x^{FPI}}{2y_{FPI}} \right). \quad (1a)$$

Similarly, the angle subtended by the beam in the longitudinal (z) direction is the cone angle, ϕ_{cone} :

$$\phi_{cone} = 2 \tan^{-1} \left(\frac{FOV_z^{AOR}}{2y_{AOR}} \right) = 2 \tan^{-1} \left(\frac{FOV_z^{FPI}}{2y_{FPI}} \right), \quad (1b)$$

where FOV_z^{AOR} and FOV_z^{FPI} are the z-extent of the primary radiation beam at the axis of rotation (AOR) and at the FPI, respectively. The x-ray tube was a General Electric (Milwaukee, WI) Maxiray 75 operated at 120 kVp (measured) with 0.5-mm Cu added filtration. Exposure was measured using an RTI Electronics (Molndal, Sweden) PMX-III multimeter and is reported either in terms of the exposure in air at isocenter, X_{iso} , or at the center of the FPI, X_{FPI} . A typical FPI-CBCT acquisition involved 300 projections at 1 mAs per projection (at which the FPI exhibits linear response and is strongly input-quantum-limited³), giving a total scan exposure in air of $X_{iso} \sim 4.6 \times 10^{-4}$ C/kg (~ 1.8 R). The exposure per projection at the center of the FPI ranged from $X_{FPI} \sim (1.3-7.7) \times 10^{-8}$ C/kg (i.e., $\sim 50-300$ μ R, corresponding to $\sim 0.5\%-3\%$ of sensor saturation,³ depending on object thickness).

A simple phantom was constructed to allow volumetric imaging under conditions of variable x-ray scatter. The essential requirements in the phantom design included: (1) al-

lowance of FPI-CBCT imaging without lateral truncation of the projection data; (2) composition approximating water; and (3) variation in phantom thickness across a range similar to that of human anatomy. As illustrated in Fig. 1, the phantom consisted of a water-filled cylinder (11 cm diameter) surrounded by slabs of polymethyl methacrylate (PMMA). Note that only the cylinder rotated during FPI-CBCT acquisition, and the PMMA slabs (supported on a platform above the rotation stage) were stationary and did not impinge on the volume of reconstruction. Thus reconstructed images show only the water-filled cylinder and not the surrounding PMMA. The magnitude of x-ray scatter at the detector plane was varied by adjusting the fan angle (two settings, $\phi_{\text{fan}} = 14^\circ$ and 22° ; see below), the cone angle (varied continuously), and/or the thickness of PMMA, T_{PMMA} (across a range corresponding to the AAPM standard phantoms for measurement of entrance exposure²⁷). In order to examine the effects of x-ray scatter alone, without the confounding influence of beam-hardening²³ that results from variation in T_{PMMA} , FPI-CBCT reconstructions are shown for cases in which ϕ_{cone} alone was varied (with ϕ_{fan} and T_{PMMA} fixed).

The FPI was the same as that used in previous studies of FPI-CBCT performance,¹⁻⁴ manufactured by PerkinElmer Optoelectronics and based on a 512×512 matrix of α -Si:H photodiodes and thin-film transistors (TFTs) at $400\text{-}\mu\text{m}$ pixel pitch. The FPI incorporates a 133-mg/cm^2 $\text{Gd}_2\text{O}_2\text{S:Tb}$ x-ray converting screen and can be addressed at up to five frames per second (fps) at 16-bit precision. FPI-CBCT acquisition involved a repeated, synchronized sequence of: (1) delivery of a radiographic exposure; (2) reading of the FPI projection image; and (3) incremental rotation of the object. For all scans, 300 projections were acquired, with incremental rotation of the object by 1.2° through 360° and with the FPI offset from a symmetrical position by $1/4$ the detector element spacing.²⁸ Since the FPI was operated at a fairly low frame rate of 0.625 fps, a complete scan took 8 min. Cone-beam reconstructions [$512 \times 512 \times (1-512)$ voxels] were performed using a modified FDK algorithm⁹ for filtered back-projection on a Sun (Fremont, CA) UltraSparc workstation.

The range in selected fan angle, cone angle, and object thickness correspond to conditions expected in the clinical setting. The FPI described above is too small ($20.5 \times 20.5\text{ cm}^2$) for volumetric imaging of large anatomy in this geometry; therefore, a larger FPI²⁹ ($41 \times 41\text{ cm}^2$ active area, not tiled) forms the basis of the clinical prototype that is being implemented on a medical linear accelerator in either of two geometries: (1) a "centered" geometry (illustrated in Fig. 1); and (2) an "offset" geometry in which the detector is offset from the central axis by up to half the FPI width.³⁰ With the larger FPI, the centered geometry allows imaging of objects with a maximum width of $\sim 25.5\text{ cm}$ ($\phi_{\text{fan}} \sim 14^\circ$) without truncation of the projection data—sufficient for imaging of head, neck, and extremity sites. Imaging of larger anatomy (e.g., a pelvis with lateral extent up to $\sim 40\text{ cm}$) is accomplished using the offset geometry with approximately the same fan angle. Imaging of such large anatomy without truncation in a centered geometry would require a detector width of $\sim 64\text{ cm}$ ($\phi_{\text{fan}} \sim 22^\circ$). Measurements were performed us-

ing both $\phi_{\text{fan}} = 14^\circ$ and 22° , with results shown for the former unless otherwise stated. The cone angle was varied from $\phi_{\text{cone}} \sim 0.5^\circ$ (corresponding to $\text{FOV}_z^{\text{AOR}} = 0.9\text{ cm}$ and $\text{FOV}_z^{\text{FPI}} = 1.4\text{ cm}$, i.e., ~ 35 slices in a full-resolution reconstruction) to $\phi_{\text{cone}} \sim 10.5^\circ$ (corresponding to $\text{FOV}_z^{\text{AOR}} = 19\text{ cm}$ and $\text{FOV}_z^{\text{FPI}} = 30\text{ cm}$, i.e., ~ 750 slices).

B. Magnitude of x-ray scatter

The SPR at the detector plane was measured in a manner similar to that of Johns and Yaffe.¹⁴ As shown in Fig. 1, a Pb blocker ($\sim 9\text{-mm}$ -diam disk, $\sim 10\text{ mm}$ thick) was placed at the entrance of the phantom on the central axis of the beam. For each measurement of SPR, ten projections were acquired with the FPI, five with the blocker in place and five with the blocker removed. The ensemble of pixel values in the shadow of the blocker from the former five gave the "scatter only" signal, and that in the latter five gave the "scatter + primary" signal. The pixel dark values (i.e., the "offsets") were subtracted from each image, and tube output fluctuations were corrected by normalizing each image according to the measured exposure. The SPR was obtained by dividing the "scatter only" signal by the difference between the "scatter only" and "scatter + primary" signal. Off-focal radiation¹⁴ was assumed negligible, and the energy response of the FPI (i.e., the signal per incident fluence) was assumed equivalent for the primary and scattered x-ray spectra. Measurements of SPR were performed using Pb blockers ranging in diameter from ~ 5 to 15 mm in order to determine the correction factor associated with nonzero disk size. The factor was determined from a linear fit to the results (SPR versus disk diameter) extrapolated to zero disk size. For example, for a medium-sized phantom (15-cm PMMA) the correction factor was ~ 1.017 for the nominal 9-mm disk (i.e., SPR values reported were increased by $\sim 1.7\%$ from the measured values).

Measurements were first performed in order to benchmark the observed SPR to values corresponding approximately to human anatomy. For these measurements, the water-filled cylinder was removed, and the PMMA slabs were placed in simple rectangular arrangements approximating the AAPM standard phantoms²⁷ for exposure measurement of various anatomical sites (e.g., $\sim 5\text{-cm}$ PMMA for "extremity," $\sim 10\text{ cm}$ for "chest," $\sim 18\text{ cm}$ for "abdomen," and $\sim 30\text{ cm}$ referred to herein as "pelvis"). Only in these measurements was the phantom intended to approximately represent human anatomy. The SPR was also measured for each configuration of ϕ_{fan} , ϕ_{cone} , and T_{PMMA} used in measurements (viz., scatter fluence distributions, artifacts, contrast, and noise; see below) in which PMMA slabs surrounded the water-filled cylinder as in Fig. 1. In those measurements, the PMMA does not necessarily represent human anatomy (e.g., in the case of the water-filled cylinder flanked by sidelobes of PMMA); rather, the PMMA thickness was merely one means of continuously varying the SPR at the detector.

A second type of measurement was performed to determine the spatial distribution of x-ray scatter in the detector plane, again using the geometry of Fig. 1. First, a series of 20

“low scatter” projection images of the cylinder were acquired under conditions that minimized SPR [i.e., small fan angle, cone angle $\sim 0.5^\circ$, and $T_{\text{PMMA}} = 0$ cm, for which $\text{SPR} = (2.10 \pm 0.27)\%$]. Then, without moving the cylinder, projection images were acquired as a function of SPR by increasing ϕ_{fan} , ϕ_{cone} , and T_{PMMA} . Each series of 20 images was averaged, corrected for offset variations, and normalized to a constant value in the unattenuated beam. The spatial distribution of x-ray scatter energy fluence in the detector plane was computed from the difference between the images acquired as a function of SPR and the image acquired under “low-scatter” conditions. Knowledge of the magnitude and shape of such x-ray scatter distributions is an important component of scatter correction algorithms, which are the subject of on-going investigation.

C. Shading artifacts and CT number inaccuracy

Two types of shading artifact²³ were measured in transaxial slices of FPI-CBCT images: (1) the artifact in which voxel values in the image of a uniform water cylinder are reduced and nonuniform, forming a “cup”; and (2) the artifact in which the voxel values between two dense objects are reduced, forming a “streak.” For the former, images of the water-filled cylinder were acquired as a function of ϕ_{cone} and T_{PMMA} . To quantify the inaccuracy of voxel values, the mean value $\langle \mu \rangle$ in the water-filled interior of the cylinder was compared to the attenuation coefficient for water ($\mu_{\text{H}_2\text{O}} = 0.020 \text{ mm}^{-1}$, computed from the energy-dependent attenuation coefficient³¹ and the x-ray spectrum of the primary beam³²), yielding the inaccuracy:

$$\Delta = 100 \times \frac{\langle \mu \rangle - \mu_{\text{H}_2\text{O}}}{\mu_{\text{H}_2\text{O}}} \quad (2a)$$

To quantify the degree of spatial nonuniformity, voxel values near the center of the reconstruction, μ_{center} , were compared to those at ~ 5 mm inside the edge of the cylinder, μ_{edge} , giving the degree of “cupping:”

$$t_{\text{cup}} = 100 \times \frac{\mu_{\text{edge}} - \mu_{\text{center}}}{\mu_{\text{edge}}} \quad (2b)$$

The streak artifact was measured using two 2.8-cm-diam “bone” inserts placed within the water cylinder [SB3 cortical bone from the Gammex RMI (Middleton, WI) electron density phantom, with specified electron density, ρ_e , of 1.707 times that of water, physical density, ρ , of 1.84 g/cm^3 , and approximate CT# of 1367.8]. Although the small scale of the phantom prohibits direct interpretation of the results with respect to large human anatomy (e.g., concerning the cup artifact in a transaxial image of a pelvis, or the streak artifact between femoral heads), it does provide qualitative visualization of the magnitude of such artifacts as a function of SPR across a range that is representative of that anticipated in the clinical setting.

D. Effect of x-ray scatter on contrast

The effect of x-ray scatter on object contrast was investigated using a “breast-equivalent” insert placed within the water cylinder [BR SR1 breast from the Gammex RMI electron density phantom, with specified ρ_e , of 0.980 times that of water, ρ of 0.99 g/cm^3 , and approximate CT# of -46.7]. Contrast is defined as the difference between the ensemble average of voxel values in an insert compared to that in water (adjacent to and at the same radius as the insert) and was measured as a function of SPR. FPI-CBCT images of the contrast phantom were acquired as a function of SPR through variation of ϕ_{cone} and T_{PMMA} , and the resulting degradation in contrast was compared to the following analytical description.

Following Johns and Yaffe,¹⁴ we consider the primary and scatter fluence (P and S , respectively) behind a uniform cylinder of diameter d and attenuation coefficient μ_1 . In the unattenuated beam, the primary and scatter fluence are P_0 and S_0 , respectively, giving for the measured value $\hat{\mu}_1$:

$$\hat{\mu}_1 d = \ln\left(\frac{P_0}{P}\right) + \ln\left(\frac{1 + S_0/P_0}{1 + S/P}\right) \quad (3a)$$

Therefore,

$$\begin{aligned} \hat{\mu}_1 &= \frac{1}{d} \left[\ln\left(\frac{P_0}{P}\right) + \ln\left(\frac{1 + S_0/P_0}{1 + S/P}\right) \right] \\ &= \mu_1 + \frac{1}{d} \ln\left(\frac{1 + S_0/P_0}{1 + S/P}\right) \end{aligned} \quad (3b)$$

Since the second term is negative, scatter causes voxel values in the reconstruction to be lower than the true attenuation coefficient. We now consider a second object of diameter d_2 and attenuation coefficient μ_2 that is contained within the first (e.g., as the breast-equivalent insert is contained in the water cylinder). We take α to be the relative size of the second object, such that $d_2 = \alpha d$, and define δ to be the true difference in attenuation coefficients. With $\hat{\mu}_1$ and $\hat{\mu}_2$ representing measured values of μ_1 and μ_2 , respectively, and considering the diameter, d , such that $d = d_1 + d_2$ and $d_1 = (1 - \alpha)d$, we have:

$$\begin{aligned} \hat{\mu}_1 d_1 + \hat{\mu}_2 d_2 &= \ln\left(\frac{P_0}{P e^{\delta \alpha d}}\right) + \ln\left(\frac{1 + S_0/P_0}{1 + S/P e^{\delta \alpha d}}\right), \\ \hat{\mu}_1 (1 - \alpha)d + \hat{\mu}_2 \alpha d &= \ln\left(\frac{P_0}{P e^{\delta \alpha d}}\right) + \ln\left(\frac{1 + S_0/P_0}{1 + S/P e^{\delta \alpha d}}\right), \\ \alpha(\hat{\mu}_1 - \hat{\mu}_2) &= \hat{\mu}_1 - \frac{1}{d} \left[\ln\left(\frac{P_0}{P e^{\delta \alpha d}}\right) + \ln\left(\frac{1 + S_0/P_0}{1 + S/P e^{\delta \alpha d}}\right) \right], \\ \hat{\mu}_1 - \hat{\mu}_2 &= \frac{\hat{\mu}_1}{\alpha} - \frac{1}{\alpha d} \left[\ln\left(\frac{P_0}{P e^{\delta \alpha d}}\right) + \ln\left(\frac{1 + S_0/P_0}{1 + S/P e^{\delta \alpha d}}\right) \right], \end{aligned} \quad (3c)$$

which is the measured contrast, \hat{C} . Combining Eqs. (3b) and (3c) gives:

$$\begin{aligned}
\hat{C} &= \hat{\mu}_1 - \hat{\mu}_2, \\
&= \frac{1}{\alpha d} \left[\ln \left(\frac{P_0}{P} \right) + \ln \left(\frac{1 + S_0/P_0}{1 + S/P} \right) \right] - \frac{1}{\alpha d} \left[\ln \left(\frac{P_0}{P e^{\delta \alpha d}} \right) \right. \\
&\quad \left. + \ln \left(\frac{1 + S_0/P_0}{1 + S/P e^{\delta \alpha d}} \right) \right], \\
&= \frac{1}{\alpha d} \left[\ln \left(\frac{P_0}{P} \frac{P e^{\delta \alpha d}}{P_0} \right) + \ln \left(\frac{1 + S_0/P_0}{1 + S/P} \frac{1 + S/P e^{\delta \alpha d}}{1 + S_0/P_0} \right) \right], \\
&= \delta + \frac{1}{\alpha d} \ln \left(\frac{1 + S/P e^{\delta \alpha d}}{1 + S/P} \right). \quad (3d)
\end{aligned}$$

The measured contrast, \hat{C} , differs from the actual difference in linear attenuation coefficients, δ , by a term related to the SPR, and since the absolute magnitude of this term increases with SPR, the result is degradation in contrast. For example, considering $\mu_2 < \mu_1$ (i.e., the second object is "dark"), then δ is positive and the second term is negative; therefore, contrast is reduced. Similarly, taking $\mu_2 > \mu_1$ (i.e., the second object is "white"), then δ is negative and the second term is positive; therefore, the absolute value of the contrast is reduced. This simple analytical description is valid only for conditions where the two objects vary in linear attenuation coefficient by a small perturbation. The analytical form is nondivergent for $\alpha > 0$, and the range in δ and α for which the equation holds is set by the assumption that the presence of the second object significantly influences neither the measurement of $\hat{\mu}_1$ nor the SPR.

E. Effect of x-ray scatter on voxel noise

The noise in FPI-CBCT images was measured as a function of exposure and voxel size and compared to the analytical form derived by Barrett, Gordon, and Hershel.²⁶ Voxel noise, σ_{vox} , was determined as described previously¹ from the average of the standard deviations in circular realizations taken from transaxial slices in water (40 circular realizations at radii of 2–3 cm from the center of reconstruction). The effect of exposure was determined by measuring σ_{vox} for FPI-CBCT scans with total exposure in air ranging from $X_{\text{iso}} \sim (1.3\text{--}11.3) \times 10^{-4}$ C/kg (i.e., $\sim 0.5\text{--}4.4$ R). The voxel noise in FPI-CBCT reconstructions has been shown previously to decrease in proportion to the inverse-square-root of exposure^{1,5} in agreement with the analytical description of Barrett, Gordon, and Hershel:²⁶

$$\frac{\sigma_{\text{vox}}^2}{\mu^2} = \frac{k E_x f_c e^{\mu d/2} I}{\rho \mu h \eta D_{\text{center}} a_{\text{res}}^3}, \quad (4)$$

where E_x is the x-ray energy (taken as the mean energy of the spectrum,³² 60 keV), f_c is a Compton factor (equal to the ratio of linear and energy attenuation coefficients), μ is the average linear attenuation coefficient, d is the diameter of the cylinder, ρ is the density of water, η is the efficiency of detection (taken as the measured low-frequency detective quantum efficiency,^{1,5,6} 0.40), h is the slice thickness, a_{res} is the transaxial resolution length, D_{center} is the dose to the center of the phantom (cGy), and k is a constant for proper units.

The factor I is related to the integral in the spatial-frequency domain of the ramp function and reconstruction filter (both squared),²⁶ similar to the information bandwidth integral of Wagner, Brown, and Pastel.³³ For full-resolution reconstruction (i.e., 0.25-mm cubic voxels), the slice thickness and resolution length were taken equal to the measured FWHM of the point-spread function,¹ 0.5 mm. To examine the effect of spatial resolution on voxel noise, the resolution length in the z -dimension (a_z) was varied from $a_z = 0.5\text{--}3$ mm, while the transaxial resolution length (a_x and a_y) was held constant at 0.5 mm. This examines one method (namely, slice averaging) by which reducing spatial resolution can reduce noise, neglecting the effects of noise aliasing.^{5,34} Variation of transaxial resolution length and reconstruction filter are subjects of future investigation.

Voxel noise was measured as a function of SPR by acquiring FPI-CBCT scans of the water cylinder at various settings of ϕ_{cone} , with phantom thickness fixed at $T_{\text{PMMA}} \sim 30$ cm. For a given tube output (i.e., mAs per projection) the exposure at the FPI, X_{FPI} increases with cone angle due to increased scatter. Therefore, the voxel noise is expected to decrease with increasing cone angle in a manner consistent with the relationship between noise and dose in Eq. (4).

F. Effect of x-ray scatter on CNR

The contrast-to-noise ratio (CNR) was analyzed from volumetric images of the contrast phantom (i.e., the breast-equivalent insert in water) to examine the degradation in image quality due to x-ray scatter and to determine the extent to which the CNR can be restored by increasing dose and/or reducing spatial resolution. As described above, the contrast was taken as the difference between the ensemble averages of voxels in the breast-equivalent insert and in water. The noise was taken as the average of the standard deviations in the ensembles (and was consistent with measurements of the voxel noise in water described in the previous section). Taking the ratio of the contrast and noise, the CNR was analyzed as a function of SPR at three exposure levels: $X_{\text{iso}} \sim 1.8 \times 10^{-4}$, 2.6×10^{-4} , and 6.2×10^{-4} C/kg (i.e., 0.7, 1.0, and 2.4 R); and three values of z -dimension resolution length: $a_z = 0.5, 1$, and 2 mm, with a_x and a_y fixed at 0.5 mm. Results were compared to the analytic forms of Eqs. (3) and (4), from which we have:

$$\text{CNR}^2 = \left[\delta + \frac{1}{\alpha d} \ln \left(\frac{1 + S/P e^{\delta \alpha d}}{1 + S/P} \right) \right]^2 \cdot \frac{\rho h \eta D_{\text{center}} \alpha_{\text{res}}^3}{k \mu E_x f_c e^{\mu d/2} I}. \quad (5a)$$

Rewriting the equation to express the spatial resolution and dose required to achieve a given CNR gives:

$$\frac{\alpha_{\text{res}}^3 h}{I} D_{\text{center}} = \frac{\text{CNR}^2}{\left[\delta + \frac{1}{\alpha d} \ln \left(\frac{1 + S/P e^{\delta \alpha d}}{1 + S/P} \right) \right]^2} \cdot \frac{k \mu E_x f_c e^{\mu d/2}}{\rho \eta}, \quad (5b)$$

where the left-hand side isolates terms involving spatial resolution and dose. This expression was used to analyze the

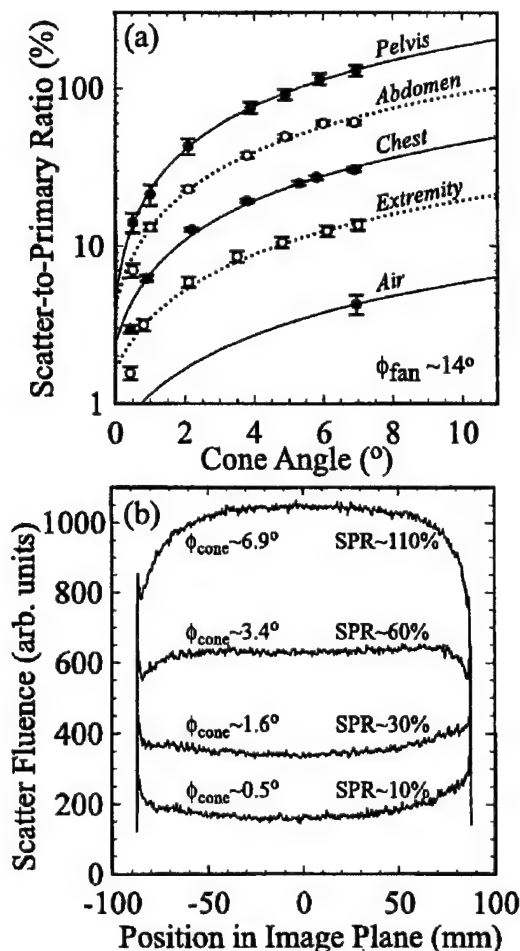


FIG. 2. (a) SPR at the detector plane measured as a function of cone angle. The curves are linear fits to the data, showing that the slope (i.e., change in SPR per degree of cone angle) increases for thicker objects. All error bars herein indicate ± 1 standard deviation from the mean. (b) Scatter fluence profiles at the detector plane for various settings of cone angle. For small cone angles, the scatter distributions are similar to those in slice-based CT, but increase significantly for larger cone angles.

dose and/or spatial resolution required to restore CNR to the value exhibited under scatter-free conditions. The approach is similar to that of Cohen,³⁵ who considered the iso-noise relationship between dose and slice thickness [as in Eq. (4)] in examining the contrast-detail performance of slice-based CT scanners, and to Joseph,³⁶ who examined the effect of image smoothing on low-contrast visualization. In examining the effects of x-ray scatter on contrast and noise in FPI-CBCT, we consider the iso-CNR relationships in Eq. (5b) as a function of SPR and compute the tradeoffs in dose and longitudinal resolution length in maintaining a given CNR. The parameters of transaxial resolution length (a_{res}) and reconstruction filter (contained in I) were not varied herein, but as discussed in Sec. III, certainly represent alternative mechanisms by which the CNR can be managed.

III. RESULTS

A. Magnitude of x-ray scatter

Figure 2(a) shows the SPR at the detector plane measured

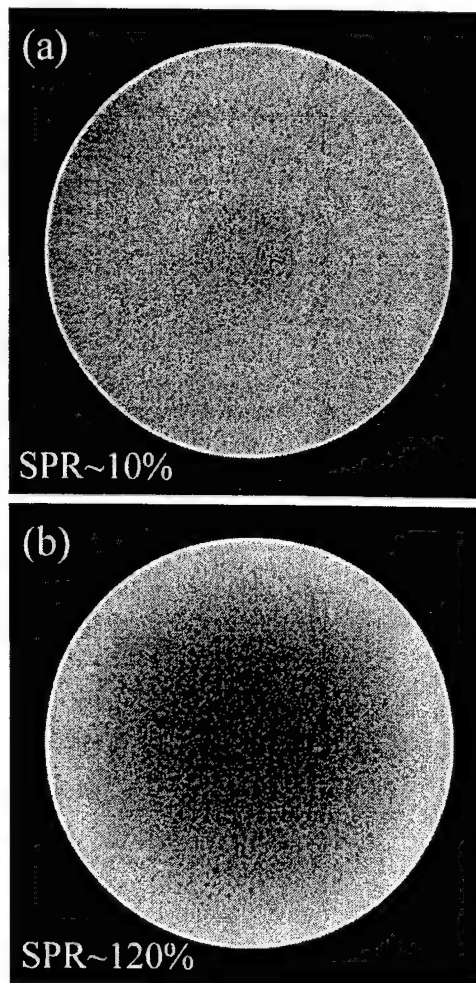


FIG. 3. Transaxial images of a uniform water cylinder acquired under conditions of (a) low- and (b) high-scatter conditions. These and subsequent images were acquired with the phantom surrounded by PMMA of thickness $T_{\text{PMMA}} \sim 30$ cm, with a fan angle of $\phi_{\text{fan}} \sim 14^\circ$, and a cone angle of $\phi_{\text{cone}} \sim 0.5^\circ$ ("low scatter") or $\phi_{\text{cone}} \sim 7^\circ$ ("high scatter"). All images herein are single transaxial slices from full-resolution FPI-CBCT reconstructions, and all image pairs [(a) and (b) throughout] were equivalently windowed and leveled for intercomparison.

as a function of cone angle for five thicknesses of PMMA: 0 cm ("air"), ~5 cm ("extremity"), ~12 cm ("chest"), ~18 cm ("abdomen"), and ~30 cm ("pelvis"), for a fan angle of $\phi_{\text{fan}} \sim 14^\circ$. These results quantify the expected trend that as the cone angle is increased (thereby allowing larger volumetric cone-beam reconstructions), the SPR at the detector increases significantly. Taking the "pelvis" as an example, the SPR increases from ~14% at $\phi_{\text{cone}} \sim 0.5^\circ$ to a level in excess of 120% for cone angles greater than $\sim 7^\circ$. The data are described well by linear fits of SPR versus cone angle, with slope (i.e., change in SPR per degree of cone angle) increasing for thicker objects. For "air" (i.e., $T_{\text{PMMA}} = 0$ cm) the slope of the line is $\sim 0.52\%$ per degree. For "extremity," "chest," "abdomen," and "pelvis," the slopes are $\sim 1.76\%$, 4.17% , 8.65% , and 17.74% per degree, respectively. These values are useful in estimating the SPR ex-

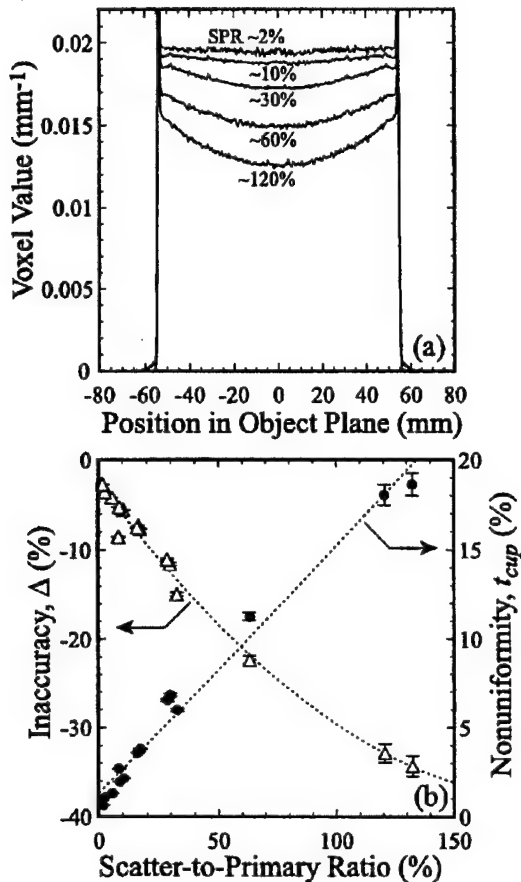


FIG. 4. (a) Signal profiles through the center of transverse images of the water phantom, showing the degree of CT# inaccuracy and image nonuniformity at various levels of SPR. The inaccuracy, Δ , defined as the percent deviation in mean reconstruction value from the expected value, is plotted versus SPR on the left-hand axis of (b). The nonuniformity, t_{cup} , defined as the relative deviation between voxel values in the center of the reconstruction compared to those at the edge, is plotted on the right-hand axis of (b).

pected for a given anatomical site and cone angle (e.g., SPR $\sim 87\%$ for the abdomen at $\phi_{cone} = 10^\circ$). Measurements of SPR were also performed for the larger fan angle, $\phi_{fan} \sim 22^\circ$, corresponding to a large FPI (at least 64 cm in width) in the centered geometry. For the larger fan angle ($\phi_{fan} \sim 22^\circ$), the SPR increases such that the slopes increase by a factor of ~ 1.33 .

Figure 2(b) shows scatter fluence profiles measured behind the water cylinder at various settings of cone angle (and, therefore, various levels of SPR). For the smaller cone angles, the scatter profiles are lower in magnitude and exhibit a concave-upward shape similar to that calculated by Glover¹⁵ for conventional fan-beam CT, where the scatter distribution is reduced in the center due to self-attenuation of scattered photons. For larger ϕ_{cone} (and, therefore, SPR), the scatter profiles increase in magnitude and exhibit an increasingly concave-downward shape due to a higher scatter contribution from out-of-plane.

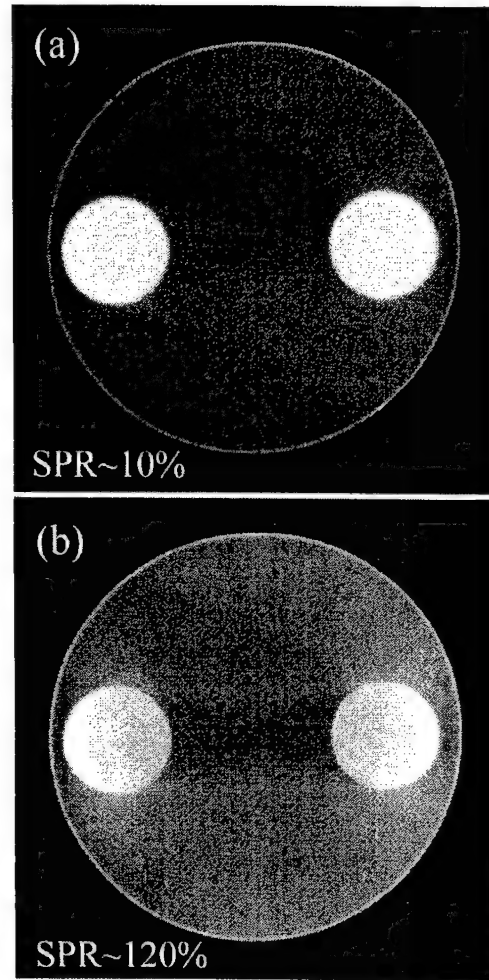


FIG. 5. Transaxial images of a water cylinder containing two bone inserts acquired under conditions of (a) low- and (b) high-scatter conditions. The former exhibits faint streak and photon starvation artifacts between the inserts. At higher SPR, the well-known streak artifact becomes prominent. These images and those of Fig. 3 qualitatively illustrate the magnitude of common x-ray scatter artifacts for scatter conditions expected in the clinical setting.

B. Shading artifacts and quantitative accuracy

FPI-CBCT images of the uniform water cylinder provided qualitative visualization and quantitative analysis of shading artifacts induced by x-ray scatter. For example, Fig. 3 shows transaxial images of the water cylinder acquired under conditions of low scatter (i.e., $\phi_{cone} \sim 0.5^\circ$ and $T_{PMMA} = 30$ cm, giving SPR $\sim 10\%$) and high scatter (i.e., $\phi_{cone} \sim 7^\circ$ and $T_{PMMA} = 30$ cm, giving SPR $\sim 120\%$). For the former, the image is uniform throughout the reconstructed volume, whereas the latter exhibits a pronounced nonuniformity in the form of reduced voxel values near the center of the image (i.e., a cup artifact^{14-16,23} common to conventional CT). The magnitude of the cup artifact is shown in Fig. 4(a), where diametric profiles are plotted for various values of SPR. For conditions of low scatter (e.g., SPR $\sim 2\%$), the signal profiles are uniform within the cylinder and exhibit reconstruction values close to the expected value of 0.020 mm^{-1} . As SPR

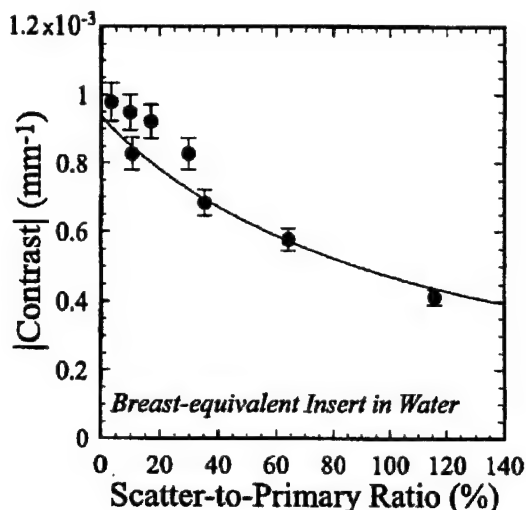


FIG. 6. Effect of x-ray scatter on FPI-CBCT contrast. The contrast between a breast-equivalent insert and water decreases from $\sim 0.0009 \text{ mm}^{-1}$ (i.e., $\sim 5\%$ relative contrast) at low scatter conditions to $\sim 0.0004 \text{ mm}^{-1}$ (i.e., $\sim 2.2\%$ relative contrast) at SPR $\sim 100\%$. The effect is described well by the simple analytical form of Eq. (3d).

increases, two effects are evident: an overall reduction (i.e., inaccuracy) in reconstruction values, and an increased severity (i.e., nonuniformity) of the cup artifact. These effects are quantified in Fig. 4(b), which plots the inaccuracy, Δ , and nonuniformity, t_{cup} , as a function of SPR. For SPR in excess of $\sim 100\%$, average reconstruction values are inaccurate (i.e., underestimated) by more than 30%. The relative degree of nonuniformity in the image increases from $t_{\text{cup}} \sim 2\%$ for SPR $\sim 10\%$ to nearly 20% cupping for SPR in excess of $\sim 100\%$.

Images of the water cylinder containing two bone inserts are shown in Fig. 5 for conditions of low and high scatter (SPR $\sim 10\%$ and $\sim 120\%$, respectively), illustrating the additional shading artifact of a dark streak between the bones.^{15,16,23} For the lower-scatter case, the streak artifact is evident but fairly subtle, accentuated by a photon starvation artifact²³ of smaller light and dark streaks between the bones. For the higher-scatter case, the streak artifact is prominent and dominates the underlying cup artifact. Moreover, note that the magnitude of voxel noise throughout the image as well as the severity of the photon starvation artifact appear to be reduced for the higher scatter case. This qualitative observation is consistent with the expectation mentioned above that for higher SPR, the exposure to the detector increases, and the voxel noise is reduced.

C. Contrast, noise, and CNR

The contrast of the breast-equivalent insert in water was measured as a function of SPR, as shown in Fig. 6. For the lowest scatter conditions, the measured contrast is $\sim 0.0009 \text{ mm}^{-1}$ (i.e., $\mu_{\text{H}_2\text{O}} = 0.0184 \text{ mm}^{-1}$ and $\mu_{\text{breast}} = 0.0175 \text{ mm}^{-1}$), corresponding to a relative contrast of 5%. This value corresponds closely to the value expected based on manufacturer specifications of approximate CT# (i.e., $\text{CT}_{\text{H}_2\text{O}} = 1000$ and $\text{CT}_{\text{breast}} = 953.3$, giving relative con-

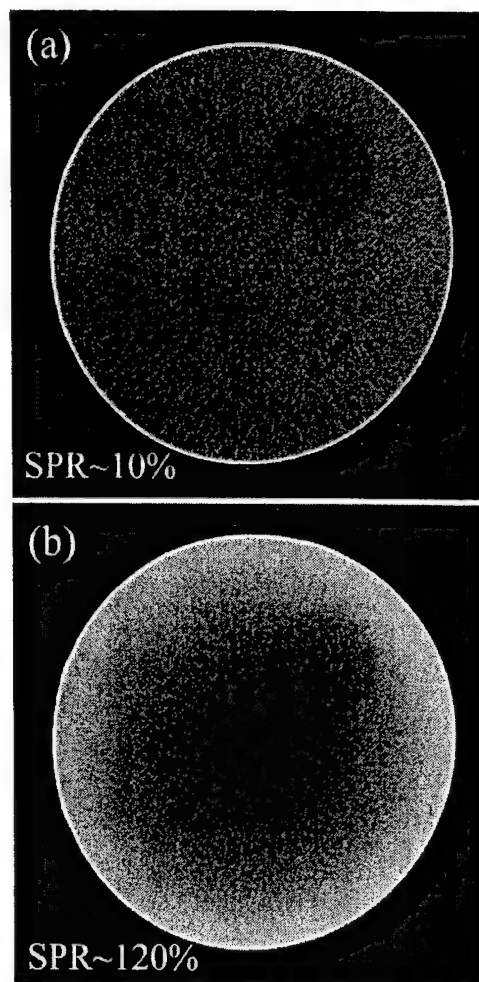


FIG. 7. Illustration of the effects of x-ray scatter on contrast, noise, and CNR in transaxial images of the water cylinder with breast-equivalent insert. At low-scatter conditions (a) the image exhibits relative contrast of 5% and CNR of ~ 1.13 , and the breast insert is well seen. At higher-scatter conditions (b) the relative contrast is degraded to 2.2%, the CNR is reduced to ~ 0.63 , and the visibility of insert is compromised. Barely visible in the upper-left quadrant of (a) is a second insert of CT solid water (slightly elevated CT#), which is largely imperceptible in (b).

trast of 4.8%). As SPR increases, however, the measured contrast of the breast insert reduces significantly. For example, at SPR $\sim 100\%$ the contrast is reduced to $\sim 0.0004 \text{ mm}^{-1}$ (i.e., 2.2% relative contrast). The curve in Fig. 6 represents the simple analytical form of Eq. (3d), which corresponds well with the measured results. The images in Fig. 7 illustrate the degradation in contrast with increased SPR. (A previous study¹ compared the image quality of the FPI-CBCT system with a conventional CT scanner for a low-contrast phantom containing the same breast insert under conditions of low x-ray scatter.)

Contrast alone, however, does not determine the visibility of structures in tomographic images; rather, the visibility of large, low-contrast objects is affected by the contrast in proportion to the voxel noise, i.e., by the CNR. Figure 8 shows the voxel noise measured in FPI-CBCT reconstructions of

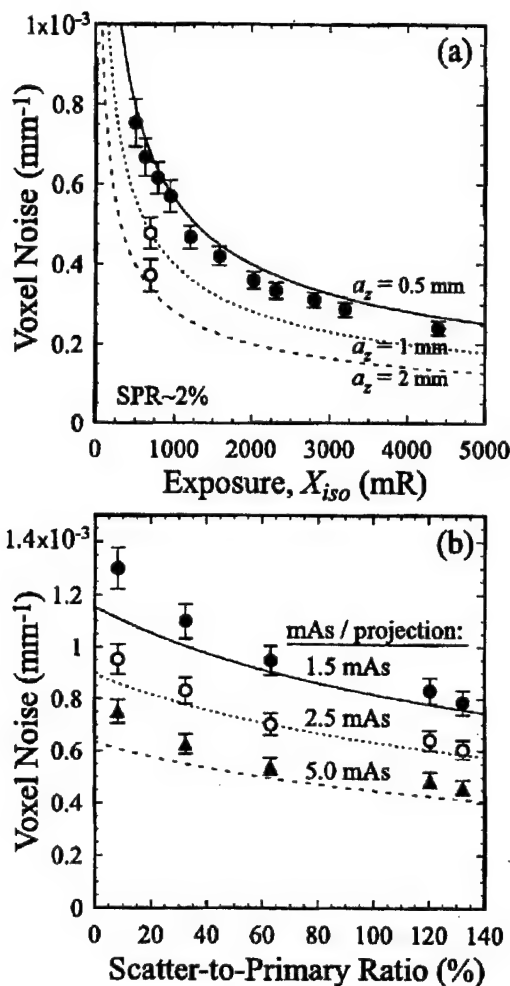


FIG. 8. Effect of x-ray scatter on voxel noise. (a) Voxel noise measured as a function of exposure, illustrating agreement with the analytic form of Eq. (4). The solid circles and curve correspond to full-resolution reconstructions, with resolution length equal to 0.5 mm. Reduction in spatial resolution reduces the noise as shown by the lower curves, in which the longitudinal resolution length, a_z , is increased to 1 mm and 2 mm. (b) Voxel noise measured as a function of SPR for three levels of x-ray tube output (1.5, 2.5, and 5.0 mAs per projection). In each case, the voxel noise reduces with SPR due to increased exposure at the detector.

the uniform water cylinder as a function of exposure and SPR. Figure 8(a) shows that the voxel noise decreases with the inverse square root of exposure, in agreement with the analytic form of Eq. (4) (solid curve) and consistent with previous results.¹ Since the analytical relation involves measured input parameters such as efficiency, resolution length, and dose and assumes monoenergetic x-rays, the uncertainty in the theoretical curve is estimated to be no better than ~10%.

The solid symbols and solid curve in Fig. 8(a) correspond to volume reconstructions in which the resolution length is equal in all dimensions, i.e., $a_x = a_y = a_z = 0.5$ mm. Also shown are empirical and theoretical results in which the longitudinal resolution length (i.e., the z-resolution, or slice thickness) is set to 1 mm (open circle with dotted curve) and

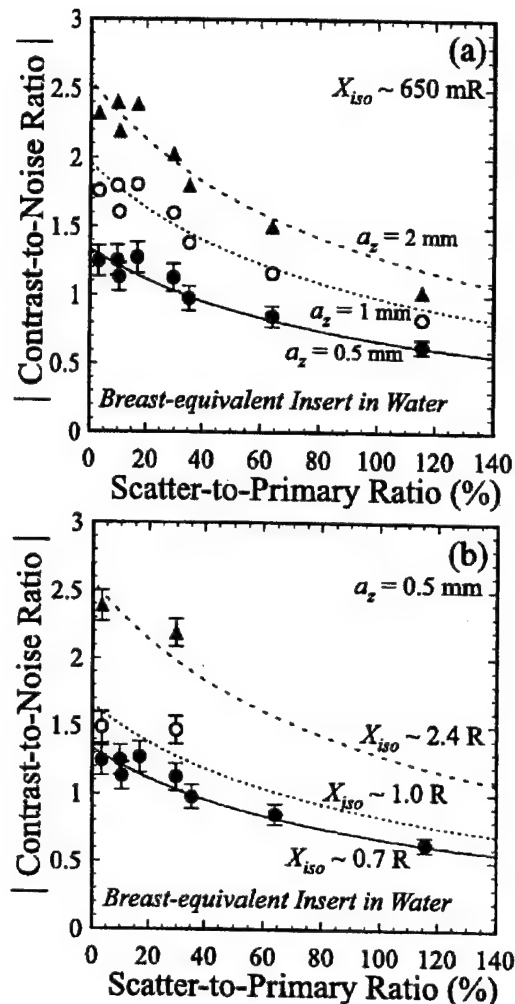


FIG. 9. Effect of x-ray scatter on the CNR in FPI-CBCT images of a breast-equivalent insert in water. The CNR was measured and calculated as a function of SPR for (a) various settings of longitudinal resolution length (i.e., slice thickness), a_z , and (b) various levels of total scan exposure. The CNR improves with reduced spatial resolution and increased exposure, since each has the effect of reducing the voxel noise.

2 mm (open circle with dashed curve), relating the intuitive trend that reduction in spatial resolution reduces the voxel noise. Due to strong band-limiting of the projection noise-power spectra (e.g., by the x-ray converter and apodization filter) prior to back-projection and 3D sampling, the effects of 3D noise-power aliasing^{5,34} are small and are neglected in the present analysis.

Figure 8(b) shows the voxel noise measured as a function of SPR at various levels of x-ray tube output. In each case, the water cylinder is surrounded by PMMA of thickness $T_{PMMA} \sim 30$ cm, corresponding to the largest object examined ("pelvis"), and the SPR was varied by adjusting the cone angle from 0.5° to 10.5° . The three curves correspond to tube output levels of 1.5, 2.5, and 5.0 mAs per projection (i.e., $X_{iso} \sim 2.3 \times 10^{-6}$, 3.9×10^{-6} , and 7.7×10^{-6} C/kg, or ~9, 15, and 30 mR, respectively). In each case, although the nominal tube output is fixed, the exposure at the detector

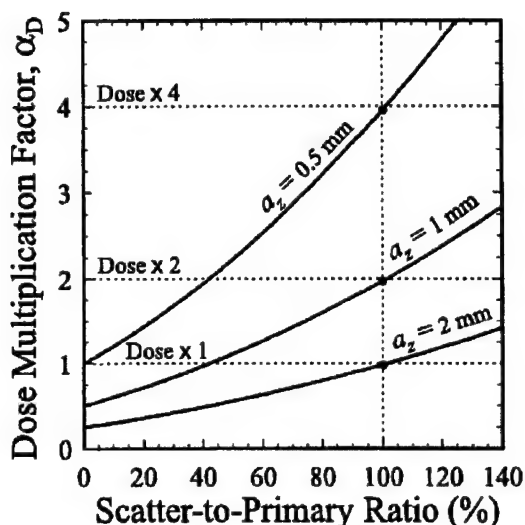


FIG. 10. Management of CNR degradation by increasing dose and/or reducing spatial resolution. The factor, α_D , by which dose must be increased to restore CNR to the level achieved in the scatter-free case is plotted as a function of SPR for three settings of longitudinal resolution length. The curves represent lines of iso-CNR in the three-dimensional space of dose, spatial resolution, and SPR described by Eq. (5b). CNR can be restored by increasing dose, reducing spatial resolution, or some compromise therein (e.g., at SPR=100%, by increasing dose by a factor of 2 and decreasing longitudinal spatial resolution by a factor of 2). Alternative means of image smoothing (e.g., combined adjustment of slice thickness, transaxial resolution length, and reconstruction filter) can be employed similarly to restore CNR without increase in dose.

increases with cone angle and SPR due to x-ray scatter, and the voxel noise is reduced accordingly. This is not to say that x-ray scatter is beneficial to image quality; rather, it reflects the fact that the detector does not distinguish between primary and scattered photons, and integrates incident quanta irrespective of their history. The effect is evident qualitatively in Figs. 3, 5, and 7, where the magnitude of voxel noise is slightly reduced in the higher SPR images.

Since for higher levels of SPR both the contrast and voxel noise are reduced, the effect of x-ray scatter on the CNR is something of a race between the degradation in contrast and the reduction in noise. The net effect is degradation in CNR, as qualitatively shown in the images of the breast insert in Fig. 7. The CNR was analyzed from such images as a function of SPR and compared to expectations based on the ratio of the analytical forms in Eqs. (3d) and (4). The solid circles and solid curve in Fig. 9(a) show the degradation in CNR with increased scatter for full-resolution reconstruction (i.e., $a_x = a_y = a_z = 0.5$ mm), and the CNR falls by a factor of 2 across the range of SPR investigated.

Since the voxel noise improves for increased exposure and/or reduced spatial resolution [Eq. (4)], the CNR is expected to improve accordingly. For example, Fig. 9(a) illustrates the effect of reduced spatial resolution on the CNR, where the longitudinal resolution length (a_z) was varied from 0.5 to 2 mm. These results indicate that the CNR at a given level of SPR can be doubled by reducing the longitudinal spatial resolution by a factor of 4. Similarly, Fig. 9(b)

illustrates the effect of increasing exposure (at full spatial resolution). The solid circles and solid curve are the same as in Fig. 9(a), while the open circles (dotted curve) and solid triangles (dashed curve) correspond to increased total scan exposure. The higher exposure measurements were not performed at SPR $> \sim 30\%$ due to tube heating limitations at increased phantom thickness, but the overall trend is conveyed by the analytical curves. As expected, CNR improves with increased exposure.

A question arises, therefore, as to how the degradation in CNR incurred from elevated levels of SPR can be managed through knowledgeable selection of dose and spatial resolution. From Eq. (5b), which isolates these terms as a function of CNR, it is straightforward to compute the factor, called α_D , by which the dose must be increased (for a given spatial resolution) in order to restore the CNR to a certain level. Conversely, one can compute the spatial resolution (for a given dose) that results in the desired CNR. Conservatively, we take the value of the CNR in the scatter-free case as the desired value, and compute α_D as a function of SPR for various settings of longitudinal resolution length, a_z . Note that these calculations are conservative moreover in that they consider adjustment of spatial resolution through variation of a_z only. However, variation of the transaxial resolution lengths, a_x and a_y , as well as the reconstruction filter (contained in the bandwidth integral, I) represent means of adjusting spatial resolution that are at least as viable. Since each of these parameters is selectable at the time of image reconstruction (within the constraints of 3D noise-power aliasing⁵), voxel noise can effectively be tuned through combined adjustment of the resolution lengths (a_x, a_y, a_z) and reconstruction filter. Whatever the choice, the resulting spatial resolution must of course be consistent with the imaging task.

Results are shown in Fig. 10, where α_D is computed for three settings of a_z , providing quantitation of the dose-resolution tradeoffs in management of x-ray scatter and CNR. For SPR of 100%, for example, the top curve indicates that CNR can be restored to the level achieved in the scatter-free case (at full spatial resolution) by increasing dose by a factor of 4. Alternatively, the CNR can be restored by increasing both the dose and the longitudinal resolution length by a factor of 2. Finally, CNR can be restored without any increase in dose by increasing the longitudinal resolution length by a factor of 4. The decision as to which CNR restoration strategy is best (e.g., increasing dose or reducing spatial resolution) should, of course, be based on the clinical objective.

IV. DISCUSSION AND CONCLUSIONS

The magnitude of x-ray scatter with which flat-panel cone-beam CT must contend is high, even for systems employing large air gaps consistent with optimal imaging geometry.⁶ The analogy to projection imaging is obvious: just as 2D projection imagers must contend with higher levels of scatter than 1D linear scanning detectors, so must 3D volumetric imagers (e.g., FPI-CBCT) contend with higher

levels than conventional tomographic imagers (e.g., slice-based CT). The benefits of volumetric imaging, however, warrant investigation of how best to reduce x-ray scatter and manage its deleterious effects. Strategies to be considered include the selection of the imaging geometry,⁶ the use of air gaps or scatter-rejection grids,^{24,25} the incorporation of scatter correction algorithms,^{22,23} and knowledgeable selection of acquisition and reconstruction parameters consistent with a given clinical objective.

Such considerations are relevant also in the development of helical CT scanners, e.g., multi-slice CT scanners,³⁷ employing cone angles somewhat higher than traditional fan-beam systems. Although the cone angles for multi-slice CT systems are typically much smaller than envisioned for FPI-CBCT, even a slight increase in SPR at the detector can have significant deleterious effect. For example, Fig. 2(a) shows that for a cone angle of 1°, the SPR corresponding to imaging of large anatomy (e.g., the pelvis) is ~20% for the described geometry. As shown in Fig. 9, this corresponds to ~15% degradation in CNR compared to the scatter-free case.

The shading artifacts and quantitative inaccuracy in CT# observed in FPI-CBCT are of similar form to (but of greater magnitude than) conventional, slice-based CT.¹⁴ It must be considered, however, that such artifacts and inaccuracy are only significant to the extent that they impede the clinical objective, and that the goal in FPI-CBCT imaging is not necessarily the same as with conventional CT. Specifically, the FPI-CBCT system being developed for therapy guidance^{1,13} need not replicate the image quality achieved by diagnostic imaging technology; rather, it should provide information that is of sufficient quality and geometric accuracy to confidently guide a given procedure. To the extent that artifacts and CT# inaccuracy impede such a clinical objective, the use of correction algorithms or modified acquisition methods may be warranted.

High levels of x-ray scatter were found to significantly degrade the visualization of soft-tissue structures, causing a loss in CNR consistent with analytical descriptions of contrast¹⁴ and noise.²⁶ This warrants careful consideration of how the effects of scatter can best be managed. First, it is clear from Fig. 2 that the cone angle should be kept as small as possible such that the volume of interest is still accommodated. For example, for FPI-CBCT imaging of the prostate (<8 cm in length), the cone angle should be limited to <~5° in order to minimize the SPR at the detector. Second, a quantitative understanding of the relationship between CNR, dose, and spatial resolution allows knowledgeable management of x-ray scatter effects. For example, as shown in Fig. 10, the dose and spatial resolution can be tuned within the constraints of the clinical objective to obtain CNR equal to that achieved under conditions of low x-ray scatter. In conclusion, the magnitude and effects of x-ray scatter in FPI-CBCT are significant, but can be managed through knowledgeable selection of the imaging geometry, the image acquisition technique, and the image reconstruction parameters as dictated by the clinical objective.

ACKNOWLEDGMENTS

The authors extend their gratitude to B. Groh (Deutsches Krebsforschungszentrum) for help with the experimental setup, to R. Clackdoyle, Ph.D. (University of Utah) for assistance with the cone-beam reconstruction algorithm, to K. Brown, Ph.D. (Elekta Oncology Systems) for provision of the flat-panel imager used in this work, and to M. K. Gauer, Ph.D. (PerkinElmer Optoelectronics) for technical information regarding the imager. This work was supported in part by the Prostate Cancer Research Program Grant No. DAMD 17-98-1-8497.

^{a)} Author to whom correspondence should be addressed: Jeffrey H. Siewerdsen, Department of Radiation Oncology, William Beaumont Hospital, 3601 W. Thirteen Mile Rd., Phone: 248-551-2219, Fax: 248-551-3784, Electronic mail: jsiewerd@beaumont.edu

¹ D. A. Jaffray and J. H. Siewerdsen, "Cone-beam computed tomography with a flat-panel imager: Initial performance characterization," *Med. Phys.* **27**, 1311–1323 (2000).

² D. A. Jaffray, J. H. Siewerdsen, and D. G. Drake, "Performance of a volumetric CT scanner based upon a flat-panel imaging array," *Medical Imaging 1999: Physics of Medical Imaging*, edited by J. M. Boone and J. T. Dobbins III, Proc. SPIE **3659**, 204–214 (1999).

³ J. H. Siewerdsen and D. A. Jaffray, "A ghost story: Spatio-temporal response characteristics of an indirect-detection flat-panel imager," *Med. Phys.* **26**, 1624–1641 (1999).

⁴ J. H. Siewerdsen and D. A. Jaffray, "Cone-beam computed tomography with a flat-panel imager: Effects of image lag," *Med. Phys.* **26**, 2635–2647 (1999).

⁵ J. H. Siewerdsen and D. A. Jaffray, "Cone-beam CT with a flat-panel imager: Noise considerations for fully 3-D imaging," *Medical Imaging 2000: Physics of Medical Imaging*, edited by J. M. Boone and J. T. Dobbins III, Proc. SPIE **3336**, 546–554 (2000).

⁶ J. H. Siewerdsen and D. A. Jaffray, "Optimization of x-ray imaging geometry (with specific application to flat-panel cone-beam computed tomography)," *Med. Phys.* **27**, 1903–1914 (2000).

⁷ R. Ning, D. Lec, X. Wang, Y. Zhang, D. Conover, D. Zhang, and C. Williams, "Selenium flat panel detector-based volume tomographic angiography imaging: Phantom studies," *Medical Imaging 1998: Physics of Medical Imaging*, edited by J. M. Boone and J. T. Dobbins III, Proc. SPIE **3336**, 316–324 (1998).

⁸ R. Ning, X. Tang, R. Yu, D. Zhang, and D. Conover, "Flat panel detector-based cone beam volume CT imaging: Detector evaluation," *Medical Imaging 1999: Physics of Medical Imaging*, edited by J. M. Boone and J. T. Dobbins III, Proc. SPIE **3659**, 192–203 (1999).

⁹ L. A. Feldkamp, L. C. Davis, and J. W. Kress, "Practical cone-beam algorithm," *J. Opt. Soc. Am. A* **1**, 612–619 (1984).

¹⁰ B. D. Smith, "Cone-beam tomography: Recent advances and a tutorial review," *Opt. Eng.* **29**, 524–534 (1990).

¹¹ H. Kudo and T. Saito, "Feasible cone beam scanning methods for exact reconstruction in three-dimensional tomography," *J. Opt. Soc. Am. A* **7**, 2169–2183 (1990).

¹² R. Clack and M. DeFrise, "Overview of reconstruction algorithms for exact cone-beam tomography," *SPIE Mathematical Methods in Medical Imaging III* **2299**, 230–241 (1994).

¹³ D. A. Jaffray, D. G. Drake, D. Yan, L. Pisani, and J. W. Wong, "Cone-beam tomographic guidance of radiation field placement for radiotherapy of the prostate," *Int. J. Radiat. Oncol., Biol., Phys.* (accepted).

¹⁴ P. C. Johns and M. Yaffe, "Scattered radiation in fan beam imaging systems," *Med. Phys.* **9**, 231–239 (1982).

¹⁵ G. H. Glover, "Compton scatter effects in CT reconstructions," *Med. Phys.* **9**, 860–867 (1982).

¹⁶ P. M. Joseph and R. D. Spital, "The effects of scatter in x-ray computed tomography," *Med. Phys.* **9**, 464–472 (1982).

¹⁷ W. Kalender, "Monte Carlo calculations of x-ray scatter data for diagnostic radiology," *Phys. Med. Biol.* **26**, 835–849 (1981).

¹⁸ H. P. Chan and K. Doi, "Physical characteristics of scattered radiation in diagnostic radiology: Monte Carlo studies," *Med. Phys.* **12**, 152–165 (1985).

- ¹⁹H. Kanamori, N. Nakamori, K. Inoue, and E. Takenaka, "Effects of scattered x-rays on CT images," *Phys. Med. Biol.* **30**, 239–249 (1985).
- ²⁰J. M. Boone and J. A. Seibert, "An analytical model of the scattered radiation distribution in diagnostic radiology," *Med. Phys.* **15**, 721–725 (1988).
- ²¹M. Honda, K. Kikuchi, and K. Komatsu, "Method for estimating the intensity of scattered radiation using a scatter generation model," *Med. Phys.* **18**, 219–226 (1991).
- ²²B. Ohnesorge, T. Flohr, and K. Klingenberg-Regn, "Efficient object scatter correction algorithm for third and fourth generation CT scanners," *Eur. J. Radiol.* **9**, 563–569 (1999).
- ²³J. Hsieh, "Image artifacts: Causes and correction," in *Medical CT and Ultrasound: Current Technology and Applications*, Proc. Of the 1995 Summer School of the AAPM, Chap. 26, edited by L. W. Goldman and J. B. Fowlkes (Advanced Medical Publishing, Madison, WI, 1995), pp. 487–518.
- ²⁴M. Endo, T. Tsunoo, and N. Nakamori, "Effect of scatter radiation on image noise in cone beam CT," *SPIE Physics of Medical Imaging 3977*, 514–521 (2000).
- ²⁵U. Neitzel, "Grids or air gaps for scatter reduction in digital radiography: A model calculation," *Med. Phys.* **19**, 475–481 (1992).
- ²⁶H. H. Barrett, S. K. Gordon, and R. S. Hershel, "Statistical limitations in transaxial tomography," *Comput. Biol. Med.* **6**, 307–323 (1976).
- ²⁷AAPM Report No. 31, *Standard Methods for Measuring Diagnostic X-ray Exposures* (American Institute of Physics, New York, 1991).
- ²⁸T. M. Peters and R. M. Lewitt, "Computed tomography with fan beam geometry," *J. Comput. Assist. Tomogr.* **1**, 429–436 (1977).
- ²⁹D. A. Jaffray, J. H. Siewerdsen, G. E. Edmundson, J. W. Wong, and A. Martinez, "Cone-beam CT: Applications in image-guided external beam radiotherapy and brachytherapy," Meeting of the World Congress on Medical Physics and Biomedical Engineering, Chicago, IL, July 23–28 (2000) (abstract).
- ³⁰P. Cho, R. H. Johnson, and T. W. Griffin, "Cone-beam CT for radiotherapy applications," *Phys. Med. Biol.* **40**, 1863–1883 (1995).
- ³¹E. Storm and H. I. Israel, "Photon cross sections from 1 keV to 100 MeV for elements Z=1 to Z=100," *Nucl. Data Tables A7*, 565–681 (1970).
- ³²D. M. Tucker, G. T. Barnes, and D. P. Chakraborty, "Semiempirical model for generating tungsten target x-ray spectra," *Med. Phys.* **18**, 211–218 (1991).
- ³³R. F. Wagner, D. G. Brown, and M. S. Pastel, "Application of information theory to the assessment of computed tomography," *Med. Phys.* **6**, 83–94 (1979).
- ³⁴M. F. Kijewski and P. F. Judy, "The noise power spectrum of CT images," *Phys. Med. Biol.* **32**, 565–575 (1987).
- ³⁵G. Cohen, "Contrast-detail-dose analysis of six different computed tomographic scanners," *J. Comput. Assist. Tomogr.* **3**, 197–203 (1979).
- ³⁶P. M. Joseph, S. K. Hilal, R. A. Schulz, and F. Kelcz, "Clinical and experimental investigation of a smoothed CT reconstruction algorithm," *Radiology* **134**, 507–516 (1980).
- ³⁷H. Hu, "Multi-slice helical CT: Scan and reconstruction," *Med. Phys.* **26**, 5–18 (1999).

**Appendix G: Cone-beam Computed Tomography with a Flat-panel
Imager: Noise Considerations for Fully3D Computed
Tomography**

Cone-Beam CT with a Flat-Panel Imager: Noise Considerations for Fully 3-D Computed Tomography

Jeffrey H. Siewerdsen and David A. Jaffray

Department of Radiation Oncology, William Beaumont Hospital, Royal Oak MI 48073

ABSTRACT

Application of flat-panel imagers (FPIs) in cone-beam computed tomography (CBCT) offers a promising new modality for fully three-dimensional (3-D) x-ray imaging. Understanding the potential performance and fundamental limitations of such technology, however, requires knowledge of the noise characteristics of the 3-D imaging system.

The noise performance of a prototype flat-panel cone-beam CT (FPI-CBCT) system is investigated empirically and theoretically in terms of voxel noise, noise-power spectrum (NPS), and detective quantum efficiency (DQE). Methods for NPS analysis common in characterizing 2-D imagers are extended to the fully 3-D case, and a general framework for NPS analysis in n dimensions is presented, including the important considerations of NPS convergence and normalization within the constraints of system linearity and stationarity. Factors affecting imager noise and NPS are numerous, including exposure, number of views, image blur, additive noise, reconstruction filter, and sampling matrix. The applicability of existing theoretical descriptions of CT voxel noise is examined. A theoretical cascaded systems model that accurately predicts the 2-D noise characteristics of the FPI is extended to describe the signal and noise transfer characteristics of the fully 3-D FPI-CBCT system employing filtered back-projection. Analysis of the fully 3-D NPS reveals features of the 3-D imaging system that might otherwise be missed and shows the significant effect of 3-D noise aliasing. Furthermore, it quantifies the performance of various FPI designs in CBCT (e.g., direct and indirect detectors, and variations therein) and provides a guide for the development of high-performance FPI-CBCT systems suited to specific clinical objectives.

1. INTRODUCTION

Continuous advances in the field of diagnostic radiology in the latter decades of the 20th century have provided the therapist of the 21st century with a wealth of image information and an arsenal of imaging technology. In addition to characterizing disease, diagnostic imaging provides spatial information that can be used to guide the delivery of localized therapies – ranging from neurosurgery to radiotherapy. Unfortunately, the value of this spatial information degrades in moving the patient between the imaging and therapy environments and in treating the disease over an extended period. Ideally, the therapist could acquire images during the therapy procedure, providing anatomical reference to previously acquired diagnostic data as well as on-line guidance and assessment of the procedure. Imaging technology for therapy guidance need not replicate the image quality achieved by diagnostic imaging technology, but it should provide visualization of the target (typically soft-tissue) and be geometrically accurate.

We are investigating the use of flat-panel imagers (FPIs) in cone-beam computed tomography (CBCT) for guiding radiotherapy procedures – specifically, external beam radiation therapy and brachytherapy. Advances in FPI technology have produced high-performance, commercially available detectors for projection radiography. Advances in CBCT reconstruction techniques provide a means of volumetric reconstruction from 2-D projections in a timely fashion. The synthesis of these technologies represents a promising solution for therapy guidance. As reported previously,¹ an experimental FPI-CBCT prototype was constructed on an optical bench to examine volumetric imaging performance within a precise, reproducible geometry. The three primary components of the prototype are: an x-ray tube (GE Maxiray-75); an object rotation stage; and an FPI (EG&G Heimann Optoelectronics RID 512-400 A0; 512x512 matrix of a-Si:H photodiodes and TFTs at 400 μm pixel pitch in combination with a 133 mg/cm² Gd₂O₂S:Tb x-ray converter). The acquisition, processing, and reconstruction steps in the FPI-CBCT system are illustrated in Fig. 1. Initial results demonstrate contrast resolution comparable to a conventional CT scanner, and isotropic, sub-millimeter spatial resolution. The results in Fig. 2 illustrate the uniform quality of volumetric images obtained with the FPI-CBCT system.

The combination of FPI technology with CBCT methods promises a new and highly adaptable imaging modality for medical applications. To exploit this technology to its fullest, however, the physical factors governing its performance must be well understood, and a methodology for directing the design and application of FPI-CBCT systems must be developed. Quantitative empirical and theoretical characterization of FPI-CBCT performance ensures that the fundamental limitations and full potential of this technology is revealed.

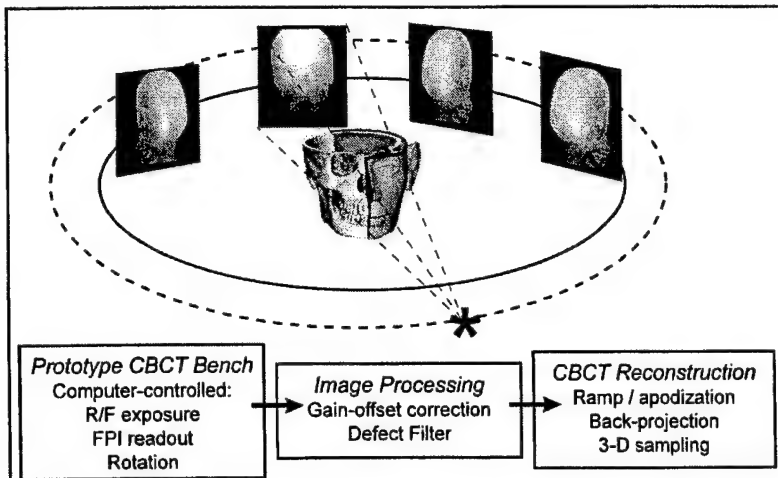


Figure 1. Illustration of a simple circular orbit imaging geometry for flat-panel cone-beam CT, along with the acquisition, processing, and reconstruction steps in the FPI-CBCT system. A series of 2-D projections are acquired at incremental rotations about the object under synchronized, computer control. These images are corrected by means of gain and offset calibration and filtration of pixel defects. Volumetric reconstruction is performed using the Feldkamp-Davis-Kress (FDK) method, in which the 2-D projection data are filtered and back-projected in a fully 3-D reconstruction space. Nominal conditions for FPI-CBCT acquisition include: 120 kVp beam; 300 projections acquired at $\Delta\theta=1.2^\circ$; and reconstruction at $0.25\times0.25\times0.25\text{ mm}^3$ voxel size.

2. BACKGROUND AND MOTIVATION

The noise characteristics of an imaging system are fundamental to an objective description of imaging performance, and a measure by which these characteristics are quantified is the spatial-frequency-dependent noise-power spectrum (NPS). Evaluated empirically, the NPS is central to the analysis of performance variables such as detective quantum efficiency (DQE) and noise-equivalent quanta (NEQ). Such measures are valuable indicators of imaging performance; however, they absorb so many parameters – including amplification, blur, additive noise, and aliasing – that the discrete underlying processes affecting image formation may not be transparent. A theoretical evaluation of NPS exposes these myriad processes explicitly and provides a measure by which the fundamental limitations of the imaging system can be quantitatively probed.

The noise characteristics of FPIs are fairly well understood and have been evaluated empirically and theoretically within numerous contexts of projection radiography. For example, the transfer characteristics of indirect-detection FPIs can be described using cascaded systems analysis² that considers the propagation of the NPS through the amplification and spatial spreading stages³ of the imaging chain. Despite a number of simplifying assumptions – e.g., linearity, stationarity, shift-invariance, energy invariance, etc. – such theoretical descriptions have shown reasonable agreement⁴ with measured NPS and DQE and were a valuable tool in the evolution of the first generation of FPIs for projection radiography.

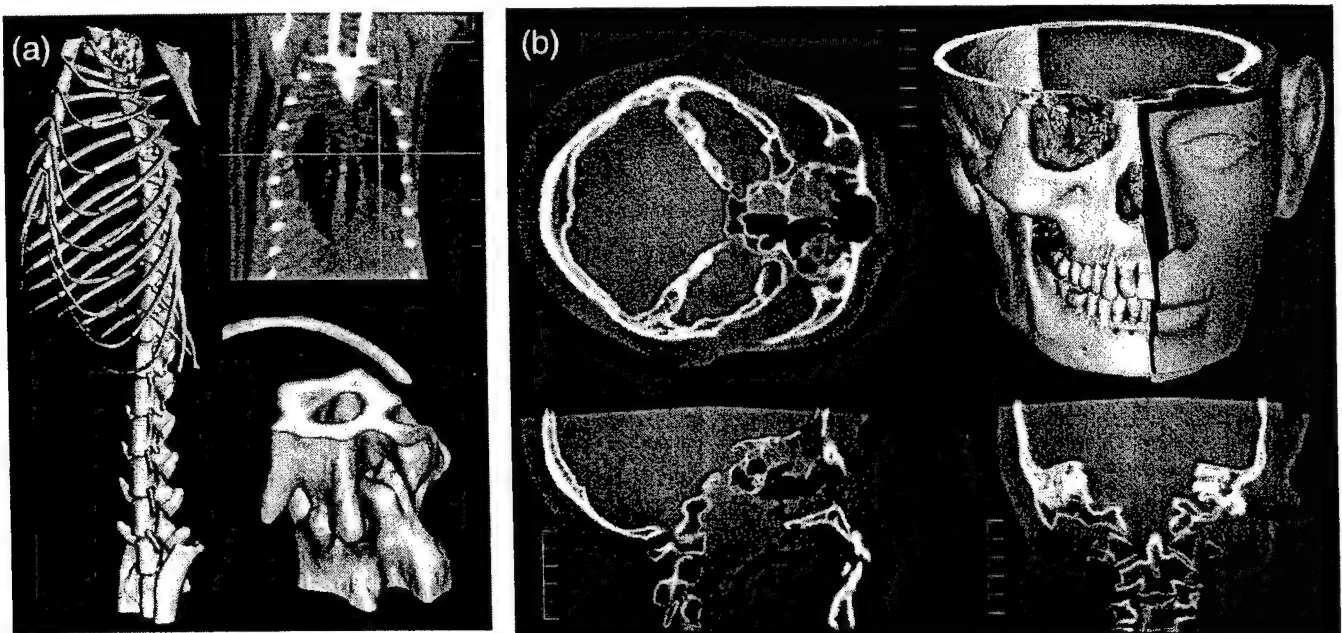


Figure 2. Example images acquired with the FPI-CBCT system. (a) A euthanized rat – volume rendering of skeletal anatomy, and soft-tissue in the region of the lungs. (b) Slices and volume-rendered views of a skull phantom. Scale indicates 1 cm per division.

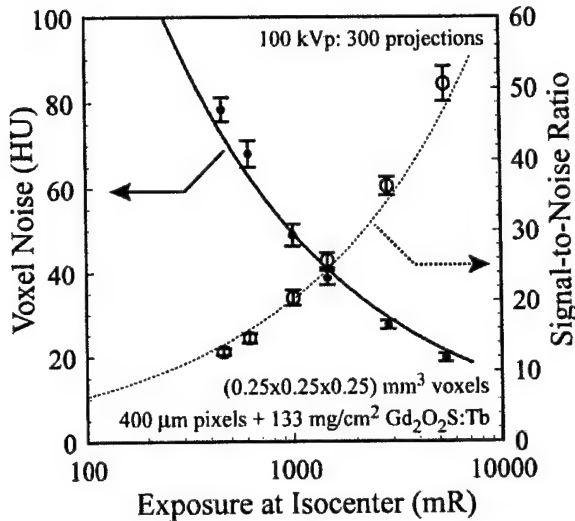


Figure 3. Voxel noise and signal-to-noise ratio (SNR) as a function of exposure as predicted by Eq. (1) and measured using the FPI-CBCT prototype. Measurements employed an 11 cm diameter water cylinder which was volume reconstructed from 300 projections at 100 kVp. Voxel noise was analyzed from the standard deviation in 10x10 voxel regions within a slice. The SNR improves from ~10 at the lowest exposure to ~50 at the highest (i.e., from a total entrance exposure of ~460 mR to ~5 R). Previous results¹ illustrated the degree of uniformity in voxel noise in transaxial and sagittal planes and showed exposure-dependence in comparison to that exhibited by a conventional CT scanner. The current analysis shows that the measured noise agrees remarkably well with Eq. (1), although the analysis does not explicitly account for factors that are known to affect FPI performance, such as additive electronics noise.

In conventional, slice-based computed tomography (CT) employing filtered back-projection reconstruction, the noise characteristics of imaging systems have been described in terms of the individual voxel noise⁵ (i.e., rms fluctuations in voxel values in the reconstructed image) as well as the frequency-dependent transfer characteristics.^{6,7} Barrett et al.⁵ examined the limitations imposed by quantum statistics on linear reconstruction techniques and derived the relationship between voxel noise, σ_{vox} , and dose, slice thickness, reconstruction filter, etc.:

$$\sigma_{vox}^2 = CT_{\#}^2 \frac{E_x f_c e^{\mu d/2}}{\rho \mu \Delta_z \eta D_0 a_{res}^3} M^2 \int T_{fil}^2(u) du \quad (1)$$

where $CT_{\#}$ is the reconstruction value (e.g., 1000 for water, herein), E_x is x-ray energy (taken as either 60 keV or the weighted mean of the x-ray spectrum), f_c is a Compton factor (equal to the ratio of the energy absorption and linear attenuation coefficients for a single slice, and approaching unity for the case of many slices), μ is the linear attenuation coefficient, d is the diameter of the object, ρ is density, Δ_z is slice thickness, η is the efficiency of the detector, D_0 is the dose at the center of the object (computed from the f -factor and measured exposure), a_{res} is the resolution distance, and the final term represents the integral of the filter function (e.g., ramp and Hamming) over the Nyquist region of the spatial-frequency domain, u . This expression illustrates a number of relevant considerations (e.g., variance inversely proportional to dose and slice thickness) and shows the effect of the filter (i.e., spatial correlation, or blur) on voxel noise. Figure 3 shows the voxel noise predicted by Eq. (1) in comparison to measurements performed using the FPI-CBCT prototype.

The noise properties of conventional, slice-based CT systems have been further quantified in terms of the spatial-frequency-dependent transfer characteristics.^{6,7} Hanson⁶ showed the effect of the reconstruction process on the NPS and NEQ and examined the detectability of large, low-contrast structures in relation to the low-frequency noise characteristics. Kijewski and Judy⁷ analyzed the NPS for filtered back-projection CT, considering the effects of the ramp and apodization filters, interpolation, back-projection, and 2-D sampling in the reconstructed slice. This analysis points out a number of pertinent considerations, including the rotational asymmetry of the NPS, and shows that sampling the reconstruction matrix (i.e., aliasing) increases the NPS at all frequencies below the Nyquist limit. Even at zero-frequency, the increase in NPS due to aliasing is significant and can degrade the detectability of large, low-contrast objects.

Below, we present a synthesis of the noise characterization techniques developed for FPI radiography and conventional CT, and we extend the results to describe the noise characteristics of a fully 3-D FPI-CBCT imaging system. The process of image formation is represented as a cascade of discrete stages – merging the general theoretical description of the NPS for the detector with a spatial-frequency-dependent description of the mathematical processes involved in CBCT reconstruction. The analysis quantifies the susceptibility of the reconstruction NPS to the shape and magnitude of the projection NPS (e.g., to the “white” or “band-limited” NPS exhibited by direct and indirect-detection FPIs, respectively). Furthermore, it illustrates the effect of noise aliasing from 3-D sampling of the reconstruction. A complete description of the processes of 3-D image formation will allow knowledgeable selection of system components (e.g., FPI design and reconstruction filters) and will serve as a quantitative guide for clinical implementation of FPI-CBCT.

3. METHODS OF NOISE-POWER SPECTRAL ANALYSIS

The NPS can be described empirically (e.g., by Fourier analysis of flood-field image data) and/or theoretically (e.g., by cascaded systems analysis of the imaging system). The following sections summarize methods for NPS analysis as prevalent in projection radiography and illustrate the extension of such techniques to the case of fully 3-D computed tomography.

3.1. Empirical Methods for NPS Analysis (in n dimensions)

The NPS of image data can be estimated by Fourier methods, provided that the imaging system is shift-invariant and stationary. Since knowledge of the NPS is prerequisite to determining DQE, there is considerable interest in reaching consensus in the empirical methods by which NPS is analyzed – precisely the subject of a recent AAPM Task Group.

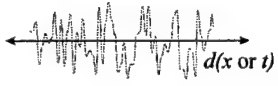
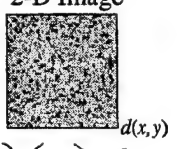
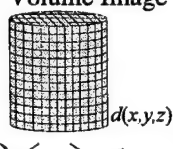
	Dimensionality: $n=1$ (e.g., time-series analysis)	Dimensionality: $n=2$ (e.g., projection radiography)	Dimensionality: $n=3$ (e.g., cone-beam CT)
Data	1-D Realization 	2-D Image 	3-D Volume Image 
Technique	$\xrightarrow{(n-1) \text{ reduced}} \sigma^2$ $\xrightarrow{(n) \text{ complete}} S(\omega)$	$\xrightarrow{(n-1) \text{ reduced}} \text{"Synthesized Slit"}$ $\xrightarrow{(n) \text{ complete}} S(u,v)$	$\xrightarrow{(n-1) \text{ reduced}} \text{"Synthesized Slice"}$ $\xrightarrow{(n) \text{ complete}} S(f_x f_y f_z)$
Noise Analysis	σ^2 $ \mathcal{F}_{1-D}[d] ^2$	$ \mathcal{F}_{2-D}[d] ^2$ $S(u;v=0)$ $ \mathcal{F}_{1-D}[d] ^2$	$ \mathcal{F}_{3-D}[d] ^2$ $S(f_x f_y; f_z=0)$ $ \mathcal{F}_{2-D}[d] ^2$
Convergence Test ($n-1$)	Test σ^2 convergent in x (weak stationarity)	Test NPS convergent in L (central slice of 2-D NPS)	Test NPS convergent in L (central slice of 3-D NPS)
W_{norm}	$\frac{\Delta_x}{N_x}$	$\frac{\Delta_x \Delta_y}{N_x N_y}$	$\frac{\Delta_x \Delta_y \Delta_z}{N_x N_y N_z}$
Units	(Signal) ² (Signal) ² ×(mm)	(Signal) ² ×(mm) ²	(Signal) ² ×(mm) ³

Table 1. Summary of empirical NPS analysis methods for 1, 2, and 3-D data, illustrating the commonality among methods in n -D.

Empirical methods of NPS analysis by "direct-digital" techniques are summarized in Table 1 for the cases of 1, 2, and 3-D data. In each case, the task is to estimate the magnitude and frequency content of fluctuations in a zero-mean data realization. (Discussion of numerous issues, such as detrending and windowing, is beyond the scope of this paper.) Analysis typically proceeds by either of two techniques: 1.) in which the dimensionality of the data is reduced by one (e.g., the "synthesized slit" technique in projection radiography); and 2.) in which the data are directly analyzed by the n -D Fourier transform. The former technique integrates the realization along some distance, L , which must be sufficiently long that the result converges on a reasonable estimate of the NPS central slice (i.e., the NPS along one of the frequency axes). Modern computers and fast algorithms for n -dimensional FFT have made the latter technique practical, and analysis of the full n -D NPS can reveal off-axis features that might otherwise be missed.⁸ Normalization is straightforward in each case, determined by the ratio of the sampling distance and number of samples per realization [and by the length of the region of integration for the $(n-1)$ technique]. Units of the NPS are those of the signal-squared, times length-to-the- n^{th} power, and the variance is equal to the n -dimensional integral over the NPS. This summary is presented so that the extension to $n=3$ (and beyond) is straightforward.

The NPS for FPI-CBCT was determined from volumetric images (120 kVp; 1.5 mm Al + 0.5 mm Cu filtration) in air, with voxel values normalized to a mean value of 0 for air and 1000 for water. Both $(n-1)$ and n -D techniques were used, with results shown for the former, which allows improved standard error for a given quantity of data. In all cases, the volumetric uniformity of σ_{vox} was checked (weak stationarity), and variance agreed with the integral NPS within 1%.

3.2 Theoretical Methods for NPS Analysis (in n dimensions)

The characteristics of the projection NPS for FPIs are well described by cascaded systems analysis. For example, a seven stage model has demonstrated reasonable agreement⁴ with measured NPS and DQE for a variety of indirect-detection FPI designs and exposure conditions. The projection NPS is characterized by a serial cascade of amplification and spatial spreading stages,^{2,3} as summarized in Table 2. The resulting NPS, $S_7(u,v)$, is a 2-D function of: incident fluence (q_0), quantum detection efficiency (g_1), optical gain (g_2), Poisson excess in g_2 (ϵ_{g2}), converter modulation transfer function, MTF (T_3), optical coupling efficiency (g_4), photodiode presampling MTF (T_5), photodiode aperture (a_{pd}), sampling distance (a_{pix}), and the additive NPS of the electronics (S_{add7}). The expression for the projection NPS is given in the top of Fig. 4, along with a plot of $S_7(u,v=0)$ and a grayscale representation of $S_7(u,v)$ within the Nyquist zone. For illustration, the NPS for an FPI exhibiting negligible spatial spreading in the conversion stage (e.g., as typically the case for direct-detection FPIs) is also plotted (dotted line).

	Stage	Physical / Mathematical Process	Parameters
2-D Image Formation	0	X-ray quanta incident on detector	q_0
	1	X-rays interacting in x-ray converter	g_1
	2	Generation and emission of photons	g_2, ϵ_{g2}
	3	Spatial spreading of optical photons	$T_3(u,v)$
	4	Coupling of optical photons to photodiode	g_4
	5	Integration of photons by photodiode	$T_5(u,v;a_{pd})$
	6	Sampling 2-D matrix of detector pixels	$III_6(u,v;a_{pix})$
	7	Pixel readout with additive noise	$S_{add7}(u,v;\sigma_{add})$
3-D CBCT Reconstruction	8	Application of ramp filter	$T_8(f_x f_z)$
	9	Application of apodization window	$T_9(f_x f_z; \alpha)$
	10	Interpolation of projection data	$T_{10}(f_x f_z)$
	11	Back-projection	$III_{11}(f_x f_y f_z; \theta)$
	12	Sampling 3-D voxel matrix	$III_{12}(f_x f_y f_z; a_{vox})$

Table 2. Extension of cascaded systems analysis to 3-D FPI-CBCT. Stages 0-7 are described in previous work that modeled 2-D FPI image formation. Stages 8-12 represent the deterministic mathematical processes involved in reconstructing fully 3-D data from multiple projections. The parameters listed for stages 8-12 are T_8 (the ramp filter), T_9 (the apodization filter), T_{10} (the interpolation function), III_{11} (vanes in frequency space), and III_{12} (3D comb-function matrix for sampling of the 3D data).

This general analysis for the spatial-frequency-dependent transfer characteristics of the 2-D imager is extended to describe the transfer characteristics of the entire 3-D imaging chain. We characterize the cone-beam reconstruction process by a cascade of five stages, each corresponding to a deterministic mathematical process in filtered back-projection. This approach is in direct analogy to the work of Kijewski and Judy,⁷ but considers a 2-D detector with generalized NPS (rather than a 1-D detector with white NPS) and describes reconstruction of a fully 3-D volume (rather than a 2-D slice). The stages are summarized in Table 2, and the transfer functions and NPS at each stage in the reconstruction process are illustrated in Fig. 4.

Taking Stage 7 as the input, with $S_7(u,v)$ equal to the projection NPS of the FPI, the reconstruction process begins with application of a ramp filter, $T_8(u)$. (Deterministic scaling, such as the logarithm and conversion to HU, is applied as appropriate but is not explicit in Fig. 4 for the sake of brevity.) Note that the standard FDK method applies the ramp filter only along u , i.e., to correct for $1/r$ blur in transaxial planes. Stage 9 represents application of an apodization filter, $T_9(u)$, selected to attenuate high-frequency amplification incurred in Stage 8. The apodization filter is typically a gentle roll-off function (e.g., Hanning, Hamming, etc.), and identification of optimal filters is a subject of considerable interest. The data are interpolated at Stage 10 so that points in the projection image correspond to points selected for back-projection, with the transfer function, $T_{10}(u,v)$, dependent on the interpolation method (e.g., bilinear, nearest-neighbor, etc.). Note that the interpolation function is applied in 2-D and is the only mechanism for reducing very high-frequency components of the NPS. Stage 11 represents the process in which the 2-D projection data are back-projected at angles, θ , corresponding to the view angles of the M projections. In the frequency domain, this corresponds to superimposing each 2-D NPS in a plane through the origin in the 3-D reconstruction space at angle θ . Superposition of the M power spectra builds up a discrete sets of planes ("vanes") in the 3-D frequency domain ($f_x f_y f_z$) separated by gaps. Finally, the reconstruction space is sampled at points in the 3-D sampling matrix, i.e., at the center of each voxel. Assuming cubic voxels of width a_{vox} , the sampling grid is a 3-D matrix of points separated by $1/a_{vox}$. In perfect analogy to the 2-D sampling process at Stage 7 of the projection imaging chain, 3-D sampling results in aliasing of the NPS, which increases the presampling NPS, $S_{11}(u,v)$. As noted by Kijewski and Judy,⁷ the non-zero value of the NPS at zero-frequency is directly attributed to aliasing, and this increased low-frequency noise, in turn, may have significant effect on the visibility of large, low-contrast structures.

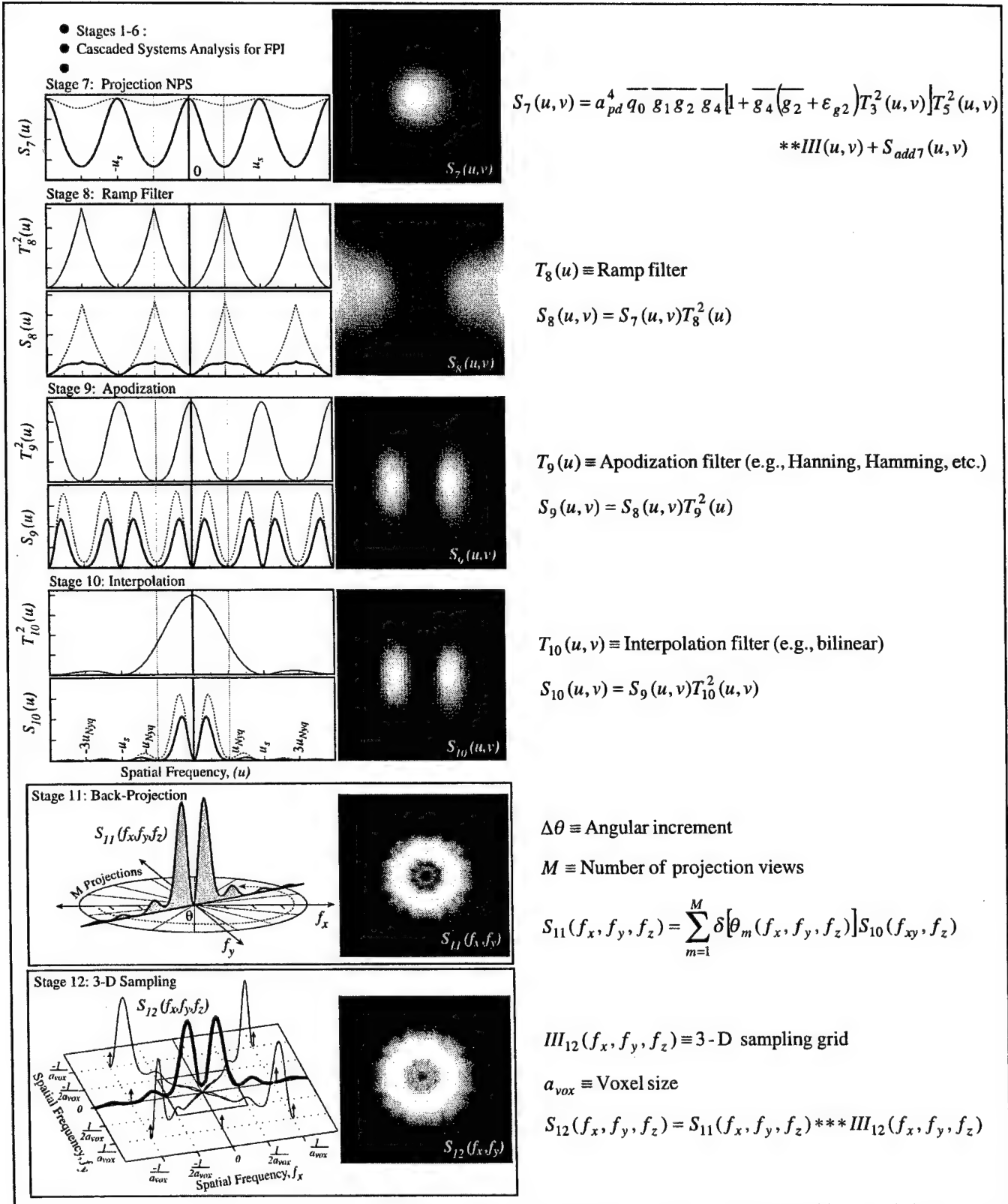


Figure 4. Cascaded systems representation of the FPI-CBCT 3-D imaging process. Plots on the left show transfer functions, T_i , and 1-D slices of NPS, S_i . For each NPS plot, the bold and dotted curves represent cases of “band-limited” (e.g., indirect-detection) and “white” (e.g., direct-detection) NPS, respectively. Grayscale images show the NPS for the former case up to the Nyquist frequency. The equations summarize the transfer characteristics of the volumetric imaging chain.

4. THE NOISE-POWER SPECTRUM FOR FLAT-PANEL CONE-BEAM CT

Theoretical predictions of the 3-D NPS were compared to measurements. As a check on the performance of the FPI, and to start on familiar ground, the 2-D projection NPS, DQE, and NEQ were evaluated as a function of exposure. Example results are in Fig. 5, which shows the projection NPS in comparison to $S_7(u;v=0)$ [Fig. 5(a)] and as a 2-D surface [Fig. 5(b)]. Reasonable agreement between measurements and theory was exhibited in all cases, with DQE ~41% at low-frequencies (descending to ~15% near the Nyquist frequency) and NEQ scaling with exposure.

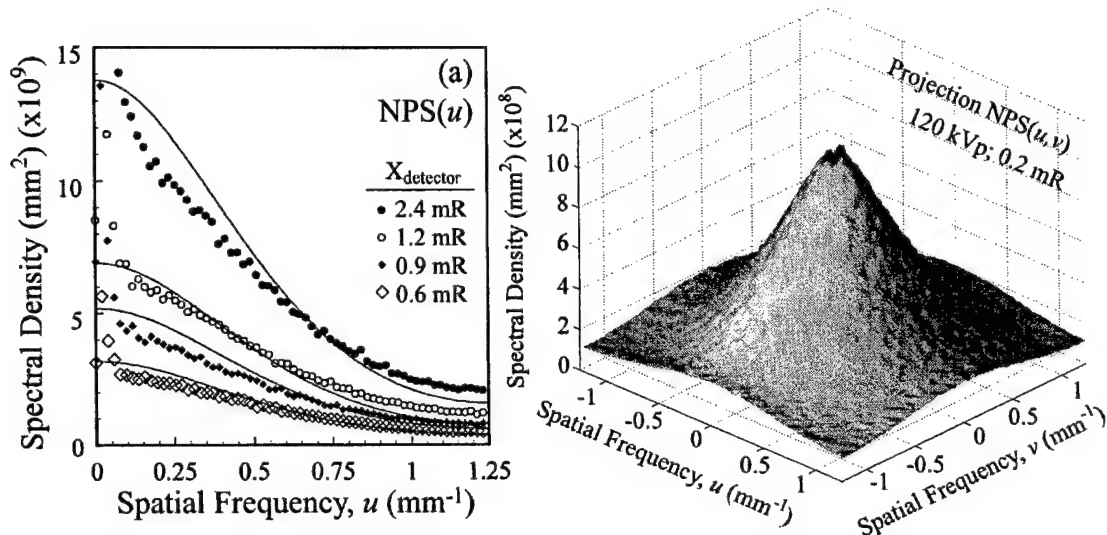


Figure 5. Projection NPS for the FPI. Measurements were performed at 120 kVp (1.5 mm Al + 0.5 mm Cu filter), with 300 flood-field projections analyzed via the direct-digital 2-D Fourier transform (i.e., the “complete” path in the $n=2$ column of Table 1). Measured projection NPS, DQE, and NEQ were in reasonable agreement with the seven-stage cascaded systems model of the FPI, as expected.

The volumetric NPS was analyzed from the 3-D images reconstructed at $(0.25 \times 0.25 \times 0.25)$ mm³ voxel size. Units for the NPS are those of the signal-squared (dimensionless HU) times volume. Results shown below were obtained using the synthesized slice technique (i.e., the $(n-1)$ “reduced” path in the $n=3$ column of Table 1). Convergence was achieved for $L > \sim 5$ mm (i.e., ~ 20 slices), and results compared well to preliminary estimates obtained using the full 3-D FFT. As shown in Fig. 6, the NPS in the (f_x, f_y) plane (i.e., the transaxial NPS) exhibits a non-monotonic shape – increasing at low spatial-frequencies (due to the ramp filter) and descending near the Nyquist frequency (due to the low-pass characteristics of the system). Theoretical results compare reasonably with the measured transaxial NPS, decreasing with exposure since the mean signal value is fixed.

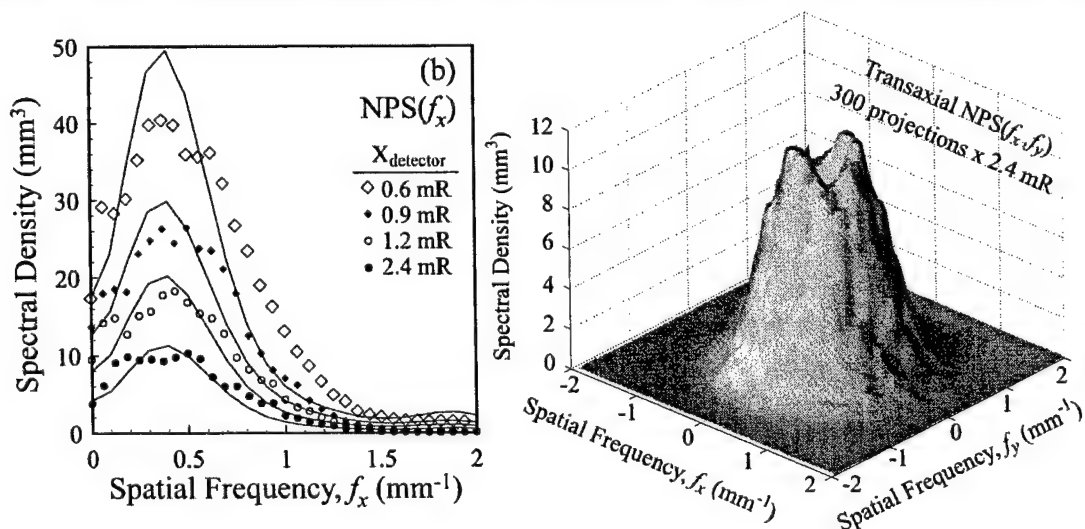


Figure 6. Transaxial NPS for the FPI-CBCT system. (a) Comparison of empirical and theoretical results in the f_x -direction for various exposure levels (per projection, at the FPI). (b) Surface plot illustrating the non-monotonic “volcano” shape of the transaxial NPS.

Figure 7 shows the volumetric NPS in the (f_x, f_z) plane (i.e., the sagittal NPS) measured as a function of exposure and shown in comparison to theoretical predictions. As in Fig. 6, the NPS exhibits spectral density that is non-monotonic in the f_x -direction, peaking near $\sim 0.5 \text{ mm}^{-1}$ (i.e., the spectrum is “green”). In the f_z -direction, however, the NPS exhibits monotonically decreasing spectral density (i.e., the spectrum is “red”), since the transfer characteristics in that dimension (i.e., the converter MTF, the pixel presampling MTF, and the interpolation function) are all band-limiting. Theoretical results compare well with measurements, and the surface plot of Fig. 7(b) illustrates the asymmetry of the volumetric NPS.

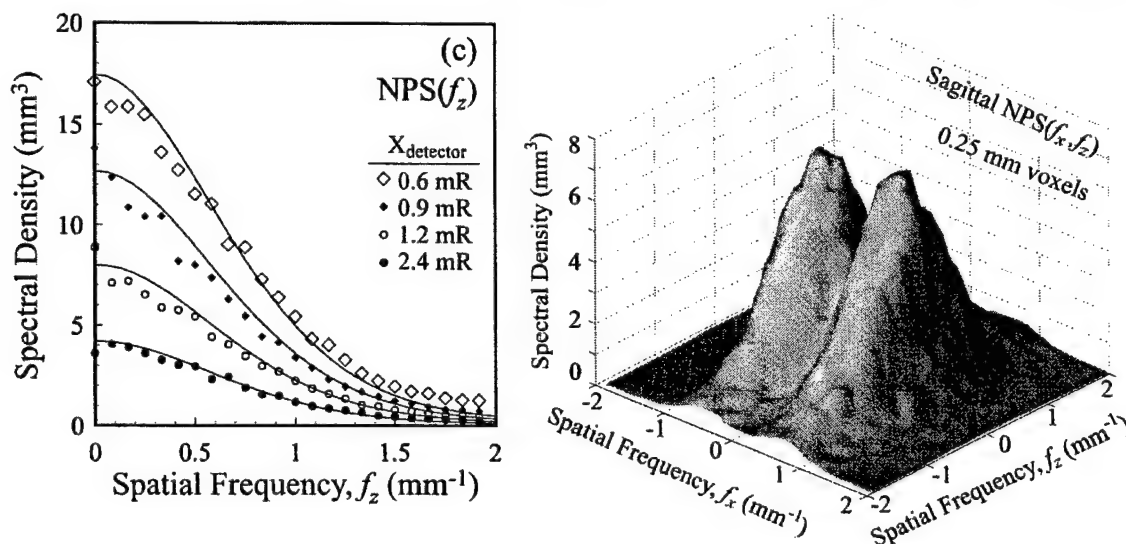


Figure 7. Sagittal NPS for the FPI-CBCT system. (a) Comparison of empirical and theoretical results in the f_z -direction at various exposure levels (per projection, at the FPI). (b) Surface plot illustrating the asymmetry of the sagittal NPS.

Finally, for purposes of illustration, the 3-D NPS [$S_{11}(f_x, f_y, f_z)$ – the presampling volumetric NPS] is shown in the volumetric surface rendering of Fig. 8. The volume data are digitally windowed and leveled to show regions of high spectral density within the sphere of the 3-D Fourier reconstruction space, and three cut-planes are shown to illustrate the NPS within each region. Grayscale intensity levels within the volume correspond to (log) spectral density values, with white representing high spectral density, and black low.

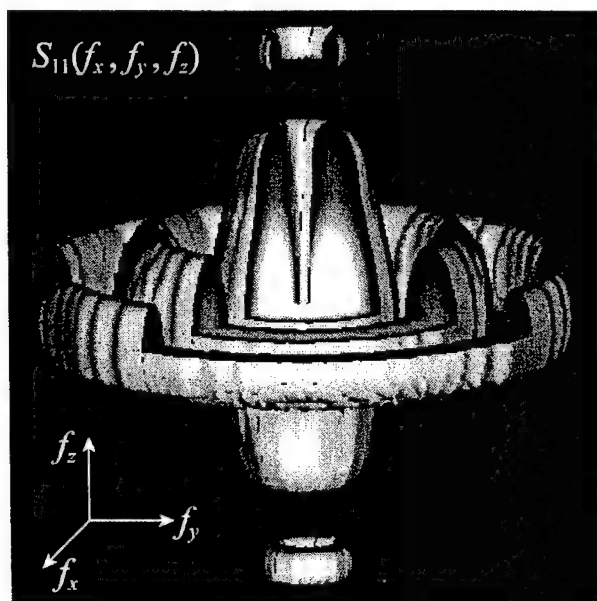


Figure 8. Volumetric surface rendering of the 3-D presampling NPS, S_{11} , of the FPI-CBCT system. The frequency domain over which the presampling NPS is shown is $\pm 5 \text{ mm}^{-1}$ in each direction, corresponding to ± 2.5 times the Nyquist limit (2 mm^{-1} , for $a_{\text{vox}} = 0.25 \text{ mm}$). In the transaxial planes, the apparent gaps between the rings of high spectral density correspond to regions of low NPS. For the presampling NPS, spectral density at the Nyquist frequency is close to zero (but not necessarily equal to zero), depending on the choice of apodization function. At the sampling frequency, spectral density is zero due to the interpolation filter. The tori above and below the (f_x, f_y) plane correspond to lobes in the NPS resulting from the product of the projection NPS (S_7) and the interpolation filter at odd multiples of the projection Nyquist frequency. (See Stages 7 and 10 in Fig. 4.) The axes in the lower-left corner show the axis orientation.

This figure illustrates the asymmetric nature of the volumetric NPS, showing the “volcano” shape in the transaxial plane and the “band-limited” shape in the sagittal and coronal planes. The potential for significant NPS aliasing is clear when one considers that this volumetric pattern is replicated in 3-D space at multiples of the sampling frequency.

5. DISCUSSION AND CONCLUSIONS

Early results in flat-panel cone-beam CT appear promising. An experimental FPI-CBCT prototype designed to mimic the geometry of a system for image-guidance in radiotherapy has demonstrated soft-tissue visibility and sub-millimeter volumetric detail in images of small animals and anthropomorphic phantoms. However, there remain numerous physical and logistical issues that need to be examined to fully assess the suitability of this technology for therapy guidance. The purpose is not to reproduce the image quality achieved by diagnostic imaging technology; rather, it is to improve the precision of local therapy by providing image quality sufficient to accomplish specific clinical objectives.

As demonstrated in the evolution of FPIs for projection radiography, empirical and theoretical analysis of the fundamental spatial-frequency noise characteristics is a valuable means of identifying the strengths and limitations of novel imaging technology. It lays the groundwork for understanding the imaging performance and provides a quantitative (and cost-effective) means of evaluating the advantages and disadvantages of various imager designs. Ultimately, such analysis can be used to direct the development of optimized systems for specific imaging tasks. In FPI-CBCT, the case is no different. For example, the analysis presented above makes explicit the relationship between the volumetric noise characteristics (i.e., S_{12}) and the input projection NPS (i.e., S_7), which is different depending on FPI design (e.g., direct and indirect detectors, and variations therein). It quantifies the effects of filter selection, interpolation, and 3-D aliasing and allows knowledgeable selection of reconstruction parameters based on the characteristics of the detector and the desired output.

The empirical methods for 3-D NPS analysis illustrate the continuity in noise characterization for n dimensional imaging systems. The theoretical methods represent a synthesis and extension of existing noise propagation models for projection imaging (specifically for FPIs) and conventional, slice-based CT. These empirical and theoretical methods form a basic component of the quantitative evaluation of FPI-CBCT technology for therapy guidance. Considering the therapy procedure – e.g., field placement in external beam radiotherapy, or seed placement in brachytherapy – one can cast the specific clinical objective in terms of an imaging task – e.g., discrimination of target and normal tissue boundaries, or detection of a seed, respectively. The spatial-frequency-dependent imaging task⁹ may in turn be analyzed in relation to the performance characteristics (i.e., the 3-D MTF, NPS, and NEQ) of the imaging system. This approach quantitatively directs the development of FPI-CBCT systems that are best suited to the specific clinical objective.

REFERENCES

1. D. A. Jaffray, J. H. Siewerdsen, and D. G. Drake, "Performance of a volumetric CT scanner based upon a flat-panel imaging array," *Medical Imaging 1999: Physics of Medical Imaging*, J. M. Boone and J. T. Dobbins III, Eds., *Proceedings of SPIE* Vol. 3659, 204-214 (1999).
2. I. A. Cunningham, M. S. Westmore, and A. Fenster, "A spatial-frequency dependent quantum accounting diagram and detective quantum efficiency model of signal and noise propagation in cascaded imaging systems," *Med. Phys.* 21(3) 417-427 (1994).
3. M. Rabbani, R. Shaw, and R. Van Metter, "Detective quantum efficiency of imaging systems with amplifying and scattering mechanisms," *J. Opt. Soc. Am. A*, 4(5) 895-901 (1987).
4. J. H. Siewerdsen, L. E. Antonuk, Y. El-Mohri, J. Yorkston, W. Huang, and I. A. Cunningham, "Signal, noise power spectrum, and detective quantum efficiency of indirect-detection flat-panel imagers for diagnostic radiology," *Med. Phys.* 25(5), 614-628 (1998).
5. H. H. Barrett, S. K. Gordon, and R. S. Hershel, "Statistical limitations in transaxial tomography," *Comput. Biol. Med.* 6: 307-323 (1976).
6. K. M. Hanson, "Detectability in computed tomographic images," *Med. Phys.* 6(5) 441-451 (1979).
7. M. F. Kijewski and P. F. Judy, "The noise power spectrum of CT images," *Phys. Med. Biol.* 32(5) 565-575 (1987).
8. J. T. Dobbins III, D. L. Ergun, L. Rutz, D. A. Hinshaw, H. Blume, and D. C. Clarke, "DQE(f) of four generations of computed radiography acquisition devices," *Med. Phys.* 22(10) 1581-1593 (1995).
9. International Commission on Radiation Units and Measurements Report No. 54, *Medical Imaging – the Assessment of Image Quality* (Bethesda MD, 1996).

Appendix H: Performance Comparison of MV and kV Cone-Beam CT

Performance comparison of MV and kV cone-beam CT

B. A. Groh ^(a,b), J. H. Siewerdsen ^(b), D. G. Drake ^(b), J. W. Wong ^(b), and D. A. Jaffray ^(b)

^(a) Deutsches Krebsforschungszentrum, Abteilung Medizinische Physik E0400,
69120 Heidelberg, Germany

^(b) Department of Radiation Oncology, William Beaumont Hospital
Royal Oak, MI 48073

Corresponding Author:
David A. Jaffray, Ph.D.
Department of Radiation Oncology
William Beaumont Hospital
3601 W. Thirteen Mile Rd.
Royal Oak, MI 48073

Phone: 248-551-7024
Fax: 248-551-3784
E-mail: djaffray@beaumont.edu

Abstract:

The performance of cone-beam CT (CBCT) systems for image-guided radiotherapy using kilovoltage and megavoltage energies is examined in this study. The inherent contrast for the different energy regimes and the signal-to-noise ratio (SNR) versus dose are investigated analytically and experimentally. The measurements are done using two CBCT systems incorporating flat-panel imagers for kV and MV energies. To predict the performance of the systems a theoretical analysis is used, which describes the voxel SNR in the reconstructed image. Theoretical predictions and experimental results agree within one standard deviation. The comparison of kV and MV CBCT demonstrates that kV imaging exhibits higher inherent contrast and achieves far better SNR at lower dose. The voxel SNR in a 25 cm diameter water phantom is 38 times higher for the kV system. The kV system exhibits superior performance in resolving low contrast objects at a lower dose than the MV system. The kV system clearly resolves 2.8 cm diameter objects with an electron density contrast of 2 % at a central dose of 1.0 cGy, whereas the MV system can only resolve objects of 4 % contrast at a dose of about 32 cGy. The potential performance of different MV detectors was examined using the theoretical analysis. In each case considered, kV CBCT still provides superior SNR. The results demonstrate the dose penalty associated with MV CT for equivalent SNR performance.

Key words: flat-panel imager, signal-to-noise in CT, kilovoltage, megavoltage

Running title: *Groh et al.* Performance comparison of MV and kV cone-beam CT

I. Introduction

With the introduction of intensity modulated radiotherapy (IMRT) it has become possible to create highly conformal dose distributions for dose escalation and normal tissue avoidance. Unfortunately, the benefits of IMRT are limited when large margins have to be used to accommodate uncertainties in target and normal tissue position at the time of treatment. In sites where day-to-day organ motion is present, image-guided therapy offers the possibility for reduced margins and dose escalation. One possible solution for image-guided (IG) therapy involves acquisition of a 3D image of the patient in treatment position for each fraction. Based on these images, delivery can be adjusted on a daily basis, permitting tighter conformation to the clinical target volume. Such IG systems must meet certain requirements, including: i.) operation in the treatment room; ii.) minimal invasion for the patient; iii.) sufficient speed as not to significantly prolong treatment time; iv.) free from distortions; and v.) the ability to differentiate soft tissue with sufficient spatial resolution to allow the desired margin reduction. A strong candidate for such an IG system is integrated cone-beam computed tomography (CBCT). Compared to radiographic approaches, CBCT does not rely on a fixed relation between target, normal tissue and the imaged bony anatomy. Compared to other IG systems, volumetric CT images are also compatible with daily treatment planning or post-treatment planning for subsequent fractions. Other in-room imaging modalities, such as ultra-sound (US), can currently not be used directly for treatment planning; they are used to match with the planning CT. This registration approach is limited in the presence of deformations. Several investigators have proposed two possible methods for integration of CT imaging with radiotherapy environment. One uses the megavoltage treatment (MV) source of the linear accelerator [1-6] while the other uses an auxiliary kilovoltage (kV) source [7-9].

There are many factors that affect the imaging performance of CBCT imaging systems. In this study the contrast of soft tissue structures and the signal-to-noise ratio (SNR) are examined as a function of x-ray energy from kV to MV. Other factors that could have a profound effect on imaging performance at various energies include beam hardening, x-ray scatter, focal spot size, and spatial resolution of the x-ray detector; these are not examined in detail in this investigation.

The ability of an x-ray imaging system to differentiate soft tissues is affected by the difference in attenuation coefficient at a given energy between the contrasting objects. For kV CT imaging (30 – 140 keV) the contrast changes

with energy, because both the photoelectric and Compton effects contribute significantly to attenuation. For MV energies (1 – 6 MeV) and for materials with low atomic number (Z), the Compton effect is by far the dominant interaction process, in which case the attenuation coefficient is proportional to electron density and is nearly independent of Z . Object contrast is therefore constant over a wide range of energies in the MV regime. For higher energies (e.g. 50 MeV) pair production becomes increasingly important and leads to an increase in contrast [6]. Since most medical linear accelerators provide a maximum photon energy of 18-25 MeV, these very high energies (i.e. > 25 MeV) were not investigated. The theoretical inherent contrast was computed analytically using materials of interest for radiation therapy from kV to MV energies.

Even high contrast objects may not be perceptible if the imaging system exhibits poor SNR performance. Such performance can be predicted using a model [2,10,11] that describes the noise characteristics of x-ray computed tomography. While such theoretical predictions generally consider that kV is superior in terms of SNR per unit dose for thicknesses and materials in the human body, no investigation has been undertaken to compare these theoretical predictions with measured results from realistic kV and MV x-ray systems. This paper examines theoretical and experimental SNR performance at kV and MV energies using well characterized kV and MV flat-panel imagers (FPIs). The results allow quantitative comparison of the performance of radiotherapy IG systems for both the kV and MV energy ranges.

II. Material and Methods

A.) Theoretical estimation of performance:

1.) Contrast versus energy:

Contrast, C , to soft tissue, as defined by ICRU 44 [12], was investigated for low Z materials, which have a density similar to water. The materials considered were: water (mass density $\rho=1\text{g/cm}^3$), soft tissue ($\rho=1.06$), eye lens ($\rho=1.07$), breast ($\rho=0.99$), muscle ($\rho=1.05$), and adipose tissue (fat) ($\rho=0.95$). Brain ($\rho=1.04$) was also investigated but is not shown in any of the graphs, as its contrast is almost the same as for muscle. All attenuation coef-

ficients and densities were taken from [13]. Contrast was calculated relative to soft tissue. The following definition of contrast was used to reflect the role of soft-tissue as the reference material:

$$(1) \quad C(E) = \frac{\mu_{object}(E) - \mu_{soft-tissue}(E)}{\mu_{soft-tissue}(E)}$$

The change in C with energy depends on the atomic number Z of the material. The relative magnitude of the contrast dependence on Z and electron density is examined for tissues of interest.

2.) Signal-to-noise ratio:

The voxel SNR in the reconstructed image of a water cylinder can be predicted by the following equation [2,10]:

$$(2) \quad SNR = \sqrt{\frac{\eta \epsilon^3 \Delta z \mu_0^2 D \rho}{KE \mu_{en} \exp(\mu_0 d / 2)}}$$

Where ϵ is the reconstructed voxel size and Δz is the slice thickness. μ_0 and μ_{en} are the linear attenuation and the energy transfer coefficients for water [13], ρ is the mass density of water, D is the central dose to the phantom, E the energy of the primary photons, and d is the diameter of the cylinder. η is the quantum detection efficiency (QDE) of the detector, calculated analytically for the kV FPI [13], and simulated using Monte Carlo methods for the MV FPI [14]. The analytical calculation is based on the following equation: $\eta = 1 - \exp(-\mu_{ph} * t_{ph})$, where t_{ph} is the thickness of the phosphor screen and μ_{ph} its attenuation coefficient. The QDE for both FPIs is displayed in Fig. 1. The theoretical prediction was also used to calculate the SNR of a standard CT Xenon gas (5 atm, thickness $t=5$ cm) detector with a QDE of 1% [1] at 2 MeV and a fluoroscopic CsI system with a QDE of 18 % [15] for 2 MeV. Values for ϵ are 0.5 mm for the MV FPI and 0.25 mm for the kV FPI. These values correspond to the voxel size of the reconstruction and the iso-center projected pixel size of the detectors. An ϵ value of 0.5 mm was assumed for the CsI and Xe detectors in order to compare SNR at equivalent spatial resolution. Although the spatial resolution of these detectors is lower than 0.5 mm (2.5 mm and 3mm, respectively) and reconstruction in a smaller grid may not be reasonable.

The factor K in equation (2) describes the influence of different filters used in the reconstruction ($K=0.091$ for the Hamming filter) [11]. It was computed using the following equation:

$$(3) \quad K = \varepsilon^3 \pi^2 \int_{-\frac{1}{2\Delta t}}^{\frac{1}{2\Delta t}} f^2 |W(f)|^2 df$$

f being the spatial frequency. Δt is the sampling step size as dictated by the detector pixel size and was set to equal the voxel size ε in the reconstruction. This is consistent with the ε in equation (2). $W(f)$ is the window function used in the filtering, e.g. a Hamming window herein.

The theory assumes that the signal within one ray is uncorrelated with neighboring rays, i. e., there is no spatial correlation due to the detector. Blurring within the phosphor of the detector will introduce correlation between rays and would therefore lower the noise estimate. The significance of ignoring the potential blur will depend on the pixel and voxel size. We assume that blurring has a negligible influence on the noise as long as the pixel aperture is the dominant component of the detector MTF. The process of interpolation during the backprojection is another source of correlation. Both effects were not accounted for in the theory. Furthermore, the theory does not account for any additional noise introduced by the readout electronics.

B.) kV cone-beam CT imaging system

The kV system has been described in detail previously [9]. To summarize, the system is mounted on a benchtop that mimics the accelerator geometry with a source to rotation axis distance of 103.3 cm and a source-detector distance of 165.3 cm resulting in a magnification factor of 1.6. The system consists of 3 components: an x-ray tube, a rotation stage, and an FPI. All components operate under computer control. The rotation stage has an angular precision of better than 0.1° . The x-ray tube (General Electric Maxi-ray 75) is a 300 kHU tube with a minimum filtration of 1.5 mm Al and an additional filtration of 0.127 mm Cu. A 100 kVp beam (mean energy of 60 keV) [16] was used for all measurements reported here. It has a nominal focal spot size of 0.6 mm. The field size at iso-center was $12.8 \times 12.8 \text{ cm}^2$. The FPI [17] (PerkinElmer Optoelectronics RID 512-400 A0) incorporates a 512×512 array of a-Si:H photodiodes and TFTs at a pixel pitch of $400 \mu\text{m}$. The images are digitized to 16 bit. An

x-ray converter (Kodak Lanex Fast (Back) screen) is placed in direct contact with the photodiode array. The imager was operated at an integration time of 3200 ms, and x-ray exposures were synchronized with readout. The images were reconstructed in a grid of $0.25 \times 0.25 \times 0.25 \text{ mm}^3$ using the FDK [18] algorithm corresponding to the pixel size of $400 \mu\text{m}$ and a magnification of 1.6.

C.) MV cone-beam CT (CBCT)

1.) The MV imaging system

A photograph of the MV system is shown in Fig. 2. The system is based on an Elekta SL20 medical linear accelerator and an FPI. The SL20 can deliver 6 MV and 18 MV photons and field shaping is achieved by an 80 leaf collimator. The FPI was attached to the drum of the accelerator. The power supply and the data cable of the FPI were kept outside of the drum for this study but could easily be integrated in the accelerator. The flat-panel imager (PerkinElmer Optoelectronics RID 256-L) incorporates a Kodak Lanex Fast Back $\text{Gd}_2\text{O}_2\text{S:Tb}$ phosphor (133 mg/cm^2) and a 1 mm copper plate. The phosphor is directly coupled to an active matrix array of $\alpha\text{-Si:H}$ photodiodes and TFTs. The array consists of 256×256 square pixels with a pixel pitch of $800 \mu\text{m}$. The array can be addressed at frame times of 79 ms, 100 ms, 200 ms, 400 ms, 800 ms, 1600 ms and 3200 ms. Images are digitized by an analog-to-digital converter (ADC) to 12 bits.

2.) Imaging geometry and procedure

The FPI was mounted to the drum of the accelerator 159 cm from the source, with a cylindrical phantom placed at iso-center (i.e. 100 cm from the source). The dose to the center of the phantom was computed to be 0.015 cGy per x-ray pulse for the $12 \times 12 \text{ cm}^2$ field used in this study. This dose was estimated using Tissue-Air-Ratio (TAR) tables. For each image the gantry angle was recorded with a precision of 0.04° by digitizing the gantry angle readout voltage.

The FPI was operated asynchronously from the accelerator; therefore the problem of interference between radiation pulses and detector readout was solved in the following way. A fixed pulse repetition time (160 ms, corre-

sponding to 6 MU/min) was chosen for the accelerator, and the integration times of the detector were set accordingly. Since the integration times 800 ms and 1600 ms are multiples of 160 ms, it was assured that exactly 5 or 10 pulses hit the detector. The line pattern appearing in some rows in some projections due to a phase difference between the addressing of the array and the x-ray pulses were not corrected. Using the 200 ms integration time, 1 pulse or 2 pulses could hit the detector; therefore, frames where two pulses hit the detector were determined off-line and rejected. The rejection was based on the analysis of the signal along the central column. If this line showed an abrupt increase in signal the frame was rejected, because this increase indicates a second pulse. Figure 3 shows the mean signal of 10 central rows for all 374 used projections. The mean value is 250 with a standard deviation of 2.3 %. This verifies that all rows used in the reconstruction were only hit by one pulse.

For all images 6 MV photons were used; and the gantry speed was set to 36 MU/360° for the two shorter detector integration times and 72 MU/360° for the longest integration time. This corresponds to dose levels of 6 cGy, 32 cGy and 65 cGy to the center of the phantom. For frame times of 1600 ms rotation was completed after 437 projections, for 800 ms after 428 projections and for 200 ms after 1701 projections, respectively. For the two longer integration times all recorded frames were used for the reconstruction whereas for the 200 ms integration time frames were selected as described in the above section.

3.) Correction for flex

The mechanical flex in the imaging system was measured by placing an 8 mm diameter ball bearing (bb) 6 mm below iso-center and recording 2000 images over 360°. The centroid of the bb in each image was determined automatically. The path of the bb is shown in Fig. 4 for the transverse and longitudinal directions. A more detailed description of the method is found in Ref. [19]. The maximum displacement is about 3.6 pixels in transverse and 1.5 pixels in the longitudinal direction. The flex correction method relies on the assumption that flex is reproducible, which was shown in [20] for an Elekta SL20 linear accelerator and different kV and MV imagers.

4.) Data processing

All recorded projections were dark and gain-corrected by subtracting an averaged dark field and then dividing the image by a measured gain field, which is the average of background corrected flood fields divided by the mean of these fields. A small number of defect pixels were median-filtered. To correct for variations in the intensity of the photon source, the signal of 9 pixels outside the phantom shadow was used as a reference signal.

5.) Reconstruction

Volumes were reconstructed using the FDK algorithm [18] correcting the backprojection ray for each projection for flex by using the data from the bb measurement. No correction in the filtering process was applied, as the error is small [21]. Since the reconstruction algorithm expects the angles for each projection to be equally spaced, the recorded angles were not used. The mean measured angular increment for all 3 sets was within 1% of the constant angular increment and the standard deviation was always less than 0.35 degree. Images were reconstructed with a voxel size of $0.5 \times 0.5 \times 0.5 \text{ mm}^3$, corresponding to the $800 \text{ }\mu\text{m}$ pixel pitch of the MV FPI and a magnification of 1.6. The small cone angle (4.6°) employed in these investigations was not expected to introduce any visible artifacts [22].

D.) Measurement of SNR and contrast phantom

To measure the SNR and contrast performance, a phantom was built from an 11 cm plastic cylinder filled with water in the upper half and with six 2.8 cm diameter cylinders made from tissue equivalent materials in the lower half. Figure 5 shows a sketch of the phantom with the six inserts: liver (electron density relative to water: $\rho_e=1.05$), polyethylene ($\rho_e=0.945$), solid water ($\rho_e=1.0$), breast ($\rho_e=0.98$), brain ($\rho_e=1.039$) and resin ($\rho_e=1.02$). The mean and standard deviation in voxel values were determined and the SNR calculated from slices reconstructed in the water-only portion of the phantom. This was done along 20 concentric circles in an annulus about the center of the image. For each circle an SNR value was determined and the standard deviation gave an estimate of the error in the SNR measurement.

Three MV images sets of the water were recorded at the three dose levels described in section II C. Six kV image sets of the water were acquired with in-air, on-axis exposure levels of 0.461 R, 0.614 R, 0.998 R, 1.459 R, 2.841

R and 5.376 R. The exposures were converted to dose at the center of the cylindrical phantom using an f factor of 0.915 cGy/R for the mean energy of 60 keV [23]. Since backscatter is not taken into account in the dose calculation for equation (2) these doses were computed without backscatter. But backscatter is a significant factor at kV energies, we estimated an backscatter factor of 1.3 for the geometry used [23]. kV images of the contrast phantom were acquired using a dose of 1.0 cGy. 300 projections were acquired for all kV measurements. Since more projections were acquired in the MV experiments the influence of number of projections on SNR was investigated in a companion study. This was done by keeping the overall exposure constant and altering the number of projections from 200 to 1200 in the kV case. No significant change was detected over the range of projections examined, and the influence of the number of projections was considered negligible for $N_{\text{projections}} \geq 200$.

III. Results

A.) Contrast

The theoretical contrast to the ICRU 44 soft tissue for the representative materials is shown in Fig. 6 (a). The contrast is constant within the MV energy range and increases at lower energies for all but one of the samples. Only the muscle equivalent material shows no significant change with energy, because its composition is very similar to the ICRU 44 soft-tissue. The other materials increase in contrast from 2 MeV to 60 keV by a factor 1.5 for water, 4.8 for fat, 6.5 for breast and -21.4 for eye lens. A slight increase in contrast at 6 MeV is caused by pair production. Figure 6 (b) shows the contrast calculated from the mass attenuation coefficient μ/ρ . This iso-dense contrast is diminished in the MV range to a great extent compared to the “full” contrast whereas the kV contrast is preserved, showing the influence of the atomic number dependence of photoelectric effect in that energy range.

B.) Theoretical prediction and measurement of SNR

Figure 7 shows the theoretical predictions of SNR for the kV and MV FPIs and for two other MV detectors. Two dose levels (1 and 10 cGy) are shown for the kV and three (1, 10 and 100 cGy) for the MV calculations. The cal-

culations were performed assuming 11 cm, 25 cm and 40 cm diameter water cylinders, a slice thickness of 5 mm and a $0.5 \times 0.5 \text{ mm}^2$ voxel size. The arrows on the lower axis indicate the mean energies of 60 keV and 2 MeV for the kV and MV CBCT systems, respectively. Figure 8 contains the measured and predicted SNRs for the kV and the MV CBCT systems. These results correspond to a resolution of $0.5 \times 0.5 \times 0.5 \text{ mm}^3$ voxels for the MV and $0.25 \times 0.25 \times 0.25 \text{ mm}^3$ for the kV reconstructions. This corresponds to the detector resolution of the respective systems. The solid lines represent the predicted theoretical performance based on equation 2. Excellent agreement between theory and measurement is demonstrated for both energies and all dose levels. Theory predicts an 61-fold increase in SNR for the 11 cm phantom, 38-fold for the 25 cm and 23-fold for the 40 cm thick phantom when changing from MV to kV flat-panel CBCT.

C.) Images of contrast phantom

Measured kV and MV reconstructions of the contrast phantom are shown in Fig. 9, each with a slice thickness of 5 mm. In the high dose MV images the four highest contrast objects are visible. In the 6 cGy image, liver and polyethylene are the only inserts which are detectable. Dark current variations in an unstable column in the MV FPI introduce ring artifacts in the center of the three MV images. Figure 9 (d) shows the same phantom imaged with the kV system at 1.0 cGy, and all inserts are visible. It's interesting to note that the wall of the plastic cylinder is also only visible in the kV image illustrating the presence of high Z in the plastic.

IV. Discussion and Conclusion

The objective of this study is to evaluate the performance of CBCT for IG in external beam radiotherapy. SNR and inherent contrast are investigated for a MV and a kV CBCT system. To extend the experimental results to different detectors a theoretical prediction of SNR versus dose has been presented. The results of measurements and calculations show clearly the superior performance of kV CBCT in terms of SNR versus dose. An IG system based on integrated MV CBCT seems not likely using currently available FPIs due the substantial dose requirement for visualization of soft-tissue structures.

Measurements and predictions of the SNR agree very well for both the kV and MV energy ranges. The underestimation of the 6 cGy MV SNR in Fig. 8 may be caused by the presence of additive noise in the electronics of the FPI. For higher doses the contribution of this source of noise decreases and the theory seems to underestimate the SNR. Blur in the detector and the interpolation process in the backprojection during the reconstruction may also be contributing factors. These processes correlate the signal in pixels of the FPI and thereby lower the noise. Neither amplifier noise nor the correlation by blur and interpolation are accounted for in the theory. The good agreement between theory and measurement suggests that the combined impact of these three effects be of minor significance for the FPIs and dose levels employed in this study.

The inherent contrast calculations show how the Z dependence of photoelectric effect increases the contrast for kV CT. The iso-dense contrast in Fig. 6 (b) shows the additional photoelectric contrast indicating a small increase in overall contrast even for soft tissues. For high Z materials, like bone, this increase will be even larger, but the density difference of bone to water will still provide substantial contrast at MV energies. As the inherent contrast calculations suggest, kV CT numbers may not always mirror electron densities due to the influence of photoelectric effect. On the other hand, the Compton effect is dominant for MV and MV CT numbers will be a better representation of electron densities. One example is the lens that shows a negative contrast to water suggesting an electron density lower than water. Whereas the electron density is in fact higher than water, as is indicated in the MV contrast. In the reconstructions this effect can be seen for the brain insert, which has a higher electron density as water but appears darker. But this could be avoided by using a harder kV spectrum, as can be seen in [9]. Since only a few samples with electron densities close to water are investigated this study does not allow a good comparison of kV and MV CBCT concerning electron density reconstruction. Other factors that have an impact on imaging performance were not examined here. Beam hardening will certainly have a larger significance on kV imaging than on MV imaging. This influence can be seen in Fig. 7 (a-b), the shape of the MV curves does not change whereas the kV curves show large differences in shape with phantom thickness. But beam hardening will rather result in artifacts in the kV reconstructions than in a drastic change in SNR compared to MV. The contribution of scatter to noise in CBCT has so far not been investigated, but it is again unlikely that the scatter will favor one system decreasing the SNR performance of either the kV or MV CBCT system significantly, although

the kV scatter-to-primary ratio is higher [24]. But high scatter values in kV and MV may prohibit the use of CBCT for direct treatment planning.

This study also demonstrates that the integration of MV CBCT with a clinical linear accelerator using FPI is feasible and the flex can be corrected. Although no integrated kV CBCT data were shown in this study, this also applies to the integration of kV CBCT, as reported in [25]. But due to the high dose required to achieve an SNR performance with the same resolution in the tissue integrated MV CBCT can at the moment not meet the IG requirements stated in the introduction. Detectors with a significantly higher DQE would have to be developed to make MV CT viable.

Acknowledgements

This research was funded in part by the Prostate Cancer Research Program Grant #DAMD-17-98-1-8497, the National Cancer Institute (CA66074), and Elekta Oncology Systems. B. Groh would like to thank the German Academic Exchange Service (DAAD) for funding his stay at William Beaumont Hospital.

References

- 1 K. J. Ruchala, G. H. Olivera, E. A. Schloesser, and T. R. Mackie, "Megavoltage CT on a tomotherapy system," *Phys. Med. Biol.* **44**, 2597-2621 (1999).
- 2 W. Swindell, R. G. Simpson, J. R. Oleson, C. Chen, and E. A. Grubbs, "Computed tomography with a linear accelerator with radiotherapy applications," *Med. Phys.* **10**, 416-420 (1983).
- 3 S. Midgley, R. M. Millar, and J. A. Dudson, "A feasibility study for megavoltage cone beam CT using commercial EPID," *Phys. Med. Biol.* **43**, 155-169 (1998).
- 4 B. M. Hesse, L. Spies, and B. A. Groh, "Tomotherapeutic portal imaging for radiation treatment verification," *Phys. Med. Biol.* **43**, 3607-3616 (1998).
- 5 H. Guan and Y. Zhu, "Feasibility of megavoltage portal CT using an electronic portal imaging device (EPID) and a multi-level scheme algebraic reconstruction technique (MLS-ART)," *Phys. Med. Biol.* **43**, 2925-2937 (1998).
- 6 A. Brahme, B. Lind, and P. Nafstadus, "Radiotherapeutic computed tomography with scanned photon beams," *Int. J. Radiat. Oncol. Biol. Phys.* **13**, 95-101 (1987).
- 7 D. A. Jaffray, D. G. Drake, M. Moreau, A. A. Martinez, and J. W. Wong, "A radiographic and tomographic imaging system integrated into a medical linear accelerator for localization of bone and soft-tissue targets," *Int. J. Radiat. Oncol. Biol. Phys.* **45**, 773-789 (1999).
- 8 T. R. Mackie, T. Holmes, S. Swerdloff, P. Reckwerdt, J. O. Deasy, J. Yang, B. Paliwal, and T. Kinsella, "Tomotherapy: a new concept for the delivery of dynamic conformal radiotherapy," *Med. Phys.* **20**, 1709-1719 (1993).
- 9 D. A. Jaffray and J.H. Siewerdsen, "Cone-Beam computed tomography with a flat-panel imager: initial performance characterization," *Med. Phys.* **27**, 1311-1323 (2000).
- 10 H.H. Barrett, S.K. Gordon, and R.S. Hershel, "Statistical limitations in transaxial tomography," *Comput. Biol. Med.* **6**, 307-323 (1976).
- 11 D. A. Chesler, S. J. Riederer, and N. J. Pelc, "Noise due to photon counting statistics in computed X-ray tomography," *J. Computer Assisted Tomography* **1**, 64-74 (1977).

- 12 International Commission on Radiation Units and Measurements, Tissue Substitutes in Radiation Dosimetry and Measurement, ICRU Report 44, (ICRU, Bethesda, MD) (1989).
- 13 J. H. Hubbell and S. M. Seltzer, Tables of X-Ray Mass Attenuation Coefficients and Mass Energy-Absorption Coefficients (version 1.02), [Online]. Available: <http://physics.nist.gov/xaamdi> [1999, December 6]. National Institute of Standards and Technology, Gaithersburg, MD (1997).
- 14 D. A. Jaffray, J. J. Battista, A. Fenster, and P. Munro, "Monte Carlo studies of x-ray energy absorption and quantum noise in megavoltage transmission radiography," *Med. Phys.* **22**, 1077-1088 (1995).
- 15 M. A. Mosleh-Shirazi, P. M. Evans, W. Swindell, S. Webb, and M. Partridge, "A cone beam megavoltage CT scanner for treatment verification in conformal radiotherapy," *Radiother. Onc.* **48**, 319-328 (1998).
- 16 D.M. Tucker, G.T. Barnes, and D.P. Chakraborty, "Semiempirical model for generating tungsten target x-ray spectra," *Med. Phys.* **18**, 211-218 (1991).
- 17 J.H. Siewerdsen, D.A. Jaffray, "A ghost story: spatio-temporal response characteristics of an indirect-detection flat-panel imager," *Med. Phys.* **26**, 1624-1641 (1999).
- 18 L. A. Feldkamp, L. C. Davis, and J. W. Kress, "Practical cone-beam algorithm," *J. Opt. Soc. Am. A* **1**, 612-619 (1984).
- 19 R. Fahrig and D.W. Holdsworth, "Three-dimensional computed tomography reconstruction using a C-arm mounted XRII: Image-based correction of gantry motion nonidealities," *Med. Phys.* **27**, 30-38 (2000).
- 20 L. Pisani, D. Lockman, D. Jaffray, D. Yan, A. Martinez, and J. Wong, "Setup error in radiotherapy: on-line correction using electronic kilovoltage and megavoltage radiographs," *Int. J. Radiat. Oncol. Biol. Phys.* **47**, 825-839 (2000).
- 21 M. Grass, R. Koppe, E. Klotz, R. Proksa, M. H. Kuhn, H. Aerts, J. Op de Beek, and R. Kemkers, "Three-dimensional reconstruction of high contrast objects using C-arm image intensifier projection data," *Computerized Medical Imaging and Graphics* **23**, 311-321 (1999).
- 22 H. Kudo, T. Saito, "Feasible cone beam scanning methods for exact reconstruction in three-dimensional tomography," *J. Opt. Soc. Am. A* **7**, 2169-2183 (1990).
- 23 F. M. Khan, *The physics of radiation therapy* (Williams and Wilkins, Baltimore/London, 1984), p 125.

- 24 D. A. Jaffray, J. J. Battista, A. Fenster, and P. Munro, "X-ray scatter in megavoltage transmission radiography: Physical characteristics and influence on image quality," *Med. Phys.* **21**, 45-60 (1994).
- 25 D. A. Jaffray, J. H. Siewerdsen, B. A. Groh, D. G. Drake, J. Wong, A. A. Martinez, "Cone-beam computed tomography on a medical linear accelerator using a flat-panel imager," *Proc XIIIth ICCR (Heidelberg)*, 558-560 (2000).

Figure 1: Quantum detection efficiency of the kV and MV flat-panel imager. The QDE was analytically calculated for the kV panel using attenuation coefficients from [13] and simulated using Monte Carlo methods for the MV panel. Both panels incorporate a 133 mg/cm^2 $\text{Gd}_2\text{O}_2\text{S:Tb}$ phosphor, and the MV FPI has an additional 1 mm copper plate. The energy range for both energies is also indicated (30 – 100 keV and 200 keV – 6 MeV). The large difference in QDE is suggestive of a favorable aspect of the kV system. The QDE for the CsI:Tl and Xenon kV CT detectors are also displayed at 2 MeV.

Figure 2: Picture of the integrated MV CBCT system based on an Elekta SL20 linear accelerator and a flat-panel imager mounted to the drum of the gantry. Attached to the table is the test phantom used to measure signal-to-noise ratio and contrast. The phantom is placed at iso-center 100 cm from the source, and the detector is mounted at 159 cm from the source. The field of view is $12.5 \times 12.5 \text{ cm}^2$.

Figure 3: Mean signal in 10 central rows of all 374 used projections for the 200 ms integration time measurement. Given a x-ray photon pulse repetition time of 160 ms one or two pulses can hit the detector. The mean shows clearly that the detector was always hit by one pulse in the used projections. The mean signal is 250 ADU with a standard deviation of 2.3 %.

Figure 4: Measured Flex for transverse and longitudinal directions. The graph shows the relative position of an 8 mm ball bearing (placed at a known position relative to the iso-center) caused by mechanical flex in the system over a 360° rotation of the accelerator gantry. Zero indicates the mean of each position. These measurements were the basis for flex correction.

Figure 5: Illustration of the Signal-to-Noise (SNR) and contrast test phantom. The phantom consists of a plastic cylinder in which 6 low contrast objects embedded in water occupy in the lower half, and the upper half was completely filled with water. The phantom has a diameter of 11 cm, the contrast cylinders have a diameter of 2.8 cm and are 7 cm high. The plastic cylinder wall is 1 mm thick (See Text for details). Numbers indicate electron density relative to water of each insert.

Figure 6 (a): Contrast of different tissue equivalent materials to soft tissue (ICRU 44). Contrast was computed as the difference from the soft-tissue value. The energy range of the used 100 kVp x-ray tube is indicated (30 keV to 100 keV). The contrast decreases with increasing energy and is fairly constant in the MV energy range. A slight change in contrast at highest energies is caused by pair production. (b) Iso-dense contrast to soft-tissue computed

using the mass attenuation coefficients μ/ρ . By dividing the attenuation by the mass density (approximately equal to the electron density) the Compton effect is reduced to a minimum and only the contrast caused by photoelectric effect or pair production for high energies is shown. The lines are interpolated between the points calculated from tabulated attenuation, and the points are indicated with the + symbol in the eye (lens) curve.

Figure 7: Signal-to-noise ratio versus energy. The arrows indicate the mean energies E_m of the two used polyenergetic spectra (60 keV and 2 MeV). The SNR was computed for 4 different detectors: a kV FPI, an MV FPI, a fluoroscopic CsI:Tl system and a standard CT Xenon gas detector. All detectors were assumed to have the same spatial resolution allowing reasonable CT reconstructions at 0.5 mm voxel size and 5 mm slice thickness. The calculations were done assuming a phantom diameter of 11 cm in a), 25 cm in b), and 40 cm in c). As the phantom gets thicker the gap between kV and MV gets smaller because of the higher attenuation for kV. But even for the 40 cm phantom the kV imager shows a clear advantage in terms of SNR vs. dose. Both FPIs incorporate a 133 mg/cm² Gd₂O₂S:Tb phosphor screen but the MV panel has an additional 1 mm of copper. The CsI:Tb crystals have a thickness t of 1 cm, the Xenon detector of $t=5$ cm and the gas is kept at a pressure of 5 atm. kV doses have to be multiplied by a backscatter factor of 1.3, which is not included in the theoretical prediction.

Figure 8: Theoretical prediction and measurements of voxel SNR in CBCT reconstructions. Squares represent the kV results, circles the MV, and the error bar is one standard deviation. Solid lines represent the theoretical prediction. The kV reconstruction consists of 0.25 mm³ voxels, and the MV of 0.5 mm³ voxels. The overestimation of SNR for low doses may be caused by additive noise in the detector. For higher doses additive noise is insignificant and blurring in the detector may cause the slight underestimation for these doses. But these effects are not accounted for in the theory. The kV doses must be multiplied by a backscatter factor of 1.3.

Figure 9: Reconstructions of the contrast phantom for 3 different MV and one kV dose levels. The materials were liver in the upper left corner then going clockwise to polyethylene, solid water, breast, brain and resin. The liver, polyethylene, breast and resin inserts are clearly differentiable in the kV image. Even water is detectable by a

small ring. The brain insert, which has a higher electron density than water appears darker. In the MV image only 4 inserts are detectable in the two high dose images. Solid water and resin are not visible. In the 6 cGy image only liver and polyethylene are detectable. Compared to the kV image the brain insert shows the expected higher contrast to water. Due to instabilities in the MV FPI some ring artifacts appear in the center. As the cylinder was clamped to a metal post in the MV system it is not perfectly round, compared to the kV image, where the cylinder was standing upright. The fact that the 1 mm wall of the plastic cylinder is visible in the kV image indicates a high Z component in the plastic.

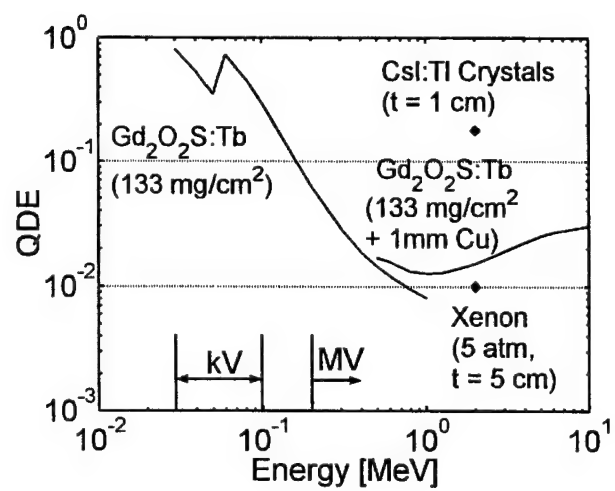


Figure 1

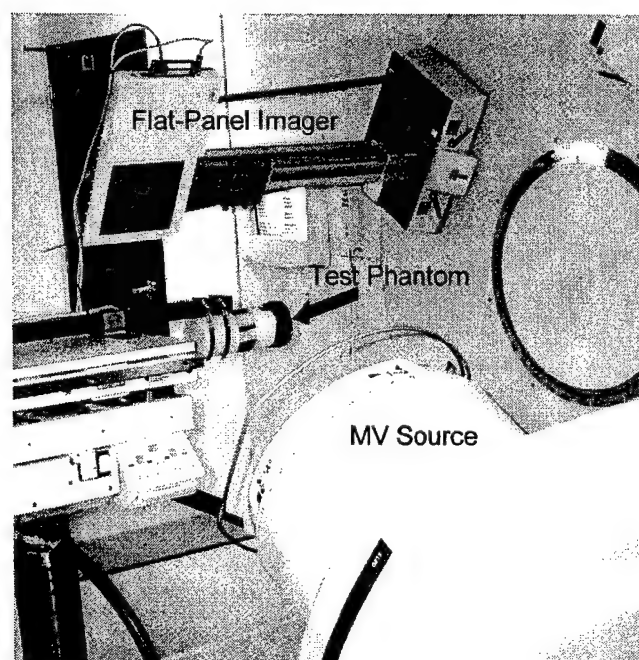


Figure 2

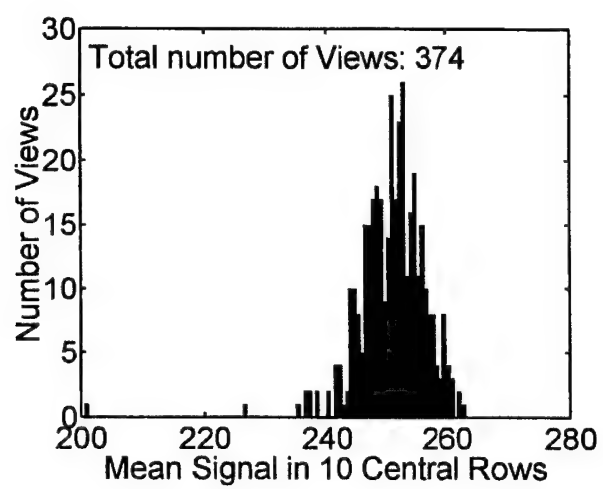


Figure 3

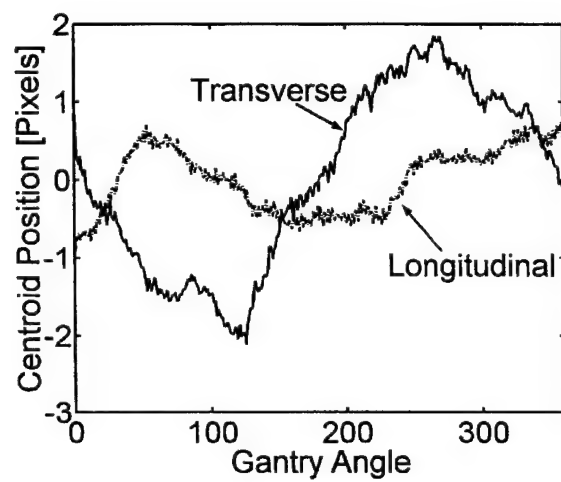


Figure 4

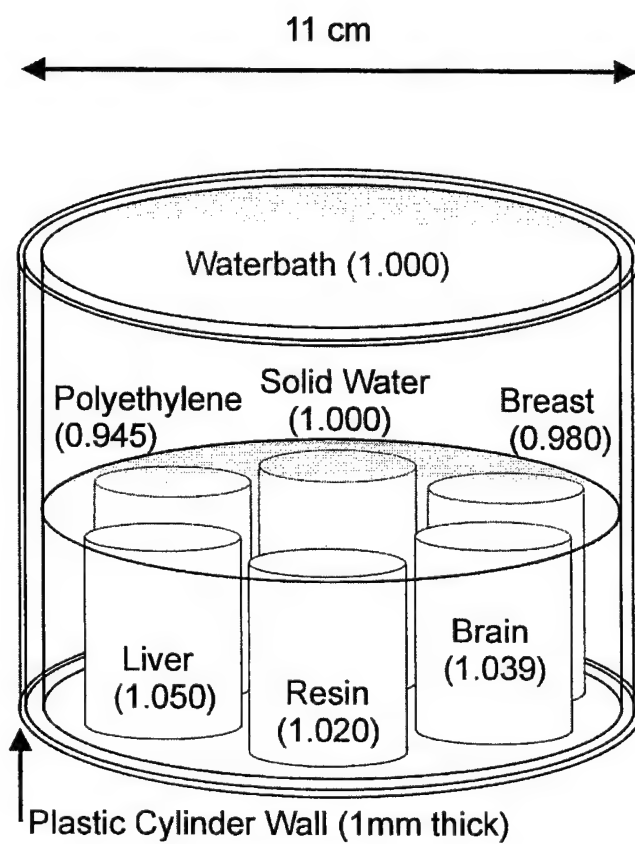


Figure 5

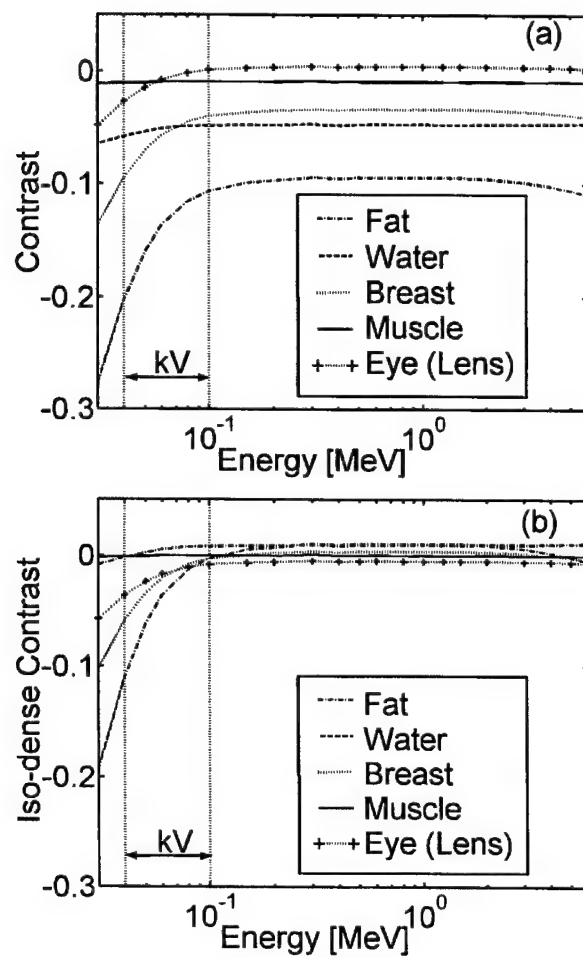


Figure 6

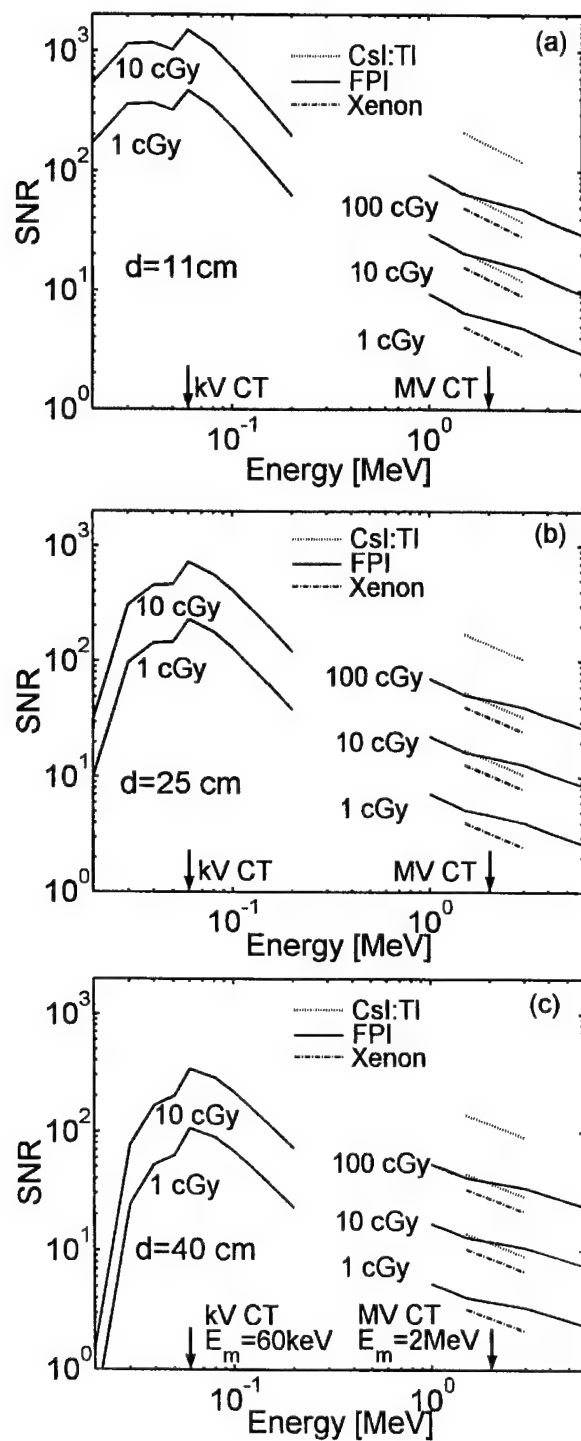


Figure 7

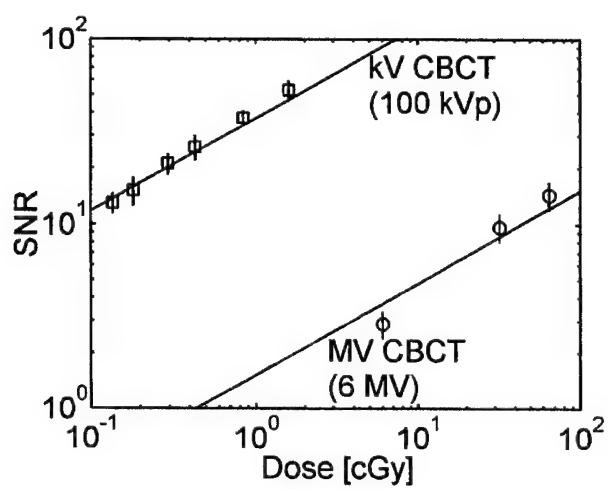


Figure 8

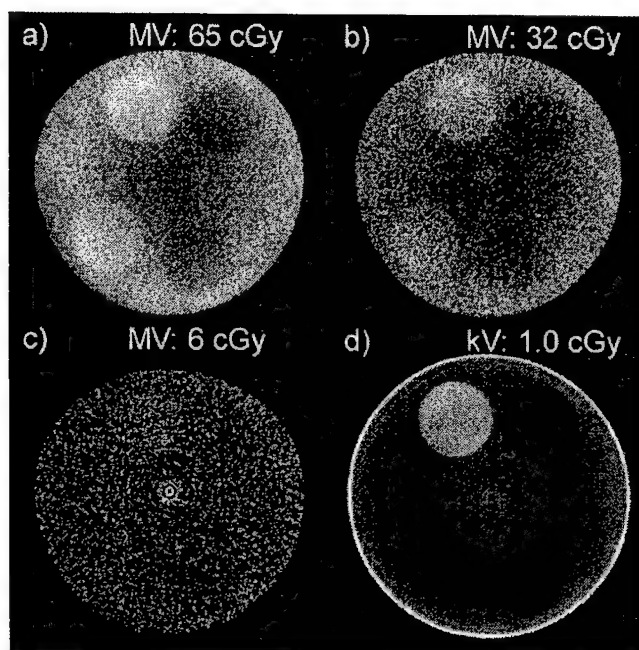


Figure 9

**Appendix I: Flat-panel Cone-beam Computed Tomography for
Image-guided Radiation Therapy**

Flat-Panel Cone-Beam Computed Tomography for Image-Guided Radiation Therapy

D.A. Jaffray, J.H. Siewerdsen, J.W. Wong, A.A. Martinez

Department of Radiation Oncology
William Beaumont Hospital
Royal Oak, MI 48073

Correspondence:

David A. Jaffray, Ph.D.
Department of Radiation Oncology
William Beaumont Hospital
3601 W 13 Mile Rd.
Royal Oak, MI
48073
Phone: (248) 551-7024
FAX: (248) 551-3784
e-mail: djaffray@beaumont.edu

Acknowledgements

The authors would like to acknowledge Dr. R. Clackdoyle and Dr. F. Noo for providing their Feldkamp reconstruction algorithm. This algorithm formed the basis of the reconstruction code used in these investigations. Dr. Marcel van Herk for providing the image viewer library employed in the cone-beam acquisition system. The skills of Mr. Walter Jendhoff are acknowledged and will be greatly missed as he pursues other endeavors. The support of Elekta Oncology Systems is greatly appreciated. The financial support of the Prostate Cancer Research Program (DAMD17-98-1-8497) made these investigations possible.

ABSTRACT

Purpose: Geometric uncertainties in the process of radiation planning and delivery constrain dose escalation and induce normal tissue complications. An imaging system has been developed to generate high-resolution, soft-tissue images of the patient at the time of treatment for the purpose of guiding therapy. The performance of the imaging system is evaluated and the application to image-guided radiation therapy is discussed.

Materials and Methods: A kilovoltage imaging system capable of radiography, fluoroscopy, and cone-beam computed tomography has been integrated with a medical linear accelerator. Kilovoltage x-rays are generated by a conventional x-ray tube which is mounted on a retractable arm at 90° to the treatment source. A 41x41cm² flat-panel x-ray detector is mounted opposite the kV tube. The entire imaging system operates under computer-control with a single application providing calibration, image acquisition, processing, and cone-beam CT reconstruction. Cone-beam CT imaging involves acquiring multiple (330) kV radiographs as the gantry rotates through 360° of rotation. A filtered back-projection algorithm is employed to reconstruct the volumetric images. Geometric non-idealities in the rotation of the gantry system are measured and corrected during reconstruction. Qualitative evaluation of imaging performance is performed using an anthropomorphic head phantom and a coronal contrast phantom. The influence of geometric non-idealities is examined by deactivating the correction scheme.

Results: Images of the head phantom were acquired with 1.2 R of exposure and illustrate the sub-millimeter spatial resolution that is achieved with the cone-beam approach. High resolution sagittal and coronal views demonstrate nearly isotropic spatial resolution. Flex corrections on the order of 0.2 cm were required to compensate gravity-induced flex in the support arms of the source and detector, as well as, slight axial movements of the entire gantry structure. Images reconstructed without flex correction suffered from loss of detail, ghosting, and streak artifacts. Reconstructions of the contrast phantom demonstrate the soft-tissue imaging capability of the system. A contrast of 47 Hounsfield Units was easily detected in a 0.1 cm thick reconstruction for an imaging exposure of 1.2 R (in-air, in absence of phantom). The comparison with a conventional CT scan of the phantom further demonstrates the spatial resolution advantages of the cone-beam CT approach.

Conclusions: A kV cone-beam CT imaging system based on a large area, flat-panel detector has been successfully adapted to a medical linear accelerator. The system is capable of producing images of soft-tissue with excellent spatial resolution at acceptable imaging doses. Integration of this technology with the medical accelerator will result in an ideal platform for high-precision, image-guided radiation therapy.

Keywords: radiotherapy, cone-beam computed tomography, linear accelerator, image guidance, flat-panel detectors

INTRODUCTION

Volumetric planning in radiation therapy has spurred the broad implementation of intensity modulated radiation therapy (IMRT) through its clear illustration of the improved dose distributions that can be achieved with this technology. Similarly, volumetric planning has pressured the community to better understand the geometric uncertainties inherent in the delivery process, resulting in methods for the engineering of three-dimensional (3-D) margins that can accommodate these uncertainties.¹⁻⁶ While the use of appropriate margins is critical if target volume coverage objectives are to be satisfied, it has become very clear that substantial increases in prescription dose could be safely pursued if these margins could be reduced.^{7,8} Investigations of the geometric uncertainties in radiation therapy illustrate the many challenges in reducing these uncertainties beyond current levels. Investigations of internal organ motion⁹⁻²⁰ have demonstrated that, for many sites, substantial reductions in geometric uncertainty require the visualization of internal structures in the reference frame of the treatment unit. The development of volumetric imaging systems for on-line image guidance has been a major focus of research in the past 5 years.

Many investigators have examined the use of the treatment beam to perform megavoltage (MV) computed tomography (CT) of the patient in treatment position. This was first proposed in 1983 by Swindell et al.²¹ and has been extended to a cone-beam implementation by Mosleh-Sharazi et al.²² Other investigators have employed various two-dimensional (2-D) detectors to perform MV cone-beam CT on conventional accelerators.²³⁻²⁶ In 1987, Brahme et al.²⁷ proposed the development of MV CT based on the 50 MV scanning photon beam of the racetrack microtron, this approach offers elevated contrast due to the increasing pair-production cross-section at x-ray energies over 1.022 MeV. More recently, Ruchala et al. have reported on the development of a helical MV CT scanner in conjunction with the Tomotherapy project.²⁸ While many investigators have been evaluating MV CT for radiotherapy verification, the only system to reach routine clinical use is that which has been developed by Nakagawa et al.²⁹ In their procedure, a pre-treatment MV CT slice is used to verify the patient setup for stereotactic radiosurgery of the lung. While utilization of the MV source for imaging seems to offer an elegant solution in terms of imaging and delivery with the same source, it faces the enormous challenge posed by the poor detection efficiency of x-ray detectors in the MV energy range.³⁰ The low efficiency results in poor signal-to-noise performance for clinically acceptable doses (<10 cGy). Furthermore, the increased radiation transport in the x-ray detector reduces the spatial resolution that can be expected at these energies.

Introducing existing imaging technologies into the therapy setting is another alternative. The clear value of integrated imaging and delivery compelled Uematsu et al. to install of a conventional CT scanner and a

conventional simulation unit in the radiotherapy suite.³¹ This approach offers volumetric imaging and real-time fluoroscopy in the treatment room. Reference between the imaging and delivery systems is maintained through a single, pivoting table that can dock to each system. The system has been employed in a variety of treatment sites, demonstrating the many advantages of integrated imaging and delivery.³²⁻³⁴

It has been our approach to integrate a kilovoltage (kV) x-ray source and large area flat panel detector on a medical linear accelerator for fluoroscopy, radiography, and cone-beam volumetric CT.^{8,35-38} The cone-beam method allows a volumetric CT image to be reconstructed from data collected during a single rotation of the gantry. This approach offers the combined functionality that has been identified by Uematsu et al.³¹ in a single integrated imaging and delivery system. Geometric cross-calibration of the imaging and delivery systems allows volumetric images to be collected in the reference frame of the delivery system.^{8,38} In this form, a highly integrated model can be envisioned in which the control system of the treatment unit orchestrates the interplay of the imaging and delivery components on a single machine. Such an approach offers the flexibility to employ a treatment procedure specific imaging strategy - whether real-time fluoroscopy, radiography, cone-beam CT, or an appropriate combination of all three. Integration will allow image-guided procedures to be performed within the tight time constraints found in the radiation therapy setting.

In previous publications the feasibility of cone-beam CT based image-guidance has been explored using a kV imaging system based upon a phosphor screen optically coupled to a charge-coupled device (CCD). The drawbacks of the CCD-based approach have been identified³⁹ and a new approach based upon large-area flat-panel detectors has been proposed.⁴⁰ The adaptation of this technology to a medical linear accelerator and an evaluation of its performance is the subject of this paper.

MATERIALS AND METHODS

Imaging System

A kilovoltage imaging system capable of radiography, fluoroscopy, and cone-beam computed tomography has been integrated with a medical linear accelerator (Elekta, SL-20, Elekta Oncology Systems, Atlanta, GA). Kilovoltage x-rays are generated by a conventional x-ray tube (Eureka Rad-92, Varian Sapphire Housing, see Table I) which has been mounted on a retractable arm that extends from the accelerator's drum structure (see Figure 1a). The tube's focal spot is located at 90° to the MV source and 100 cm (± 0.2 cm) from the rotation axis of the accelerator, sharing a common axis of rotation with the MV treatment source. The x-ray tube is powered by a 45 kW high-frequency x-ray generator that operates under computer control. A 41x41cm² flat-panel x-ray detector (Figure 1b; RID 1640, 1024x1024, Perkin-Elmer Optoelectronics, Wiesbaden, Germany) is mounted opposite the kV tube at a gantry position of -90° and a nominal detector to focal spot distance of 155

cm. The detector has many features that make it ideally suited to cone-beam CT including a high x-ray cross-section and efficient, distortion-free read-out. Such detectors were initially developed for radiography and fluoroscopy applications and these areas continue to drive improvements in their performance. The characteristics of the detector used in this system are listed in Table I. The entire imaging system operates under computer-control with x-ray exposure and detector readout synchronized via software running under the Windows NT operating system (Figure 2a). Calibration, image acquisition, processing, and cone-beam CT reconstruction execute on a personal computer equipped with a 500 MHz Pentium Xeon processor and 1 Gb of RAM.

Imaging Geometry

Accurate cone-beam CT reconstruction from x-ray radiographs requires that the projection geometry for each radiograph is known at the time of reconstruction. For systems that are well-described by a simple rotation, the projection geometry can be calculated from the angular increment provided the source, axis-of-rotation, and detector positions are well known for at least one projection. The system under investigation here cannot be described by a simple rotation. The substantial mass of the x-ray tube and detector combined with their distance from the drum face (125 cm) result in substantial flex of these components during gantry rotation.⁴¹ This flex is accommodated through a calibration procedure that maps all the non-idealities present during gantry rotation to small in-plane translations of the detector. The calibration procedure begins by placing a small steel bearing (0.8 cm diameter) at the nominal treatment isocenter of the treatment gantry. X-ray projections are taken of the bearing as the gantry rotates clock-wise through 360°. The displacement of the projected bearing location with respect to the detector is measured and the bearing location is adjusted to minimize these displacements. With the displacements minimized, a final set of projections is acquired taking some 330 projections over 360°. The centroid of the bearing in each image is determined automatically via software and recorded. From this analysis a calibration map of centroid position versus gantry angle is established. The method is insensitive to the bearing position along the axis of rotation, therefore, the bearing position is not adjusted in this dimension during the calibration procedure.

Imaging Procedure

In the current system, x-ray generation and image acquisition operate independently of gantry motion. The gantry rotation speed is selected to provide a reasonable angular increment between projections (1-2°). Measurements of angular velocity performed during system development demonstrate that the angular velocity of the gantry is not constant, however, stability increases with average velocity. The angular velocity and detector read-out rate were selected such that velocity was maximized while not introducing precise timing

requirements in the control of the detector read-out and x-ray exposure. The timing diagram for the imaging procedure is illustrated in Fig. 2b. In this approach, the image acquisition interval is set by the frame rate of the detector. The x-ray exposure immediately follows image storage with the gantry angle sampled immediately prior and following exposure. The average of the two samples is used to index the previously acquired projection calibration files and generate a geometric description of the projection. This image acquisition cycle continues until the gantry has completed 360° of rotation.

Immediately prior to acquisition, a set of 20 frames are read from the detector in the absence of x-rays to characterize the offset present in the detector signal. An additional set of dark frames is acquired in conjunction with a set of open field exposures at the same technique as employed during the cone-beam CT acquisition. Based on these images, each projection of the cone-beam CT data set is then corrected for pixel-to-pixel offset and gain variations. Defective pixels in the sensor have been previously identified and the pixel values at these locations are corrected using a 3x3 median filter. The open-field signal in each image is normalized to remove variations in x-ray exposure.

The algorithm employed to reconstruct the cone-beam CT images from the projections is based on that reported by Feldkamp et al.⁴² Briefly, the projections are weighted and filtered in one-dimension. The resulting images are interpolated at four times resolution and stored for sampling during back-projection. The geometric calibration for each image modifies the back-projection vectors to accommodate flex in the mechanical assembly. The influence of flex on the reconstructed images can be evaluated by comparing images reconstructed with and without the flex correction.

Phantom Studies

Overall performance of the system was evaluated using two phantoms: (i) an anthropomorphic head phantom, and, (ii) a contrast phantom oriented coronally.

The anthropomorphic phantom (The Phantom Laboratory, Salem, NY) consists of the head and torso of a human skeleton embedded in plastic. With the head of the phantom suspended off the end of the treatment couch, three hundred and twenty-one projections (120 kVp, 25 mA, 0.025 s) were acquired over 183 seconds as the gantry rotated through 360°. The in-air exposure (in the absence of phantom) delivered to the isocenter for this technique is 1.2 R. Four image sets were reconstructed from the projection data including a cubic volume (341×341×341 at 0.075 cm voxel pitch) and three orthogonal slices (transverse, coronal, sagittal) at full resolution (1024×1024 at 0.025 cm voxel pitch).

The contrast phantom is shown schematically in Fig. 3a and consists of twelve, 2.9 cm diameter inserts placed in a 16.7 cm diameter water bath 5 cm in depth. The inserts and their nominal CT numbers are listed in Fig. 3a.⁴³ The phantom was placed at the isocenter of the accelerator gantry on a radio-translucent support (Fig. 3b). The x-ray technique was identical to that employed for the head phantom (see above). Three hundred and thirty projections were acquired over 360° requiring 188 seconds. Four adjacent coronal slices were reconstructed at full resolution (1024×1024 at 0.025 cm voxel pitch) and averaged together to produce a 0.1 cm thick coronal slice. Images of the contrast phantom were also acquired on a conventional CT scanner (Philips SR-7000, Philips Medical Systems, Atlanta, GA) using a non-helical technique (120 kVp, 200 mA, 1 s, Standard Head Filter, 0.1 cm slice thickness, 0.1 cm table index). The technique delivered a 4.5 R exposure to isocenter (measured in the absence of the phantom). The entire length of the phantom was scanned in 180 seconds, generating 180 slices. A $25 \times 25 \text{ cm}^2$ field-of-view (FOV) was reconstructed at a resolution of 0.049 cm (512×512).

RESULTS

Geometric Non-idealities

The graphs in Fig. 4 describe the measured geometric non-idealities in the present system. Figure 4a presents an analysis of the measured gantry angle during three different cone-beam CT acquisitions. The angular velocity of the gantry was found to vary by a factor of two over the roughly 180 seconds that it takes to travel through 360°. Given that the projections are sampled at a fixed time interval (0.570 s), a higher density of projections are acquired near 0° than at $\pm 180^\circ$. The angular increment varied from 0.7 to 1.6° over the course of the acquisition. No weighting corrections were applied to accommodate these variations.

In addition to the variations in angular increment, the system also suffers from instability in the geometric relationship between the kV focal spot and the flat-panel detector. The graph in Fig. 4b illustrates the influence of gantry angle on the projected isocenter at the detector plane. If one assumes that the focal spot travels on a circular trajectory that is well described by gantry angle, then the observed displacement in projected isocenter can be attributed to flex in the detector arm or gross motion of the gantry with respect to the treatment room. The plot in Fig. 5b suggests that both types of motion are occurring in this case. The deviations in the u-coordinate are indicative of flex in the arm, while deviations in the v-coordinate are indicative of translation of the gantry along its axis during rotation (i.e. a cork-screw motion). Overall, the magnitude of this motion is less than 0.2 cm in both dimensions. The variations in angular increment and observed flex are taken into consideration during reconstruction by adjusting the back-projection to be consistent with the geometry of acquisition.

Phantom Studies

Cone-beam CT reconstructions of the anthropomorphic head phantom are shown in Fig. 5. The full FOV reconstruction (Fig. 6a) was performed at one-third resolution (0.075 cm voxel pitch) to illustrate the large FOV achieved with a single rotation of the gantry in the cone-beam approach. The large FOV and high spatial resolution of the cone-beam system are illustrated in Figs. 5b-d. Each of these images was reconstructed from the same cone-beam CT data set. The transverse image (Fig. 5b) is the conventional presentation of CT data. Figures 5c&d illustrate the fully volumetric nature of the cone-beam CT data showing excellent spatial resolution in all three dimensions. Trabecular bone structure is clearly visible in the vertebral column (Figs. 5e&f). Overall, the images are of very high quality. A slight vertical streak artifact can be seen in the sagittal cut. The source of this artifact is currently under investigation.

Figure 6 illustrates the importance of correcting for flex and gantry displacement during reconstruction. Cone-beam reconstructions of the anthropomorphic head phantom were performed with the flex correction scheme disabled and compared with those reconstructed with the flex correction active. The influence of the small corrections (<0.2 cm) is very clear when the corrected and uncorrected reconstructions are compared. The non-rigidity manifests itself in three ways: (1) an overall reduction in the visibility of detail (as seen in the anterior aspect of the hard palate in Figs. 6d&e), and, (2) the introduction of misregistration artifacts (as seen by a double bone edge along the anterior aspect of the posterior cranial fossa, directly adjacent to the mastoid air cells in Figs. 6a&b), and, (3) through the introduction of streak artifacts (horizontal streaks through the mastoid air cells in Fig. 6b). The streak artifacts are expected to become more pronounced for higher contrast objects, obscuring surrounding low contrast structures of interest. These images illustrate the importance of minimizing geometric inconsistencies between acquisition and reconstruction. Every effort should be made to eliminate geometric non-idealities or guarantee their reproducibility.

The imaging results for the coronal contrast phantom are presented in Fig. 7. The cone-beam CT image (Fig. 7a) was reconstructed at a voxel pitch of 0.025 cm with four adjacent slices averaged to effect a 0.1 cm slice in the coronal plane. Overall, the image contains significant spatial detail as well as soft-tissue contrast. The lowest detectable contrast insert is breast at 47 HU. An image of the same phantom acquired on the conventional CT scanner is presented in Fig. 7b. A direct comparison of spatial resolution and contrast detection is not possible due to differences in the voxel size (factor of 4 in voxel volume) and total dose used to form the two images. However, it is interesting to note that the two scans were acquired in the same amount of time (180 s) and the conventional CT scanner was operated at its limit of spatial resolution in the axial dimension (slice thickness of 0.1 cm). This difference in axial resolution is clearly visible in Figs. 7c&d. A low-contrast streak artifact in the x-dimension can be seen around the higher contrast bone inserts. In

conventional CT, this type of artifact is seen in the transverse plane for systems with a geometric misalignment and results from inconsistencies in the back-projection of opposing views. The presentation of such artifacts in the coronal plane indicates an axial misregistration among projections. The artifact is most likely due to subtle variations in the axial displacement of the gantry between acquisitions. Previous investigations have demonstrated hysteresis effects for this motion (i.e. the axial position of the gantry depends on both angle and direction of rotation). Further study of the stability of these corrections is required.

Overall, the cone-beam CT image demonstrates the system's capacity for high spatial resolution and soft-tissue imaging. In addition to these features, a comparison of cone-beam and conventional CT highlights the lack of any obvious geometric distortions in the cone-beam CT image.

DISCUSSION

A kV cone-beam CT system has been adapted to the gantry of a medical linear accelerator for image-guided radiation therapy. The results demonstrate that the system is capable of imaging human anatomy with excellent spatial resolution and soft-tissue sensitivity. Prior investigations have demonstrated that flat-panel detectors are suitable for cone-beam CT.^{37,40,44-48} The results reported here demonstrate that they can be applied under non-ideal geometric conditions. The magnitude of the geometric non-idealities observed in these investigations are not representative of what would be observed on all accelerator gantries. Furthermore, in-field adjustments can easily be performed to minimize the observed cork-screw motion of the Elekta SL-series gantry. The variations in angular velocity seem to be well accommodated by the reconstruction code, however, tighter integration of the imaging and accelerator control system will allow data sets to be acquired at regular angular increments.

One outstanding area of concern is in the increased presence of x-ray scatter in the cone-beam CT geometry. Scattered x-rays reaching the detector can lead to cupping artifacts and to a reduction in contrast-to-noise performance. Recent investigations have demonstrated that there are several ways of addressing these issues.⁴⁷ The first approach is to minimize the amount of x-ray scatter reaching the detector while maintaining a high detector efficiency. Our results suggest that a source-to-detector distance between 150 and 160 cm is optimal for the system reported here under conditions of high x-ray scatter, such as would be found in imaging the pelvis. The lack of any scatter artifacts in the images presented here supports this assertion. With the system geometry optimized, other methods of managing x-ray scatter can be pursued including (i) proper selection of the voxel size during reconstruction and (ii) increasing the imaging dose. These choices require procedure specific information, such as, the required spatial resolution for therapy guidance, the dimensions of the imaged anatomy, and the clinical constraints on imaging dose.⁴⁸

It is the overall objective of these investigations to develop a system that permits the radiation oncologist to confidently deliver highly conformal radiation dose distributions in the human body with a level of conformation more in keeping with radiosurgical practice than conventional radiation therapy. Given the exquisite detail visible in the images presented here, it seems clear that such a system would begin to reduce the distinction between these two disciplines, allowing exciting questions with regard to fraction size to emerge. A great deal of work remains in the development of this technology into the form necessary for high-precision image-guided radiation therapy, however, there appear to be no technological road blocks to this development. Given the results presented above, there are several questions that should be addressed if the overall objective is to be considered achievable.

What is the maximum reconstructed field-of-view with this technology? In the system described above, the reconstruction FOV is limited to a cylinder 26.5 cm in length and 26.5 cm in diameter. This limitation is a result of the requirement that the entire extent of the imaged object remain in the detector's FOV for all projections. Cho et al.⁴⁹ have developed a method to increase the reconstruction FOV of small detectors by offsetting the detector with respect to the central axis. This approach requires the collection of projections over a full 360°. An offset scheme with 7.6 cm of overlap at the detector would provide a 48 cm reconstruction FOV – comparable to that of a conventional CT scanner. This development is of critical importance for sites below the head and neck.

What is the fastest acquisition time? In the current system, acquisition of a complete cone-beam data set requires approximately 180 seconds. Improvements to the synchronization software would allow these acquisition times to be reduced by a factor of two (i.e. 90 seconds) with the detector read-out rate (0.285s/frame) limiting acquisition. Faster frame rates (30 frames/sec) have been reported for similar detectors,⁵⁰ such a frame-rate would allow 330 projections to be acquired in under 15 seconds. At this rate, the maximum angular velocity of the gantry (1 revolution per minute) becomes the limiting factor. This restriction is attributed to the IEC (International Electromechanical Commission, Geneva, Switzerland) recommendations with respect to the motion of medical devices and may need to be reconsidered considering the advantages of faster image acquisition rates.

How long would the clinician have to wait for the images to reconstruct? The clinical application of cone-beam CT for image-guided therapy in an on-line setting requires images to be available within a few moments of acquisition. The images presented in this paper were reconstructed on a 500 MHz Pentium Xeon processor equipped with 1Gb of RAM requiring from a few minutes for a single high-resolution transverse slice to 21 hours for a 341x341x341 cube. Very little effort has been invested in accelerating these reconstruction times because high-speed reconstruction are commercially available and can be readily adapted for cone-beam CT

reconstruction of the data presented here.^{51,52} Such systems are capable of reconstructing 256^3 volumes from 300 projections (1024×1024) in under 60 seconds.⁵¹ Given this level of performance, it is possible that the imaging data will be available within moments of the completion of acquisition.

How is integrated cone-beam CT different from conventional CT in directing therapy? The significant difference between conventional CT and cone-beam CT in this regard is that cone-beam CT data can be referenced directly to the treatment machine coordinates without the use of skin marks, body frame, or calibrated couch movements. The use of cone-beam CT for guiding therapy requires the development of a calibration scheme to cross-calibrate the imaging and treatment components of the accelerator. In this approach, every voxel in the reconstructed image can be located relative to the MV source and various field shaping devices. An interface is envisioned in which the graphical representations of these components can be presented relative to the recently acquired cone-beam CT images. Of course, if this system is capable of calculating dose it would be of great interest to visualize the dose with respect to the imaged anatomy. Thus, it is becoming clear that a reasonable interface to the accelerator may contain many of the features currently found in a 3-D treatment planning system. The cone-beam system also has the significant advantage of high-quality fluoroscopy and radiography in the treatment room, permitting simplified radiographic verification of patient positioning as well as fluoroscopic monitoring during the delivery process – the latter being of particular importance with the increased use of small treatment fields as found in step-and-shoot or dynamic IMRT.

What must be developed to make full use of this imaging technology? An area of critical importance for clinical implementation is in the tight integration of the imaging system within the linear accelerator's control system. It is clear that clumsy imaging procedures will not succeed in today's busy treatment centers. Only through the development of a highly integrated imaging and delivery system will this technology begin to make clinical inroads. An unfortunate case in point can be found in the very slow acceptance of the portal imaging technology. While this technology has been available in one form or another for many years, it has yet to be adopted in the mainstream. This is a consequence of the lack of appropriate tools for image interpretation and failure to fully integrate these systems into a clinically acceptable practice. It is hoped that we can learn from this experience and not have the technology developed here suffer a similar fate.

CONCLUSION

Overall, the results of these investigations support the hypothesis that cone-beam CT based on large area, flat-panel detectors is an excellent candidate for image-guided high-precision radiation therapy. Previous investigations of the fundamentals of flat-panel performance and their application to cone-beam CT have demonstrated that such an approach can provide the performance necessary for soft-tissue imaging in the

treatment geometry. The results reported here demonstrate that this technology can be successfully adapted to a conventional medical linear accelerator accommodating the presence of geometric non-idealities. While it is clear that the technology is capable of producing volumetric images of a patient in treatment position, it may not be immediately clear how these images will be employed in directing therapy.

We propose the development of a new generation of radiation therapy treatment machines capable of integrated imaging and delivery, providing a means for seamless target identification, real-time monitoring and efficient delivery. Such a system is based upon cone-beam CT imaging and cone-beam radiation delivery. In this approach, the advantages inherent in the clinical flexibility of the conventional gantry structure are further heightened through the capacity for low-dose soft-tissue imaging and fluoroscopic monitoring.

REFERENCES

1. ICRU Report 50. Dose specification for reporting external beam therapy with photons and electrons. International Commission on Radiation Units and Measurements, Washington, D.C., 1978
2. Mageras GS, Kutcher GJ, Leibel SA. A method of incorporating organ motion uncertainties into three-dimensional conformal treatment plans. *Int J Radiat Oncol Biol Phys* 35:333-342, 1996
3. Killoran JH, Kooy HM, Gladstone DJ, et al. A numerical simulation of organ motion and daily setup uncertainties: implications for radiation therapy. *Int J Rad Oncol Biol Phys* 37:213-221, 1997
4. McKenzie AL, van Herk M, Mijnheer B. The width of margins in radiotherapy treatment plans. *Phys Med Biol* 2000 Nov; 45(11):3331-42
5. Yan D, Lockman D, Brabbins et al. An off-line strategy for constructing a patient-specific planning target volume in adaptive treatment process for prostate cancer. *Int J Radiat Oncol Biol Phys*. 2000 Aug 1;48(1):289-302.
6. van Herk M, Remeijer P, Rasch C, Lebesque JV. The probability of correct target dosage: dose-population histograms for deriving treatment margins in radiotherapy. *Int J Radiat Oncol Biol Phys* 2000 Jul 1;47(4):1121-35
7. Balter JM, Chen GTY, Pelizzari CA, et al. On-line repositioning during treatment of the prostate: a study of potential limits and gains. *Int. J. Rad. Oncol. Biol. Phys.* 27, 137-143 (1993).
8. Jaffray DA, Drake DG, Yan D, et al. Conebeam tomographic guidance of radiation field placement for radiotherapy of the prostate. *Int. J. Rad. Onc. Biol. Phys.* (accepted) (1999).
9. Roeske JC, Forman JD, Mesina CF, et al. Evaluation of changes in the size and location of the prostate, seminal vesicles, bladder, and rectum during a course of external beam radiation therapy. *Int. J. Rad. Onc. Biol. Phys.* 33(5) 1321-1329 (1995).
10. Stroom JC, Koper PC, Korevaar GA, et al. Internal organ motion in prostate cancer patients treated in prone and supine treatment position. *Radiother. Oncol.* 51(3) 237-248 (1999).
11. Hanley J, Lumley MA, Mageras GS, et al. Measurement of patient positioning errors in three-dimensional conformal radiotherapy of the prostate. *Int. J. Rad. Onc. Biol. Phys.* 37(2) 435-444 (1997).
12. Lattanzi J, McNeeley S, Pinover W, et al. A comparison of daily CT localization to a daily ultrasound-based system in prostate cancer. *Int. J. Rad. Oncol. Biol. Phys.* 43, 719-725 (1999).
13. Balter JM, Sandler HM, Lam K, et al. Measurement of prostate movement over the course of routine radiotherapy using implanted markers. *Int. J. Rad. Onc. Biol. Phys.* 31(1) 113-118 (1995).
14. Crook JM, Raymond Y, Salhani D, et al. Prostate motion during standard radiotherapy as assessed by fiducial markers. *Radiother. Oncol.* 37: 35-42 (1995).
15. Althof VGM, Hoekstra CJM, and te Loo HJ. Variation in prostate position relative to adjacent bony anatomy. *Int. J. Rad. Onc. Biol. Phys.* 34(3) 709-715 (1996).
16. van Herk M, Bruce A, Kroes G, et al. Quantification of organ motion during conformal radiotherapy of the prostate by three dimensional image registration. *Int. J. Rad. Onc. Biol. Phys.* 33(5) 1311-1320 (1995).
17. Remeijer P, Rasch C, Lebesque JV, and van Herk M. A general methodology for three-dimensional analysis of variation in target volume delineation. *Med. Phys.* 26(6) 931-940 (1999).
18. Kubo HD, Hill BC. Respiration gated radiotherapy treatment: a technical study. *Phys Med Biol.* 41:83-91, 1996

19. Balter JM, Ten Haken RK, Lawrence TS, et al. Uncertainties in CT-based radiation therapy treatment planning associated with patient breathing. *Int J Rad Oncol Biol Phys* 36:167-74, 1996
20. Hanley J, Debois MM, Raben GS, et al. Deep inspiration breath-hold technique for lung tumors: the potential value of target immobilization and reduced lung density in dose escalation. *Int J Rad Oncol Biol Phys* 36, Suppl 18, 1996
21. Swindell W, Simpson RG, Oleson JR, et al. Computed tomography with a linear accelerator with radiotherapy applications. *Med. Phys.* 10(4) 416-420 (1983).
22. Mosleh-Shirazi MA, Evans PM, Swindell W, Webb S, Partridge M. A cone-beam megavoltage CT scanner for treatment verification in conformal radiotherapy. *Radiother. Oncol.* 48(3):319-28 (1998)
23. Hesse BM, Spies L, Groh BA Tomotherapeutic portal imaging for radiation treatment verification. *Phys Med Biol* 43(12):3607-16 (1998)
24. Groh BA, Spies L, Hesse BM, and Bortfeld T, Megavoltage computed tomography with an amorphous silicon detector array, *International Workshop on Electronic Portal Imaging*, pp 93-94, Phoenix AZ, 1998.
25. Midgley S, Millar RM, and Dudson JA. A feasibility study for megavoltage cone beam CT using commercial EPID. *Phys. Med. Biol.* 43, 155-169 (1998).
26. Guan H and Zhu Y. Feasibility of megavoltage portal CT using an electronic portal imaging device (EPID) and a multi-level scheme algebraic reconstruction technique (MLS-ART). *Phys. Med. Biol.* 43, 2925-2937 (1998).
27. Brahme A, Lind B, and Nafstad P. Radiotherapeutic computed tomography with scanned photon beams. *Int. J. Radiat. Oncol. Biol. Phys.* 13, 95-101 (1987).
28. Ruchala KJ, Olivera GH, Schloesser EA, and Mackie TR. Megavoltage CT on a tomotherapy system. *Phys. Med. Biol.* 44(10) 2597-2621 (1999).
29. Nakagawa K, Aoki Y, Tago M, et al. Megavoltage CT-assisted stereotactic radiosurgery for thoracic tumors: original research in the treatment of thoracic neoplasms. *Int J Radiat Oncol Biol Phys.* 48(2):449-57. (2000)
30. Groh BA, Siewerdsen JH, Drake DG, et al. Performance comparison of MV and kV cone-beam CT. *Med. Phys.* (accepted)
31. Uematsu M, Shioda A, Tahara K, et al. Focal, high dose, and fractionated modified stereotactic radiation therapy for lung carcinoma patients: a preliminary experience. *Cancer* 82(6), 1062-1070 (1998).
32. Uematsu M, Sonderegger M, Shioda A, et al. Daily positioning accuracy of frameless stereotactic radiation therapy with a fusion of computed tomography and linear accelerator (focal) unit: evaluation of z-axis with a z-marker. *Radiother. Oncol.* 50(3), 337-339 (1999).
33. Uematsu M, Fukui T, Shioda A, Tokumitsu H, et al. A dual computed tomography linear accelerator unit for stereotactic radiation therapy: a new approach without cranially fixated stereotactic frames. *Int. J. Radiat. Oncol. Biol. Phys.* 35(3), 587-592 (1996).
34. Uematsu M, Shioda A, Suda A, et al. Intrafractional tumor position stability during computed tomography (CT)-guided frameless stereotactic radiation therapy for lung or liver cancers with a fusion of CT and linear accelerator (FOCAL) unit. *Int J Radiat Oncol Biol Phys.* 48(2):443-8. (2000)
35. Jaffray DA, Drake DG, Moreau MM, et al. A radiographic and tomographic imaging system integrated into a medical linear accelerator for localization of bone and soft-tissue targets. *Int. J. Rad. Onc. Biol. Phys.* 44(5) (1999).
36. Jaffray DA, Drake DG, Moreau M, and Wong JW. Radiographic and tomographic localization of bone and soft-tissue targets on a clinical accelerator. *Int. J. Radiat. Oncol. Biol. Phys.* (in press, 1999).

37. Jaffray DA, Siewerdsen JH, and Drake DG. Performance of a volumetric CT scanner based upon a flat-panel imaging array. *Medical Imaging 1999: Physics of Medical Imaging*, J. M. Boone and J. T. Dobbins III, Eds., Proceedings of SPIE Vol. 3659, 204-214 (1999).
38. Pisani L, Lockman D, Jaffray D, et al. Setup Error in Radiotherapy: On-line Correction Using Electronic Kilovoltage and Megavoltage Radiographs. *Int J Radiat Onc Biol Phys* 47(3) 825-39 (2000)
39. Drake DG, Jaffray DA, and Wong JW. Characterization of a fluoroscopic imaging system for kilovoltage and megavoltage radiography. *Med. Phys.* 27(5) 898-905 (2000)
40. Jaffray DA and Siewerdsen JH. Cone-beam computed tomography with a flat-panel imager: initial performance characterization. ,” *Med. Phys.* 27(6) 1311-23. (2000)
41. Moreau M, Drake D, and Jaffray D. A novel technique to characterize the complete motion of a medical linear accelerator. *Med. Phys.* 25(7) A191 (1998).
42. Feldkamp LA, Davis LC, and Kress JW. Practical cone-beam algorithm. *J. Opt. Soc. Amer. A.* 1(6) 612-619 (1984).
43. Electron density CT Phantom RMI 465 (Gammex RMI, Madison WI).
44. Siewerdsen JH and Jaffray DA. A ghost story: spatio-temporal response characteristics of an indirect-detection flat-panel imager. *Med. Phys.* 26(8) 1624-1641 (1999).
45. Siewerdsen JH and Jaffray DA. Cone-beam computed tomography with a flat-panel imager: effects of image lag. *Med. Phys.* 26(12) 2635-2647 (1999).
46. Siewerdsen JH and Jaffray DA. Cone-beam CT with a flat-panel imager: noise considerations for fully 3-D imaging. *Medical Imaging 2000: Physics of Medical Imaging*, J. M. Boone and J. T. Dobbins III, Eds., Proceedings of SPIE Vol. 3336, pp. 546-554 (2000).
47. Siewerdsen JH and Jaffray DA. Optimization of x-ray imaging geometry (with specific application to flat-panel cone-beam computed tomography). *Med. Phys.* 27(8) 1903-1914 (2000).
48. Siewerdsen JH and Jaffray DA. Cone-beam computed tomography with a flat-panel imager: Magnitude and effects of x-ray scatter. *Med. Phys.* 28(2) (2001).
49. Cho P, Johnson RH, Griffin TW. Cone-beam CT for radiotherapy applications. *Phys. Med. Biol.* 40, 1863-1883 (1995).
50. Granfors PR. Performance characteristics of an amorphous silicon flat panel x-ray imaging detector. *Medical Imaging 1999: Physics of Medical Imaging*, J. M. Boone and J. T. Dobbins III, Eds., Proceedings of SPIE Vol. 3659, 480-490 (1999).
51. Private communication, Horst Bruning, Ph.D., TeraRecon Inc., (San Mateo CA).
52. Private communication, Raul Brauner, Mercury Computing Inc., (Chelmsford, MA).

Figure Captions

Figure 1: (a) Medical linear accelerator modified for kV cone-beam computed tomography (CT). A kV x-ray tube has been mounted on a retractable arm at 90 degrees with respect to the treatment source. A large-area ($41 \times 41 \text{ cm}^2$) flat-panel imager is mounted opposite the kV x-ray tube on a fixed mount. (b) Photo of the large-area flat-panel detector employed in this investigation (black) in comparison to a smaller detector employed in previous investigations^{30,40,44-47} and an anthropomorphic head phantom. Labels indicate the pixel format and pixel pitch of the imagers (i.e., 1024×1024 pixels and 512×512 pixels at $400 \mu\text{m}$ pitch, respectively) as well as the approximate sensitive area (i.e., $\sim 41 \times 41 \text{ cm}^2$ and $\sim 21 \times 21 \text{ cm}^2$, respectively).

Figure 2. (a) Screen capture representation of the Windows NTTM-based application developed to acquire, process, reconstruct, and store projection and cone-beam CT datasets. Fields for patient information, treatment data, and image datasets are integrated with the clinical database. Processes for image acquisition and processing are similar to those previously described,⁴⁰ and reconstruction is performed using a modified version of the cone-beam filtered backprojection.⁴² The host workstation used in this work was a 500 MHz Pentium Xeon PC with 1GB of RAM. (b) Timing diagram illustrating synchronization of imager readout, gantry rotation, and x-ray exposure. The period between image frames is constant throughout acquisition ($T_{\text{frame}} = 570 \text{ ms}$). Gantry rotation initiates prior to the first projection and is measured by means of a calibrated potentiometer circuit. Gantry angle is sampled twice at each projection – immediately prior to and immediately following delivery of the x-ray exposure – and averaged to yield the angle of the projection view. X-ray exposures (120 kVp; 25 mA; 25 ms in this investigation) were reproducible within $\sim 3\%$, with slight variations in tube output normalized according to the detector signal measured in a region of the field that was unoccluded in all projections. To achieve fast data transfer and storage, all projections for a single acquisition (330 images nominally) were stored in host memory (660 MB allocated for storage of projection data).

Figure 3. Contrast phantom used in preliminary evaluation of the accelerator-based cone-beam CT system. (a) Schematic illustration of the contrast phantom, consisting of 12 electron density inserts (Gammex RMI, Middleton WI) in water. Electron density relative to water (ρ_e^{rel}) and approximate Hounsfield unit (HU) are listed in the table for each insert. (b) Schematic illustration of the contrast phantom oriented coronally with respect to the linear accelerator-based cone-beam CT imaging system. Such orientation of the phantom illustrates the contrast performance of the imaging system in the x - z plane and illustrates the uniform volumetric spatial resolution characteristics of the imaging system (i.e., spatial resolution in the z -dimension similar to that in the transaxial x - y plane, unlike in conventional CT, where z -resolution is limited by slice thickness).

Figure 4. Geometric non-idealities in the accelerator-based cone-beam imaging system. (a) Angular velocity measured as a function of gantry angle at a specified “assisted set-up” (ASU) value of 20, which is intermediate

to the fastest and slowest ASU speeds. Non-uniform angular velocity – e.g., by a factor of ~ 2 between $\theta=0^\circ$ and $\theta=\pm 180^\circ$ – results in non-equiangular intervals in the projection data (acquired at fixed intervals of T_{frame}). Gantry rotation is fastest at $\theta=\pm 180^\circ$ (MV head at nadir), slowest at $\theta=0^\circ$ (MV head at zenith), and described by a parabolic curve (solid line). Error bars span two standard deviations. (b) Projected location of the center of rotation of the focal spot as a function of gantry angle. The range of motion is fairly small (~ 0.2 cm), with high- and low-frequency components found to be highly reproducible.⁴¹

Figure 5. Cone-beam CT images of the anthropomorphic head phantom. (a) Surface rendering of the volume data identifying axial, coronal, and sagittal planes and illustrating the uniform volumetric spatial resolution of the data. The image in (a) was reconstructed using a $(26.5 \times 26.5 \times 26.5)$ cm³ field-of-view with 0.075 cm voxels (i.e., ~ 3 times the nominal voxel pitch of 0.025 cm). (b) Axial, (c) coronal, and (d) sagittal cuts through the volume data reconstructed at full resolution (1024×1024 voxels at 0.025 cm voxel pitch). The data illustrate the uniform quality and quantity of image data acquired in a cone-beam CT acquisition. The high spatial resolution is illustrated further in by magnifying the bony anatomy surrounding the brain stem (e&f). The potential for high-precision radiotherapy of the spine becomes evident.

Figure 6. Influence of flex-induced geometric non-idealities on reconstructed images of the anthropomorphic head phantom. Images reconstructed with the flex correction [magnified (a) axial and (d) sagittal views] are compared to those reconstructed without the corrections [(b) axial and (e) sagittal]. Close inspection of the images reveals subtle qualitative differences, including blurring of trabecular detail and slightly increased streak artifacts for the reconstructions without flex correction. Differences images [(c) axial and (f) sagittal] highlight the regions most influenced by the presence of flex and indicate the overall pattern of misregistration introduced when geometric non-idealities are ignored. Three manifestations of the flex have been identified in the difference images (1) loss of detail, (2) misregistration of signal leading to image shift or phantom signal, and (3) the appearance of streaks that may obscure the visibility low-contrast objects.

Figure 7. Coronal images of the contrast phantom (i.e., images in the x - z plane) acquired using the accelerator-based cone-beam CT system and using a conventional CT scanner. (a) Coronal slice through cone-beam CT dataset (voxel dimension: $0.025 \text{ cm} \times 0.1 \text{ cm} \times 0.025 \text{ cm}$), with the slice thickness of 0.1 cm obtained by averaging four adjacent slices reconstructed at nominal voxel size. (b) Coronal slice through conventional CT scan of the contrast phantom (voxel dimension: $0.05 \text{ cm} \times 0.1 \text{ cm} \times 0.05 \text{ cm}$). The image in (b) corresponds to a cut through 180 consecutive transaxial slices, whereas that in (a) is a cut from the volume data acquired from a single rotation about the phantom. Magnified views (c) and (d) illustrate the differences in spatial resolution in the z -dimension. For the cone-beam CT data, resolution is comparable that in the transaxial plane (~ 0.05 cm). For the conventional CT image, on the other hand, z -resolution is limited by the slice thickness (in this case, 0.1 cm).

Tables

Table I. Characteristics of imaging system components.

Linear Accelerator	
Manufacturer	Elekta Oncology Systems
Model	SL-20, SLi/MLCi
Mass	~5 ton
Range of Rotation	$\pm 185^\circ$
Maximum Angular Velocity	1 rpm
kV X-ray Source	
Manufacturer	Varian Associates
Model	RAD-92, Sapphire Housing
Mass (tube, housing, collimator)	44.6 kg
Anode Heat Capacity	600 kHU
Target Angle	12°
Focal Spot Size	0.6, 1.2 mm
Inherent Filtration	2 mm Al.
Additional Filtration	0.127 mm Cu
Generator	40 kW High-Frequency
Flat-Panel X-ray Detector	
Manufacturer	Perkin-Elmer Optoelectronics
Model	RID-1640 AL1
Mass	22 kg
Detector Housing Dimensions	$67.2 \times 59.9 \times 4.4 \text{ cm}^3$
X-ray Converter	$133 \text{ mg/cm}^2 \text{ Gd}_2\text{O}_2\text{S:Tb}$
Detector Size	$41 \times 41 \text{ cm}^2$
Pixel Matrix Format	1024×1024
Pixel Pitch	$400 \mu\text{m}$
Detector Pixel Elements	a-Si:H Photodiode and Thin-Film Transistor (TFT)
Fill Factor	0.80
Photodiode Capacitance	8.4 pF
Photodiode Bias Voltage (V)	-6 V
Photodiode Charge Capacity	~48 pC
Charge Transfer Time	35 μs
ASIC Charge Capacity	5 pC
Maximum Frame Rate	3.5 fps
Detector Dynamic Range	> 83 dB
Image Lag	< 3%
Digitization	16 bits

Table II. Summary of imaging geometry and acquisition / reconstruction parameters.

kV Imaging Geometry	
Focal Spot-Isocenter Distance (nominal)	100 cm
Focal Spot – Detector Distance (nominal)	155 cm
Cone Angle	15°
Field of View (at isocenter)	(26.5 x 26.5) cm ²
Location of Projected Isocenter on Detector: (Fig.4)	
<i>u</i> -Coordinate (pixel address)	517.6 ± 1.1
<i>v</i> -Coordinate (pixel address)	496.3 ± 1.2
Cone-Beam CT Acquisition Parameters	
Tube Potential	120 kVp
Tube Current	25 mA
Exposure Time	25 ms
Number of Exposures (nominal)	330
Total mAs for CBCT Acquisition	206 mAs
Tube Output (mR/mAs in air at isocenter)	5.7 mR/mAs
Total Exposure (mR in air at isocenter)	1.2 R
Angular Range of Projection Views	360°
Average Angular Velocity of Gantry	(2.0±0.2) °/sec
Average Angular Increment	(1.1 ±0.3)°
Detector Readout Interval (Frame Time)	570 ms
Time for CBCT Acquisition	188 sec
Processing & Reconstruction Parameters	
Flood-Field Processing	Gain / Offset Correction
Pixel Defect Filter	3x3 Median Filter
Reconstruction Filter	Hamming
Reconstruction Field of View (at isocenter)	(26.5 x 26.5 x 26.5) cm ³
Reconstruction Matrix (nominal)	(1024 x 1024 x 1024) voxels
Voxel Dimensions (nominal)	(0.025 x 0.025 x 0.025) cm ³

**Appendix J: Flat-Panel Cone-Beam CT: A Novel Imaging
Technology for Image-guided Procedures**

Flat-Panel Cone-Beam CT: A Novel Imaging Technology for Image-Guided Procedures

J. H. Siewerdsen^{*a}, D. A. Jaffray^a, G. K. Edmundson^a, W. P. Sanders^b, J. Wong^a, and A. A. Martinez^a

^aDepartment of Radiation Oncology; ^bDepartment of Diagnostic Radiology
William Beaumont Hospital, Royal Oak MI

ABSTRACT

The use of flat-panel imagers for cone-beam CT signals the emergence of an attractive technology for volumetric imaging. Recent investigations demonstrate volume images with high spatial resolution and soft-tissue visibility and point to a number of logistical characteristics (e.g., open geometry, volume acquisition in a single rotation about the patient, and separation of the imaging and patient support structures) that are attractive to a broad spectrum of applications. Considering application to image-guided (IG) procedures – specifically IG therapies – this paper examines the performance of flat-panel cone-beam CT in relation to numerous constraints and requirements, including time (i.e., speed of image acquisition), dose, and field-of-view. The imaging and guidance performance of a prototype flat-panel cone-beam CT system is investigated through the construction of procedure-specific tasks that test the influence of image artifacts (e.g., x-ray scatter and beam-hardening) and volumetric imaging performance (e.g., 3-D spatial resolution, noise, and contrast) – taking two specific examples in IG brachytherapy and IG vertebroplasty. For IG brachytherapy, a procedure-specific task is constructed which tests the performance of flat-panel cone-beam CT in measuring the volumetric distribution of Pd-103 permanent implant seeds in relation to neighboring bone and soft-tissue structures in a pelvis phantom. For IG interventional procedures, a procedure-specific task is constructed in the context of vertebroplasty performed on a cadaverized ovine spine, demonstrating the volumetric image quality in pre-, intra-, and post-therapeutic images of the region of interest and testing the performance of the system in measuring the volumetric distribution of bone cement (PMMA) relative to surrounding spinal anatomy. Each of these tasks highlights numerous promising and challenging aspects of flat-panel cone-beam CT applied to IG procedures.

1. INTRODUCTION

Modern diagnostic medicine commands a vast and versatile arsenal of medical imaging technologies that provide exquisite visualization and characterization of disease. Bringing such technology to bear on behalf of the therapist – e.g., surgeons, interventional radiologists, and radiation oncologists – is a subject of considerable interest, evidenced by the widespread activity in merging advanced imaging tools (particularly volumetric imaging) with the therapy environment. For example, the value of computed tomography (CT) in guiding neurosurgical procedures has been recognized for nearly two decades,¹ and CT is a fairly common component of multi-modality IG interventional procedures. Similarly, the value of integrated imaging and therapy is recognized in efforts to bring CT into the theatre of radiation therapy.² In these and other implementations for IG procedures, it is important to understand that diagnostic imaging technology need not translate directly into the therapy setting – i.e., it need not reproduce the diagnostic data; rather, it must perform at a level sufficient to accomplish a given image-guidance task. Furthermore, there may be even more challenging requirements defined by the procedure – e.g., patient access, speed, and so forth – that may take precedent over image acquisition.

The advent of flat-panel imagers (FPIs) applied to cone-beam CT appears to offer a promising technology for volumetric imaging, providing 3-D visualization of soft and bony tissues with excellent spatial resolution (typically sub-millimeter). This technology could potentially deliver a powerful and elegant solution for IG procedures by combining the speed and flexibility of digital radiography / fluoroscopy with the wealth and quality of spatial information provided by volume CT – in a single device and in an open geometry. Considerable effort has been devoted to investigating the fundamental physical characteristics and performance of flat-panel cone-beam CT, and early results are promising. Advancing this technology to application to IG therapies, however, requires consideration of the numerous clinical, engineering, and logistical constraints associated with specific procedures. Furthermore, an understanding of how the physical performance of the imaging system relates to accomplishing a specific imaging task is essential to revealing the potential and limitations of the technology. Such an understanding also provides a guide for knowledgeably adapting the imaging technology to various image-guidance tasks. This paper provides a brief examination of issues surrounding the application of flat-panel cone-beam CT to IG procedures, highlighting some of the more significant clinical constraints within which the technology must perform and investigating performance with regard to procedure-specific imaging tasks.

2. FLAT-PANEL CONE-BEAM CT

2.1 Experimental Platforms for Flat-Panel Cone-Beam CT

Early investigation of the fundamental performance of flat-panel cone-beam CT has employed a number of experimental platforms, including a benchtop system,³ a rotating CT gantry,⁴ a rotating medical linear accelerator gantry,⁵ and an isocentric C-arm. Each of these experimental prototypes incorporates a conventional x-ray tube and an FPI, from which multiple 2-D projections acquired as a function of position about an object are used to reconstruct a fully 3-D image of the object – e.g., using various forms of the FDK algorithm⁶ for cone-beam filtered back-projection. Figure 1(a) illustrates one such embodiment in which the x-ray source and FPI are operated synchronously, with the object to be imaged placed on a computer-controlled rotation stage. In this case, the detector is a $41 \times 41 \text{ cm}^2$ FPI, comprising a 1024×1024 matrix of a-Si:H photodiodes and thin-film transistors at $400 \mu\text{m}$ pixel pitch.⁷ This experimental platform provides a geometrically precise test-bed for investigation of fundamental physical performance issues in flat-panel cone-beam CT, including the effects of image lag,⁸ detector performance,⁹ x-ray scatter,¹⁰ and imaging geometry¹¹ on cone-beam reconstructions. Platforms involving a rotating gantry structure introduce the additional complexity of orbit non-idealities, including variability in angular velocity and mechanical flex; however, such non-idealities have been shown to be manageable by means of a simple calibration procedure and angle-dependent shifts of the projection data.^{5,12} While volumetric images of high-contrast objects (e.g., bone and contrast-enhanced vasculature) have been demonstrated using a C-arm mounted XRII,¹³ implementation of C-arm mounted FPIs offer the possibility of high-quality volumetric imaging including visualization of soft-tissues. An early prototype for C-arm based flat-panel cone-beam CT is shown in Fig. 1(b), where a smaller ($21 \times 21 \text{ cm}^2$) FPI is attached to a portable isocentric C-arm. Such embodiments potentially offer significant economic and clinical advantages for IG procedures, including relatively low capital cost, an open geometry with excellent patient access, and multi-mode radiographic, fluoroscopic, and volumetric imaging from a single imaging device.

2.2 Physical Performance

Flat-panel imagers are ideally suited to cone-beam CT in several respects, providing a large-area, distortionless, real-time detector that is robust in a rotating geometry and immune to stray magnetic fields. Still, there are numerous performance requirements, including speed, dynamic range, and efficiency, that present significant challenges to FPI technology. For example, analysis of the detective quantum efficiency (DQE) reveals that conditions corresponding to volumetric imaging of large anatomy, such as the pelvis, places strict requirements on FPI electronic noise and efficiency of x-ray conversion. Toward such ends, the FPI of Fig. 1(a) exhibits low electronic noise that is void of correlation and approaches the theoretical lower limit of the pixel dark noise,⁷ thereby allowing the FPI to operate at low exposures without significant degradation in DQE. However, there is still significant room for improvement through incorporation of improved x-ray converters. For example, as shown in Fig. 2(a), the DQE is limited to $\sim 40\%$ at low spatial-frequencies, which can be improved to $\sim 60\%$ through incorporation of a thick CsI:Tl layer.¹⁴ These and other advances are at the heart of the on-going development of FPIs for radiography and fluoroscopy, all to the advantage of deployment in cone-beam CT.

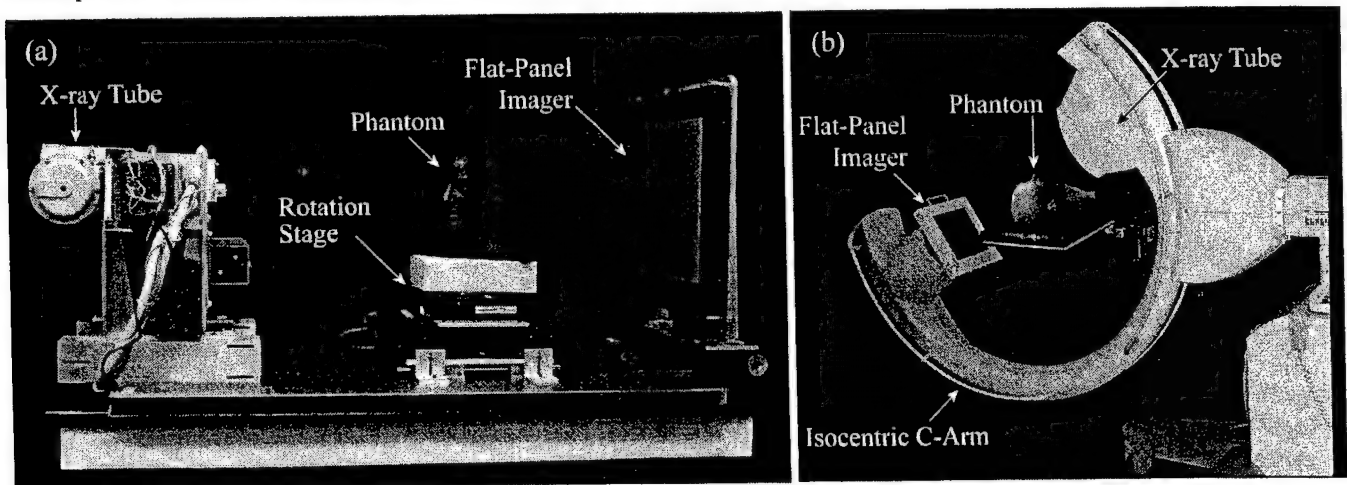


Figure 1. Example experimental platforms for flat-panel cone-beam CT. (a) Benchtop system developed to investigate physical performance issues under a well-defined geometry. (b) Prototype for flat-panel cone-beam CT in which an FPI is docked to the front of the XRII on an isocentric C-arm [Siemens SireMobil, Erlangen Germany] for research, and removed to return the C-arm to clinical use. A dedicated prototype (not shown) incorporates the larger-area FPI mounted directly on a higher-power C-arm [Siemens PowerMobil].

Also shown in Fig. 2 are flat-panel cone-beam CT images acquired with the large-area benchtop prototype. The surface-rendered image of a skull phantom [Fig. 2(b)] illustrates the uniform quality and quantity of volumetric data throughout a fairly large field-of-view (FOV) ($25.6 \times 25.6 \times 25.6 \text{ cm}^3$). Furthermore, the excellent 3-D spatial resolution is evident in the high level of skeletal detail visible throughout the reconstruction. This feature is illustrated moreover in the sagittal image of an amputated limb [Fig. 2(c)] reconstructed at full resolution (0.25 mm voxels). In addition to the high level of detail in bony anatomy (trabecular structure and joint spaces), the image also demonstrates soft-tissue visualization and discrimination between muscle, fat, and necrotic flesh – in dimensions (i.e., sagittal and coronal planes) otherwise afforded only by high-resolution spiral CT or MRI. For IG procedures, however, one must consider not only the visibility of anatomical structures, but also their visibility in the presence of interventional tools. In Fig. 2(d), a transaxial image is shown of a low-contrast phantom that was used previously³ to demonstrate soft-tissue visibility comparable to that achieved with a conventional CT scanner. In Fig. 2(d), however, a 1.23 mm diameter syringe needle was introduced to the phantom, causing some artifacts associated with beam-hardening, but no significant loss in the visibility of low-contrast structures.

2.3 Flat-Panel Cone-Beam CT as a Modality for Image-Guidance

In addition to the physical performance and volumetric image quality demonstrated in early investigations of flat-panel cone-beam CT, this technology appears to offer a number of logistical features that are particularly well-suited to IG procedures. Since volumetric images can be reconstructed from projections acquired from a single rotation about the patient (rather than multiple rotations in a helical path), the mechanical embodiment of flat-panel cone-beam CT can be relatively simple, e.g., in comparison to a CT scanner. Specifically, the volumetric image (e.g., ~26 cm in longitudinal extent) can be acquired without translation of the patient, thereby decoupling the imaging system from the patient support. Implemented in a structure such as a C-arm or other “two-headed” gantry, this allows for volumetric imaging within an open geometry, with the associated advantages of improved patient access and even portability. Some interventional procedures have already begun to utilize FPI technology in its ability to provide high-quality radiographic and fluoroscopic imaging; implementation of flat-panel cone-beam CT gives the added potential of combined radiographic, fluoroscopic, and tomographic imaging in a single imaging device. Therefore, although there are numerous medical applications with a demand for high-quality volumetric imaging (e.g., screening and diagnosis), it is application in IG procedures – specifically IG therapy – that best captures the advantageous characteristics of flat-panel cone-beam CT. Moreover, this technology is highly adaptable with regard to specific IG tasks, and characteristics such as the imaging geometry, dose, spatial resolution, and handling of artifacts can be tuned within logistical constraints in a manner that best suits a particular clinical objective.

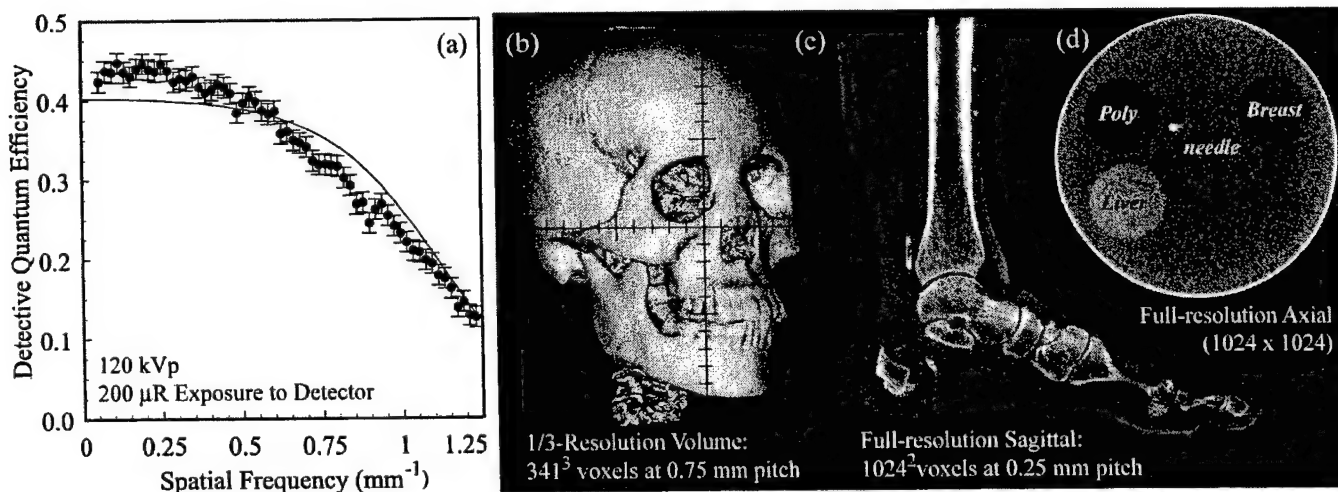


Figure 2. Physical performance and example images in flat-panel cone-beam CT. (a) DQE measured and predicted¹⁵ for the FPI of Fig. 1(b), which comprises a $133 \text{ mg/cm}^2 \text{ Gd}_2\text{O}_2\text{S:Tb}$ x-ray converter. (b) Surface rendering of a skull phantom [(341x341x341) voxels at 0.75 mm voxel pitch]. (c) Sagittal image of an amputated limb [(1024x0124) voxels at 0.25 mm voxel pitch]. (d) Transaxial image of a low-contrast phantom with a steel syringe needle inserted in the FOV. Despite the presence of slight streak and image lag artifacts, the presence of the needle did not seriously degrade the visibility of low-contrast structures from that previously³ demonstrated. Results throughout this paper were obtained using a 120 kVp beam, with ~1.5 mm Al and 0.127 mm Cu added filtration. Unless otherwise noted, volumetric images were reconstructed from 300 projections acquired at 1.2° increments with 0.15 mAs per projection.

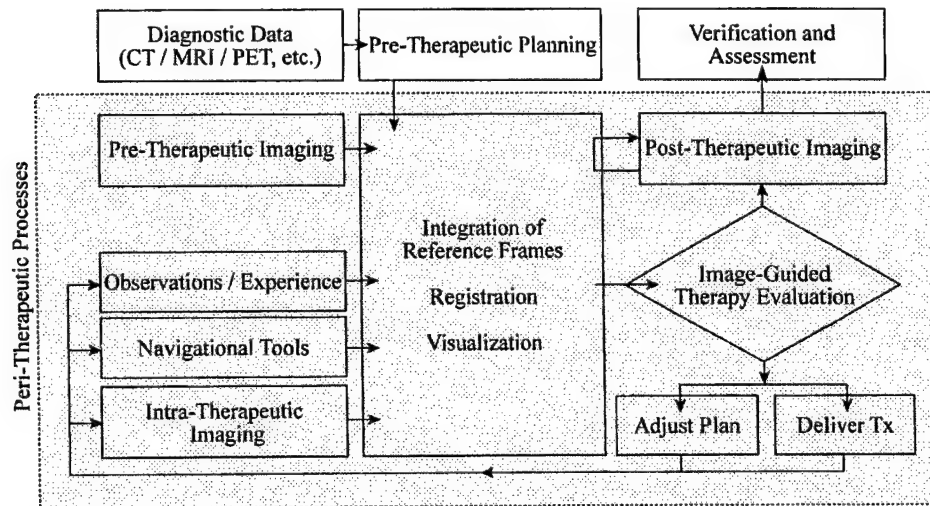


Figure 3. Flow diagram illustrating the processes involved in image-guided therapy, where “therapy” is considered in a general sense (e.g., ranging from radiation therapy to neurosurgery). The focus of these processes is the “image-guided therapy evaluation” (diamond shape) – i.e., the continuous assessment on the part of the therapist to adjust the current therapeutic plan, deliver treatment according to the current plan, or conclude the procedure. The shaded area designates “peri-therapeutic processes” for which timing is critical – i.e., the temporal aspects of information acquisition, feedback, analysis, and evaluation are critical to therapeutic success.

3. APPLICATION TO IMAGE-GUIDED PROCEDURES

While there remain challenging issues to be investigated to ensure that the full potential of flat-panel cone-beam CT is revealed, application of the technology to IG procedures (specifically IG therapy) broadens the onus from matters of physical performance to matters of ensuring that the system can function within clinical and logistical constraints, and that the resulting image information is relevant and useful to therapy guidance. The even broader question of *how* the image data are put to use in therapy – e.g., integration with navigational reference frames – is somewhat beyond the scope of the current paper but is of equal importance. In considering the constraints and requirements imposed upon flat-panel cone-beam CT for IG procedures, at least three challenging issues must be addressed – time, dose, and field-of-view – each considered below in the context of peri-therapeutic imaging.

3.1 Peri-Therapeutic Imaging

Figure 3 presents a generalized model of processes in IG therapy, including input from diagnostic procedures, the cycle of peri-therapeutic processes, and post-therapeutic assessment. Depending on the specific type of therapy (e.g., radiation therapy, neurosurgery, interventional procedures, etc.), the particulars of each process will vary or could be merged, but are present to some extent. Although the model illustrates the flow of information surrounding the “image-guided therapy evaluation,” it does not necessarily convey the temporal relationships between processes – some occurring instantaneously and/or continuously, and others in a finite time interval. The entire process begins with the input of diagnostic data and the formation of a plan as to how best to “treat.” Vital to the peri-therapeutic process is a mechanism for integration of reference frames (e.g., registration / fusion of data relative to the world reference frame) that allows the therapist to interact with (e.g., visualize) the information. Pre-therapeutic imaging provides a measure of state “today” and sets the peri-therapeutic cycle in motion, wherein the therapist continually evaluates a course of action – adjusting the current plan, delivering treatment, or concluding the procedure. Intra-operatively, the decisions of the therapist feed back in the cycle through her observations and experience, the available navigational tools and therapeutic instruments, and temporally proximal information provided by intra-therapeutic imaging – all integrated to the world reference frame and made available to the therapist for further evaluation. When the therapy session is finally judged to be complete, post-therapeutic imaging provides information for verification and assessment of the procedure. Peri-therapeutic imaging, therefore, refers to the pre-, intra-, and post-therapeutic imaging processes occurring in the arena of therapy. It is this facet of IG procedures to which flat-panel cone-beam CT appears particularly well suited.

3.2 Speed of Image Acquisition

This issue of time is implicit and vitally important to the processes illustrated in Fig. 3, and the questions of how fast and how often images can be acquired must be answered for any imaging technology entering the arena of IG procedures. For flat-panel cone-beam CT, the issue of *how fast* depends primarily on three parameters – the speeds of FPI readout, gantry motion, and image reconstruction – and in the case that each occurs in parallel, the slowest represents the bottleneck.

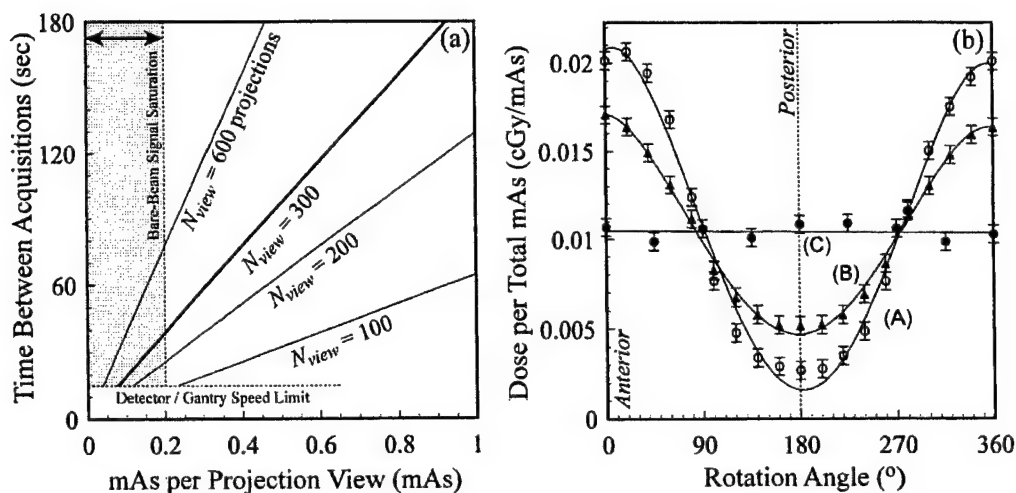


Figure 4. (a) Time required between volume acquisitions as a function of x-ray tube heat loading. The gray region at left indicates the sensitive range of the FPI in Fig. 1(a). (See discussion in text, below.) (b) Absolute dose (per unit total mAs) measured in a cylindrical "head" phantom at three positions [(A) periphery, (B) half-radius, and (C) center] as a function of projection view angle. A typical volume acquisition for the system in Fig. 1(a) involves 300 views across 360° at 0.15 mAs per view, giving a total of 45 mAs – i.e., ~0.5 cGy.

The FPI in Fig. 1(a) provides a maximum frame rate of ~3 frames per second (fps), while panels developed for fluoroscopy demonstrate frame rates of ~30 fps. Therefore, depending on the number of projection views (N_{view}), acquisition of projection data can occur in just a few seconds. For example, for $N_{view} = 100$ acquisition requires ~3 s for a fast FPI [~33 s for the FPI in Fig. 1(a)]. For $N_{view} = 300$, which has been shown to provide soft-tissue visualization without significant view-aliasing artifacts, acquisition of projection data requires ~10 s for a fast FPI [~100 s for that in Fig. 1(a)]. Speed of gantry motion depends on the mechanical embodiment. For implementation on an accelerator for radiation therapy,⁵ rotation through 360° is currently restricted to 60 s by IEC recommendations. The isocentric C-arm in Fig. 1(b) (SireMobil) and the prototype dedicated to flat-panel cone-beam CT (PowerMobil) can each rotate through ~180° in ~120 s. Image reconstruction can be expedited through dedicated hardware featuring parallel processing units for image processing and reconstruction. For example, a 32-processor subsystem (TeraRecon XTrillion, San Mateo CA) can produce a (512^3) volume reconstruction from ~300 (512^2) projections in ~80 s. Therefore, no single parameter – speed of FPI readout, gantry motion, or reconstruction – represents an obvious bottleneck; furthermore, considering the on-going developments in FPIs for fluoroscopy and reconstruction hardware for cone-beam CT, it is likely that the volume can be made available immediately on completion of gantry motion. Other considerations, however, may detract from such an ideal situation – e.g., the use of image gating (e.g., active breathing control¹⁶) to reduce motion artifacts, or alternative geometries (e.g., offset-detector geometry¹⁷) and/or non-circular trajectories¹³ that may or may not support simultaneous acquisition and reconstruction.

The issue of *how often* volume images can be acquired depends on at least two constraints: heat loading of the x-ray tube and acceptable radiation dose limits. Taking as example the anode heat capacity (270 kHU) and cooling rate (~230 HU/s) of the C-arm (PowerMobil) based flat-panel cone-beam CT prototype, Fig. 4(a) plots the time required between acquisitions assuming (as a conservative estimate) that the heat load for a single acquisition is deposited instantaneously and that the next acquisition can proceed only after cooling the anode completely. In that case, the heat load input for an acquisition is $\sim(1.35)(\text{kVp})(\text{mAs})(N_{view})$, where mAs is the mAs per projection view. The time between acquisitions, therefore, is given by that product divided by the anode cooling rate and is plotted in Fig. 4(a) as a function of mAs. For example, an acquisition with $N_{view} = 300$ at 0.1 mAs (giving ~50% of detector saturation) requires a waiting period of ~20 s before the next acquisition. It is unlikely, therefore, that heat loading poses a serious constraint on the frequency of acquisitions in most cases, which is consistent with the commonly recognized advantage that cone-beam CT relaxes tube loading requirements through high efficiency of x-ray utilization (e.g., compared to fan-beam CT).

3.3 Radiation Dose

Consideration of radiation dose is central to application of flat-panel cone-beam CT in IG procedures, affecting the range of procedures for which use of this technology is appropriate as well as the number of times that such devices can be used peri-therapeutically in a given session. Measurements of absolute dose were performed using the system in Fig. 1(a) with a Farmer chamber and polystyrene phantoms approximating "head" and "abdomen" object size. Absolute dose was measured at three locations within each phantom (at center, half-radius, and periphery). For example, Fig. 4(b) shows measurements for the case of the head phantom at a cone angle giving full coverage of the large-area FPI (~15° cone angle,

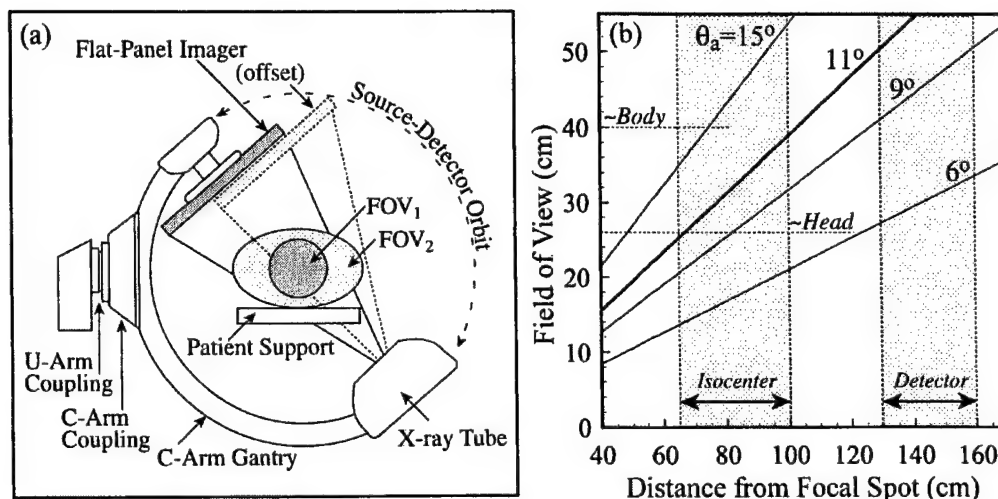


Figure 5. (a) Illustration of FOV constraints for a centered geometry, accommodating smaller anatomy (FOV₁ shaded dark gray), and an offset geometry,¹⁷ accommodating larger anatomy (FOV₂ shaded light gray) but requiring 360° orbital extent. (b) Maximum lateral FOV as a function of distance from source for various anode target angles. Ranges in S_{AD} and S_{DD} are indicated in gray. A large anode angle is required for large FOV, although this can be relaxed by tilting the tube (within focal spot size constraints) or cross-mounting the tube.

giving ~26x26 cm² FOV at isocenter). At the center of the phantom, dose is constant across all projection views at ~0.01 cGy per total mAs (where total mAs equals N_{view} times the mAs per projection). For nominal acquisition conditions (300 views at 0.15 mAs per projection), this corresponds to a total dose of ~0.47 cGy. The dose at the half-radius and periphery is obtained by integrating the measured curves across the orbital range, giving a total dose at these locations that is similar to that at the center of the phantom (~0.47 and ~0.49 cGy, respectively, at 0.15 mAs per projection). These values decrease at smaller cone angles due to reduced x-ray scatter.

These results are encouraging in several respects. First of all, the dose is fairly low – less than the dose from a conventional CT scan and comparable to less than a minute of fluoroscopic imaging. Secondly, the implementation of FPIs with improved DQE offers the potential for further reduction in dose without degradation in physical performance. Finally, the ability to image at low dose opens a valuable degree of freedom in managing other factors of physical performance. For example, the higher levels of x-ray scatter associated with cone-beam geometry have been shown to result in loss of contrast-to-noise ratio, which can be recovered through knowledgeable selection of parameters such as resolution and/or dose.¹⁰

3.4 Field-of-View

Lateral truncation of the object in projection views can cause significant reconstruction artifacts – especially if high-contrast structures are presented inconsistently between views; therefore, it is highly desirable that the FOV encompass the lateral extent of the object in all views (e.g., ~25 and ~40 cm for a typical “head” and “body,” respectively). Although, advances in reconstruction techniques, such as local tomography, will help to relax this restriction, lateral truncation brings important considerations for imaging geometry, FPI size, and design of the x-ray source. The imaging geometry depends on the mechanical embodiment (e.g., source-to-isocenter and source-to-detector distance ranging from ~65 to 100 cm and ~135 to 170 cm for the C-arm and linear accelerator platforms, respectively); furthermore, the geometry should accommodate the patient and support without impeding access. Moreover, selection of imaging geometry should knowledgeably account for the effects on physical performance, including spatial resolution and scatter rejection.¹¹ Current FPI fabrication supports the creation of monolithic panels up to ~41 cm in width, with imagers up to ~80 cm in width conceivable through tiling. Some of these issues are illustrated for the case of a C-arm or similar structure in Fig. 5(a). For the FPI in a centered geometry (i.e., the FPI matrix nearly centered on the axis of the x-ray beam), the FOV is typically constrained to smaller anatomy. The FOV can be nearly doubled using an offset geometry,¹⁷ although this technique requires acquisition of projections across 360°. Considering the geometrical constraints and ranges in FOV, however, it becomes clear that the ideal proportions of an FPI for cone-beam CT may be less a square (e.g., 41x41cm²) and more a rectangle (e.g., ~26x64 cm²), providing sufficient lateral FOV for large anatomy while maintaining areal FOV for radiographic/fluoroscopic imaging and volume imaging.

Figure 5(b) illustrates the constraints and requirements that large FOV places on the design of the x-ray source, considering the simple tangent rule relating anode angle and lateral FOV. The results indicate that a large anode angle (e.g., greater than 11°) is required for typical (longitudinally mounted) tube orientations. Tilting the tube (within the constraints of focal spot blur) or cross-mounting the tube (so that anode angle limits only the longitudinal FOV) mollify these restrictions.

4. PROCEDURE-SPECIFIC IMAGING TASKS

An advantage of flat-panel cone-beam CT lies in its adaptability – e.g., through knowledgeable selection of parameters (such as speed, dose, spatial resolution, and imaging geometry) within clinical and logistical constraints to satisfy a specific image-guidance task. Two such cases are considered below to examine somewhat qualitatively the performance of flat-panel cone-beam CT in guiding procedures varying widely in terms of constraints and imaging task.

4.1 Procedure-Specific Imaging Task 1: Image-Guided Brachytherapy

A phantom was designed to test the imaging performance of the flat-panel cone-beam CT system in Fig. 1(a) under conditions corresponding to a procedure-specific task in prostate brachytherapy – specifically, to visualize the distribution of Pd-103 seeds relative to the prostate capsule and surrounding anatomy in the presence of severe x-ray scatter and beam-hardening artifacts. The abstract pelvis phantom is illustrated in Fig. 6(a), designed according to a statistical average of image data from our patient CT database, except that (due to a 26 cm FOV restriction) the diameter (20 cm) is significantly smaller than a typical pelvis (~40 cm). Figs. 6 (b, c) show images prior to seed insertion, where despite the presence of x-ray scatter artifacts, the prostate capsule and surrounding tissues are fairly well seen – even at full resolution ($0.25 \times 0.25 \times 0.25 \text{ mm}^3$ voxels). Figs. 6 (d-f) show images with the Pd-103 seeds in place, illustrating the strong artifacts associated with the Pb markers within each seed. Clearly, x-ray scatter and beam-hardening correction algorithms¹⁸ should significantly improve overall image quality, but it is worth noting that even without such and at full-resolution, the task of visualizing the seeds relative to surrounding soft-tissues is largely satisfied.

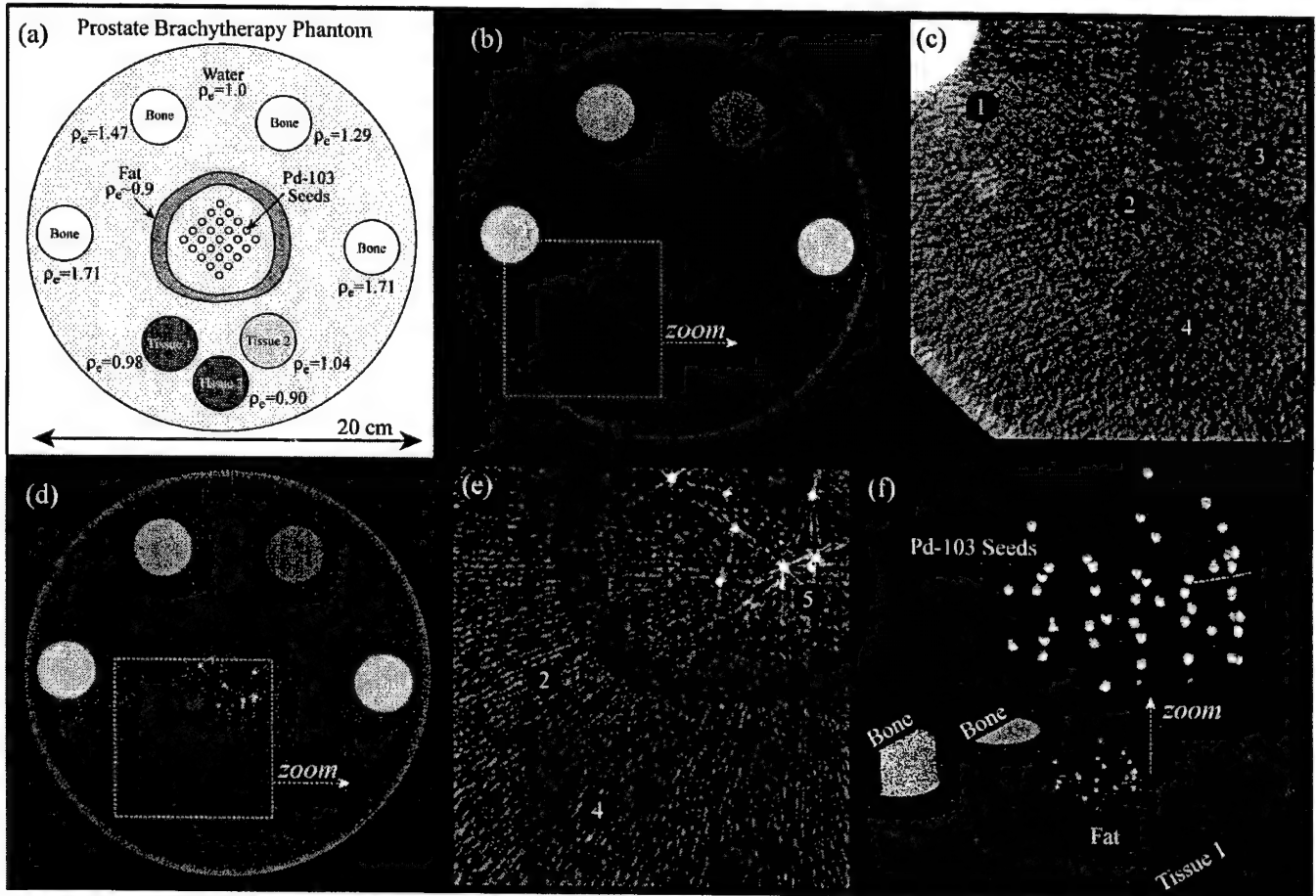


Figure 6. (a) Illustration of the prostate brachytherapy phantom, labeling materials and electron density (relative to water). (b) Transaxial image showing a “pre-therapeutic” image. (All images in this figure are full-resolution; 0.25 mm slice thickness.) (c) Magnified view, showing that despite the presence of artifacts ❶, image quality is sufficient to visualize the layer of fat ❷ from the prostate ❸ and posterior soft-tissues ❹. (d) Transaxial image with Pd-103 seeds inserted in the region of the prostate. (e) Magnified view, showing that the Pb markers in each seed produce significant beam-hardening streak artifacts ❺ that somewhat compromise the visibility of surrounding structures. (f) Surface renderings of the seed distribution in relation to surrounding tissues. The lower part of the image shows the seeds in a 3-D perspective, and the upper part zooms in on the seeds, windowed to show the Pb markers (and a persistent streak artifact).

4.2 Procedure-Specific Imaging Task 2: Image-Guided Vertebroplasty

A second procedure-specific task was constructed to examine the peri-therapeutic value of flat-panel cone-beam CT for guiding a vertebroplasty procedure. Results are summarized in Fig. 7, showing pre-operative (a-c), intra-operative (d,e), and post-operative (f-h) images acquired using the flat-panel cone-beam CT prototype in Fig. 1(a).

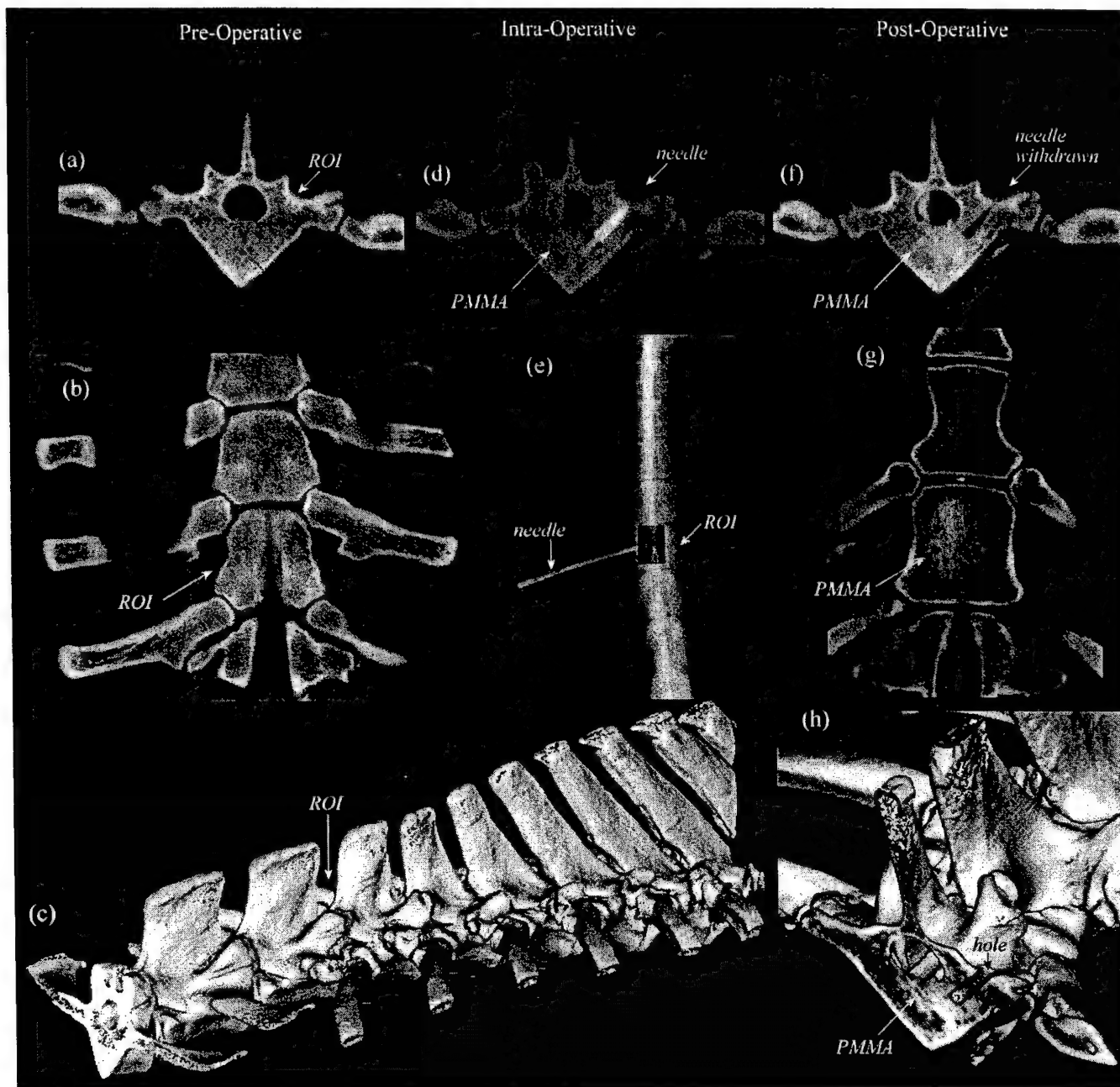


Figure 7. Flat-panel cone-beam CT guidance of vertebroplasty. An idealized procedure was performed in which PMMA bone cement was injected into a region of an ovine spine. This test illustrates the quality of data that would be available to the therapist with flat-panel cone-beam CT if the peri-therapeutic process included fast reconstruction/visualization tools. (a-c) Pre-operative axial, coronal, and volumetric images of the region of interest. (d) Half-resolution axial slice near the needle tip as PMMA is injected into the vertebral body. (e) Example fluorograph used to guide needle placement, illustrating multi-mode R/F/CT capability. (f,g) Post-operative axial and coronal images of the region of interest, where the PMMA is visible as an enhanced region within the vertebral body. In this test, no barium was added to the PMMA. These images clearly show that the PMMA flowed beyond the vertebral body and into vasculature and the dural space of the spinal canal. Fast reconstruction and visualization tools in the peri-therapeutic process would help avoid such problems. (h) Post-operative volume image of the PMMA distribution within the region of interest. Note the hole left by the needle.

5. DISCUSSION AND CONCLUSIONS

Considerable attention has been paid to quantifying the imaging performance of flat-panel imagers in cone-beam CT, e.g., concerning detector performance, noise and spatial resolution, optimal geometry, and the effects of image lag and x-ray scatter. As the technology proves itself to be a viable means of high-quality volumetric imaging, it is natural to consider the spectrum of applications to which it can be applied. While there are numerous fields of medicine that could potentially benefit from such technology, it is image-guided procedures – specifically IG therapy – that best captures the unique advantages of flat-panel cone-beam CT, including volumetric imaging of soft and bony tissue, an open geometry, and combined R/F/CT modes of image acquisition. Directing the application of flat-panel cone-beam CT in IG procedures, however, requires consideration not only of the imaging physics, but also of numerous engineering, clinical, and logistical challenges, including: design of suitable gantry structures (e.g., C-arms or other open platforms); development of advanced reconstruction hardware and techniques (particularly regarding speed and artifact suppression); integration of navigational tools; and creation of fast, convenient methods of integrating and visualizing image data in appropriate reference frames.

This paper has briefly outlined some of the logistical issues regarding platforms for flat-panel cone-beam CT applied to IG procedures. Three of the most notable concerns are time (i.e., speed and frequency of image acquisition), dose to patient, and field-of-view. The question of speed is likely to be answered by a combination of fast FPI readout electronics (e.g., 30 fps) and reconstruction hardware featuring dedicated parallel processors. Patient dose in flat-panel cone-beam CT appears low, comparable to less than a minute of fluoroscopy, and with the potential for further reduction through implementation of FPIs with enhanced DQE. The third issue, field-of-view, is perhaps the most onerous, demanding careful consideration of imaging geometry, source design and orientation, detector size, allowed orbits, and orbital extent – all in relation to the size of patient anatomy to be imaged. Of course there are other concerns as well that are subjects of on-going investigation – e.g., geometric accuracy and uniformity, the issue of breathing motion, and the implementation of gated image acquisition techniques such as ABC.¹⁶ In light of these challenging issues, it becomes clear that while flat-panel cone-beam CT is a highly adaptable technology, there is not likely to be a single embodiment that provides a blanket solution across all IG procedures; rather, design of the imaging system should account carefully for the specific image-guidance task.

The two procedure-specific imaging tasks discussed herein qualitatively illustrate some of the challenging and promising aspects of flat-panel cone-beam CT for IG therapy. For IG brachytherapy of the prostate, the large FOV poses a significant challenge and requires investigation into alternative acquisition methods and orbits (e.g., double-scan trajectory with offset detector geometry) and/or improved methods of local / limited view reconstruction. Artifacts resulting from, e.g., x-ray scatter and beam-hardening – although significant – require attention only to the extent that they limit the imaging task, since the goal is to guide therapy (and not reproduce the quality of diagnostic images). The IG vertebroplasty example demonstrates the excellent volumetric image quality that can be achieved with flat-panel cone-beam CT, but highlights the fact that fast reconstruction and visualization are key to a useful implementation of the technology. The range of IG procedures to which flat-panel cone-beam CT could potentially be applied is almost as broad as the spectrum of procedures in modern practice, including, for example: spinal fixation and screw placement; minimally invasive intracranial procedures; orthopedics, particularly in extremities; vascular procedures; tumor ablation; and needle biopsy, providing visualization of the soft-tissue target and the interventional device (e.g., needle, stent, etc.) in a multi-mode R/F/CT capacity.

With this broad spectrum of IG applications in mind, we have begun development of an image-guided operating room (IGOR) laboratory within the Research Institute at William Beaumont Hospital, creating a theatre in which new IG technologies and surgical techniques can be brought together in pre-clinical investigation, with flat-panel cone-beam CT (e.g., using a C-arm gantry) as a central imaging resource. The past few years have witnessed an important convergence of technologies (e.g., FPIs, reconstruction hardware, navigational tools, etc.) that allows such investigation, providing an opportunity to explore not only the performance of flat-panel cone-beam CT but also the means by which this technology can best be brought to bear on clinical image-guidance tasks.

ACKNOWLEDGEMENTS

This work was supported by National Institutes of Health grant R01 CA89081-01 and Prostate Cancer Research Program Grant No. DAMD 17-98-1-8497. The authors gratefully acknowledge Dr. Kevin Brown (Elekta Oncology Systems, Surrey England) for provision of the flat-panel imagers and Dr. Mario Gauer (PerkinElmer Optoelectronics, Wiesbaden Germany) for technical information regarding FPI operation and performance. The assistance of Drs. Jochen Kusch and Marcus Zimmermann-Ritterer (Siemens Medical Systems, Erlangen Germany) in providing the C-arms and related technical information is greatly appreciated. The mechanical skills of Mr. Walter Jendhoff (Beaumont Service Corp.) were indispensable to this work, and the advice and assistance of Mr. John Locy (Department of Anatomic Pathology) is greatly appreciated. The authors thank Dr. Donovan Bakalayar (Department of Radiology) for provision of the head and body phantoms used in the dose measurements.

REFERENCES

1. L. D. Lunsford, A. E. Rosenbaum, and J. Perry, "Stereotactic surgery using the 'therapeutic' CT scanner," *Surg. Neuro.* 18(2) 116-122 (1982).
2. M. Uematsu, A. Shioda, K. Tahara, et al., "Focal, high dose, and fractionated modified stereotactic radiation therapy for lung carcinoma patients: a preliminary experience," *Cancer* 82(6): 1062-1070 (1998).
3. D. A. Jaffray, J. H. Siewerdsen, and D. G. Drake, "Performance of a volumetric CT scanner based upon a flat-panel imaging array," *Medical Imaging 1999: Physics of Medical Imaging*, SPIE Vol. 3659, 204-214 (1999).
4. R. Ning, X. Tang, R. Yu, D. Zhang, and D. Conover, "Flat panel detector-based cone beam volume CT imaging: detector evaluation," *Medical Imaging 1999: Physics of Medical Imaging*, SPIE Vol. 3659, 192-203 (1999).
5. D. A. Jaffray, J. H. Siewerdsen, J. W. Wong, and A. A. Martinez, "Flat-panel cone-beam CT for image-guided radiation therapy," *Int. J. Radiat. Oncol. Biol. Phys.* (submitted Jan. 2001).
6. L. A. Feldkamp, L. C. Davis, and J. W. Kress, "Practical cone-beam algorithm," *JOSA A*. 1(6) 612-619 (1984).
7. D. A. Jaffray and J. H. Siewerdsen, "A volumetric cone-beam CT system based on a 41x41 cm² flat-panel imager," *Medical Imaging 2001: Physics of Medical Imaging*, Proc. SPIE (2001).
8. J. H. Siewerdsen and D. A. Jaffray, "Cone-beam computed tomography with a flat-panel imager: effects of image lag," *Med. Phys.* 26(12) 2635-2647 (1999).
9. J. H. Siewerdsen and D. A. Jaffray, "Cone-beam CT with a flat-panel imager: noise considerations for fully 3-D imaging," *Medical Imaging 2000: Physics of Medical Imaging*, SPIE Vol. 3336, pp. 546-554 (2000).
10. J. H. Siewerdsen and D. A. Jaffray, "Cone-beam computed tomography with a flat-panel imager: Magnitude and effects of x-ray scatter," *Med. Phys.* 28(2) 220-231 (2001).
11. J. H. Siewerdsen and D. A. Jaffray, "Optimization of x-ray imaging geometry (with specific application to flat-panel cone-beam computed tomography)," *Med. Phys.* 27(8) 1903-1914 (2000).
12. R. Fahrig and D. W. Holdsworth, "Three-dimensional computed tomographic reconstruction using a C-arm mounted XRII: image-based correction of gantry motion nonidealities," *Med. Phys.* 27(1) 30-38 (2000).
13. M. Grass, R. Koppe, E. Klotz, R. Proksa, M. H. Kuhn, H. Aerts, J. Op de Beek, and R. Kemkers, "Three-dimensional reconstruction of high contrast objects using C-arm image intensifier projection data," *Comp. Med. Imag. Graph.* 23: 311-321 (1999).
14. P.R. Granfors, "Performance characteristics of an amorphous silicon flat panel x-ray imaging detector," *Medical Imaging 1999: Physics of Medical Imaging*, SPIE Vol. 3659, 480-490 (1999).
15. J. H. Siewerdsen, L. E. Antonuk, Y. El-Mohri, J. Yorkston, W. Huang, and I. A. Cunningham, "Signal, noise power spectrum, and detective quantum efficiency of indirect-detection flat-panel imagers for diagnostic radiology," *Med. Phys.* 25(5), 614-628 (1998).
16. J. Wong, M. Sharpe, and D. Jaffray, "The use of active breathing control (ABC) to minimize breathing motion in conformal therapy," in *Proceedings of the 12th International Conference on the Use of Computers in Radiation Therapy*, D. Leavitt and G. Starkschall Eds., 220-222 (1997).
17. P. Cho, R.H. Johnson, T.W. Griffin, "Cone-beam CT for radiotherapy applications," *Phys. Med. Biol.* 40, 1863-1883 (1995).
18. J. Hsieh, R. C. Molthen, C. A. Dawson, and R. H. Johnson, "An iterative approach to the beam hardening correction in cone beam CT," *Med. Phys.* 27(1) 23-29 (2000).

*Electronic mail: jsiewerd@beaumont.edu; Phone: 248-551-2219; Fax: 248-551-0089; Department of Radiation Oncology, William Beaumont Hospital, 3601 West Thirteen Mile Rd., Royal Oak, MI 48073-6769

**Appendix K: A Volumetric Cone-Beam Computed Tomography
System Based on a 41x41 cm² Flat-Panel Imager**

A Volumetric Cone-Beam CT System Based on a 41x41 cm² Flat-Panel Imager

D.A. Jaffray and J.H. Siewerdsen
William Beaumont Hospital, Royal Oak, MI 48073

ABSTRACT

Cone-beam computed tomography (CBCT) based upon large-area flat-panel imager (FPI) technology is a flexible and adaptable technology that offers large field-of-view (FOV), high spatial resolution, and soft-tissue imaging. The imaging performance of FPI-based cone-beam CT has been evaluated on a computer-controlled bench-top system using an early prototype FPI with a small FOV (20.5×20.5 cm²). These investigations demonstrate the potential of this exciting technology. In this report, imaging performance is evaluated using a production grade large-area FPI (41×41 cm²) for which the manufacturer has achieved a significant reduction in additive noise. This reduction in additive noise results in a substantial improvement in detective quantum efficiency (DQE) at low exposures. The spatial resolution over the increased FOV of the cone-beam CT system is evaluated by imaging a fine steel wire placed at various locations within the volume of reconstruction. The measured modulation transfer function (MTF) of the system demonstrates spatial frequency pass beyond 1 mm⁻¹ (10% modulation) with a slight degradation at points off the source plane. In addition to investigations of imaging performance, progress has also been made in the integration of this technology with a medical linear accelerator for on-line image-guided radiation therapy. Unlike the bench-top system, this implementation must contend with significant geometric non-idealities caused by gravity-induced flex of the x-ray tube and FPI support assemblies. A method of characterizing and correcting these non-idealities has been developed. Images of an anthropomorphic head phantom qualitatively demonstrate the excellent spatial resolution and large FOV achievable with the cone-beam approach in the clinical implementation.

Keywords: cone-beam computed tomography, amorphous silicon, flat-panel detector, radiation therapy

1. INTRODUCTION AND MOTIVATION

The development of a versatile volumetric image-guidance technology promises to improve the quality of localized therapeutic procedures. Increases in geometric precision brought about through intra-therapeutic guidance will both reduce therapy-induced complications and increase the probability of successful outcome – ultimately leading to new and refined applications of proven therapies. Cone-beam computed tomography based upon recently developed flat-panel imager technology provides volumetric imaging that can be readily adapted to a variety of therapy settings. Investigations of FPI-based CBCT have begun to quantitatively reveal the potential and limitations of this exciting technology.¹⁻⁹ In this report, the performance improvements of our second generation CBCT system based upon a large area FPI (41×41cm²) are described. The adaptation of this system to a medical linear accelerator for on-line image-guided radiation therapy demonstrates the suitability of this technology for intra-therapeutic guidance.

2. LARGE-AREA FLAT-PANEL DETECTOR

A large area FPI (41×41cm²), shown in Fig. 1(a), has replaced the smaller panel (20.5 x 20.5 cm²) reported in previous investigations.⁹ The technical characteristics of the two panels are described in Table I. Functionally, the new imager is a larger version of the former, with readout electronics more appropriately tuned to lower-dose application. An evaluation of additive electronic noise has been performed using previously published methods.¹⁰ The various additive electronic noise sources and their magnitudes are plotted as a function of frame time in Fig. 2(a). The manufacturer has made substantial improvements in performance, reducing the total additive noise to less than 4000 e for frame rates of interest (>0.5 frames/sec). This compares favorably with the ~22,000 e of additive noise observed in the smaller detector. This reduction is achieved through the elimination of row and frame correlated noise and the reduction in amplifier noise by a factor of 4. These are substantial improvements that will significantly improve detector performance at low exposures. The influence of additive noise on the zero-frequency detective quantum efficiency (DQE) was studied using a cascaded systems model that analyzes signal and noise propagation in the FPI.¹¹ Figure 2(b) shows the predicted dependence of DQE on exposure for the previous FPI (curve 1), the current large-area FPI (curve 2), and an equivalent panel incorporating a 250 mg/cm² CsI:Tl x-ray converter (curve 3). For exposures below 0.1 mR, the large-area panel is expected to perform much

better than the original prototype. Maintaining DQE at these low exposures is a paramount concern for application in CBCT where the total patient dose is distributed over multiple low-dose projections. This new detector has been integrated into the bench-top system used in previous investigations as well as a gantry-based system adapted to a medical linear accelerator.

3. BENCH-TOP SYSTEM

3.1 Description

The bench top system is illustrated in Figure 1(b). The main components of the system are the x-ray tube, the rotation stage, and the large-area FPI. These three components are mounted rigidly to an optical bench, the operation of which is described elsewhere.⁹ Implementation of the large area FPI altered the various geometric parameters of the system - these are described in Table II. In addition to improvements in the detector, the control system has also been improved to allow geometric calibration, image acquisition, processing and reconstruction in an integrated Windows NT-based application. The software runs on a 500 MHz Pentium Xeon processor equipped with 1GB of RAM. A modified Feldkamp cone-beam CT reconstruction algorithm has been implemented that permits reconstruction from projections acquired on non-ideal circular trajectories (see Table II).¹²

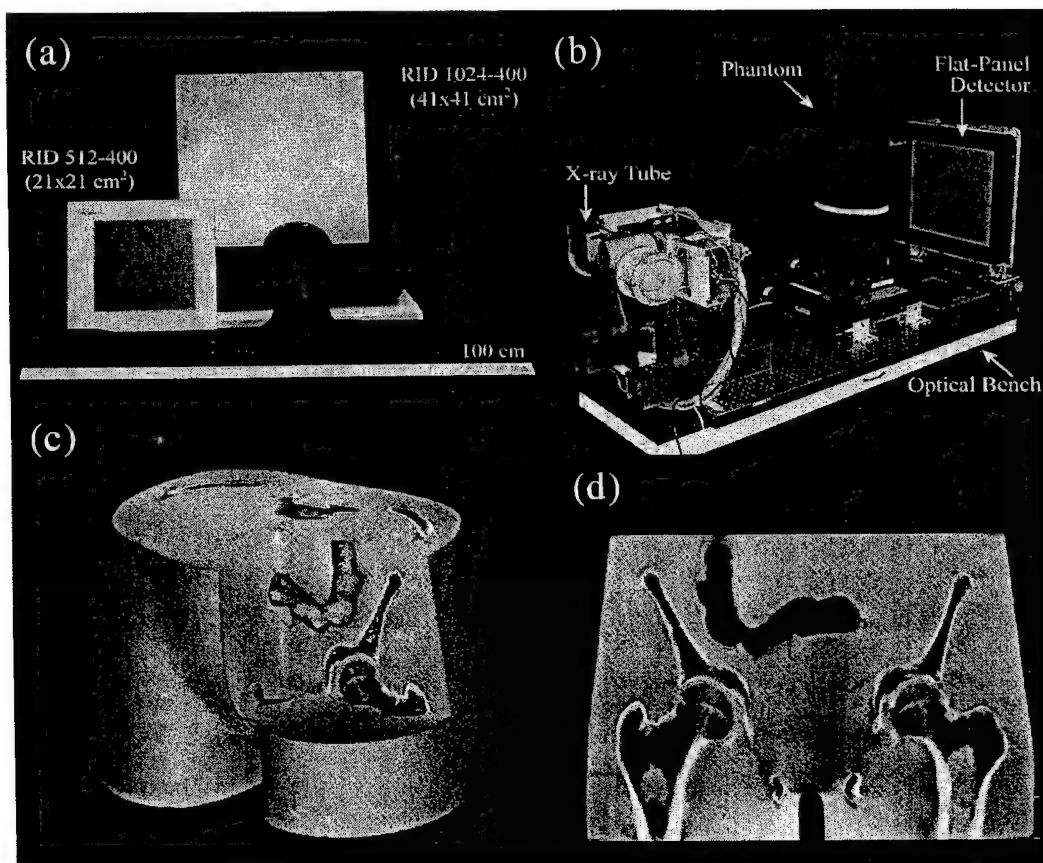


Figure 1. (a) Flat-panel imagers employed in the investigations of kV cone-beam CT. The large area ($41 \times 41 \text{ cm}^2$) production panel (black) replaces the smaller ($20.5 \times 20.5 \text{ cm}^2$) prototype panel used in initial investigations, providing 4 times the sensitive area and offering higher performance (see Table I). (b) Bench-top apparatus for examining the performance of flat-panel x-ray detectors in cone-beam computed tomography. The x-ray tube, rotation and translation tables, and FPI are mounted in a precisely determined, computer-controlled geometry on an optical bench. (c) Volumetric rendering of an anthropomorphic pelvis imaged on the bench-top system. The large field-of-view (FOV) was achieved by acquiring two sets of cone-beam projections with the detector offset. (d) Coronal slice reconstructed at full resolution (1590×1024), illustrating the excellent axial resolution achieved with the cone-beam approach.

Flat-Panel X-ray Detector	Previous	Current
Manufacturer	EG&G Heimann Optoelectronics	PerkinElmer Optoelectronics
Model	RID-512 400 A0	RID-1640 AL1
Mass	8 kg	22 kg
Detector Housing Dimensions	$33 \times 32 \times 4.6 \text{ cm}^3$	$67.2 \times 59.9 \times 4.4 \text{ cm}^3$
X-ray Converter	133 mg/cm ² Gd ₂ O ₂ S:Tb	
Detector Size	$20.5 \times 20.5 \text{ cm}^2$	$41 \times 41 \text{ cm}^2$
Pixel Matrix Format	512 × 512	1024 × 1024
Pixel Pitch	400 μm	
Detector Pixel Elements	a-Si:H Photodiode and Thin-Film Transistor (TFT)	
Fill Factor	0.80	
Photodiode Capacitance	8.4 pF	
Photodiode Bias Voltage	-5V	-6 V
Photodiode Charge Capacity	~42 pC	~48 pC
Charge Transfer Time	35 μs	
ASIC Charge Capacity	23 pC	5 pC
Maximum Frame Rate	5 fps	3.5 fps
Detector Dynamic Range	> 80 dB	> 83 dB
Image Lag	< 3%	
Digitization	16 bits	

Table I. Summary of manufacturer specifications for the $20.5 \times 20.5 \text{ cm}^2$ and $41 \times 41 \text{ cm}^2$ flat panel imagers.

3.2 Field-of-View

The large area of the FPI allows a substantial increase in the field-of-view (FOV) of the CBCT system. For the geometry employed on the bench, the reconstruction FOV is a 25.8 cm diameter cylinder, 25.8 cm in length. This FOV is sufficient for imaging the head and neck region of adults; however, it is typically not sufficient for the thorax or pelvis. The large FOV demonstrated in the images of the anthropomorphic pelvis [Figs. 1(c-d)] was achieved by acquiring two sets of projections with the detector in two positions ($\pm 9.3 \text{ cm}$ offset). For each projection angle, a single 1489×1024 projection was created by stitching two 1024×1024 projections. A 25 pixel wide transition region about the axis of rotation (AOR) was employed to eliminate discontinuities in the stitched image. In this region, the image signal was calculated as a weighted sum of the two

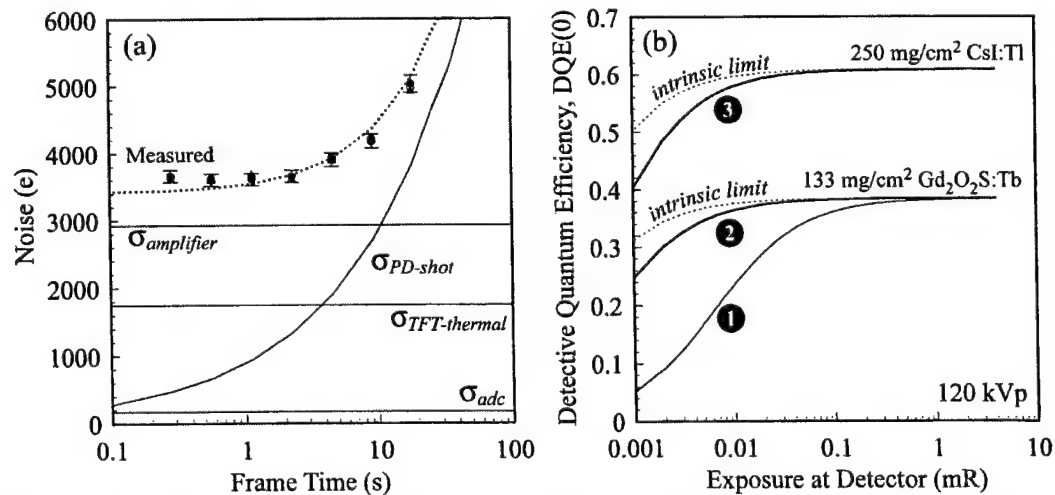


Figure 2. Improvements in detector performance. (a) Measurements of additive electronic noise versus frame time for the $41 \times 41 \text{ cm}^2$ FPI (black circles). Additive noise sources such as TFT thermal noise ($\sigma_{\text{TFT-thermal}}$), photodiode shot noise ($\sigma_{\text{PD-shot}}$), digitization noise (σ_{adc}), and amplifier noise ($\sigma_{\text{amplifier}}$) were computed as described previously,¹⁰ showing that the new FPI is operating within a factor of ~2 of its intrinsic dark noise limit. (b) Zero-frequency DQE calculated as a function of exposure to the detector using a cascaded, linear systems model.¹¹ The dependence is shown for three detectors: (1) the early prototype FPI with amplifier noise, $\sigma_{\text{amplifier}} \sim 12,700 \text{ e}$, (2) the large-area production FPI with improved read-out electronics ($\sigma_{\text{amplifier}} \sim 3,000 \text{ e}$), and (3) a large-area production FPI incorporating a 250 mg/cm² CsI:Tl x-ray converter. The dashed lines indicate the intrinsic limit (no amplifier noise) for the $41 \times 41 \text{ cm}^2$ configurations shown here.

kV Imaging Geometry	Bench Top System	Gantry-based System
Focal Spot – Isocenter Distance (nominal)	100.2 cm	100 cm
Focal Spot – Detector Distance (nominal)	159.4 cm	155 cm
Cone Angle	14.4°	14.8°
Field of View (at isocenter)	(25.8 × 25.8) cm ²	(26.5 × 26.5) cm ²
Location of Projected Isocenter on Detector:		
u-Coordinate (pixel address)	511.5±0.1	517.6 ± 1.1
v-Coordinate (pixel address)	513.4±0.1	496.3 ± 1.2
Cone-Beam CT Acquisition Parameters		
Tube Potential	120 kVp	
Total Filtration	2.5mm Al + 0.129mm Cu	2.0 mm Al +0.129mm Cu
Number of Exposures (nominal)	300	330
Tube Output (mR/mAs in air at isocenter)	9.3 mR/mAs	5.7 mR/mAs
Angular Range of Projection Views	360°	
Average Angular Velocity	1.1°/sec	(2.0±0.2)°/sec
Average Angular Increment	1.2°	(1.1 ±0.3)°
Detector Readout Interval (Frame Time)	1.14 sec	570 ms
Time for CBCT Acquisition	342 sec	188 sec
Processing and Reconstruction Parameters		
Flood-Field Processing	Gain / Offset Correction	
Pixel Defect Filter	3x3 Median Filter	
Reconstruction Filter	Hamming	
Reconstruction Field of View (at isocenter)	(25.8) ³ cm ³	(26.5) ³ cm ³
Reconstruction Matrix (nominal)	(1024 × 1024 × 1024) voxels	
Voxel Dimensions (nominal)	(0.25 × 0.25 × 0.25) mm ³	

Table II: Geometric, acquisition, and reconstruction parameters for the bench-top and gantry-based systems.

projections. The projections were then filtered and resampled at one-third resolution (0.12 cm). A 496x496x341 volume was reconstructed and is shown in Fig. 1(c). A substantial cupping artifact was visible in the reconstructed image but was removed through a single three-dimensional (3-D) parabolic shading correction. The weighting factors for the parabolic shading correction were chosen manually to minimize the global shading. The influence of x-ray scatter on local signal

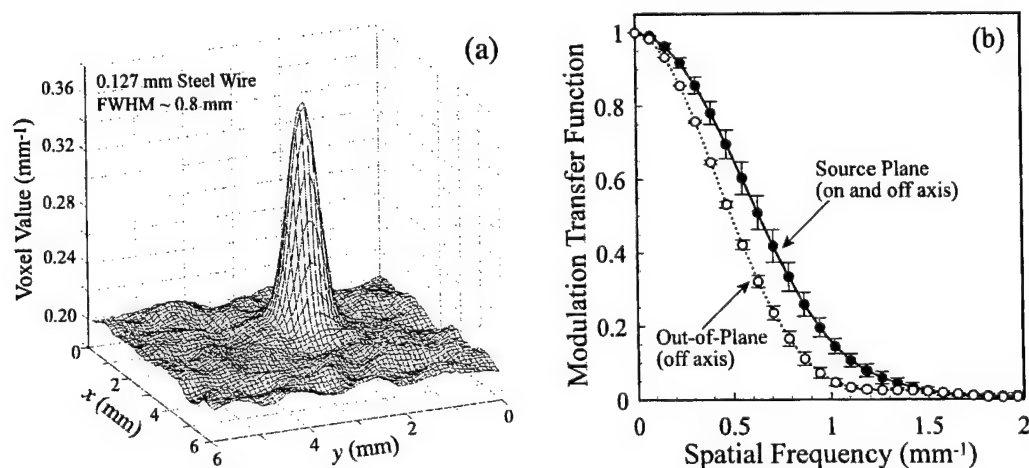


Figure 3. Spatial resolution of the flat-panel CBCT system. (a) Surface plot of the system response as approximated by measurements of a thin (0.127 mm) steel wire. (b) MTF of the CBCT system determined from images of the steel wire. The system MTF was obtained by correcting the measured MTF for the in-plane frequency content of the wire. The MTF was measured at three locations in the volumetric FOV: (i) 2 cm off the AOR on the source plane; (ii) 8 cm off the AOR on the source plane; and (iii) 8 cm off the AOR at 10 cm above the source plane. The system MTF on the source plane did not vary with position within experimental uncertainty. The reduction in system MTF with axial position may be caused by a small misalignment between the AOR and the readout columns of the FPI.

uniformity was not corrected with this method and is clearly visible near regions of sharp contrast as visible about the perineum. As an alternative to stitching projections, Cho et al.¹³ have developed an offset-detector scheme that gives equivalent FOV but requires only one 360° rotation.

3.3 Spatial Resolution

The spatial resolution of the CBCT system was measured using a 127 μm (0.005") diameter steel wire oriented longitudinally in a 12 cm diameter water bath and imaged at three locations: 1) on the source plane at ~2 cm from the axis of rotation (AOR); 2) on the source plane at ~8 cm from the AOR; and 3) 10 cm above the source plane at 8 cm from the AOR. Forty adjacent slices containing the wire were reconstructed with 0.1 mm in-plane resolution and axial resolution of 0.25 mm. The forty slices were averaged along the z-dimension into 10 groups of 4 slices each. A surface plot of the reconstructed spread function for location #1 is shown in Fig. 3(a), giving FWHM of ~0.8 mm. The system MTF in the axial plane was calculated by projecting the measured spread function in one dimension (i.e., Radon transform), computing the discrete Fourier transform, and dividing by the frequency content of the wire. This calculation was performed for each of the 10 groups. The system MTF was taken to be the average, with error bars corresponding to the standard deviation among the 10 groups. The results are plotted in Fig. 3(b) for each of the three measured positions. The frequency pass of the system exceeds 1 mm^{-1} in the source plane. The MTF of the system is significantly reduced at 10 cm above of the source plane, possibly due in part to a small rotation between the AOR and the readout columns of the FPI.

4. CONE-BEAM CT SYSTEM ON A MEDICAL LINEAR ACCELERATOR

4.1 Description

The large-area flat-panel imager has been adapted to an isocentric medical linear accelerator equipped with a 600 kHU x-ray tube [Fig. 4(a)]. The x-ray tube is mounted to the drum structure of the accelerator on a retractable arm that extends ~130 cm from the gantry face, allowing the focal spot of the tube to reach the plane occupied by the MV treatment source. The tube is driven by a 45 kW high-frequency x-ray generator (Ideal, Innerscan Inc., Chicago IL) and has 2 mm of Al (inherent) and 0.127 mm of Cu (added) filtration. The FPI is mounted opposite the x-ray tube at a source-detector distance of approximately 155 cm. The imager is supported by a fixed mount comprised of three extruded Al struts holding the FPI parallel to the rotation axis of the drum, approximately centered on the central ray of the kV x-ray beam. X-ray exposure, detector read-out and gantry motion is coordinated using the same Windows-NT based software application as described in Section 3.1. The software application monitors gantry angle through a precision potentiometer, directs x-ray exposure, and collects the resulting projections in host memory.

In comparison to the investigations performed on the bench-top, the accelerator-based system must contend with sources of geometric non-ideality: (i) variations in angular projection increment, and (ii) geometric instability between the focal spot and imager. The variations in angular increment result from mechanical imbalance of the gantry structure due to the added weight of the panel and support arm. Gantry movement is achieved through the 'assisted set-up (ASU)' movements of the accelerator. Under this mode, the various components of the accelerator are instructed to move under computer control. Unfortunately, the control system for gantry rotation does not fully compensate for the mechanical imbalance, resulting in substantial variations in angular velocity with gantry angle. The angular velocity was found to vary from 1.5°/sec to 3.0°/sec through 360°, excluding periods of acceleration/deceleration at the start and stop of acquisition.

The motion of the FPI and x-ray tube through the gravitational field during gantry rotation results in deflection of the support arms, which significantly alters the geometric relationship between the focal spot and FPI. A method to measure and accommodate these deflections has been developed. Multiple radiographs of a 0.8 cm steel ball-bearing (BB) placed near isocenter are acquired as the gantry rotates through 360°. Centroid analysis of the BB shadow in each projection describes (i) the relative position of the BB and isocenter, (ii), gravity-induced motion between the focal spot and panel, and, (iii) gross displacements of the gantry structure in the world reference frame. Displacements between the BB and isocenter appear as nearly sinusoidal and can be corrected by repositioning the BB. The non-sinusoidal motion is attributed to flex and gross displacement of the gantry structure. These motions are recorded and converted to a correction map that adjusts the back-projection geometry during reconstruction. The measured motion of the BB shadow on the face of the imager with gantry angle is presented in Figure 4(b). The motion contains both low-frequency and high-frequency motion with changing gantry angle. Movement of the projected BB location in the axial direction (v, parallel to AOR) is also seen in this analysis and results from axial displacement of the gantry structure with rotation (corkscrew motion). Overall, the motion is small (± 1 mm on the panel) considering the large scale of the motion (2 m diameter circle) and the length of the support arms (~1.3 m).

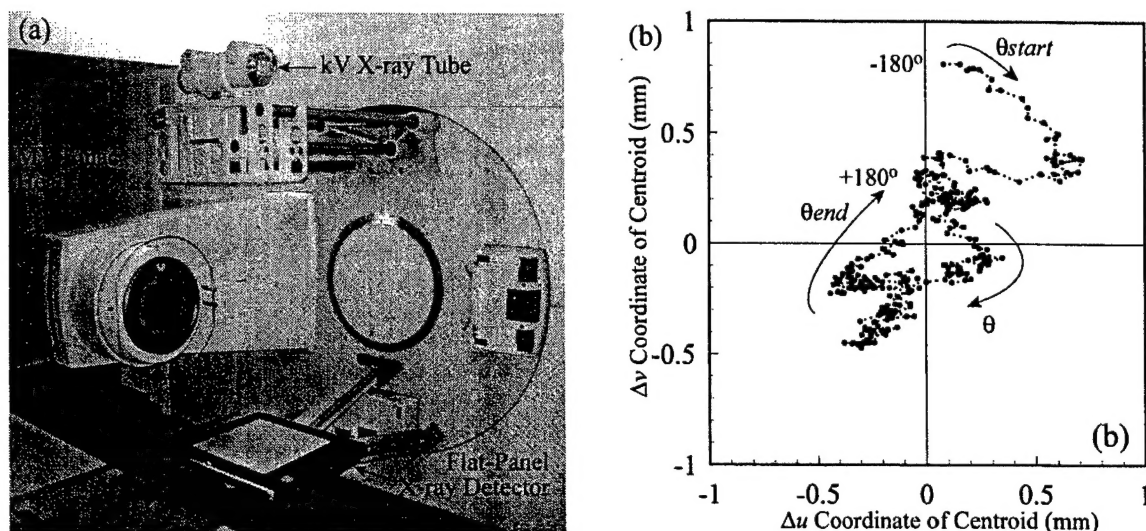


Figure 4. Flat-panel cone-beam CT on a medical linear accelerator. (a) The large-area FPI is mounted on the gantry structure of the accelerator opposite a 600 kVp x-ray tube. (b) The substantial mass of the components result in gravity-induced flex in the source and detector supports during gantry rotation. Movement between the source and detector is characterized using a ball bearing placed at the nominal isocenter of the kV imaging system. The projected isocenter moves with respect to the detector during gantry rotation. These measurements are employed during reconstruction to improve the accuracy of the back-projections.

4.2 Imaging of Head Phantom

System performance was evaluated qualitatively using an anthropomorphic head phantom. The phantom consists of the head and torso of a human skeleton embedded in plastic (The Phantom Laboratory, Salem NY). With the head of the phantom suspended off the end of the treatment couch, 321 projections (120 kVp, 25 mA, 0.025 s) were acquired over 183 seconds as the gantry rotated through 360°. The in-air exposure (in the absence of phantom) delivered to the isocenter for this technique is 1.2 R. A low-resolution volume (341×341×341 voxels at 0.75 mm voxel pitch) and high-resolution sagittal slice (1024×1024 voxels at 0.25 mm voxel pitch) were reconstructed for presentation and are shown in Fig. 5. The volumetric surface rendering of the reconstruction [Fig. 5(a)] illustrates the large FOV achieved with a single rotation of the gantry in the cone-beam approach. Figures 5(b-d) illustrate the excellent spatial resolution in the axial dimension and the large FOV achieved in a single acquisition. Each of these images was reconstructed from the same cone-beam CT data set, with correction for geometric non-idealities based on the measurements in Fig. 4(b). The images presented at a higher magnification [Figs. 5(c-d)] further emphasize the spatial detail of the system, qualitatively demonstrating detail within individual teeth as well as visualization of trabecular bone structure in the cervical spine.

5. SUMMARY, CONCLUSIONS, AND FUTURE WORK

Investigations of flat-panel cone-beam CT performance on a laboratory system have demonstrated the potential of this exciting new technology for image-guidance tasks.^{1,4-9} Several key issues have been addressed in these investigations, including flat-panel imager performance, detector lag and lag artifacts, optimal geometric conditions, and the influence of x-ray scatter on contrast-to-noise performance. The conclusions drawn from these investigations strongly support the hypothesis that flat-panel cone-beam CT is well suited for applications in image-guidance. Evaluation of additive noise in the large area panel highlights the progress in flat-panel imager technology, with low additive noise dramatically improving detector DQE at low exposure levels. This is of great importance in cone-beam CT where the entire object must be included in the detector FOV to guarantee a consistent data set. Overall, advances in FPI performance continue to make them attractive detectors for cone-beam CT.

Our first clinical implementation of this exciting technology is in image-guided external beam radiation therapy. The challenges in adapting this technology to a clinical system have been integration with the treatment machine and accommodation of geometric non-idealities. The results reported here suggest that the geometric non-idealities can be managed through a calibration procedure that records the non-idealities, allowing corrections to be applied during reconstruction. Investigations of soft-tissue imaging performance on the medical linear accelerator-based system are required to determine if these corrections will satisfy the requirements for image-guided radiation therapy.

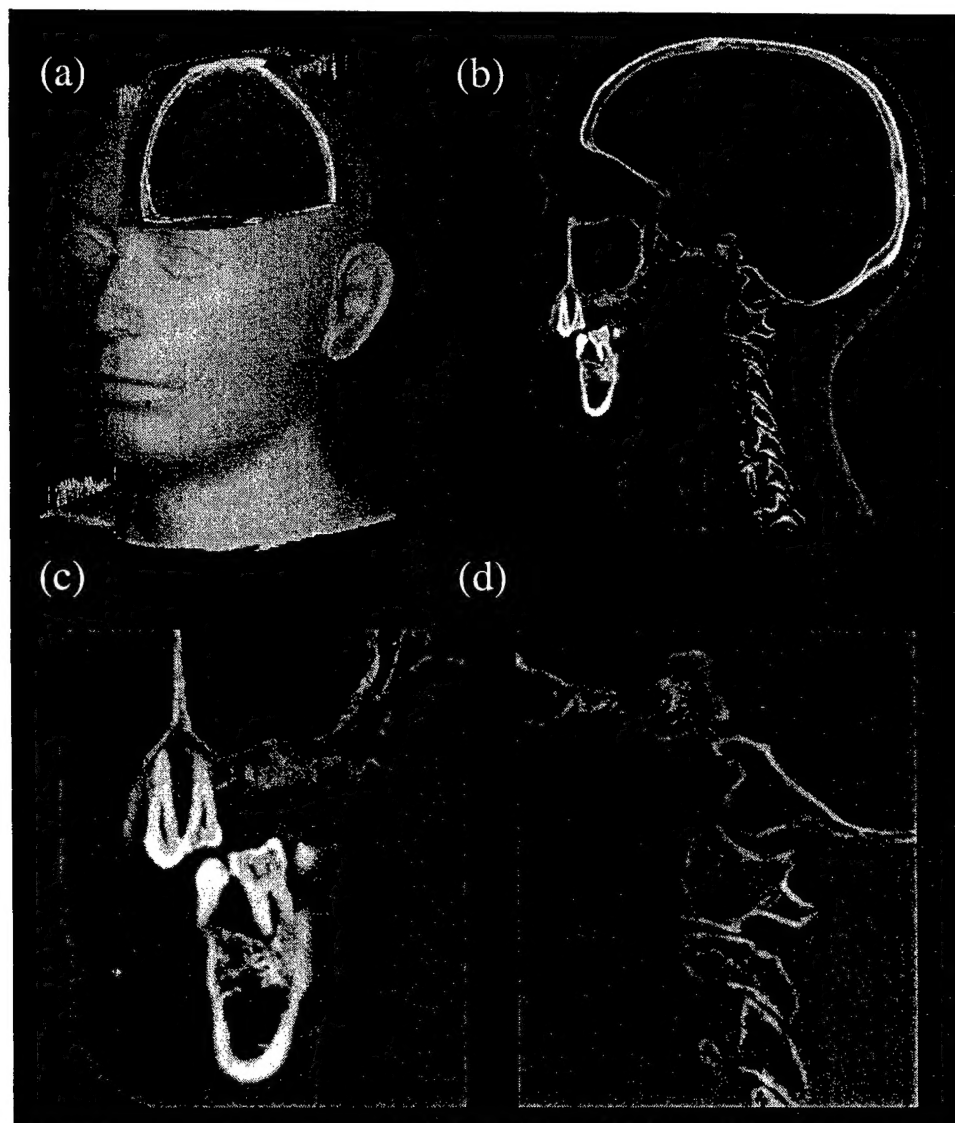


Figure 5. Cone-beam CT images acquired on the medical linear accelerator. (a) Volumetric rendering of an anthropomorphic head phantom reconstructed [$389 \times 389 \times 389$ voxels at $(0.75 \text{ mm})^3$] from 330 projections acquired over 360° . (b) A single sagittal slice [$1 \times 1024 \times 1024$ at $(0.25 \text{ mm})^3$] illustrates the high spatial resolution that can be achieved in the axial dimension with the cone-beam approach. The spatial resolution of the system is demonstrated in the magnified sagittal views shown in (c) and (d). It is important to emphasize that the resolution demonstrated here has been achieved on the medical linear accelerator-based system in the presence of geometric non-idealities.

The development of a medical linear accelerator with integrated volumetric imaging promises unprecedented geometric precision in radiation delivery. The implications for radiation therapy practice are both exciting and challenging to predict; however, it is clear that intra-therapeutic guidance will reduce the barriers leading to innovative applications of this proven therapy.

ACKNOWLEDGMENTS

The authors would like to thank Mr. T. Wilkins and Mr. Walter Jendhoff for their assistance with the CBCT system and Dr. M. K. Gauer for providing technical information concerning the FPI. The support and encouragement of Dr. A. Martinez and Dr. J. Wong are greatly appreciated. These investigations are supported in part by the National Institute of Health (NCI R01-CA89081), the U.S. Army Prostate Cancer Research Program (DAMD17-98-1-8497), and by Elekta Oncology Systems.

REFERENCES

1. D. A. Jaffray and J. H. Siewerdsen, "Cone-beam computed tomography with a flat-panel imager: initial performance characterization," *Med. Phys.* 27(6) 1311-1323 (2000).
2. R. Ning, D. Lee, X. Wang, Y. Zhang, D. Conover, D. Zhang, and C. Williams, "Selenium flat panel detector-based volume tomographic angiography imaging: phantom studies," *SPIE Medical Imaging 1998: Physics of Medical Imaging*, J. M. Boone and J. T. Dobbins III, Eds., Vol. 3336, 316-324 (1998).
3. R. Ning, X. Tang, R. Yu, D. Zhang, and D. Conover, "Flat panel detector-based cone beam volume CT imaging: detector evaluation," *SPIE Medical Imaging 1999: Physics of Medical Imaging*, J. M. Boone and J. T. Dobbins III, Eds., Vol. 3659, 192-203 (1999).
4. J. H. Siewerdsen and D. A. Jaffray, "Cone-beam computed tomography with a flat-panel imager: effects of image lag," *Med. Phys.* 26(12) 2635-2647 (1999).
5. J. H. Siewerdsen and D. A. Jaffray, "Cone-beam CT with a flat-panel imager: noise considerations for fully 3-D imaging," *Medical Imaging 2000: Physics of Medical Imaging*, SPIE Vol. 3336, pp. 546-554 (2000).
6. J. H. Siewerdsen and D. A. Jaffray, "Cone-beam computed tomography with a flat-panel imager: Magnitude and effects of x-ray scatter," *Med. Phys.* 28(2) 220-231 (2001).
7. J. H. Siewerdsen and D. A. Jaffray, "Optimization of x-ray imaging geometry (with specific application to flat-panel cone-beam computed tomography)," *Med. Phys.* 27(8) 1903-1914 (2000).
8. J. H. Siewerdsen, D. A. Jaffray, G. K. Edmundson, W. P. Sanders, J. Wong, and A. A. Martinez, "Flat-panel cone-beam CT: A novel imaging technology for image-guided procedures," *SPIE Medical Imaging 2001: Visualization, Display, and Image-Guided Procedures* Vol. 4319 (2001).
9. D. A. Jaffray, J. H. Siewerdsen, and D. G. Drake, "Performance of a volumetric CT scanner based upon a flat-panel imaging array," *Medical Imaging 1999: Physics of Medical Imaging*, SPIE Vol. 3659, 204-214 (1999).
10. J. H. Siewerdsen and D. A. Jaffray, "A ghost story: spatio-temporal response characteristics of an indirect-detection flat-panel imager" *Med. Phys.* 26(8) 1624-1641 (1999).
11. J. H. Siewerdsen, L. E. Antonuk, Y. El-Mohri, J. Yorkston, W. Huang, and I. A. Cunningham, "Signal, noise power spectrum, and detective quantum efficiency of indirect-detection flat-panel imagers for diagnostic radiology," *Med. Phys.* 25(5), 614-628 (1998).
12. Personal communication, R. Clackdoyle and F. Noo.
13. P. Cho, R.H. Johnson, T.W. Griffin, "Cone-beam CT for radiotherapy applications," *Phys. Med. Biol.* 40, 1863-1883 (1995).